# Search for Large Spatial Extra Dimensions with Dimuon Events from 7 TeV pp collisions at CMS

Von der Fakultät für Mathematik, Informatik und Naturwissenschaften der RWTH Aachen University zur Erlangung des akademischen Grades eines Doktors der Naturwissenschaften genehmigte Dissertation

vorgelegt von

Diplom-Physiker

**Stefan Antonius Schmitz**

aus Düsseldorf

Berichter: Univ.-Prof. Dr. Thomas Hebbeker
Univ.-Prof. Dr. Christopher Wiebusch

Tag der mündlichen Prüfung: 17.07.2013

Diese Dissertation ist auf den Internetseiten der Hochschulbibliothek online verfügbar.

# Abstract

Data recorded by the CMS (Compact Muon Solenoid) experiment is analyzed to study the production of high-mass muon pairs in proton-proton collisions at the LHC (Large Hadron Collider). Most of the presented results are based on a dataset of 5.3 fb$^{-1}$ at a center-of-mass energy of $\sqrt{s} = 7$ TeV. The interpretation of the measured dimuon mass spectrum focuses on a potential non-resonant signal from s-channel graviton exchange. Such a signature of new physics is motivated by the ADD (Arkani-Hamed, Dimopoulos, Dvali) model of large spatial extra dimensions.

The main background for the search is given by the SM (Standard Model) prediction of neutral current Drell-Yan events. Other background sources like for example $t\bar{t}$ production are also considered. The Standard Model expectation is evaluated based on simulation studies and can be tested for dimuon masses below the signal region. Estimates of theory uncertainties on the background prediction and uncertainties related to the detector performance are included in the statistical evaluation of the measurement.

The dimuon mass spectrum observed in the 2011 CMS dataset is found to be compatible with the SM expectation. For masses greater than 1.3 TeV, signal cross sections of greater than 0.84 fb$^{-1}$ can be excluded at 95% confidence level. This result corresponds to an exclusion of values below 3.0 TeV for the ADD model parameters $\Lambda_\mathrm{T}$. A combination of dimuon, dielectron and diphoton results based on a dataset of about 2.0 fb$^{-1}$ extends the excluded range to $\Lambda_\mathrm{T} < 3.3$ TeV. Also limits based on the 2012 CMS dataset at collision energies of $\sqrt{s} = 8$ TeV and some aspects of the CMS search for new dilepton resonances are briefly discussed.

# Zusammenfassung

Die Produktion von Myon Paaren in Proton-Proton Kollisionen am LHC (Large Hadron Collider) wird mit vom CMS (Compact Muon Solenoid)-Experiment aufgezeichneten Daten analysiert. Die vorgestellten Ergebnisse basieren hauptsächlich auf einem Datensatz mit 5.3 fb$^{-1}$ bei einer Schwerpunktsenergie von $\sqrt{s} = 7$ TeV. Die Interpretation des gemessenen Dimyon-Spektrums erfolgt hauptsächlich in Hinblick auf ein mögliches nicht-resonantes Signal durch Gravitonaustausch im s-Kanal. Eine solche Signatur neuer Physik lässt sich durch das ADD (Arkani-Hamed, Dimopoulos, Dvali)-Modell räumlicher Extradimensionen motivieren.

Der Hauptuntergrund für eine solche Analyse ist durch den Standardmodell (SM) Drell-Yan Prozess mit neutralem Ladungsstrom gegeben. Weitere Untergründe wie zum Beispiel die Produktion von top-Quark Paaren werden ebenfalls untersucht. Die Vorhersagen des Standardmodells werden mit Simulationstudien evaluiert und können für Dimyon-Massen unterhalb der Signalregion getestet werden. Abschätzungen der Unsicherheiten der SM Vorhersagen und Unsicherheiten bezüglich der Detektor-Performance werden in die statistische Auswertung miteinbezogen.

Das 2011 von CMS gemessene Dimyon-Massenspektrum erweist sich als kompatibel mit der durch die Vorhersagen des Standardmodells gegebenen Erwartung. Wirkungsquerschnitte eines Signalbeitrags größer als 0.84 fb$^{-1}$ werden oberhalb einer Dimyon-Masse von 1.3 TeV mit einem Konfidenzlevel von 95% ausgeschlossen. Dieses Ergebnis entspricht einem Ausschluss von Werten des ADD Modellparameters $\Lambda_\mathrm{T}$ unterhalb von 3.0 TeV. Eine Kombination von Dimyon-, Dielektron- und Diphoton-Daten mit einem Datensatz von ungefähr 2.0 fb$^{-1}$ erweitert den ausgeschlossenen Bereich auf $\Lambda_\mathrm{T} < 3.3$ TeV. Zusätzlich werden Ausschlussgrenzen basierend auf den 2012 von CMS bei einer Schwerpunktsenergie von $\sqrt{s} = 8$ TeV aufgezeichneten Daten und einige Aspekte der CMS Suche nach neuen Dilepton-Resonanzen in kurzer Form dargestellt.

# Contents

# 1 Introduction

The Large Hadron Collider (LHC) including the experiments employed at its collision points is one of the most ambitious large scale scientific projects that have ever been realized. The time period between the initial vision and the beginning of data taking spanned roughly three decades. Contributions have been made by scientists from so many countries that it is not exaggerated to speak of a worldwide effort. The European laboratory for particle physics CERN hosts the experiment and serves as the main hub for coordinating the research activities between the contributing research institutions. One of the particle detectors that have been built for the analysis of proton-proton and heavy-ion collisions at the LHC is the Compact Muon Solenoid (CMS) experiment. CMS covers an extensive physics program, ranging from precision measurements of observables defined in the current Standard Model of particle physics to searches for new phenomena that could alter our understanding of physics on a fundamental level.

The years 2009-2010 marked the main transition from the phase of construction and commissioning to the era of LHC operation. Since then, data from proton-proton (pp) and heavy-ion collisions has been recorded at significantly higher center-of-mass energies than at any previous particle collider. Data taking during 2011 (pp collisions at $\sqrt{s} = 7$ TeV) and 2012 (pp collisions at $\sqrt{s} = 8$ TeV) continued without any major unexpected interruptions. This is certainly an outstanding achievement for a project of such scale and technological complexity.

A large number of theories going beyond the current Standard Model of particle physics have been proposed. Many of them predict the possibility of new phenomena observable at LHC collisions and justify hopes for fundamental discoveries in the near future. Models with extra dimensions are one such class of theories. The idea that additional space-time dimensions could have relevance for fundamental physics goes at least back to the work of Kaluza and Klein in the early 20th century [1, 2]. A revival of physics models with additional spatial dimensions took place in the late 1990s when is was realized that they could provide a new perspective on problems related to the difference between the fundamental energy scales of electroweak physics and gravity [3].

One of the most studied models with extra dimensions starts from the postulation of additional compact flat extra dimensions. It is then assumed that the graviton field which emerges from adding local fluctuations to the metric tensor permeates all spatial dimensions, while the Standard Model fields are confined to the 3-dimensional subspace extending in the familiar three non-compact dimensions. Working out the interactions of the graviton with the Standard Model particles in this setup, it is found that one conceivable phenomenological signature of extra dimensions is given by the virtual exchange of gravitons. At the LHC, a process to look out for could be the decay of such gravitons to lepton pairs. The described setup predicts a spectrum of equally coupling graviton modes with different masses that becomes very dense at high energies. As a consequence, graviton exchange at collider experiments is expected to become separable from the Standard Model background only at high invariant masses of the decay products. Figure 1.1 shows an attempt to capture some aspects of the described model setup with an artistic approach.

In the presented analysis, data from LHC proton-proton collisions recorded at CMS is used to search for an excess of muon pairs at high invariant masses. To be able to interpret such a measurement correctly, one first needs to study the involved backgrounds and uncertainties.

The analysis focuses on the evaluation of data recorded in 2011. Latest results with 2012 data are briefly mentioned, but not discussed in detail. The results do not provide any significant evidence for the existence of extra dimensions as postulated in the model outlined above, but allow for the exclusion of a large range of model parameters that were not yet tested.

Aspects of Standard Model physics and models with spatial extra dimensions, with emphasis on the ADD (Arkani-Hamed, Dimopoulos, Dvali) scenario [3], are reviewed in chapters 2 and 3. Background information on statistical methods is presented in chapter 4. Specifications and performance of the selection of dimuon events are discussed in chapters 6 and 7. The text then proceeds with an analysis of the dominant background from the Standard Model Drell-Yan process and other background sources (chapters 8 and 9). Studies concerning the simulation of expected ADD signal contributions and the optimization of the dimuon mass range defining the signal region are presented in chapters 10 and 11. Chapters 12 and 13 discuss the evaluation of the dimuon mass measurement and its statistical interpretation, also including limits on the ADD model parameters derived from a combination with dielectron and diphoton data. A conclusion summarizing main results is provided in chapter 14.

Focusing on the used methods of statistical analysis, appendix A describes aspects of the CMS search for a dilepton resonances and discusses some recent results. Appendices B and C briefly discuss the interface between the ROOSTATS and BAT software packages and the implementation of two specific probability distributions in ROOFIT.

The presented work is connected to the CMS physics analysis summaries [4, 5, 6, 7, 8] and the CMS journal publications [9, 10]. The amount of content directly transfered from these documents is limited as none of them discuss the evaluation of limits on large extra dimensions with the full 2011 CMS dataset. In those cases where content from the mentioned documents is included, it is made clear in the text. This mostly concerns some of the shown figures and tables.
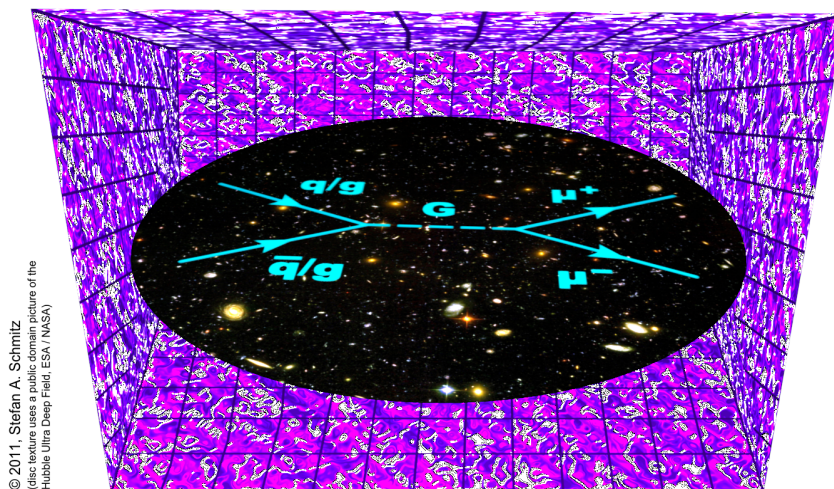


**Figure 1.1** Artistic attempt of an visualization of virtual graviton exchange in a model with large spatial extra dimensions. (©2011, Stefan A. Schmitz; disc texture uses a public domain picture of the Hubble Ultra Deep Field, ESA/NASA)

# 2 Selected Aspects of Standard Model Physics

Our contemporary understanding of the phenomenology of particle physics is based on what is often called the *Standard Model* (SM) of particle physics. The general structure of this model is outlined in section 2.1. Of course, a description of the SM within a few pages can only scratch the surface of the underlying concepts. Notation and line of thought in section 2.1 are similar to a discussion of similar scope in [11]. References including more detailed accounts on SM physics that have been used as material for compiling section 2.1 are [12, 13, 14, 15, 16].

Some basic information concerning the topic of parton distribution functions which play a vital role for the prediction of event rates at hadron colliders is presented in section 2.2. In section 2.3, the neutral Drell-Yan (DY) process is reviewed because of its importance as a background in the presented search and its connection to processes with virtual graviton exchange. The discussion is limited to the Born level. Simulating the DY background including higher order perturbative corrections is described later in chapter 8. Due to its relevance for motivating models with large spatial extra dimensions with phenomenology observable at TeV energies, the chapter concludes with a brief discussion of the hierarchy problem, which emerges as a consequence of the SM Higgs mechanism.

## 2.1 The Structure of the Standard Model

The Standard Model of particle physics describes the interactions of the fundamental components of matter in terms of a *quantum field theory*. Formally, one can construct the SM starting from a Lagrangian density $\mathscr{L}$. Special relativity restricts the considered models to Lorentz invariant Lagrangian densities. For example, the Dirac equation of a fermion field $\psi_n$ (a 4-component complex spinor representing particles with spin $1/2$) is generated by Euler-Lagrange equations for $\bar{\psi}_n$ if one starts from the Lagrangian

$$\mathscr{L}_{\text{fermion},n} = \bar{\psi}_n \left( i\slashed{\partial} - m \right) \psi_n \quad , \tag{2.1}$$

where $\bar{\psi}_n = \psi_n^\dagger \gamma_0$ and $\slashed{\partial} = \gamma_\mu \partial^\mu$. The fermion fields included in the SM are six *quark* fields ($n = 1\ldots 6$), and six *lepton* fields ($n = 7\ldots 12$).

A quantum field theory based on the Lagrangian density

$$\sum_{n=1}^{12} \mathscr{L}_{\text{fermion},n} \tag{2.2}$$

would only describe the propagation of non-interacting fermions. Interactions can be introduced by requiring invariance of the Euler-Lagrange equations under a group of local unitary transformations

$$U = e^{i\alpha_a(x)T^a} \quad . \tag{2.3}$$

In this shorthand notation, the operators defining the group generators are labeled as $T_a$, $a = 1\ldots k$. The respective symmetries of the SM are fixed by the group structure

$$SU(3)_C \otimes SU(2)_W \otimes U(1)_Y \quad , \tag{2.4}$$

where the indices refer to the charges *color* ($C$), *weak isospin* ($W$) and *hypercharge* ($Y$) associated with the group as required by the Noether theorem. The Lagrangian densities $\mathscr{L}_{\text{fermion},n}$ do not feature any of these symmetries. However, the symmetry requirements can be fulfilled by adding terms that involve additional *boson* fields. Including kinetic terms for these additional fields allows for the propagation and self interaction of the boson fields.

Only the quark fermion fields are charged under $SU(3)_C$. The corresponding eight color-charged boson fields are called *gluons* and the resulting quantum field theory is *quantum chromodynamics* (QCD)[1]. A treatment of the *electroweak theory* [18, 19, 20, 21] associated with the $SU(2)_W \otimes U(1)_Y$ symmetry that is compatible with experimental results requires a differentiation between left-handed components $\psi_L$ and right-handed components $\psi_R$ that one receives from the projectors

$$P_{\text{L}} = \frac{1}{2}\left(1 - \gamma^5\right) \quad \text{and} \quad P_{\text{R}} = \frac{1}{2}\left(1 + \gamma^5\right) \quad . \tag{2.5}$$

Such a theory is called *chiral*. The left-handed fermion fields form $SU(2)_W$ lepton doublets $(l_{j,L}, \nu_{j,L})_j^T$, $(u_{j,L}, d_{j,L})_j^T$ and right handed $SU(2)_W$ singlet states[2] $u_{j,R}$, $d_{j,R}$, $l_{j,R}$, $\nu_{j,R}$ with family index $j = 1\ldots 3$. The boson fields of $SU(2)_W$ and $U(1)_Y$ are labeled as $W_i$, $i = 1\ldots 3$ and $B$.

In the process of *electroweak symmetry breaking* (section 2.4), the massless photon $\gamma$, and the massive $Z$ and $W^\pm$ bosons emerge as mixed states of the $W_i$ and $B$ bosons. In the limit of $m_Z, m_{W^\pm} \to \infty$ one arrives at an effective theory with $U(1)_Q$ symmetry, where $Q$ corresponds to the electric charge. The corresponding quantum field theory is quantum electrodynamics (QED).

Most of what has been mentioned so far has been formulated in terms of classical field theories. The formal transition towards a quantum field theory can be made by elevating the fields to field operators that act on a Fock space and by imposing equal time commutation relations between the field operators that imply the validity of the spin statistics theorem.

The probability of finding $n$ free incident particles in state $|p_1, \ldots, p_n\rangle_{\text{i}}$ in the $m$ particle state $|p'_1, \ldots, p'_m\rangle_{\text{f}}$ after leaving the relevant interaction region can be written as

$$\begin{aligned} S_{fi} = {}_{\text{f}}\langle p'_1, \ldots, p'_m \,|\, p_1, \ldots, p_n\rangle_{\text{i}} &= \langle p'_1, \ldots, p'_m \,|S|\, p_1, \ldots, p_n\rangle \\ &= (2\pi)^4\, \delta^4\left(\sum_{\text{f}} p'_f - \sum_{\text{i}} p_i\right) i\,\mathscr{M} \quad , \end{aligned} \tag{2.6}$$

with scattering matrix $S$ and matrix element $\mathscr{M}$. Matrix elements for scattering processes can be calculated with a diagrammatic approach in which a set of *Feynman rules* allows to define $\mathscr{M}$ at a given perturbative order in the coupling constants of the theory. Some examples of diagrams for a specific SM process are shown in figure 8.12. Beyond leading order in perturbative theory, the coupling constants become dependent on the energy scale of the process. While the electroweak couplings stay small in the infrared limit, QCD becomes strongly coupled. Even at center-of-mass energies in the TeV range it is therefore far from obvious how reliable perturbative calculations are for observables like cross sections in proton-proton collisions. This problem is discussed further in section 2.2. The property that the QCD coupling becomes small at high energy scales [23, 24] is usually referred to as *asymptotic freedom*. Another important aspect of QCD is related to the empirical finding that the massless gluons are never observed as free particles. Colored particles in a final state are always found to be arranged in colorless bound mesons (quark-antiquark) or baryon (quark-quark-quark) states. This particular behavior of QCD is called *confinement*.

---

[1] A list of references may be found in [17].

[2] Depending on how neutrino masses are generated, the right-handed neutrino $\nu_{j,R}$ may be omitted (e.g. [22]).

## 2.2 Parton Distribution Functions

It has been mentioned in section 2.1, that QCD becomes strongly coupled at low energies. Accordingly, even the calculation of high energy observables in proton-proton collisions cannot be described only by perturbative physics, because the composition of the proton in terms of its partonic constituents is governed by the non-perturbative regime. At high partonic center-of-mass energies it may be assumed that parton-parton interactions take place at time scales that are short compared to the characteristic time scales at which the parton composition of the proton fluctuates and that are also too short for other partons to interact with the final state [25]. It is the content of one of the QCD *factorization theorems* (e.g. [25]) that many observables which can be defined for the inelastic collisions of two hadrons $\mathcal{H}_1, \mathcal{H}_2$ (here: two protons colliding at the LHC) at a given order of perturbation theory may be calculated as (e.g. [26])

$$
\sigma\left(\mathcal{H}_1 + \mathcal{H}_2 \to X + \text{hadron remnants}\,;\, Q, \mu_F, \mu_R\right) =
$$
$$
\sum_{i,j} \int dx_1 dx_2 \, f_{i,h_1}\left(x_1, Q, \mu_F\right) f_{j,h_2}\left(x_2, Q, \mu_F\right) \hat{\sigma}\left(\mathcal{P}_i + \mathcal{P}_j \to X,\, x_1,\, x_2,\, Q,\, \mu_F, \mu_R\right) \quad , \tag{2.7}
$$

where the indices $i,j$ label the different types of contributing partons. The *parton distribution function* (PDF) for parton $\mathcal{P}_i$ at hadron momentum fraction $x$, process scale $Q$, and choice of the factorization scale $\mu_F$ is given by $f_i\left(x, Q, \mu_F\right)$. $\hat{\sigma}$ describes the high-energy parton-parton interaction that can be calculated perturbatively, and $\mu_R$ is the renormalization scale. In practical applications, one often chooses $\mu_F = \mu_R = Q$. For the evaluation of the mass spectrum from SM Drell-Yan dimuon events, $Q$ can be identified with the dimuon mass. Attempts to interpret and motivate a choice of $\mu_F$ for this particular process include the approach in [27]. Any detailed quantitative evaluation of the parton distribution function requires specific input from actual measurements. The DGLAP [28, 29, 30] equations allow to extrapolate the PDFs from a given scale $Q$ to a scale $Q'$. This allows for the calculation of the PDF density in regions where it is not directly constrained by measurements (e.g. high mass Drell-Yan production at the LHC). Both the theoretical calculations and the measurements that go into an estimate of parton distributions functions are subject to various sources of uncertainties. For many LHC analyses, it is found that these uncertainties are relevant for the physics interpretation of the measurements. In the presented work (section 8.4), the PDF uncertainties are evaluated based on recommendations from the PDF4LHC group [31, 32].

## 2.3 The neutral DY Process at LO

The electroweak neutral Drell-Yan (DY) process[3] [33] $q\bar{q} \to \mu^+\mu^-$ is reviewed because of its importance as a background in the presented analysis. At Born level, the process can be calculated by applying the Feynman rules of the electroweak theory (for example [15]) to the $2 \to 2$ s-channel diagram shown in figure 8.12.i. In the following equations, the process is considered in the center-of-mass frame and amplitudes are applied with spin average with respect to the initial state and summation over color and final state spin. Starting from the expressions for the

---

[3]From here on, the terms *neutral DY process* and *DY process* are used synonymously.

squared amplitudes as for example stated in [34], one can express the differential cross section $d\sigma/d\Omega$ as

$$
\begin{aligned}
\frac{d\sigma}{d\Omega}_{|DY,LO} &= \frac{\pi^2\alpha^2}{768} \cdot \frac{1}{\hat{s}} \cdot \left\{ \left( c_1 + |D_z\left(\hat{s}\right)|^2 \cdot \hat{s}^2 \cdot \left[ c_2 + c_3 \cdot \left( 1 - \frac{m_z^2}{\hat{s}} \right) \right] \right) \cdot (1 + \cos\theta^*)^2 \right. \\
&\quad \left. + \left( c_1 + |D_z\left(\hat{s}\right)|^2 \cdot \hat{s}^2 \cdot \left[ c_4 + c_5 \cdot \left( 1 - \frac{m_z^2}{\hat{s}} \right) \right] \right) \cdot (1 - \cos\theta^*)^2 \right\} \quad (2.8) \\
&= C_1\left(\hat{s}\right) \cdot (1 + \cos\theta^*)^2 + C_2\left(\hat{s}\right) \cdot (1 - \cos\theta^*)^2 \quad,
\end{aligned}
$$

where $\theta^*$ is defined as the scattering angle of the positively charged muon in the dimuon center-of-mass frame, $\hat{s} = (p_{q_1} + p_{\bar{q}_2})^2$ is the partonic center-of-mass energy, $m_z$ the mass of the $Z$ boson, and $\alpha$ the fine-structure constant. Expressions for $|D_z\left(\hat{s}\right)|$ and the constants $c_i$ can be found in appendix D.1. The constants $c_i$ depend on the Weinberg angle and the electric charge and third component of the weak isospin of the initial state quarks. If all values $c_i$ except for $c_1$ are set to zero, one recovers the formula for the QED photon exchange. The relation $C_1\left(\hat{s}\right) \neq C_2\left(\hat{s}\right)$ is the cause of the observed forward-background asymmetry in the SM DY process. DY lepton pairs from proton-proton collisions are typically not measured in their center-of-mass frame. To calculate $\theta^*$, one can boost the muon momenta $p_{\mu,i}^{\nu}$, $i = 1, 2$ to their center-of-mass system with $\vec{v} = \left(-p^1/p^0, -p^2/p^0, -p^3/p^0\right)^T$, where $p^{\nu} = p_{\mu,1}^{\nu} + p_{\mu,2}^{\nu}$.[4]

## 2.4 SM Higgs Mechanism of Electroweak Symmetry Breaking and the Hierarchy Problem

The following brief discussion of the SM Higgs mechanism [35, 36, 37, 38, 39] is loosely oriented along the lines of arguments presented in the more detailed treatment of the topic in [15]. The $\mathrm{SU}(2)_W \times U(1)_Y$ symmetry used to model the electroweak interactions in the SM does not allow for mass terms of the gauge bosons. The SM however is only able to model nature if mass terms for the bosons are present and correspond to the observed $W^{\pm}$ and $Z$ mass states. It is therefore an important question if it is possible to extend the Lagrangian of the electroweak interactions between quarks and leptons in a way that maintains the gauge invariance, allows for the required vector boson mass terms, and keeps the resulting theory renormalizable [40]. The *Higgs mechanism* of spontaneous symmetry breaking is able to meet all these requirements. Here the discussion will be limited to the most popular version of the Higgs mechanism which adds a term

$$
\mathcal{L} = (D_\alpha\phi)^\dagger (D^\alpha\phi) - \mu^2\phi^\dagger\phi + \lambda\left(\phi^\dagger\phi\right)^2 \quad ; \quad \phi = \frac{1}{\sqrt{2}}\begin{pmatrix} \phi_1 + i\phi_2 \\ \phi_3 + i\phi_4 \end{pmatrix} \quad (2.9)
$$

to the Lagrangian, in which $\phi$ contains two complex scalar fields with hypercharge 1 that form a weak isospin doublet. $D_\mu$ denotes the covariant derivative of the electroweak gauge group. For $\mu^2 > 0$ and $\lambda > 0$, the choice of $\phi = 0$ does not correspond to a minimum of the $\phi$-potential. However, for a perturbative approach one needs to expand around the ground state of the system. This behavior characterizes the concept of *spontaneous symmetry breaking*. With the choice of an appropriate potential minimum and gauge one arrives at a Lagrangian containing the three massive vector boson fields $W^{\pm}$ and $Z$, the massless vector boson field $A$, and a massive scalar Higgs field $h$. The desired properties of the theory are therefore established at the expense of

---

[4]This can be verified by inserting $\vec{v}$ into the equations of Lorentz transformation.

postulating the existence of an additional neutral massive scalar particle (the *Higgs boson*). At tree level, the Higgs boson is found to couple to the $W^\pm$ and $Z$ gauge bosons.

The introduction of the Higgs doublet allows for $SU(2)_W \times U(1)_Y$ invariant terms (color and family indices suppressed)

$$
\begin{aligned}
\mathcal{L}_{l,\text{Higgs}} &= -g_l \bar{l}_L \phi l_R + \text{h.c.} \\
\mathcal{L}_{q,\text{Higgs}} &= -g_d \bar{q}_L \phi d_{i,R} - g_u \epsilon^{ab} \bar{q}_{L,a} \phi_b^\dagger u_R + \text{h.c.}
\end{aligned}
\tag{2.10}
$$

with left-handed doublets $l_L$ (leptons) and $q_L$ (quarks) and right-handed singlets $l_R$ (leptons) and $u_R, d_R$ (quarks), which generate fermion mass terms in the Lagrangian that one receives after taking into account the electroweak symmetry breaking (e.g. [41]). However, each fermion mass requires adding a new Yukawa (i. e. higgs-fermion) coupling $g_f$.

In 2012, both the CMS and ATLAS collaborations have observed a new particle at a statistical significance that surpasses the $5\sigma$ criterion conventionally used for defining a *discovery* [42, 43]. All the properties of the signature are currently found to be compatible with a Higgs boson as postulated by the version of the Higgs mechanism outlined above, at a mass of about 125 GeV.

This implies that $m_h \approx m_W \approx m_Z$. Contributions to $m_h^2$ from 1-loop diagrams induce corrections to the Higgs mass proportional to $\Lambda^2$, where $\Lambda$ is the selected UV cutoff. To arrive at a *physical* Higgs mass of order 0.1 TeV, one needs to introduce counterterms that compensate for the cutoff dependent contributions (e.g. [44]). Naively, $\Lambda$ is expected to be associated with a scale of new physics. However, the only such energy scale that we know of for sure is the Planck scale, suggesting $\Lambda^2 \approx M_{\text{Pl}}^2 \approx 10^{36}$ GeV$^2$. Such a choice of $\Lambda$ requires that the ratio of cutoff and counterterm contributions is extremely close to 1 if one wants to arrive at the $\mathcal{O}(0.1\,\text{TeV})$ physical Higgs mass. But within the SM no mechanism seems to be driving such a *fine-tuning*. Generally, this *hierarchy problem* of the difference between the Planck scale and the physical Higgs mass is one of the reasons for optimism in the particle physics community that new physical phenomena beyond the SM predictions could be discovered at the LHC. This is because the problem seems to be resolved or at least reinterpreted if there is physics beyond the SM implying that the correct choice of $\Lambda$ in the SM would be in the TeV range. As outlined in the next chapter, large extra dimensions offer one way of motivating such a choice.

To give a rough quantification of the expected amount of fine-tuning, one can evaluate the 1-loop corrections to the Higgs mass $m_h$ given by [45]

$$
\Delta m_h^2 = \frac{3 \cdot \Lambda^2}{8 \cdot \pi^2 \cdot v^2} \left( m_h^2 + 2m_W^2 + m_Z^2 - 4m_t^2 \right) \quad,
\tag{2.11}
$$

with vacuum expectation value $v$. Using $v = 246$ GeV, $m_h = 125$ GeV, $m_W = 80$ GeV, $m_Z = 90$ GeV, and $m_t = 173$ GeV, an indicator for the required fine-tuning [46, 47] can be defined by

$$
f(\Lambda) = \frac{|\Delta m_h^2|}{(0.125\,\text{TeV})^2} \approx 3.3 \frac{\Lambda^2}{\text{TeV}^2} \quad.
\tag{2.12}
$$

Accordingly, $f(1\,\text{TeV}) \approx 3$ and $f(10\,\text{TeV}) \approx 3 \cdot 10^2$. Based on these considerations one might naively suspect that the scale of new physics *beyond the SM* (BSM) should be $< 10$ TeV to avoid a surprising amount of fine-tuning.

# 3 Aspects of Physics Beyond the Standard Model with Extra Spatial Dimensions

The existence of extra spatial dimensions is the defining building block in a multifaceted class of models making predictions for physics beyond the Standard Model. Section 3.1 outlines main features of one specific model referred to as the *ADD scenario of large spatial extra dimensions*. The selected material focuses on those properties of the considered model that are needed to study the decay of virtual gravitons to lepton pairs. A few relevant notational conventions are summarized in appendix E.2. The asymptotic safety scenario for gravity with ADD extra dimensions provides an approach towards addressing the UV divergences emerging in perturbative calculations of the effective quantum field theory. Possible phenomenological consequences for the exchange of virtual gravitons are reviewed in section 3.2. Section 3.3 briefly outlines two alternative models postulating spatial extra dimensions which also have a potential for dilepton signatures that could be discovered in LHC collisions. Constraints on models with large extra dimensions from experiments are discussed in section 3.4.

## 3.1 Exchange of Virtual Gravitons Decaying to Muon Pairs in the ADD Scenario of Large Spatial Extra Dimensions

Large spatial extra dimensions [3] allow to lower the fundamental Planck scale in the space including the extra dimensions. This might make it possible to study effects of quantum gravity in proton-proton collisions at the LHC. At the same time, the proposal offers a new perspective on the hierarchy problem discussed in section 2.4. The references used for compiling this section include both journal articles [3, 48, 49, 50, 34, 51, 52] and other literature including proceedings and lecture scripts [53, 54, 55, 56, 57].

To study the phenomenology of the ADD scenario of spatial extra dimensions, several assumptions are made.

- The $3 + 1$-dimensional space-time is extended with $n$ flat extra dimensions.

- All extra dimensions are assumed to be compactified on a torus with periodic boundary conditions and equal compactification radius R for each extra dimension.

- The complete space-time is a direct product of the 4-dimensional Minkowski space and the compactified extra dimensions.

- Only gravity propagates in the full higher-dimensional space-time. All SM particles are confined to a (rigid) 3+1 *brane*. A brane may be thought of as a lower-dimensional "sheet" in the full space-time. Any extension of the SM fields into the extra dimensions is assumed to be negligible.

These conditions characterize one possible scenario covered by the original ADD proposal. Detailed studies of its phenomenology have been presented in the literature on extra dimensions, which make it the most frequently used framework for experimental tests of the ADD proposal.

For the rest of this work the selected specific setup will simply be referred to as "the ADD model".

An immediate consequence of the ADD model is that one expects to observe a change in Newtons force law if gravity is probed at length scales comparable to the radii of the extra dimensions. To see this, one can start from generalizing the field equation

$$\rho\left(\vec{r'}\right) \propto \mathrm{div}\vec{F}\left(\vec{r'}\right) \tag{3.1}$$

with mass density $\rho$ and gravitational force field $\vec{F}$ to $3 + n$ dimensions. Applying Gauss's law and restricting the discussion to radial fields one can write

$$m \propto \int_V \mathrm{div}\vec{F} = \int_A \vec{F} \propto F\left(r\right) r^{n+2} \tag{3.2}$$

where $m$ is the mass in a $3 + n$ dimensional spherical volume $V$ with radius $r$ enclosed by the surface $A$. This implies

$$F\left(r\right) \propto \frac{1}{r^{n+2}} \tag{3.3}$$

in the limiting scenario $r \ll R$. For $r > R$, the surface increase with r is restricted to the non-compact dimensions and one recovers Newton's gravitational force law. As a consequence, it is possible to set direct bounds on the size of the extra dimensions by testing the validity of the $1/r^2$ scaling of the gravitational force at short distances.

The Einstein-Hilbert action is defined as

$$S_4 = M_{\mathrm{Pl}}^2 \int d^4x \sqrt{|g_4|}\left(R_4 + \mathcal{L}_M\right) \quad , \tag{3.4}$$

where $g_4$ is the determinant of the metric tensor and $|g_4| = -g_4$. $R_4$ is the Ricci scalar[1]. $\mathcal{L}_M$ defines the action of the considered matter and gauge fields.

The field equations of general relativity are the Euler-Lagrange equations of the Einstein-Hilbert action. The formal extension of the exclusively gravity related part of this action to $3 + n$ spatial dimensions can be (e.g. [57]) written as

$$S_{4+n,\mathrm{grav}} = M_{\mathrm{D}}^{n+2} \int d^{4+n}z \sqrt{|g_{4+n}|}R_{4+n} \quad , \tag{3.5}$$

with metric tensor (determinant $g_{4+n}$, $|g_{4+n}| = (-1)^{n+1}g_{4+n}$) and Ricci scalar $R$ generalized to $3 + n$ spatial dimensions. It is possible to determine what gravity looks like on the 3-brane by considering a fluctuation of the metric tensor that is restricted to the Minkowski metric of the non-compact dimensions. Ricci scalar and determinant of the metric tensor are then given by $R_{4+n} = R_4$ and $\sqrt{|g_{4+n}|} = \sqrt{|g_4|}$. The corresponding action simplifies to

$$S_{4+n,\mathrm{grav}} = M_{\mathrm{D}}^{n+2} \cdot V \cdot \int d^4x \sqrt{|g_4|}R_4 \quad , \tag{3.6}$$

with $V = (2 \cdot \pi \cdot R)^n$. Comparing with equation 3.4 for $n = 0$ one arrives at the relation [3]

$$M_{\mathrm{Pl}}^2 = V \cdot M_{\mathrm{D}}^{n+2} = (2 \cdot \pi \cdot R)^n \cdot M_{\mathrm{D}}^{n+2} \quad . \tag{3.7}$$

This suggests that the fundamental Planck mass $M_{\mathrm{D}}$ can be lowered far below the effective Planck mass $M_{\mathrm{Pl}}$ if the extra dimensions are sufficiently large. Arkani-Hamed, Dimopoulos and

---

[1]For the presented discussion it is sufficient to think of the Ricci scalar as a specific function of the components of the metric tensor and their (multiple) spatial derivatives with respect to the space-time coordinates.

Dvali observed that already for 2 extra dimensions the bounds on $R$ allowed for $M_D$ to be of order 1 TeV. Accordingly, gravity might become strong sufficiently close to the electroweak scale to avoid the necessity of an excessive amount of fine-tuning in the SM Higgs sector. However, one may certainly ask what kind of physics actually regulates the size of the extra dimensions and the localization of the SM fields on the brane. First attempts to approach such questions were already included in [3] and can also be based on arguments derived in the framework of string theory [58].

To study interactions between gravity and the SM fields, one starts from the action

$$S_{4+n,\text{int}} = M_D^{n+2} \int d^{4+n}x \sqrt{|g_{4+n}|} \mathcal{L}_M \left(g, \text{SM fields}\right) \quad . \tag{3.8}$$

Expanding the $4 + n$ metric $g$ as $g^{\hat\mu\hat\nu} = \eta^{\hat\mu\hat\nu} + \frac{1}{2 \cdot M_D^{(n/2)+1}} \mathfrak{h}^{\hat\mu\hat\nu}$ results in linearized field equations with interaction terms involving $\mathfrak{h}^{\hat\mu\hat\nu}$ and the SM fields. They correspond to the action [57]

$$S_{4+n,\text{int}} = \int d^{4+n}z \frac{1}{M_D^{(n/2)+1}} T^{\hat\mu\hat\nu} \mathfrak{h}_{\hat\mu\hat\nu}(z) \quad , \tag{3.9}$$

where $T^{\hat\mu\hat\nu}$ is the energy-momentum tensor defined as

$$T^{\hat\mu\hat\nu} = \frac{1}{\sqrt{|g|}} \left. \frac{\delta \mathcal{L}_M}{\delta g_{\hat\mu\hat\nu}} \right|_{g_{\hat\mu\hat\nu}=\eta_{\hat\mu\hat\nu}} \quad . \tag{3.10}$$

Further analysis of equation 3.9 shows that not all components of $\mathfrak{h}_{\hat\mu\hat\nu}$ correspond to physical fields [48, 49, 50]. The fields actually coupling in some way to the energy-momentum tensor can be characterized as a tensor field $h_{\mu\nu}$ (graviton) and a scalar field $\phi$ (dilaton). Based on equations derived in [48, 49], one can write

$$S_{4+n,\text{int}} = \int d^4x\, d^n y \frac{1}{M_D^{(n/2)+1}} \left( T_{\mu\nu}(x)\, \delta(y)\, h^{\mu\nu}(x,y) + \sqrt{\frac{2}{3(n+2)}} T_\mu^\mu(x) \delta(y)\, \phi(x,y) \right) \tag{3.11}$$

On the way towards equation 3.11 one has used that the energy-momentum tensor for the considered model setup is given by

$$T_{\hat\mu\hat\nu}(z) = \eta_{\hat\mu}^\mu \eta_{\hat\nu}^\nu T_{\mu\nu}(x)\, \delta(y) \quad . \tag{3.12}$$

As suggested in [48], the dilaton interactions will in the following be neglected.

Periodicity in the compact toroidal extra dimensions allows to perform a Fourier expansion of $h_{\mu\nu}(x,y)$ in $y$, which can be expressed as

$$h_{\mu\nu}(x,y) = \sum_{k_1=-\infty}^{\infty} \cdots \sum_{k_n=-\infty}^{\infty} \frac{1}{\sqrt{V}} h_{\mu\nu}^{\vec{k}}(x)\, e^{i\frac{k^j y_j}{R}} \quad . \tag{3.13}$$

This procedure links a field in $z = (x, y)$ to a tower of 4-dimensional *Kaluza-Klein* (KK) *modes* in $x$. Each mode corresponds to a summand in equation 3.13. One important consequence of the decomposition into KK modes can be motivated by evaluating the action

$$
\begin{aligned}
S_{4+d,kin} \quad &\propto \quad \int d^{4+n}z \partial^{\hat{\rho}} h^{\mu\nu}(z)\, \partial_{\hat{\rho}} h_{\mu\nu}(z) \\
&\propto \quad \frac{1}{V} \int d^{4+n}z \sum_{\vec{k}} \sum_{\vec{l}} \partial^{\hat{\rho}} \left( h^{\mu\nu\,\vec{k}}(x)\, e^{i\frac{\vec{k}*\vec{y}}{R}} \right) \partial_{\hat{\rho}} \left( h_{\mu\nu}^{\vec{l}}(x)\, e^{i\frac{\vec{l}*\vec{y}}{R}} \right) \\
&\propto \quad \int d^4x \int d^n y \sum_{\vec{k}} \sum_{\vec{l}} \left[ \partial^{\rho} h^{\mu\nu\,\vec{k}}(x)\, \partial_{\rho} h_{\mu\nu}^{\vec{l}}(x) - \frac{i^2 \vec{k}*\vec{l}}{R^2} \right] e^{i\frac{\vec{k}*\vec{y}}{R}} e^{i\frac{\vec{l}*\vec{y}}{R}} \\
&\propto \quad \int d^4x \sum_{\vec{k}} \partial^{\rho} h^{\mu\nu\,\vec{k}}(x)\, \partial_{\rho} h_{\mu\nu}^{-\vec{k}}(x) - \frac{\vec{k}^2}{R^2} h^{\mu\nu\,\vec{k}} h_{\mu\nu}^{-\vec{k}} \quad (3.14)
\end{aligned}
$$

The last step makes use of the orthogonality of complex exponential functions. It can be seen that the Fourier expansion results in a tower of graviton modes that acquire mass terms with $m_{\vec{k}} = \vec{k}^2/R^2$. $S_{4+n,\text{int}}$ can be written as

$$
\begin{aligned}
S_{4+n,\text{int}} \quad &= \quad \int d^4x\, d^n y\, \frac{1}{M_{\mathrm{D}}^{(n/2)+1}} T^{\mu\nu}(x)\, \delta(y) \sum_{\vec{k}} \frac{1}{\sqrt{V}} h_{\mu\nu}^{\vec{k}}(x)\, e^{i\frac{\vec{k}*\vec{y}}{R}} \\
&= \quad \sum_{\vec{k}} \int d^4x\, \frac{1}{M_{\mathrm{D}}^{(n/2)+1} \sqrt{V}} h_{\mu\nu}^{\vec{k}}(x)\, T^{\mu\nu}(x) \\
&= \quad \sum_{\vec{k}} \int d^4x\, \frac{1}{M_{\mathrm{Pl}}} h_{\mu\nu}^{\vec{k}}(x)\, T^{\mu\nu}(x) \quad . \quad (3.15)
\end{aligned}
$$

This result shows that each mode couples with equal strength $\frac{1}{M_{\mathrm{Pl}}}$ to the energy-momentum tensor. In the considered model, only the large number of modes accessible in high energy collisions makes it possible for collider experiments to be sensitive to the presence of the extra dimensions. The mass differences between modes are given by [52]

$$
\Delta m = \frac{\Gamma(n/2) M_{\mathrm{D}}^{2+n}}{2\pi^{n/2} M_{\mathrm{Pl}}^2 m^{n-1}} \quad . \quad (3.16)
$$

For instance, $\Delta m$ evaluates to $2 \cdot 10^{-3}$ eV for $n = 6$, $M_{\mathrm{D}} = 5$ TeV, and $m = 1$ GeV. This exemplifies that at masses $m$ where the mode density may lead to any sizable signal contribution it is not possible to resolve single graviton modes with a realistic detector. As a next step, canonical quantization can be used to construct a quantum field theory from the tower of graviton fields $h^{\vec{k}}$ and their interaction with the SM fields as given by the action 3.15. Here the discussion will focus on the graviton-fermion interactions contributing to s-channel graviton exchange with a dilepton final state [59].

Figure 3.1 shows the Feynman diagrams corresponding to the leading order contributions to the DY dimuon matrix element from a single KK graviton mode $\vec{k}$.

To evaluate all ADD DY contributions, it is necessary to consider the complete set of graviton modes. Any dependence of the amplitude on the model parameters $M_{\mathrm{D}}$ and $n$ is encoded in the sum

$$
S(s) = \frac{1}{M_{\mathrm{Pl}}^2} \sum_{\vec{k}} \frac{1}{s - m_{\vec{k}}^2 + i m_{\vec{k}} \Gamma_G\left(m_{\vec{k}}\right)} \quad , \quad (3.17)
$$

as in the formula for the leading order amplitude the propagator is the only term depending explicitly on the mode of the graviton through its mass. The evaluation of the mode sum $S(s)$ has first been discussed in references [48, 49, 50]. As the mass separation between adjacent
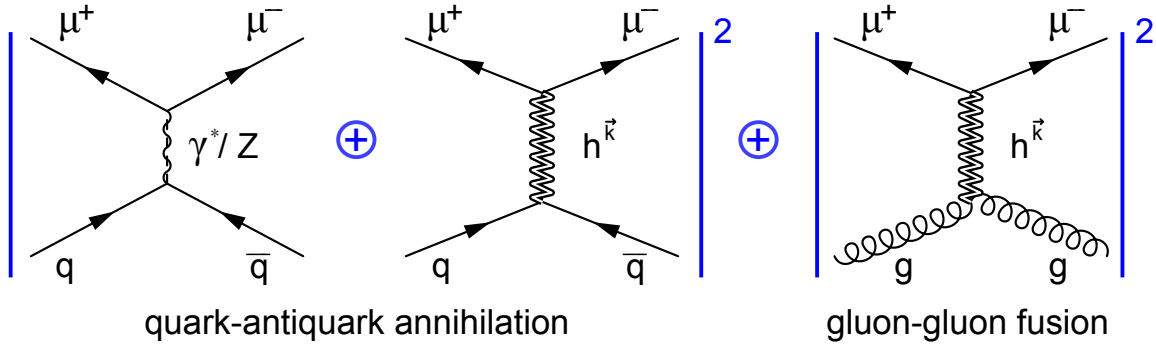
**Figure 3.1** Leading order Feynman diagrams contributing to DY dimuon production in the ADD model.

graviton modes is much smaller than the detector resolution, one can rewrite equation 3.17 as an integral with respect to a mode density continuous in $m$. For $n \geq 2$, one needs to introduce an UV mass cutoff as the integral diverges. Using the narrow width approximation, one receives the result [52]

$$S\left(s\right) = \frac{\pi^{n/2}\Lambda^{n-2}}{\Gamma\left(n/2\right)M_{\mathrm{D}}^{2+n}}F_n\left(\frac{s}{\Lambda^2}\right) \quad , \tag{3.18}$$

where $\Lambda$ is the UV cutoff[2]. The effective field theory of the ADD model cannot predict the appropriate choice of the UV cutoff. As a high mass search for the decay of virtual gravitons is sensitive to the choice of $\Lambda$, the results need to be interpreted with care. It has been argued that considerations of unitarity restrict reasonable choices of $\Lambda$ to $\lesssim M_{\mathrm{D}}$ [48]. In the presented analysis, the problems related to the cutoff will be acknowledged by treating the maximum dimuon mass that is considered for the inclusion of signal contributions as an additional model parameter. Further insights may be gained through additional assumptions on the nature of (quantum) gravity. As briefly outlined in section 3.2, asymptotic safety scenarios provide an approach to improve the predictions for the UV behavior of the effective theory.

Equation 3.18 allows to calculate differential cross sections as a function of $M_{\mathrm{D}}$, $n$ and $\Lambda$. However, publicly available simulation tools for the process like Pythia8 [60] consider the limit $s \ll \Lambda^2$ for which equation 3.18 simplifies to [51, 52]

$$S\left(s\right) = \begin{cases} \dfrac{\pi^{n/2}}{\Gamma\left(n/2\right)} \cdot \dfrac{\Lambda^{n-2}}{M_{\mathrm{D}}^{n+2}} \equiv \dfrac{8}{M_{\mathrm{T}}^4} & ;\ n > 2 \\[2ex] \dfrac{\pi}{M_{\mathrm{D}}^4}\ln\dfrac{s}{\Lambda^2} & ;\ n = 2 \\[2ex] \dfrac{-i\pi}{M_{\mathrm{D}}^3\sqrt{s}} & ;\ n = 1 \end{cases} \tag{3.19}$$

For $n > 2$, this result relates to the *GRW* (Giudice, Rattazzi, Wells) *parameter convention* in [48] with parameter $(\Lambda_{\mathrm{T}})$ and the *HLZ* (Han, Lykken, Zhang) *parameter convention* in [49] with parameters $(M_{\mathrm{s}}, n)$ via

$$\Lambda_{\mathrm{T}}^4 = \frac{\pi}{2}M_{\mathrm{T}}^4 \tag{3.20}$$

$$\frac{1}{\Lambda_{\mathrm{T}}^4} = \frac{2}{n-2}\frac{1}{M_{\mathrm{s}}^4} \quad . \tag{3.21}$$

---

[2] A closed-form expression for $F_n\left(\frac{s}{\Lambda^2}\right)$ is given in [52].

The latter of these two equations is based on formulas for converting between different parameter conventions pointed out in [53], which also includes the relation with the parameter convention in [50] and the case $n = 2$ in [49]. As effects of higher order corrections which introduce additional degrees of freedom are not available in the form of an inclusive event simulation, it is reasonable that the presented search focuses on the variables that describe the signal events at LO.

Expressions for the squared amplitudes for leading order s-channel graviton exchange in the ADD model are given in [34]. For example, starting from these formulas the differential cross section for the process $gg \to h \to \mu^+\mu^-$ in the center-of-mass system for $n > 2$ can be expressed as

$$\frac{d\sigma}{d\Omega}_{|gg \to h \to \mu^+\mu^-} = \frac{\pi^2}{256(n-2)^2 M_{\mathrm{s}}^8} \cdot s^3 \left( 1 + \frac{1}{2} \sin^2(\theta^*) cos^2(\theta^*) \right) \tag{3.22}$$

As for all $2 \to 2$ processes with unpolarized initial states, the final state properties can be defined in terms of $\hat{s}$ and $\theta^*$. Comparing the angular distribution 3.22 for graviton exchange via gluon-gluon fusion in equation 3.22 with equation 2.8 for the SM DY process motivates that in principle one might not only consider the dimuon mass but also the angular distribution to differentiate between the DY process in the SM and the ADD model of large extra dimensions.

The presented discussion shows that an effective field theory in the ADD model motivates to search for a non-resonant enhancement of high mass dimuon events at CMS. The design and implementation of such a search at CMS are detailed in the presented work. Implications of the measured dimuon mass spectrum on the ADD scenario are evaluated in terms of the model parameters in the GRW and HLZ conventions.

## 3.2 The Asymptotic Safety Scenario of Quantum Gravity

It has been suggested that general relativity can provide a consistent quantum field theory if it has the property of *asymptotic safety* [61]. The asymptotic safety scenario specifies a set of requirements that would allow to construct a UV-complete theory of quantum gravity based on the Einstein-Hilbert action. As for example outlined in [62], the existence of a non-trivial UV fixed point is a crucial prerequisite of the hypothesized scenario. The idea of asymptotically safe gravity has recently received renewed attention through work that extends studies of the original proposal to models with additional spatial extra dimensions [63, 64]. Those models which have been evaluated so far provide the required fixed point properties, but do not represent a complete quantum field theory of gravity. Still, the results may be seen as encouraging for the hypothesis that the UV behavior of a quantized theory of gravity with extra dimensions could be governed by the scenario of asymptotic safety. All of the apparent UV problems encountered in the past would then be related to shortcomings of the perturbative approach.

Possible implications on the phenomenology of virtual graviton exchange in models with extra dimensions have been discussed in [65, 66, 67][3]. Effects on the dimuon signature discussed in section 3.1 may be expressed in terms of a mode dependent suppression factor on the gravitational coupling. Some of the approximations studied in the literature imply a rapid decline of the dimuon signature at a specific energy scale. The possibility of such a behavior is roughly taken into account in the presented dimuon search by introducing a cut-off on the ADD signal contributions beyond a maximum dimuon mass $M_{\max}$. The interpretation of the measurement in terms of the asymptotic safety scenario could be improved with the implementation of approximations for the modification of the gravitational coupling in a software tool for the simulation of ADD events. This has already been done for processes with real graviton emission and there

---

[3]An introduction to the topic may also be found in [68]

is reason for optimism that in the near future such code will also become available for processes with virtual graviton exchange [69].

## 3.3 Other Models with Spatial Extra Dimensions

Apart from the ADD scenario, there are also other models that involve the concept of extra spatial dimensions. Among the most studied examples are models with *warped extra dimensions* (RS models) [70][4] and the scenario of *universal extra dimensions* (UED) [72]. In contrast to the ADD model, their LHC signature could be a resonant enhancement of events in the dilepton spectra resulting from the decay of specific KK modes. Resonance searches analyze the dilepton mass spectrum in a way that is complementary to searches for non-resonant high-mass dilepton signatures. In the context of the presented work, some contributions have also been made to the statistical analysis of dilepton data in search for a narrow resonance and its interpretation in the RS-1 model. The corresponding methods and results are discussed in appendix A.

The Randall-Sundrum (RS) model can be constructed from the observation that the metric

$$ds^2 = e^{-2k|y|}\eta_{\mu\nu}dx^\mu dx^\nu - dy^2 \tag{3.23}$$

can provide a solution to the Einstein equations. More specifically, this is the case when $y$ corresponds to the coordinate of a single extra dimension compactified on a circle where pairs of opposite coordinate points $(-y, y)$ on the circle have been identified with each other ($S^1/\mathbb{Z}_2$ orbifold). $k$ is a constant that specifies the *warp factor* $\exp{(-2k|y|)}$. The resulting setup can be interpreted as a slice of Anti-de-Sitter space between two branes at $|y| = 0$ (Planck brane) and $|y| = L$ (TeV brane). As in the ADD model, all the SM fields are assumed to be confined on a brane (the TeV brane). The Higgs vacuum expectation value in the RS setup is exponentially suppressed with respect to the corresponding fundamental parameter in the action. This makes it possible to select all fundamental parameters at the same energy scale and allows for a potential solution to the SM hierarchy problem. The weakness of gravity can be interpreted as a consequence of the localization of the wave function of the massless graviton mode close to the Planck brane (e.g. [55]). A more complete description of the RS model requires to specify a mechanism that stabilizes the radius of the extra dimension. A possible approach is to introduce a massive scalar field that is allowed to propagate in the extra dimension [73]. Apart from selecting a finite value for $L$ (RS-1 model), it is also possible to consider the limiting case $L \to \infty$ (RS-2 model) [74]. The collider phenomenology in the RS-1 model can be characterized in terms of the mass $M_1$ of the first massive graviton mode and the parameter $\tilde{k} = k/\bar{M}_{\text{Pl}}$ which controls the graviton coupling.

The UED scenario postulates the existence of one or more compact extra dimensions in which all SM fields can propagate. This implies that each of them can be associated with a tower of KK modes. An analysis of couplings between gauge bosons and fermion shows that there is a symmetry (KK parity) that requires the conservation of a multiplicative quantum number $(-1)^k$, where $k$ refers to the number of the KK mode of the interacting particle (e.g. [75]). An interesting consequence is that the lightest massive KK mode can provide a dark matter candidate. The exchange of $k = 2$ modes could lead to a signature observable at LHC collision energies.

---

[4]Helpful introductions to the RS model may be found in [55, 71].

## 3.4 Experimental Constraints on Large Extra Dimensions

Models with spatial extra dimensions lead to phenomenological consequences that suggest several experimental approaches to searches for evidence of a signal or constraining the model parameters. Results related to large spatial extra dimensions in the ADD model that are not from the LHC experiments are summarized in section 3.4.1. Section 3.4.2 lists results that have been put forward by LHC experiments, also covering models with spatial extra dimensions other than the ADD scenario. The journal references for results published by the LHC collaborations reflect the status as of December 2012. Updates with the 2012 dataset are expected for most of the mentioned searches. For brevity's sake, preliminary public results and reinterpretations of LHC results from outside the detector collaborations are mostly omitted.

### 3.4.1 Non-LHC Searches for Large Spatial Extra Dimensions in the ADD Model

Torsion balance experiments provide direct tests of Newton's inverse square law that would be expected to change at short distance in the presence of ADD extra dimensions. Such measurements constrain the size of the largest extra dimensions to values below 0.044 mm [76]. The measurements exclude the possibility of $M_D$ being anywhere close to the TeV range for a single extra dimension ($n = 1$), and latest results for $n = 2$ constrain $M_D$ to values of greater than 3.6 TeV [26].

For $n \leq 3$, strong constraints on ADD models with $M_D$ in the TeV energy range have been placed based on astrophysics measurements. Graviton production from nucleon-nucleon scattering can lead to a significant change in the cooling process of proto-neutron stars [77]. Hence it is possible to derive limits from the measurement of neutrinos produced in the SN 1987a supernova [78]. Other analyses have focused on the possibility of an excess in $\gamma$-radiation due to halos of gravitationally bound gravitons surrounding neutron stars [79]. The strongest constraints are claimed by the latter type of study, with the obtained limits translating into the bounds $M_D > 27$ TeV for $n = 2$ and $M_D > 2.4$ TeV for $n = 3$ [26].

It is interesting to note that it may be possible to sidestep limits based on the low energy graviton modes in the ADD model by introducing a small warp factor [80]. This can be seen as an argument suggesting that also for $n \leq 3$ limits from collider experiments can still be of interest.

Constraints on virtual-graviton signatures in the ADD model of extra dimensions have been obtained at HERA [81, 82], LEP [83, 84, 85, 86, 87, 88, 89], and the Tevatron [90, 91]. Numerical results and references concerning the complementary searches for graviton production can be found in the PDG review article on extra dimensions [26]. By now the sensitivities for ADD models achieved by the previous collider experiments have been reached or surpassed by analyses with LHC data.

### 3.4.2 Searches for Spatial Extra Dimensions at the LHC

At the LHC, limits on large spatial extra dimensions from signatures of s-channel graviton exchange have been presented based on measurements in the dielectron, dimuon and diphoton channels at ATLAS [92, 93] and CMS [94, 9]. The results presented in this work are connected to the CMS references [9] and preceding preliminary results restricted to the dimuon channel with 2010 [4] and 2011 data [5]. The searches exclude ADD models with $\Lambda_T < 3.2$ TeV (ATLAS, combination of $ee$, $\mu\mu$ and $\gamma\gamma$ measurements) and $\Lambda_T < 3.3$ TeV (CMS, combination of $ee$, $\mu\mu$ and $\gamma\gamma$ measurements). Latest CMS dilepton results with 2012 data as summarized in section 13.3 [8, 95] extend the excluded parameter range to $\Lambda_T < 4.1$ TeV.

A reinterpretation of 2010 CMS and ATLAS dijet results [96, 97] suggests that strong bounds on ADD models can also be derived from LHC measurements of dijet angular distributions [52]. The main reason for this are the high signal cross sections of the $q\bar{q} \rightarrow q\bar{q}$ process with a $t$-channel graviton exchange. A full experimental analysis of this signature has not yet been presented by one of the LHC collaborations.

Limits on graviton production in the ADD model have been derived from the jet plus MET and photon plus MET final states at both ATLAS [98, 99] and CMS [100, 101]. At $n = 4$, the most stringent limits from these searches are at $M_D = 2.9$ TeV (ATLAS) and $M_D = 2.9$ TeV (CMS).

New dilepton and diphoton resonances in RS models have been studied at ATLAS [102, 93] and CMS [103, 94]. Both experiments exclude values of $M_1 < 2.1$ TeV for $k/\bar{\mathrm{M}}_{\mathrm{Pl}} = 0.1$. Aspects of the updated statistical analysis in the CMS search for dimuon and dielectron resonances with a part of the 2012 dataset [6] and implications of this results for RS limits are discussed in appendix A. Other analyses that have been interpreted in the context of RS models are the ATLAS searches for $WW$ and $ZZ$ resonances [104, 105].

Also models with universal extra dimensions [72] have been considered by the LHC experiments. Limits have been set based on diphoton events with additional missing transverse energy created in the particle cascades initiated by the pair-production of higher KK modes of quarks at ATLAS [106] and by looking for higher KK modes of the W boson at CMS [107].

In recent years, the possibility of signatures from microscopic black holes in models with extra dimensions at the LHC has received considerable attention [108, 109, 110]. An excess of LHC events with several high energetic physics objects in the final state has been proposed as a potential signature of the microscopic black hole decay. Searches for such a signal have been studied by both ATLAS and CMS [111, 112]. ATLAS has also presented an analysis that focuses on events with same-sign muons and high track multiplicity [113]. The results from these searches have been used to constrain the parameter space of models for microscopic black hole production in models with extra dimensions.

# 4 Statistical Methods

Any investigation of a complex dataset has to address the question of how to evaluate its structure and implications. The contained information needs to be condensed into a set of quantities from which the analyst can draw scientific conclusions. Typical examples are problems like parameter estimation and hypothesis testing. There are several conceptually differing approaches to statistical data analysis, which may in practice be competing. This implies that even within the bounds of what in a scientific community is generally conceived as an acceptable "toolbox", the individual opinions of the analyzers can play an important role in the choice of the statistical analysis strategy. The preferentially used methods in high energy physics are certainly to some degree influenced by field-specific conventions that have evolved in the course of time. Subscribing to these conventions means that one can profit from an existing pool of practical experience with similar applications, and makes it more likely that there are available software tools providing a code base for one's specific use case. At the same time it is ensured that a large fraction of potential recipients of the results will have a good understanding of how to read and interpret them. On the other hand, such field-specific conventions can sometimes increase the gap between the current status of statistical research and its application.

The following subsections review the statistical methods that are employed in the analysis. For the evaluation of the final results in a search for new physics one is mainly interested in the range of model parameters that are disfavored by the measurement (limit setting) and the persuasive power of a potential observation of new physics (significance estimation). The actual results imply that currently the focus lies somewhat more on the side of limit setting. The following sections outline some aspects of the *Frequentist approach* and the *Bayesian approach* to data analysis and also contain a brief review of the definition of *p-values*. A general discussion of the relation between Frequentist and Bayesian reasoning (e.g. [114]) is beyond the scope of this chapter. It may suffice to say that at the current point it seems as if any general consensus on the question of if and in which way such a relation exists has not been reached in the field of high energy physics[1].

## 4.1 Frequentist Approach

To substantiate the Frequentist notion of probability one can consider $n$ independent observations of a given real or imagined process. The probability of a statement $S$ like "event $A$ will happen" or "the results will be between $A$ and $B$" may then be defined as (e.g. [116])

$$Pr\left(S\right) = \lim_{n \to \infty} \left( \frac{\text{number of observations for which } S \text{ is true}}{n} \right) \tag{4.1}$$

Two important notions formulated in the context of hypothesis testing are the *type-I error rate* $\alpha$ and the *type-II error rate* $\beta$ [117]. For a hypothesis test considering two *simple* hypotheses $H_0$ (*null hypothesis*) and $H_1$ (*alternative hypothesis*) they are defined as

$$\alpha = Pr\left(\text{reject } H_0 \text{ if } H_0 \text{ is true}\right) \tag{4.2}$$

$$\beta = Pr\left(\text{accept } H_0 \text{ if } H_0 \text{ is false}\right) \quad . \tag{4.3}$$

---

[1]A lot of interesting material about the current state of statistical methodology in high energy physics can be found in the proceedings of the PHYSTAT conference series (e.g. PHYSTAT 2011 [115]).

$\alpha$ is called the *size* of the test. $1 - \beta$ is often referred to as the *power* of the test as it specifies the probability to accept $H_1$ if it is true.

One may assume that for a given statistical model determined by a set of parameters $\rho$ the probability to observe a random variable $X = x_0$ is given by $Pr(X = x_0) = f(x_0; \rho)$. Then $f$, interpreted as a function of $\rho$ for given $x_0$, is called the *likelihood* function. In general, the likelihood is not a probability density in the parameters $\rho$. For example, integrating the likelihood of the normal distribution $N(0; \sigma, \mu = 0)$ with mean $\mu = 0$ and standard deviation $\sigma > 0$ diverges. A noteworthy exception is the Poisson likelihood with mean of the Poisson distribution $\lambda$ which happens to take the form of a gamma distribution in $\lambda$. As the Poisson distribution is encountered very frequently in high energy physics, this may lead to potential misconceptions about the general properties of the likelihood. In the following, likelihoods will be labeled as $L$. The parameters $\rho$ of the model may be subdivided into a set of parameters $\nu$ which one wants to investigate and a set of parameters $\theta$ which influence the inference on $\nu$, but are either considered to be fixed or *nuisance parameters* which may be related to supplementary likelihoods. A test statistic of high practical relevance is the likelihood ratio $L(\nu; \theta | H_0) / L(\nu; \theta | H_1)$. A hypothesis test can be constructed by rejecting $H_0$ if the likelihood ratio is observed to be below a predefined threshold, corresponding to a specific error rate $\alpha$. The Neyman-Pearson lemma [118] then states that the likelihood ratio is an optimal test statistic in the sense that it constructs the test of highest power $1 - \beta$ for a given size $\alpha$. While for complicated models the assumptions that are needed for the Neyman-Pearson lemma do usually not hold true, they are often still met as an approximation. In such cases it is reasonable to expect that the likelihood ratio and related test statistics like the profile likelihood ratio discussed in section 4.3 will perform well.

An important statistical use case is parameter estimation. To calculate *confidence regions* on a set of parameters $\nu$ (*confidence intervals* in case of one parameter), one considers a set of $n$ observed values of the selected test statistic $\{t_n\}$ from an ensemble of hypothetical experiments. The confidence region or interval at *confidence level* $1 - \alpha$ is defined by an ordering rule that specifies in which way values of $\nu$ are included in intervals $I(\nu; t_{\text{obs}})$ so that the set of $n$ such intervals evaluated on $\{t_n\}$ will contain the true value of $\nu$ with probability $1 - \alpha$ for $n \to \infty$. An example is the Feldman-Cousins construction [119] that specifies an ordering rule based on a likelihood ratio. In practice, this particular rule means that values $\nu$ with decreasing likelihood ratio are added to the interval until one reaches the desired size $\alpha$. The situation in which a specific type of interval construction for a given ensemble of hypothetical experiments fails to exactly meet a requested value of $1 - \alpha$ is specified as *overcoverage* ($\alpha_{\text{true}} < \alpha$) or *undercoverage* ($\alpha_{\text{true}} > \alpha$).

## 4.2 *p*-Values

The concept of $p$-values[2] [121] allows to link observations to a "degree of surprise" (e.g. [122]). Defining a $p$-value requires to first select a test statistic $t$. One then introduces a relation $\triangleright$ between values of the test statistic so that $t_2 \triangleright t_1$ implies that $t_2$ is regarded as casting more doubt on a null hypothesis $H_0$ than $t_1$. Given an observed value of the test statistic $t_{\text{obs}}$, the $p$-value of $H_0$ with respect to $t$ is defined as the probability $(Pr)$

$$Pr(t \triangleright t_{\text{obs}} | H_0) \equiv p \quad . \tag{4.4}$$

Observing a low $p$-value implies that one has either made an unlikely observation or should reconsider the validity of $H_0$. However, the calculation of the p-value does not depend in any way on the explicit construction of an alternative model $H_1$. An important property of $p$-values

---

[2]A comprehensive account on $p$-values with a focus on their application in high energy physics is given in [120].

in the context of Frequentist methods is that at least in the absence of nuisance parameters rejecting $H_0$ if $p < p_{\text{lim}}$ guarantees a type-I error rate $\alpha$ of $\leq p_{\text{lim}}$. This is demonstrated in appendix D.2. More generally, one can categorize $p$-values according to their type-I error rate (e.g. [123]) as shown in definition 4.5.

$$
p \quad \text{is} \quad
\begin{cases}
\text{exact , if } Pr\left(p < \alpha \,|H_0\right) = \alpha \\
\text{conservative , if } Pr\left(p < \alpha \,|H_0\right) < \alpha \\
\text{liberal , if } Pr\left(p < \alpha \,|H_0\right) > \alpha
\end{cases}
\tag{4.5}
$$

## 4.3 CL$_\text{S}$ Technique

A popular way of constructing Frequentist confidence intervals in high energy collider physics is based on the test statistic CL$_\text{S}$ [124].

$$
\text{CL}_\text{S} = \frac{p(t|H_1)}{1 - p(t|H_0)} = \frac{p\text{-value of test statistic } t \text{ under } H_1}{1 - p\text{-value of test statistic } t \text{ under } H_0}
\tag{4.6}
$$

CL$_\text{S}$ is based on $p$-values evaluated with respect to an underlying test statistic $t$. The requirement CL$_\text{S} \leq \alpha_0$ can then be used to define a confidence interval for $H_1$ of size $\leq \alpha_0$. The denominator increases the observed value of CL$_\text{S}$ in a relevant way if the $p$-value under $H_0$ is large. A situation in which this is important occurs if one is looking for an excess of events as characterized by $H_1$ but observes a deficit of events with respect to $H_0$. The stronger the deficit is, the lower $p(t|H_1)$ will become. This effect is then to some extend counteracted by the expression in the denominator. In the considered case, the denominator term effectively reduces the size $\alpha$ of the test for models $H_1$ that can only be excluded in the presence of data that suggests a downward fluctuation from the hypothesis $H_0$. Hence it protects against excluding models for which the power of the test statistic $\beta$ is low. If and in which way such an effect is actually desirable is controversial. A recent alternative proposal for confidence intervals with protection against exclusion of models with low $\beta$ has been made in [125].

Typically, the choice of the test statistic $t$ in applications of the CL$_\text{s}$ technique is given by likelihood ratios, as motivated by the Neyman-Pearson lemma. For LHC data analyses, one often selects the profile likelihood ratio test statistic. If alternative models $H_1$ are characterized by a signal strength parameter $\nu$, where $H_0$ is recovered in the limit $\nu = 0$, the profile likelihood ratio for a measurement $x$ can be written as [126]

$$
t_{\text{profile}}\left(\nu = \nu_1\right) = \frac{L\left(x, \nu_1, \hat{\hat{\Theta}}\right)}{L\left(x, \hat{\nu}, \hat{\Theta}\right)} \quad .
\tag{4.7}
$$

The values of the nuisance parameters that maximize the likelihood for $\nu = \nu_1$ are labeled $\hat{\hat{\Theta}}$. The parameter choices $\hat{\nu}$ and $\hat{\Theta}$ maximize the likelihood with respect to all allowed values of $\nu$ and $\Theta$. It is usually mandatory to impose additional constraints on the likelihood of the nuisance parameters. These terms may be derived from auxiliary measurements, but for practical purposes it can often not be avoided to also impose constraints whose nature is unclear in terms of the Frequentist definition of probability. For such statistical models also the determination of an appropriate ensemble of hypothetical experiments that define the distribution of the test statistic $t$ under the model hypotheses can become complicated. One possible strategy to deal with such issues has been specified in the context of the search for the Higgs boson at the LHC experiments [127].

## 4.4 Bayesian Approach

The Bayesian approach to statistical inference is related to the application and interpretation of *Bayes' theorem*. Loosely speaking, the theorem provides a way to update beliefs in the light of new information $D$. Bayesian statistics may be derived formally from axioms stated in the framework of decision theory [128]. The probabilistic description of one's belief before including the new information is encapsulated in the *prior distribution* $\pi(\nu, \theta)$. Bayes' theorem then states that the updated belief should correspond to the *posterior distribution* $\Pi(\nu, \theta | D)$, given by the (normalized) product of prior and likelihood. In the applications discussed in later chapters, the new piece of information is given by the data from a measurement. Splitting the parameters of the statistical model into its parameters of interest (poi) $\nu$ and nuisance parameters $\theta$, Bayes' theorem may be written as

$$\Pi(\nu, \theta | D) = \frac{L(D; \nu, \theta) \cdot \pi(\nu, \theta)}{\int L(D; \nu', \theta') \cdot \pi(\nu', \theta') \, d\theta' \, d\nu'} \quad . \tag{4.8}$$

In practical applications, one will often not be interested in the full posterior, but its marginal distribution with respect to the parameters of interest. In this case, equation 4.8 takes the form

$$\Pi(\nu | D) = \frac{\int L(D; \nu, \theta) \cdot \pi(\nu, \theta) \, d\theta}{\int L(D; \nu, \theta) \cdot \pi(\nu, \theta) \, d\theta \, d\nu} \quad . \tag{4.9}$$

An $x\%$ *credible region* (*credible interval* in case of a connected region for a model with a single poi) $\mathcal{C}$ is defined via

$$\frac{x}{100} \stackrel{!}{=} \int_{\mathcal{C}} \Pi(\nu | D) \, d\nu \quad . \tag{4.10}$$

With this definition one still needs additional specifications to make the choice of $\mathcal{C}$ unambiguous. This is analogous to the need of choosing an ordering rule for the definition of Frequentist confidence intervals. One possibility for the construction of an $x\%$ credible interval is to exclude lower and upper tails of the posterior distribution, which each correspond to an integrated probability of $(1 - (x/100))/2$ (x% *central* credible interval). An alternative choice would be to construct the *shortest* poi region containing $x\%$ posterior probability. This will not result in a connected credible region for posteriors that are not unimodal. It is straightforward to extend this second specification to models with multiple parameters of interest.

An $x\%$ credible interval upper limit $\nu'$ can be defined as

$$\frac{x}{100} \stackrel{!}{=} \int_{l}^{\nu'} \Pi(\nu | D) \, d\nu \quad , \tag{4.11}$$

where $l$ is the lower boundary of the domain of $\nu$.

For a single parameter of interest, it is an often encountered approach to adopt a uniform (*flat*) prior on the parameter of interest in the interval $[0, c)$ and to define the posterior in the limit $c \to \infty$. The appeal of this choice is that the ignorance about the parameter of interest encoded in the flat prior suggests a certain amount of objectivity. From a presumably less naive point of view the reason for the choice of a flat prior is mainly motivated by how Bayesian results derived with a flat poi prior compare to Frequentist calculations. For some in practice relevant statistical models (e.g. the model discussed in section 4.5), limits based on an $x\%$ credible interval evaluate with a flat poi prior are close to (or even coincident with) Frequentist results, if the confidence level is set to $x\%$. Some examples are discussed in [129]. It is well known that uniform priors have some other properties that are much less desirable. For example, limits corresponding to a given amount of posterior probability $\sigma_{\mathrm{lim}}$ calculated with a poi $\sigma$ and

corresponding limits $\delta_{\text{lim}}$ calculated with a poi $\delta = f(\sigma)$ that can be translated to limits on $\sigma$ via $\sigma'_{\text{lim}} = f^{-1}(\delta_{\text{lim}})$, will generally result in $\sigma'_{\text{lim}} \neq \sigma_{\text{lim}}$. This is a consequence of flat priors not being *transformation invariant* (e.g. [130]). One approach towards an *objective* choice of priors are *reference priors* [131]. Roughly speaking, reference priors try to minimize the information content of the assumed prior [132]. The possibility of adopting reference priors in statistical analysis in high energy physics has recently received some attention [133, 134]. While at the current point the construction of these priors is still challenging, recent work may point towards algorithms that could be adopted for a generic solutions in the case of a single poi [135].

### 4.4.1 Markov Chain Integration

In most applications including nuisance parameters neither the posterior distribution itself nor its cumulative distribution will be known in analytic form. Instead one has to resort to numerical methods to solve the multidimensional integrals that define the projection on the domain of one or more parameters of interest. With rising dimensionality, conceptually simple techniques like rejection sampling or importance sampling will typically quickly grow inefficient as it becomes harder to constrain the properties of the posterior with sufficient precision. In the case of rejection sampling an intuitive argument for this behavior is that with rising dimensionality the fraction between the volume under a surface defined by $\Pi(\nu, \theta|D)$ and the volume under a surface defined by $\Pi'(\nu, \theta|D)$ with distance $\Delta$ between the surfaces will rapidly decrease with the number of parameters if $\Delta$ is kept constant. For example, with rising number $n$ of dimensions an increasing fraction of the volume in an $n$-sphere will be located close to the surface. Accordingly, estimating the volume in the sphere for high $n$ with rejection sampling will be very inefficient if one does not know the radius of the sphere very well.

In complicated models with many parameters, Markov-chain sampling methods[3] will often provide better performance. The concept of a Markov chain implies that the elements of the sample are ordered and that the statistical prescription for how an element $x_n$ is added to the sample depends only on the element $x_{n-1}$. All applications of Markov chain sampling in this work are based on the Metropolis-Hastings algorithm [137, 138]. In this algorithm, the next element $x_n$ is selected based on a suggested element $x'_n$ that is drawn from a *proposal function* $h(x'_n, x_{n-1})$. To simplify the discussion, it will here be assumed that a proposal function with $h(x'_n, x_{n-1}) = h(x_{n-1}, x'_n)$ is used. If the value of the probability distribution $f$ evaluated at $x'_n$ is larger than at $x_{n-1}$ one selects $x_n = x'_n$. If $f(x'_n) < f(x_{n-1})$ one makes a randomized choice that selects $x_n = x'_n$ with probability $a = f(x'_n)/f(x_{n-1})$ and $x_n = x_{n-1}$ with probability $1-a$. It can be shown that with any choice of $x_0$ the set of elements will converge towards a sample of $f$ for $n \to \infty$. Intuitively, the advantage of the Metropolis-Hastings algorithm is that the distribution $f$ is mostly explored in those regions where most of the probability is accumulated.

## 4.5 Counting Experiment

The statistical evaluation of limits on cross sections, and consequently model parameters, can be designed as a (single bin) *counting experiment*. This means that the statistical inference is based on a number of observed events meeting a given set of selection criteria. Here it is assumed that the observed number of events $N_{\text{obs}}$ is drawn from a Poisson distribution with mean $a$. The mean $a$ is given by the sum of the mean from the signal distribution $s$ and the means of the background distributions $b_i$. This works because independent Poisson distributed random variables with mean $a_i$ add up to a Poisson distribution with mean $a = \sum_i a_i$. Both $s$ and $b_i$ may

---

[3]An introduction to Markov chain methods that also discusses some more recent developments can for example be found in [136].

depend on a vector of nuisance parameters $\vec{\theta}$. The exact model for $a$ that is used to derive limits on BSM contributions to high mass dimuon events is specified in chapter 11 after background and signal contributions and their respective uncertainties have been discussed. Starting from the Poisson likelihood with mean $a$, two methods of setting the limits are considered.

- Limits based on the Bayesian approach are calculated according to equation 4.9. The posterior is calculated under the application of a uniform prior on the signal cross section $\sigma$ within the geometrical acceptance of the detector. The limits are obtained by evaluating the value $\sigma_{\text{lim}}$, for which

$$\int_0^{\sigma_{\text{lim}}} \Pi\left(\sigma \mid N_{\text{obs}}\right) d\sigma = 0.95 \quad .\tag{4.12}$$

- Limits motivated by Frequentist reasoning are evaluated with the $\text{CL}_\text{s}$ technique as outlined in section 4.3. The adopted conventional choice of the exclusion criterion is that signal cross sections $\sigma$ are excluded, if $\text{CL}_\text{s}\left(\sigma\right) < 0.05$ [26].

# 5 Large Hadron Collider and CMS Detector

Both the Large Hadron Collider (LHC) and the Compact Muon Solenoid (CMS) detector comprise a large number of subsystems which all have a high degree of technological complexity. The discussion in this chapter is limited to basic aspects that set the analysis of dimuon events at CMS into context with the experimental setup of collider and detector. The LHC can be operated as a proton or heavy-ion collider. In this work, all further discussion refers to proton-proton collisions.

## 5.1 The Large Hadron Collider

The Large Hadron collider (LHC) [139] is installed in a ring-shaped underground tunnel of 27 km length. Two beams of particles are circulated in opposite directions. They are brought to collision in 4 interaction regions that are used for the operation of the largest LHC particle detectors Alice [140], ATLAS [141], CMS, and LHCb [142]. Further smaller LHC experiments include LHCf [143], TOTEM [144], and MoEDAL [145]. An aerial view with indicated location of the LHC tunnel is shown in figure 5.1. Particle bunches are injected into the LHC beampipes after passing several stages of pre-acceleration. Protons are injected at an energy of 450 GeV. The particle beams are bent by superconducting dipole magnets that are cooled down to 1.9 K with superfluid helium. Additional magnet types are used to keep the beams focused and to decrease their transversal extension with respect to the beam direction in the interaction regions.

The reachable dipole fields of 8.3 T and the effective radius of the collider imply a maximum proton-proton center-of-mass energy $\sqrt{s}$ of 14 TeV. Up to now (end of the 2012 run) values of up to $\sqrt{s} = 8$ TeV have been achieved. The main datasets in 2010 and 2011 were recorded at a center-of-mass energy of $\sqrt{s} = 7$ TeV. The luminosity $\dot{\mathcal{L}}$ (here implicitly assumed to be averaged over many bunch-bunch interactions) is an important operational parameter of particle colliders. It can be defined as the ratio between the expected rate of a given type of interactions $\langle dN/dt \rangle$ and the corresponding cross section $\sigma$.

$$\dot{\mathcal{L}} = \frac{\langle dN/dt \rangle}{\sigma} \tag{5.1}$$

Accordingly, the integrated luminosity $\mathcal{L}$ of a dataset recorded during a time interval $\Delta t$ specifies the expected number of events $\langle N \rangle$ for a given cross section $\sigma$. The luminosity $\dot{\mathcal{L}}$ of a collider with highly relativistic particles can be approximated (head-on collisions of beam bunches with identical normal beam profile in the transverse directions x,y that are of constant variance over the bunch length) by

$$\dot{\mathcal{L}} = \frac{N_p^2 \cdot n_b \cdot c}{4\pi \cdot \sigma_x \cdot \sigma_y \cdot l} \quad , \tag{5.2}$$

where $N_p$ is the number of particles per bunch, $n_b$ the number of bunches per beam direction, and $\sigma_x$ and $\sigma_y$ are the standard deviations of the normal distributions in the $x$ and $y$ directions. $l$ is the length of the accelerator ring and $c$ the speed of light. Figure 5.2 shows the evolution of the integrated luminosity $\mathcal{L} = \int_{t_0}^{t} \dot{\mathcal{L}} dt$ at the CMS interaction region during 2011 proton-proton data taking.
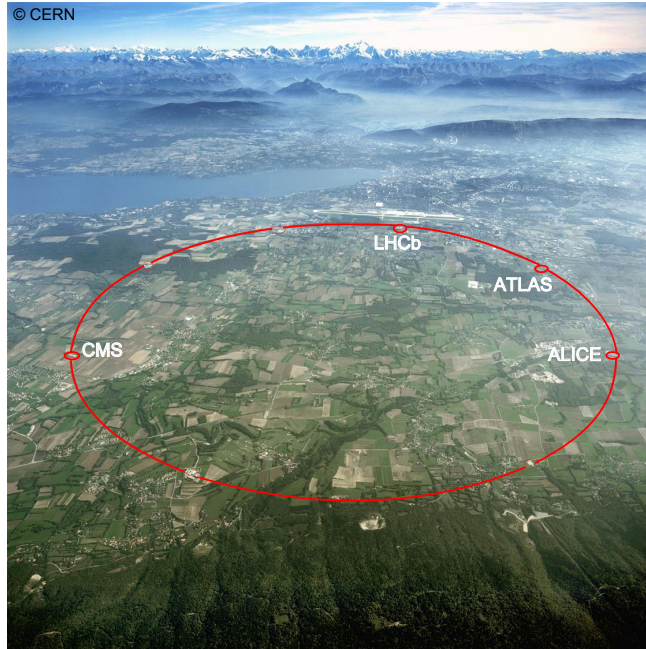
**Figure 5.1** Aerial view illustrating the scale of the LHC collider. The position of the underground tunnel and access points are indicated in red. The sites of the interaction regions are labeled with the names of the corresponding detectors. (source: [146], with emphasized tunnel location and added detector labels)
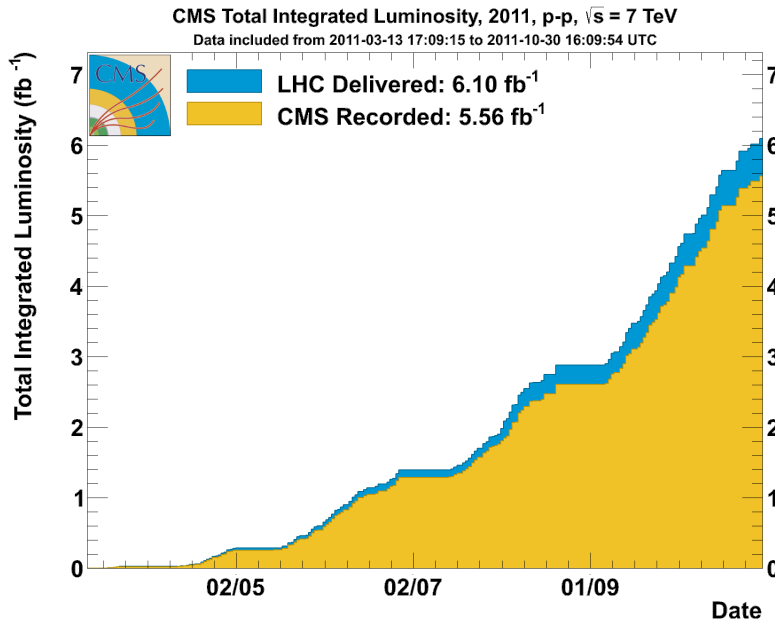


**Figure 5.2** Development of the integrated luminosity from LHC proton-proton collisions at the CMS interaction region during 2011. The figure shows the delivered LHC luminosity and the luminosity actually recorded by the CMS detector [147].

## 5.2 The CMS Experiment

CMS has been designed for the measurement of particles created in proton-proton and heavy-ion collisions at the LHC. Through the combination of different detection technologies, CMS is capable of identifying a wide range of possible types of interactions and reconstructs both specific properties of the created particles and global characteristics of the measured collision events[1].

The main body of the CMS detector is of roughly cylindrical shape with a diameter of about 14 m and a length of about 22 m. The overall weight of the detector amounts to about 12500 t. To allow for a momentum measurement of electrically charged particles through the reconstruction of their bending in an electromagnetic field, CMS employs a solenoid magnet [148, 149]. The aluminium alloyed NbTi conductor is cooled with liquid helium to reach the temperature range of superconductivity. During 2010-2012 data taking, the magnet has been operated at a magnetic field of 3.8 T. The magnetic flux outside the coil is controlled by an 10000 t iron yoke.

A schematic of the CMS detector that indicates the main subsystems is depicted in figure 5.3. The photographic picture below has been taken during the construction phase and shows a detector plane transversal to the beam line. An overview of the main detection systems is provided in the following sections. Appendix E.1 summarizes the coordinate conventions that are used throughout this work. If not mentioned otherwise, expressions like "first/last" or "front/back" are used as seen from the beam interaction region. Section 5.6 discusses the measurement of the LHC luminosity at the CMS interaction point and section 5.7 discusses a few selected aspects of the CMS software and computing infrastructure.

## 5.3 Calorimeters

Calorimeters are designed to absorb the total energy of particles and provide a signal which is in a well-understood relation to this energy. Subdividing the calorimeter into subunits allows to also recover information about the direction of flight of the measured particles and details about their showering into other particles during the process of energy deposition. The main subsystems of the CMS calorimeter are the electromagnetic calorimeter (ECAL) which is partly supplemented by a preshower detector (ES), and the hadron calorimeter (HCAL).

The ECAL is important for the identification of electrons and photons and allows for a precise measurement of their energies. Its high granularity in the $\phi$ and $\eta$ directions improves the precision at which the direction of the incident electrons and photons is determined. The ECAL also contributes to the measurement of hadrons, especially in cases where the shower has a strong electromagnetic component.

High energetic quarks and gluons create particle jets. If contained in the instrumented $\eta$-range, these jets will typically feature a large number of hadrons and deposit most of their energy in the volume of the hadronic calorimeter via strong interaction processes. The HCAL measures the amount and location of the deposited energy of the jets and is also a crucial component for evaluating the missing transverse energy.

### 5.3.1 Electromagnetic Calorimeter and Preshower Detector

The active material components of the electromagnetic calorimeter [151, 152, 149] are lead tungstate crystals. In the ECAL barrel section (EB) ($|\eta| < 1.48$), the scintillation light from

---

[1]In the following the term *event* will be used either to denote the collective interactions during a single LHC bunch crossing or the data associated with the corresponding measurement.
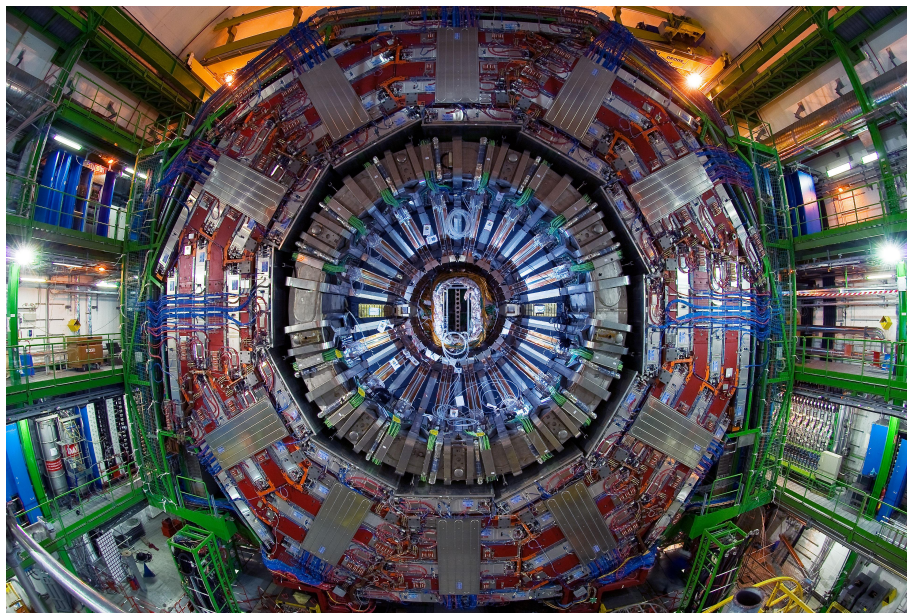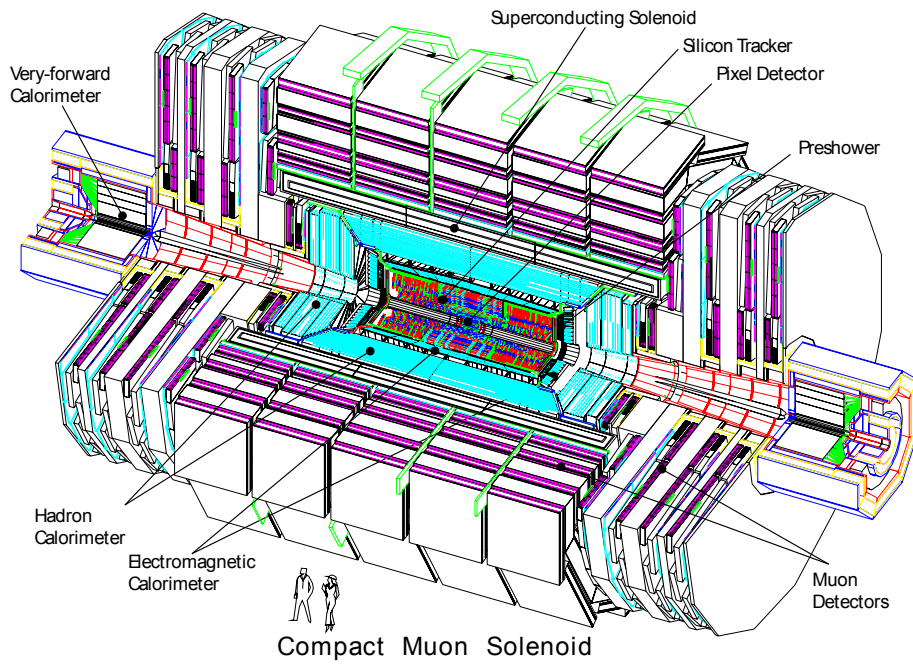
**Figure 5.3** (Top) Schematic of the CMS detector [149]. (Bottom) Photographic picture of the CMS detector during construction, showing a transversal plane of the barrel section [150].

traversing particles is measured with avalanche photodiodes. The endcap sections (EE) extending over the window $1.65 < |\eta| < 2.6$ employ vacuum phototriodes. The extension of the crystals in the $r$-direction corresponds to about $25\ X_0$ (the radiation length $X_0$ is defined as the average distance in which the energy of an electron is reduced to a fraction of $1/e$ of its initial energy due to bremsstrahlung, e.g. [153]).

The energy resolution $\sigma(E)/E$ has been measured in test beam studies [154] in which it was parametrized as

$$\frac{2.8\%}{\sqrt{E(\,\mathrm{GeV})}} \oplus \frac{12\%}{E(\,\mathrm{GeV})} \oplus 0.3\% \tag{5.3}$$

At high energies, the resolution is dominated by the constant term which is connected to the control of energy leakage, non-uniformities in the light collection and inter-calibration between different ECAL components. During data taking, this term is also influenced by the level of accuracy to which temperature, voltages and transparency loss in the crystals due to radiation damage can be monitored. In 2011, the constant term could be restricted to a level of 0.5% – 2.0%, depending on the $\eta$ coordinate [155]. The crystal transparency is evaluated by a laser monitoring system [156].

Studies with $Z \to ee$ events report an estimated systematic uncertainty on the ECAL energy scale of $\approx 1\%$ at energies close to $m_Z/2$ [157]. Methods that allow to extract information about extrapolating the uncertainty to energies up to several hundred GeV indicate that the uncertainty remains at a level of $\lesssim 2\%$ [158]. The ECAL crystals cover an area in the $\phi - \eta$ plane close to their Moliére radius (a material-dependent measure of the width of the electromagnetic shower, e.g. [159]). For this reason, and because of bremsstrahlung and electron pair production due to the material budget between collision point and ECAL, clustering algorithms need to be employed to estimate the total energies of electrons and photons [152].

Covering the range $1.65 < |\eta| < 2.6$, the preshower detector [152] is positioned between the ECAL endcaps and the inner tracking system. With two layers of radiator material both followed by a layer of silicon strip detectors, the preshower detector provides additional separation power between photons and $\pi_0 \to \gamma\gamma$ decays in the material of the inner tracker [149]. This is because the high position resolution of the hits in the silicon strips of the preshower detector still allows to distinguish the initial showers of the two photons in some cases where they are already too closely aligned to create separable showers in the ECAL crystals.

## 5.3.2 Hadron Calorimeter

The hadron calorimeter [160, 149] is built as a sampling calorimeter. The barrel and endcap sections ($|\eta| < 3.0$) are located within the solenoid. They use scintillating plastic tiles as active components. The light signals created in the wedge-shaped subcomponents (HCAL towers) extending into the $r$-direction are read out and summed up with optical fibers. Brass makes up for most of the absorber material between the scintillator layers. An additional component of the hadron calorimeter with two layers of active material is located outside of the CMS solenoid, covering the range $|\eta| < 1.3$. Including the outer HCAL detector, the minimal material depth of the HCAL (with the exception of parts of the transition region between barrel and endcap) corresponds to 11.8 hadronic interaction lengths $\lambda_I$. $\lambda_I$ is a measure of the typical distance between inelastic hadronic interactions induced by a strongly interacting particle in the material (e.g. [159]). In the range of about $3 < |\eta| < 5$, CMS employs an additional forward calorimeter component. The detection method of the forward calorimeter is based on the emission of Cherenkov light from charged particles traversing the active material given by quartz fibres.

## 5.4 Track Detectors

Track detectors are used to reconstruct the trajectories of electrically charged particles (tracks). In the presence of a magnetic field, the bending of the track can be used to measure the momentum component transverse to the field. The CMS inner tracker measures the tracks from charged high-energy particles emitted during a given bunch crossing. In CMS, associating reconstructed particles with a specific proton-proton interaction from the bunch crossing (vertex reconstruction) relies heavily on the information provided by the inner tracker. The CMS muon system which is embedded in the magnet yoke is also designed as a track detector. The high material budget between the collision point and the muon system implies low background rates from particles emitted from the proton-proton collisions other than muons, as most of their energy is expected to be absorbed in the calorimeters.

### 5.4.1 Inner Tracking System

The CMS inner (silicon) tracking [161, 162] is subdivided into two subsystems which are the silicon pixel detector and the surrounding silicon strip detector. In both cases, the detection principle is based on semiconductor technology. In simplified terms, the basic detection principle can be described as follows[2]. A junction between a p-doped and an n-doped semiconductor is operated with a reverse voltage that creates a depletion zone with only few free charge carriers. Mobile electron-hole pairs created by traversing charged particles are separated by the electric field in the depletion zone. This induces a measurable charge signal on the detector electrodes. One of the challenges encountered in the design and operation of silicon track detectors is to control the intrinsic leakage currents.

The pixel detector is the detector component closest to the interaction region of the colliding proton beams. It is composed of three cylindrical layers with the beam pipe in their center and two transversal disk components on each side. In both directions of the detection plane the achieved spatial resolution for each layer is $\approx 9$ $\mu$m [165].

The silicon strip tracker covers $|\eta| \lesssim 2.5$. Its modules are arranged in barrel (strips run approximately in the $z$ direction) and endcap sections (strips run approximately in the $r$-direction). Each module has either one detection layer or two that feature a small angle between their strip directions. This angle allows for a position measurement along the direction of the strips. For the region $|\eta| < 2.4$, tracks are likely to have 9 or more measured layer hits [149]. The spatial resolutions transversal to the strip direction from single modules vary between 23 $\mu$m and 60 $\mu$m [166].

The final step of the alignment procedure is performed with a large set of reconstructed data tracks. A global $\chi^2$ statistic is minimized to determine the alignment parameters [166]. The material budget of the tracker in the range $|\eta| < 2.5$ varies between 0.4 and 1.8 radiation lengths.

### 5.4.2 Muon System

The CMS muon system [167, 152, 149] employs several types of gas detectors [168, 169] in which the detection process starts from a traversing particle that ionizes molecules in a gas volume. Each detection unit is operated with a high voltage between anode and cathode elements. If the voltage per distance is high enough, primary electrons are accelerated sufficiently fast between scattering processes with the medium to trigger an avalanche. The electron component of the charge avalanche has high drift velocity and moves toward the anode while the slower ions move

---

[2]Introductory accounts on the detection principles of silicon track detectors can for example be found in [163] or [164].

toward the cathode. Some of the employed muon detectors only measure the anode signal. Others also read out the induced cathode signal.

As depicted in figure 5.3 (Top, the muon system is shown in magenta), most of the muon system is embedded into the yoke of the CMS magnet. The system can be subdivided into a barrel region with detection units in the range $|\eta| \lesssim 1.1$ and two endcap regions with detection units in the range $0.9 \lesssim |\eta| \lesssim 2.4$. The barrel region features 4 layers of detector components, that are referred to as *stations*. Each endcap has 4 main detector layers which are installed on the backside of the three yoke discs and in front of the first one.

DT (Drift Tube) chambers are installed in all barrel stations. The drift tubes are of roughly rectangular shape with an anode wire in their center and 2 cathode strips and 2 field shaping electrodes on the tube walls. The selected configuration results in an approximately linear relation between the distance from the primary ionization to the anode wire and the measured time of the signal. Once the signal is associated with a specific bunch crossing this can be used to improve the resolution of the track position.

RPC (Resistive Plate chamber) detectors are employed in all 4 barrel stations. They are also installed in the endcaps, where an RPC layer is mounted in front of the yoke and in the first and third disk. The basic detection unit of the RPC system is a gas filled volume between two cathode planes. This gas volume is subdivided by a layer with anode strips that is inserted parallel to the cathode planes. Signals induced by the electron avalanches are read out from the RPC strips. The distribution of the avalanche signal from a single traversing particle over the anode strips allows to use the combined information from several RPC layers for a complementary $p_T$ measurement. This $p_T$ estimate is however less precise than the $p_T$ measurements from the DT and CSC systems. The excellent time resolution of the RPC chambers allows for a clean assignment of the signal to a specific bunch crossing which makes this system an important component of the CMS muon trigger and muon identification during the full event reconstruction.

Recently presented results show that efficiencies and background rates of the DT and RPC systems are well within the design specifications [170]. Main backgrounds for a signal from a detector channel are given by the intrinsic noise [149] (i.e. noise that is not related to beam collisions) and also caused by particles that are either created directly during the proton-proton collisions or in their showering in the CMS detector. In the muon system, the latter background component is dominated by neutrons.

The CSC (Cathode Strip Chamber) system is installed in the endcap region. Each CSC contains several layers of multiwire proportional chambers. Cathode strips running in the $r$-direction are milled on one of inner chamber walls that enclose each of the gas volumes. Most of the anode wires run orthogonal to the strip direction at roughly constant values of $r$ and $\theta$. Accordingly, the anode signal is used to measure the $r$-coordinate of tracks passing the detector plane, while the distribution of the induced signal on the cathode strips is used to estimate the $\phi$-coordinate. Anode wires in the CSC planes that are closest to the interaction region are tilted at an additional angle. This compensates for the effect of the magnetic field of the CMS solenoid in this region which gives the drift velocity a $\phi$ component (*Lorentz angle*, e.g. [159]).

## 5.5 CMS Trigger System

The rates of accepted collision events have to match the available resources for data processing and long time storage. Ideally, it is the task of the trigger system to minimize the corresponding information loss by selecting the bunch crossings which are most relevant for further analysis. In practice one needs to find an acceptable compromise between the needs of the various types of analyses. For a single analysis, the trigger performance is limited by uncertainties on the event characteristics and by the acceptable bandwidths for the relevant triggers. The CMS

trigger system can be subdivided into two main stages. After establishing some basic pieces of information, all further discussion is restricted to a brief outline of the muon trigger.

The Level-1 (L1) trigger [171] operates to a large degree on custom-built electronic components. The employed buffer sizes require that a decision to pass the full event data on to the second trigger stage needs to be taken within less than a few microseconds. For this reason, only fast algorithms operating on basic information blocks provided by local subsystems can be used. Only data from the calorimeters and the muon system is available for the L1 trigger. Typical L1 rates during 2011 data taking were $\approx 70$ kHz [172].

The High Level Trigger (HLT) algorithms can access the full data associated with the event. They run on a computer farm situated at the detector site (P5). At this stage, more complicated algorithms also including data from the inner tracker can be used. In this way one achieves a better description of the event properties and can specify more sophisticated trigger criteria. To meet restrictions in bandwidth and storage capacities, some of the HLT triggers are associated with prescale factors. This means that only a fraction of the events passing these triggers are recorded. During data taking at nominal luminosity, events pass the HLT stage at rates of several hundred Hz. Basic properties of the CMS muon trigger, on which the dataset used in this work is based, are discussed in the following subsections.

### 5.5.1 Level-1 Muon Trigger

General descriptions of on the Level-1 Muon Trigger can be found in several reference texts [171, 149]. Recent accounts that discuss aspects of the performance during data taking include [173, 172, 174]. The geometrical coverage of the CMS muon trigger system is restricted to $|\eta| < 2.1$.

Trigger evaluation in the CSC chambers starts from track segments based on the hit patterns in the anode and cathode planes. Due to non-negligible drift times, data from several bunch crossings is used to assess timing and segment quality. The highest quality segments from each CSC chamber are transmitted to a Track Finder stage that merges matching segments from different stations and assigns muon direction and $p_\mathrm{T}$.

Track segments in the $\phi - z$ plane and hit patterns in the $\eta - z$ plane are evaluated in each DT chamber. Taking the angle between track and vertex direction and the number of layer hits as selection criteria, the best segments are forwarded to a Track Finder stage in which matching segments from different stations are combined, linked with data from the $\eta$ layers. Also a first $p_\mathrm{T}$ estimate is assigned to the track candidates.

The trigger subsystems in the RPC endcap and barrel detectors are segmented into towers in the $\phi$- and $\eta$-directions. For each bunch crossing, strip hits in the towers are compared to predefined track patterns. Matched patterns are used to derive a first $p_\mathrm{T}$ estimate. Accepted track candidates need to include strip hits from several RPC layers.

The muon subsystems pass up to four of their track candidates to the Global Muon Trigger stage. The Global Muon Trigger receives additional information from the Global Calorimeter Trigger which can be used to assess basic isolation properties. After combining the information from tracks that can be matched across several subsystems, the candidates are transferred to the Global Trigger. The event data is forwarded to the HLT stage if a set of $p_\mathrm{T}$ and track quality requirements is met for one or more muons.

### 5.5.2 Muon High Level Trigger

The HLT algorithms provide an improved evaluation of the physics objects identified at the L1 trigger stage. As the processing power available for each event is by far higher than at the L1 stage, a more complex tracking can be performed under inclusion of the inner tracker. The HLT

muon tracking employs the Kalman-filter which is outlined in section 6.1, in the context of the full muon reconstruction as applied on all events passing the trigger. The algorithm operates on the signals from the muon system and constructs its seeds from the L1 muon trigger objects. In a following step, the estimated track parameter in the region of the inner tracker are used to define a region in the $\phi - \eta$ plane in which Kalman-filter tracking is also performed on the hits in the inner tracker. Finally, a global fit is calculated, combining data from the tracker and the muon system to define the HLT muon trigger candidate.

During the muon HLT algorithms, energy deposits in the calorimeter or pixel tracks close to the muon candidate can be used to specify additional trigger criteria based on isolation properties. At a certain expense of robustness and efficiency, isolation criteria can be used to reduce the trigger rates due to muons that are created within the formation or decay of particles in jets. HLT processing of a typical event involving tracking takes roughly 100 ms in the presence of an average value of 10 pile-up events [175]. Depending on the luminosity, the $p_{\mathrm{T}}$ threshold for the least restrictive HLT muon trigger without prescale factor or isolation requirement in the 2011 CMS dataset varies between 15 GeV and 40 GeV. It is possible to reduce the $p_{\mathrm{T}}$ thresholds with HLT triggers that require an isolation criterion to be met by one or several triggered muon candidate .

## 5.6 Luminosity Measurement

Several ways of estimating the luminosity at the CMS beam interaction point can be considered. The most prominent methods rely either on measurements with the forward calorimeter or the pixel detector, or use fully reconstructed events that can be connected to well-understood SM quantities like the cross section of the Z resonance [176, 177, 178]. Van der Meer scans with respect to the rate of pixel clusters measured during a bunch crossing are employed as the most recent baseline method for analyses with 2011 data.

The luminosity per bunch crossing (bx) can be calculated with the equation

$$\mathcal{L}_{bx} = \frac{N_1 \cdot N_2}{A_{\mathrm{eff}}} \quad , \tag{5.4}$$

where $N_1$, $N_2$ are the bunch charges and $A_{\mathrm{eff}}$ is the effective area of the collision. The bunch charges are measured with beam current monitors [179] and could in 2010 be determined with an accuracy of 3.1% [180].

$A_{\mathrm{eff}}$ is estimated from the van der Meer scans [181], in which one measures the rate of pixel clusters per bunch crossing as a function of the horizontal and vertical distances $\delta_x$, $\delta_y$ between the beams. The recorded rate is proportional to the rate of proton-proton interactions during the bunch crossing. One can then use the relation [181]

$$A_{\mathrm{eff}} = \frac{\int R(\delta_x, \delta_y = 0) d\delta_x}{R(\delta_x = 0, \delta_y = 0)} \cdot \frac{\int R(\delta_x = 0, \delta_y) d\delta_y}{R(\delta_x = 0, \delta_y = 0)} \quad . \tag{5.5}$$

Additional corrections to equation 5.5, for example due to a beam crossing angle, are discussed in [182].

In practice, one establishes the effective pixel cross section

$$\sigma_{\mathrm{pixel}} = \langle N_{\mathrm{cluster}} \rangle / \mathcal{L}_{bx} \tag{5.6}$$

during dedicated runs with long separation between bunch trains to reduce the influence of afterglow effects. During the main runs the luminosity is then extracted by recording $\langle N_{\mathrm{cluster}} \rangle$ and solving equation 5.6 for $\mathcal{L}_{bx}$. Using the outlined procedure, latest studies show that it is possible to measure the luminosity with an uncertainty of 2.2% [177].

## 5.7 Software Framework and Computing Infrastructure

During data taking, the CMS data output amounts to roughly $1\,\mathrm{GB/s}$. Large amounts of disk space are also needed to store the samples of simulated events. At the same time, data reconstruction, event simulation, and higher-level data analyses have high demands in terms of required CPU time. Fortunately, many of the tasks that place the highest demands on the available processing power are comparatively easy to parallelize and can be efficiently executed on clusters of standard commercial CPUs. The overall amount of needed resources can only be accumulated by sharing computing tasks between different sites that provide resources. A respective infrastructure that has been developed to provide an optimized usage of the distributed computing resources in CMS and the other LHC experiments is the Worldwide LHC Computing Grid (WLCG) [183]. All CMS collaborators are provided with access rights and software tools (partially developed within the CMS collaboration) that help to access and store data on the grid and to run code on the computer clusters at the various sites.

A realistic simulation software is a crucial tool for establishing the performance of the event reconstruction in the CMS detector. Interfaced to software for the simulation of proton-proton collisions, the detector simulation allows for a prediction of both signal and background rates in a given analysis. The detector simulation is part of the CMS software framework (CMSSW) [184]. Within CMSSW, Geant4 is used to simulate the interactions of incoming particles with the detector material [185, 186]. The simulation of the digitized response of the various CMS detector components is implemented in a way that allows to store the simulation results in the same data format as the output from actual collision data. All following reconstruction steps like trigger decisions or higher level algorithms for particle identification provided by CMSSW can therefore be applied in an identical way to collision data and event simulation. Most of the code included in CMSSW is written either in C++ [187] or Python [188]. Version control with a central repository is used to set version standards for CMS physics analyses and ensures that all collaboration members have access to the latest tools.

One of the important software components used within CMSSW are the libraries of the ROOT data analysis framework [189], which have been specifically designed to cover typical functional requirements of data analysis software in high-energy physics. ROOT is also extensively used to facilitate or simplify various tasks within the analysis specific code used in the presented search for large spatial extra dimensions.

In practice, many groups of people that work on a specific analysis tend to further reduce data provided in the official CMS data format for high-level analyses by extracting only the information that is needed for the specific analysis into a custom data format that is stored at the local computing site of the person performing the analysis. This allows to adjust and reiterate many aspects of the analysis more quickly. The presented search for large extra dimensions makes use of the respective infrastructure maintained by the MUSiC analysis [190, 191] which is based on the PXL library (a component of the VISPA analysis environment) [192].

# 6 Muon Reconstruction and Event Selection

Within the CMS collaboration, baseline reconstruction algorithms and selection criteria are specified for a set of common physics objects. Here, this concerns the selection of muons at high transverse momentum. The basic structure of the muon reconstruction algorithms and the applied event selection criteria which include a few analysis specific choices are reviewed in the following sections. The resulting performance of event selection and reconstruction in the context of the presented analysis is characterized in chapter 7.

## 6.1 Muon Track Reconstruction

The CMS reconstruction of muons [193, 194, 195] starts from two sets of track candidates in the inner tracker and the muon system. Both of the two sets are constructed by separate algorithms for track finding and track parameter estimation that are optimized for the specific subsystem. Both of the algorithms rely on tracking algorithms with Kalman-filter techniques [196, 197, 198]. The use of a Kalman-filter integrates the tasks of track finding and track parameter estimation into a common framework. The method relies on a linearization of the equations or results from simulation that are used to describe the propagation of the muon between the detection layers. This linear approximation drives the choice of the 5 parameters that are used to define the track state at a given detection surface [197]. Several propagation methods are used within the CMS tracking algorithms, depending on the coordinates to which the track is extrapolated. The application of the Kalman-filter requires an initial set of track candidates that are used as *seeds* of the algorithm.

In the muon system, the Kalman-filter algorithm is seeded by trajectory states that are constructed from track segments in the DT and CSC chambers. A detailed description of the algorithm is given in [195]. After a pre-filter procedure which operates on track segments in the CSC and DT systems and hits in the RPC detectors, the final (outside-in) filter step considers all individual hits. Accepted tracks are required to include a measurement from at least one DT or CSC chamber plus one additional measurement from any of the muon detection systems.

Particle tracks in the silicon tracker are reconstructed with a combinatorial Kalman-filter [199, 200]. Seed states are constructed either from pixel hit triplets or from pixel hit pairs plus a constraint on the considered pp interaction region [201]. Several filter and smoothing steps are applied to find tracks and to provide estimates of their parameters [202]. The algorithm also includes steps for ambiguity resolution between track candidates from the combinatorial Kalman-filter that share a significant fraction of included hits.

In a following step, the two track collections are matched to form sets of combined track candidates [193]. *Tracker* muon candidates are defined by requiring compatibility between a track in the silicon tracker and at least one reconstructed track segment in a DT or CSC chamber. *Global* muon candidates require a standalone muon track that can be matched to a track in the silicon tracker. The inner track states and the standalone track states are propagated to a common surface. Matching is then performed based on a set of discriminating variables defined by the track states at this surface. The muon system improves the momentum resolution provided by the track fit in the inner tracker if the transverse momentum of the muon ($p_T$) is

in the range $\gtrsim 200$ GeV [193]. To take this into account, a track refit with the Kalman-filter is used to define the track parameters of the global muons with $p_T > 200$ GeV.

## 6.2 High $\mathbf{p_T}$ Muons

While the energy loss of relativistic muons at energies $\lesssim 100$ GeV is dominated by ionization effects, energy loss due to bremsstrahlung and electron pair production becomes important at higher energies (e.g. [203]). In iron, ionization accounts for $\approx 79\%$ of the muon energy loss at 0.1 TeV and for $\approx 24\%$ at 1 TeV [204]. Special refits of the global muon tracks have been developed to improve the performance of the standard track fits of the global muon. The high-energy refits currently in use are

- **TPFMS** (tracker-plus-first-muon-station) fit – operates on the hits from the global track but ignores those outside of the first station of muon chambers.

- **picky** fit – operates on the hits from the global track but requires hits in chambers with high hit occupancy to meet an additional $\chi^2$ criterion. A chamber with high hit occupancy can indicate the presence of an electromagnetic shower from bremsstrahlung or electron pair production.

A final choice about which fit is assigned to the muon candidate is made among the tracker, global, picky and TPFMS fits. The selection criteria are based on the transverse momenta of the track fits and the p-values of the $\chi^2$ values for the given number of degrees of freedom provided by the fit results. The procedure by which the criteria are tuned is mainly based on simulation studies.

## 6.3 Event Selection

Event selection criteria are applied to restrict the search to a robust selection of well-measured dimuon events that allow for a reliable estimation of experimental uncertainties. They are supposed to decrease the influence of reducible backgrounds while maintaining a high signal efficiency ($\approx 90\%$ for the presented analysis). The applied selection criteria are close to those also used in other CMS searches for new physics with high energy muons like the search for a dimuon resonance [103] or the search for a new $W'$ boson decaying into a muon and a neutrino [107].

### 6.3.1 Trigger and Vertex Selection

The presented analysis is based on an event selection starting from the single-muon trigger without isolation requirement or prescale factor at lowest available $p_T$ threshold. Corresponding muon $p_T$ trigger thresholds in the 2011 dataset varied from 15 GeV to 40 GeV, depending on the pile-up conditions during data taking. As the considered signal has two muons in the final state, there are two possibilities for triggering the events of interest and one expects a highly efficient and robust trigger selection. Using a trigger requiring two muon candidates would have allowed to reduce the muon $p_T$ thresholds. However, such a choice would have resulted in an overall decrease of the signal efficiency because the improvement due to the lower $p_T$ threshold is negligible for events with a dimuon mass of several hundred GeV and above.

Selected events are required to have a reconstructed track vertex with $N_{\text{dof,vtx}} > 4$, $|z_{vtx}| < 24$ cm and $\rho_{vtx} < 2$ cm. The parameter $N_{\text{dof,vtx}}$ [205] is strongly correlated with the number of

tracks associated with the vertex candidate and roughly translates into a minimum of 4 reconstructed tracks that are compatible with the vertex. $z_{vtx}$ refers to the distance of the vertex from the center of the nominal interaction region along the $z$-axis, and $\rho_{vtx}$ is the distance between the estimated vertex position and the closest point on the z-axis. These vertex requirements provide a general collision indicator. In the presented analysis, they increase the rejection power against events triggered by cosmic ray muons crossing the detector during bunch crossings.

### 6.3.2 Muon Selection

The following selection criteria are applied to all muon candidates. A summary of them is listed in table 6.1.

- The transverse momentum $p_{\mathrm{T}}$ of the muon needs to be at least 45 GeV. This value is selected because it provides a sufficient safety margin against the $p_{\mathrm{T}}$ threshold of the used muon triggers. The cut helps to avoid difficulties in the estimate of reconstruction efficiencies close to the trigger threshold.

- Accepted muons are restricted to the range $|\eta| < 2.1$. This implies that the selected region of geometrical acceptance is fully covered by the CMS muon trigger. As evaluated in section 10.1, most ADD signal muons are expected to be produced at low values of $|\eta|$. Only about 4% of the signal events with two muons in the window of acceptance $|\eta| < 2.4$ have at least one muon in the range $2.1 < |\eta| < 2.4$. Hence any potential benefits of extending the $\eta$ requirement for one of the two required muon candidates to $|\eta| < 2.4$ would be very limited. With the $|\eta| < 2.1$ criterion one also avoids complications due to increasing uncertainties of the muon reconstruction in the high-$\eta$ region.

- A muon candidate needs to be identified both as a "global" and "tracker" muon as defined in section 6.1. The selection ensures that both inner tracker and muon system take part in the muon measurement and reduces the probability of muon candidates originating from other types of particles or instrumental noise.

- Several standard requirements are imposed on the muon track to ensure the track quality.
    - The silicon tracker track must feature at least one hit in the pixel detector.
    - The silicon tracker track associated with the muon candidate is required to include more than 10 hits.
    - The silicon tracker track needs to be matched to track segments in at least two muon stations.
    - At least one hit in the muon system is required to be included in the global fit.

- The impact parameter $|d_{xy}|$ with respect to the primary vertex needs to be less than $0.2\,\mathrm{cm}$. This cut is mainly applied to reduce the background from cosmic ray muons whose tracks are not compatible with the vertex hypothesis.

- A cut on the relative tracker isolation $\left(\sum_i p_{\mathrm{T}_i}\right)/p_{\mathrm{T}}$ of 0.1 is applied to reduce contributions from muons that are produced within particle jets from quarks or gluons. Here, $p_{\mathrm{T}}$ is the transverse momentum of the muon candidate and the sum $\sum_i p_{\mathrm{T}_i}$ includes the transverse momenta of all other tracks within a cone of $\Delta R < 0.3$ centered on the direction of the muon candidate's momentum. The tracker isolation has been selected because it is robust against bremsstrahlung from high energy muons. It is possible to recover additional collision data (about 6%) by relaxing the requirements on the CMS calorimeter status as the isolation is not dependent on calorimeter information.

All events with two muons passing all cut criteria are used for the further analysis steps. There are about $1.34 \cdot 10^5$ such events in the full 2011 dataset corresponding to an integrated luminosity of 5.28 fb$^{-1}$. A summary of all applied muon cuts is given in table 6.1.

| variable | cut value | comment |
|---|---|---|
| $p_{\mathrm{T}}$ | $> 45\,\mathrm{GeV}$ | transverse momentum cut |
| $|\eta|$ | $< 2.1$ | acceptance region |
| tracker muon | true | silicon tracker track with matched segment in the muon system |
| global muon | true | standalone muon matched to tracker track |
| tracker hits | $> 10$ | track quality requirement |
| pixel hits | $\geq 1$ | track quality requirement |
| muon system hits | $\geq 1$ | track quality requirement |
| $|d_{xy}|$ | $< 0.2\,\mathrm{cm}$ | impact parameter |
| rel. track iso | $< 0.1$ | isolation requirement |
| matched stations | $> 1$ | |

**Table 6.1** Summary of the applied muon cuts.

### 6.3.3 Dimuon Selection

A cut on the opening angle $\alpha_{\mu\mu}$ between the two muon momentum vectors is applied to further reduce background contributions from cosmic radiation. While muon pairs from physics collisions are typically boosted in the CMS rest frame, muons from cosmic rays are expected to be reconstructed as muon pairs with almost exactly $p_{\mu,1} = -p_{\mu,2}$. The selected requirement on the opening angle is $\pi - \alpha_{\mu\mu} > 0.02$. Based on simulation results, it has been verified that the influence of this selection criterion on the efficiencies of other background contributions or the ADD signal is negligible.

The contributions to the dimuon invariant mass spectrum in the low mass region from virtual graviton processes in the ADD model are small with respect to the SM DY terms. However, the existence of extra dimensions can provide the major component of events in the high mass tail. The optimization of the choice of the signal region in $M_{\mu\mu}$ is discussed in section 11.

Selected muon pairs are not required to be of opposite charge. This does not lead to a significant increase of the background as the production rate of isolated same sign dimuon pairs with high energies in the SM is small if compared to the corresponding production rate of opposite sign muon pairs. Studies with cosmics [206] show that the rates of muon charge mismeasurement in the $p_{\mathrm{T}}$ range of up to several hundred GeV are expected to be $\lesssim 1\%$. Simulations with ADD signal and SM DY events indicate that the charge mismeasurement rate for dimuon events in the mass range above 1 TeV which involves even higher $p_{\mathrm{T}}$ values remains at this level. In a recent shape-based analysis [103], the muon candidates were required to be of opposite charge to avoid the drawbacks of a strongly decreased mass resolution in potential events with charge mismeasurements at high dimuon masses. The performance of the presented search for a *non-resonant* dilepton signal is less sensitive to a decrease in resolution for very high masses. Hence the concern for a potential decrease in signal efficiency due to charge mismeasurements at very high masses is given preference. In practice, the choice does not influence the results as no events with same-sign lepton pairs are found above 0.45 TeV.

# 7 Performance of the Event Selection

The muon selection criteria presented in the previous section are based on detailed studies of the muon reconstruction within the CMS collaboration. They are expected to provide a robust and efficient event selection. This general claim needs to be confirmed for each specific analysis. More specifically, it needs to be tested that the chosen criteria are efficiently selecting dimuon events and adequately reconstructing the dimuon mass.

The CMSSW simulation can not be guaranteed to reflect all relevant aspects of the detector response at a sufficient level of detail. This implies that a certain degree of uncertainty in the detector modeling is unavoidable. Additionally, the CMSSW version used for the simulation is typically not identical to the version used during data taking. This is due to the goal of a short time gap between data taking and the comparison of data with simulation results requires that the simulation efforts start some time in advance. For example, the single-muon trigger algorithms included in the simulation have notably lower $p_T$ thresholds than the algorithms employed during the later periods of 2011 data taking.

To either constrain or quantify differences between simulation and actual collision data it is therefore important to study and monitor the performance of muon triggering and muon reconstruction with the help of the actual collision data. Often the obtained results are also a driving factor for estimating uncertainties on the detector performance. Sections 7.1 to 7.3 review studies of the performance of CMS muon measurements. The most recent publicly available reference for this topic is [193]. The results are used to evaluate implications on the uncertainties of the signal and background expectation for high mass dimuon pairs. Additional uncertainties due to pileup effects are discussed in section 7.4.

## 7.1 Efficiency of Muon Trigger and Reconstruction

Both for the ADD signal and the dominant DY background, the simulated trigger efficiency in the relevant dimuon mass range is found to be $\gtrsim 99\%$ with respect to simulated events meeting the basic preselection criteria $|\eta_\mu| < 2.1$ and $p_{T,\mu} > 45$ GeV. As shown in figures 8.3 and 10.2, the simulated full selection efficiency with respect to DY background and signal is close to 90%.

*Tag and probe* methods are an important tool for testing the muon trigger and reconstruction performance in the collision data. For this type of study, one chooses a *loose* dimuon event selection that is expected to be more efficient than the selection that is tested. In a following step, one requires one muon (the *tag* object) to pass a more stringent set of selection requirements so that the event types of interest are expected to be the main component in the remaining event set. The tag and probe efficiency is then defined as the probability of the second muon (the *probe* object) passing the less efficient *tight* selection. If necessary, corrections can be applied to account for the potential bias due to events from non-DY processes like $W + $ jets production.

CMS has published results from tag and probe studies with DY muon pairs based on the 2010 dataset [193]. Within the collaboration, tag and probe studies have also been performed with the 2011 dataset. The full selection efficiencies are subdivided into several factors (trigger efficiency, track reconstruction, further reconstruction and identification, and isolation). These factors are then evaluated with specific setups of the tag and probe method. The studies include results for a tight selection that is close to the muon selection discussed in section 6.3.

In summary, it is found that there is no evidence for a difference between the efficiency in simulation and collision data that would be relevant for the presented analysis. However, due to the limited event statistics of high energy muon pairs there is a non-negligible uncertainty in extrapolating this finding towards muons from dimuon events with masses in the range of $\approx 1$ TeV and above. In this mass region, the effect of the increased electromagnetic showering from the muons could to some degree deviate from what is predicted by the simulation. Figures 10.2 and 8.3 suggest that the corresponding decrease in efficiency is expected as $\lesssim 3\%$. Taking this shift in efficiency as an indicator for the potential size of differences between the efficiency predicted by the simulation and the efficiency in the data, 3% is chosen as an estimate of the uncertainty on the selection efficiency of the background above a high mass threshold. The uncertainty on the signal efficiency is estimated as 4%, as above a given mass threshold the signal contributions tend towards higher masses than the more steeply falling background. In the later statistical treatment of efficiency uncertainties, efficiencies of $< 0$ and $> 1$ are not considered. For a Bayesian model, this can be enforced by truncating the associated prior functions if their domain is not already restricted to the allowed interval $[0, 1]$ by their initial definition.

## 7.2 Dimuon Mass Resolution

The estimated dimuon mass resolution influences the expected mass distribution of dimuon events. As the backgrounds are strongly decreasing with $M_{\mu\mu}$, an underestimate of the dimuon resolution in the simulation will lead to an observed excess of high mass events that could potentially be misinterpreted as a signal. If the uncertainty on the dimuon mass resolution is large, its influence needs to be taken into account for the calculation of observed limits and significances.

The point of main interest in the context of the presented analysis is how the resolution uncertainty affects the expectation for the integrated background above a given mass threshold $M_{\text{threshold}}$. The respective influence on the signal contribution is considerably smaller. This is
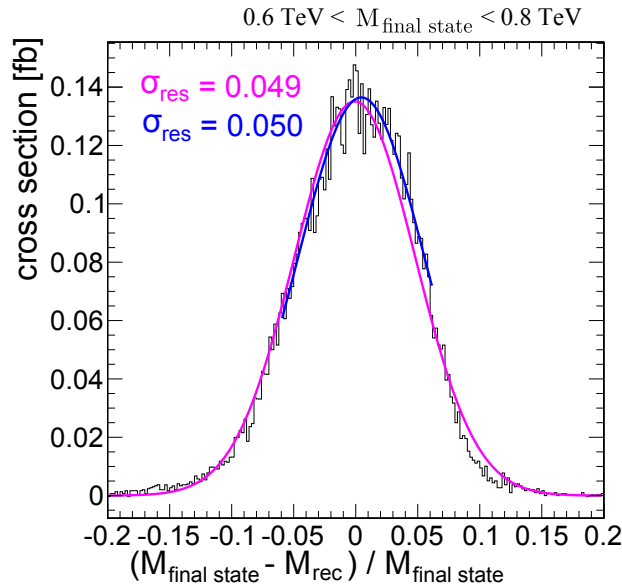


**Figure 7.1** Gaussian fits for determining the relative mass resolution $\sigma_{\text{res}}$ for simulated DY events in the range $0.6$ TeV $< M_{\text{final state}} < 0.8$ TeV.
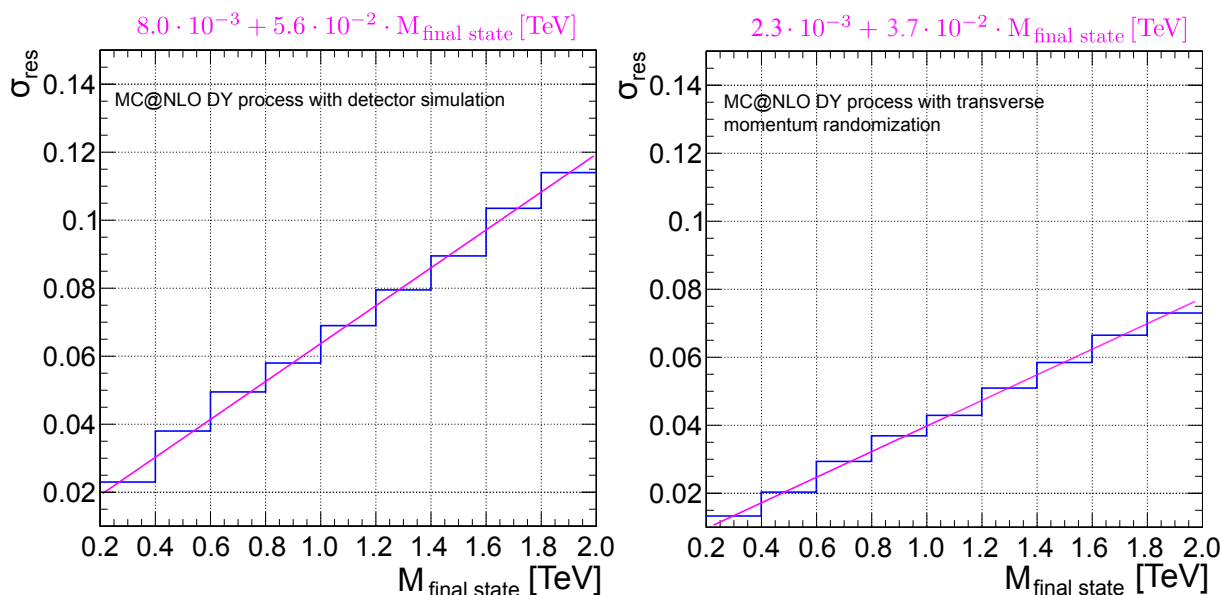
**Figure 7.2** (Left) Linear fit to the simulated relative mass resolution for the DY process as a function of $M_{\text{final state}}$. (Right) Linear fit to the relative mass resolution for the DY process as a function of $M_{\text{final state}}$. For this result, the mass resolution is evaluated by randomizing the muon $p_{\text{T}}$ values as suggested by measurements of cosmic ray muons.

because for relevant model parameters the signal is found to be comparatively flat in the vicinity of the considered range of mass thresholds.

Figure 7.1 shows the distribution of $(M_{\text{final state}} - M_{\text{rec}})/M_{\text{final state}}$ $(|\eta_\mu| < 2.1)$ for simulated DY events in the range $0.6\,\text{TeV} < M_{\text{final state}} < 0.8\,\text{TeV}$. $M_{\text{final state}}$ is the dimuon mass prediction after parton shower and hadronization[1]. $M_{\text{rec}}$ denotes the corresponding mass measurement after the simulation of detector response and event reconstruction. Figure 7.1 also shows the results from two Gaussian fits to the distribution. In the following, $\sigma_{\text{res}}^2$ is used to label the variance of these fits. One of them (magenta) corresponds to a fit to the full shown interval of the $x$-axis, the other (blue) is restricted to an interval approximately corresponding to the FWHM (full width half maximum) of the distribution. While the difference between the two fits is marginal for the shown mass interval, it increases to about $\Delta\sigma_{\text{res}} = 0.01$ for masses in the range between 1 TeV and 2 TeV. The reason for these differences is that the shape is not optimal for the description of effects like bremsstrahlung that become more relevant at high masses.

Fit results for $\sigma_{\text{res}}$ (averages between the two considered fit ranges) for different mass intervals are shown in figure 7.2 (Left). As expected, $\sigma_{\text{res}}$ increases with the dimuon mass. The relation between mass and $\sigma_{\text{res}}$ in the mass interval (0.2 TeV, 2 TeV) obtained from the simulation is approximately linear.

Resolution studies that extend up to transverse momentum values of roughly $p_{\text{T},\mu} = 0.1$ TeV can be performed with collision data from DY events. With these methods, it has been measured that the relative $p_{\text{T}}$ resolution $\sigma_{\text{res},p_{\text{T}}}$ averaged over the range $|\eta| < 2.1$ is about 0.02 [193]. The relative resolution decreases to about 0.015 for small $|\eta|$ values. At higher transverse momentum, the $p_{\text{T}}$ resolution can be measured with cosmic ray muons. These studies are restricted to

---

[1]In the context of event simulation, the term *(generated) final state* refers in the following always to simulated events that have not yet been passed to the detector simulation. If not explicitly mentioned otherwise, the generated final state includes QCD shower, EW shower, and hadronization.
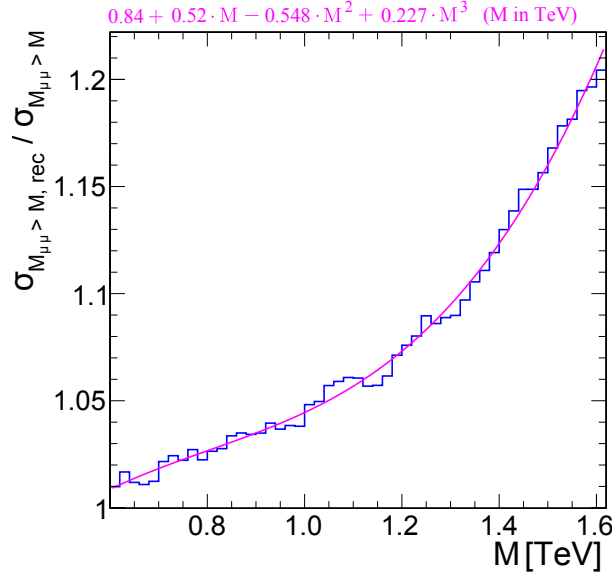
**Figure 7.3** Ratio between the DY background cross sections with the full detector simulation and a scenario with optimal mass reconstruction ($M = M_{\text{final state}}$).

$|\eta| < 0.9$ as the muon flux strongly decreases with $|\eta|$. The results indicate a relative $1/p_T$ resolution of about 0.01 at 50 GeV which increases approximately linearly to about 0.06 at 400 GeV (Tune P fit results, [193]). This allows to estimate the relative mass resolution of dimuon events by randomizing the $p_T$ values of the final state muons from the DY simulation according to the resolution results from cosmic ray measurements (while adjusting $p_z$ to keep the direction of the muon's momentum unchanged). Applying the same fitting method as described above on the resulting dimuon masses generates the mass dependent values of $\sigma_{\text{res}}$ shown in figure 7.2 (Right). It is not surprising that the resolution fits from this procedure are somewhat narrower than the corresponding results shown in figure 7.1. This is because the $1/p_T$ uncertainty from the cosmic ray measurement has here also been applied to higher values of $|\eta|$, for which a decreased resolution is expected.

A limit for a possible reduction of the background due to a detector resolution that is better in the actual collision data than in the simulation is given by the case that the mass of all selected events is reconstructed in an optimal way. The difference between this case and the baseline scenario using the masses predicted by the detector simulation is quantified in figure 7.3 as a function of a lower mass cut. In the following, the difference will also be used as an estimate of a possible increase of the background. In somewhat simplified terms this corresponds to the assumption that the increase of background due to the muon resolution is likely to be simulated correctly within a factor of 2. More detailed studies of the $p_T$ dependence in the region of higher $|\eta|$ values than currently available would be required to derive a more detailed estimate of this uncertainty. For the statistical evaluation, the domain of the prior function used to model the influence of the momentum resolution on the background may be restricted to values that do not reduce the background further than expected for an ideal detector. It is however found that this has a negligible influence on the statistical results.

## 7.3 Dimuon Energy Scale

Not only the muon $p_\mathrm{T}$ resolution but also a shift between the average reconstructed muon $p_\mathrm{T}$ at a given true $p_\mathrm{T}$ value influences the expected background and signal contributions above a given dimuon mass threshold. Again, the size of such an effect may differ between data and simulation. No significant bias of the muon energy scale has been observed in studies of $p_\mathrm{T}$ values up to 100 GeV [193]. For searches using muons in the $p_\mathrm{T}$ range of several hundred GeV and above, studies suggest a relative $p_\mathrm{T}$ scale uncertainty of $0.05/\,\mathrm{TeV}$. This number is mainly based on the analysis of a bias in the minimum of the $q/p_\mathrm{T}$ distribution measured with cosmic ray muons. Details of this method are described in [207]. Changing the reconstructed $p_\mathrm{T}$ values in the simulated DY background by $\pm 0.05 \cdot (p_{\mathrm{T,final\,state}}/1\,\mathrm{TeV}) \cdot p_{\mathrm{T,final\,state}}$ changes the DY background prediction above a given mass threshold as shown in figure 7.4. It can be seen that the respective upwards and downwards fluctuation of the background are almost of equal size. Both the upwards and the downwards shifts are approximately linear in the range $0.6\,\mathrm{TeV} < M_\mathrm{threshold} < 1.6\,\mathrm{TeV}$ and the mean of their absolute values can be parametrized as $-0.034 + 0.14 \cdot M_\mathrm{threshold}/\,\mathrm{TeV}$. In the following, this parametrization is used as an estimate of the background uncertainty above a given value $M_\mathrm{threshold}$ due to the uncertainty on the muon momentum scale.
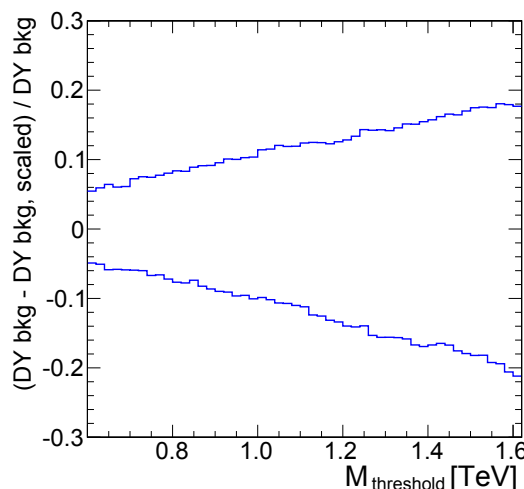


**Figure 7.4** Change in the expected DY background above a dimuon mass threshold $M_\mathrm{threshold}$ due to a $p_\mathrm{T}$ shift of $\pm 0.05 \cdot (p_{\mathrm{T,final\,state}}/1\,\mathrm{TeV}) \cdot p_{\mathrm{T,final\,state}}$.

## 7.4 Influence of Pileup

The term *pileup* refers to the presence of multiple proton-proton interactions resulting in relevant energy deposits in the detector that are associated with a given bunch crossing. Such energy deposits can be caused by interactions that took place during the evaluated bunch crossing (in-time pileup) but can also be remnants from interactions during earlier or later bunch crossings (out-of-time pileup). In a search for new physics one needs to study the effect of pileup on the selection of signal and background events. Details of the influence of pileup on a search for new physics are difficult to quantify by simulation as they tend to depend on QCD physics in the non-perturbative regime. Measurements of the influence are challenging due to the ambiguous association of energy deposits with particles from specific proton-proton interactions and can
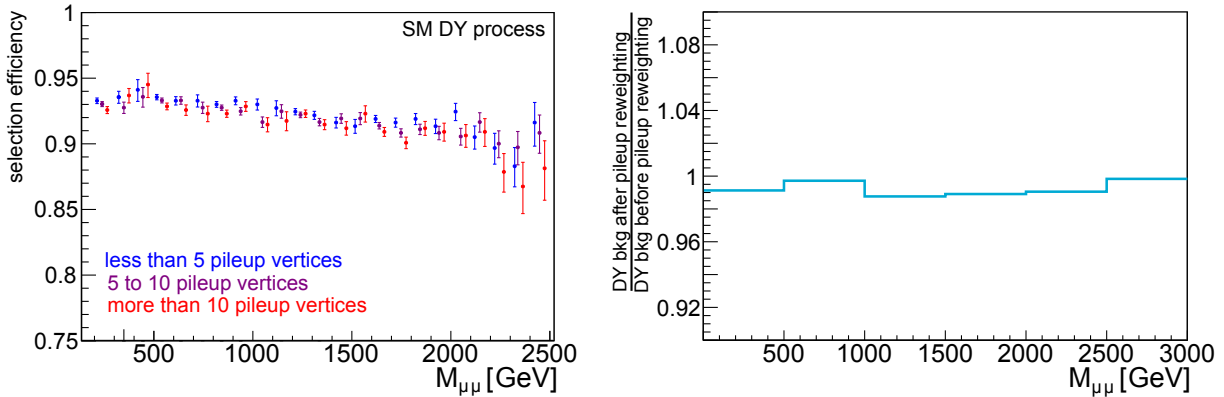
**Figure 7.5** (Left) Simulated selection efficiencies for different ranges of reconstructed primary vertices. (Right) Ratio between the DY background expectation before and after pileup-reweighting.

also suffer from limited event statistics. If possible, it is therefore beneficial to design searches in a way that avoids any strong pileup dependence. It may than suffice to show that the possible effects of pileup are so constrained that their influence on the results of the analysis is considerably smaller than that from other uncertainties. In the following discussion, it will be argued that this is the case for the dimuon selection employed in the presented search.

It is intuitive to expect that an event selection with two high energy muons and a $p_T$ relative tracker isolation will not be significantly affected by pileup effects. Still, the strong increase in pileup during 2011 data taking makes it necessary to test this assumption. Counting the number of *primary vertices* is one way of characterizing the pileup activity in a given event. This approach is reasonable because much of the influence of pileup is expected to be related to proton-proton interactions for which such a vertex can be reconstructed. A primary vertex is primarily defined by the $N_{\mathrm{dof,vtx}} > 4$ criterion introduced in section 6.3.1.

The influence of pileup on a simulated event can be modeled by adding the simulated energy deposits in the CMS detector from additional proton-proton interactions to the event description [208]. The events used for this procedure are generated as PYTHIA6 *minimum-bias* events [209], which include QCD multijet processes, elastic scattering, and single-diffractive and double-diffractive processes at low $p_T$. In most situations it may be assumed that only these types of processes contribute to the pileup in a statistically relevant way. The final states are then passed to the CMS detector simulation and the resulting detector response is added on top of the initial event description.

There is often a considerable difference between the pileup conditions that were anticipated during event simulation and those encountered in the collision data. One can deal with this problem by applying a posteriori weights on the simulated events to make their distribution resemble the data more closely. This procedure is often called *pileup-reweighting*. The basic version of this method which is applied here starts from an evaluation of the distributions of primary vertices in simulation and collision data. According to their number of vertices, the simulated events are then associated with weights that make the resulting distribution of primary vertices in the simulation identical to the measured distribution.

Reweighting scenario and dataset employed for the results shown in this section correspond to an intermediate dataset of 1.1 fb$^{-1}$. Figure 7.5 (Left) shows simulated selection efficiencies based on the simulation of the dominant DY background with MC@NLO [210, 211], evaluated for different ranges of the number of reconstructed primary vertices. It can be seen that the
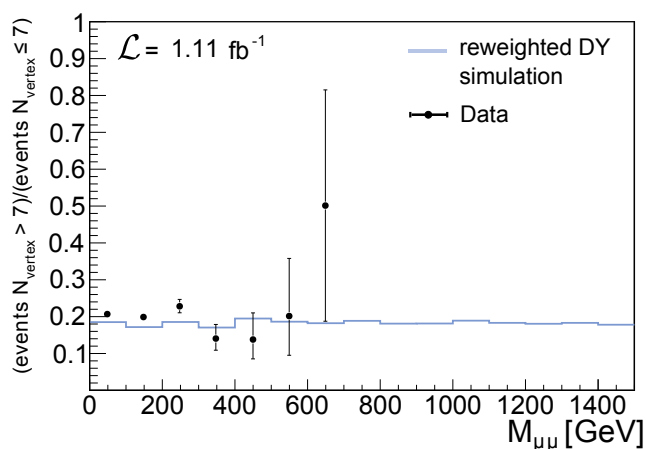
**Figure 7.6** Ratio between events with $< 7$ vertices and $\geq 7$ vertices in the pileup-reweighted DY simulation and collision data.

decrease in efficiency when going to higher vertex multiplicities is $\lesssim 1\%$. Accordingly it is expected that the influence of the pileup-reweighting procedure on the background expectation is negligible with respect to the leading uncertainties[2] in the presented search for new physics in the dimuon mass spectrum. The small influence of pileup-reweighting on the size of the expected DY background is demonstrated in figure 7.5 (Right).

One can test the robustness of the data selection against pileup effects by splitting the selected events in the data into subsets based on their number of vertices. Pileup dependence could then result in a mass dependence of the ratio of events in the subsamples. Figure 7.6 indicates that the mass dependent ratio is compatible with an approximately flat distribution.

---

[2]for example the PDF uncertainty evaluated in section 8.4.

# 8 Background from the Standard Model DY Process

The SM DY process is the dominant background to a dilepton signal from the graviton decay in the ADD scenario of large spatial extra dimensions. Combinations of model parameters that are not yet strongly disfavored by experiments from the pre-LHC era are expected to become visible at high dilepton masses in the range of at least several hundred GeV. As the graviton couples to the energy momentum tensor, also other SM processes could get influenced at comparable energy scales. This, in combination with the general scarcity of events from electroweak processes in the relevant energy range, makes it important to perform a careful study of the expected SM DY background by means of simulation. Within the uncertainties of the detector performance, one can validate the theory predictions for masses below the signal region and potentially use this data to improve the background estimate and its uncertainty. In the following sections it is discussed how a combined application of existing software tools can be used to evaluate the mass dependent SM DY background and estimate its uncertainty. If not stated otherwise, all evaluated cross sections are inclusive with respect to additional final state particles.

## 8.1 Simulation at LO

The leading order prediction for the differential cross section of the SM DY process has been reviewed in section 2.3. While the baseline result for the background estimation is based on a simulation with MC@NLO (section 8.2.1), also LO calculations are of relevance for the analysis. In some cases they are sufficient for qualitative considerations and a comparison with them allows to define a reference point for the quantification of higher order effects. Due to the potential influence of interference effects they are also important for the evaluation of the signal contribution (section 10). The Born level amplitudes of the DY process are implemented in many event generators. To achieve full consistency between the simulation of signal and background, all results in this section are calculated with PYTHIA8 [212]. The integrated cross sections of the dimuon mass spectrum as a function of a lower mass threshold including the PYTHIA8 parton shower (CTEQ6 LO PDFs, tune options *ee*:3 and *pp*:5 (4C), program version 8.142) are shown in figure 8.1 (Left). Numbers for ratios between high mass events with one muon falling into the acceptance interval $2.1 < |\eta| < 2.4$ and the number of high mass events with both muons within $|\eta| < 2.1$ are given in table 8.1. For high dimuon masses the ratio is approximately 0.05 and depends only weakly on the choice of a lower mass threshold. These numbers are of interest because as discussed in section 6.3.2 the range $2.1 < |\eta| < 2.4$ is covered by the CMS

| | $M_{\mu\mu} > 1.1$ TeV | $M_{\mu\mu} > 1.3$ TeV | $M_{\mu\mu} > 1.5$ TeV |
|---|---|---|---|
| $\frac{\#\text{events}(1\mu, 2.1 < |\eta| < 2.4)}{\#\text{events}(2\mu, |\eta| < 2.1)}$ | 0.06 | 0.05 | 0.05 |

**Table 8.1** Ratios between the number of DY LO events (PYTHIA8 including parton shower) with one muon falling into the acceptance interval $2.1 < |\eta| < 2.4$ and the number of events with both muons within $|\eta| < 2.1$, for different lower mass thresholds.
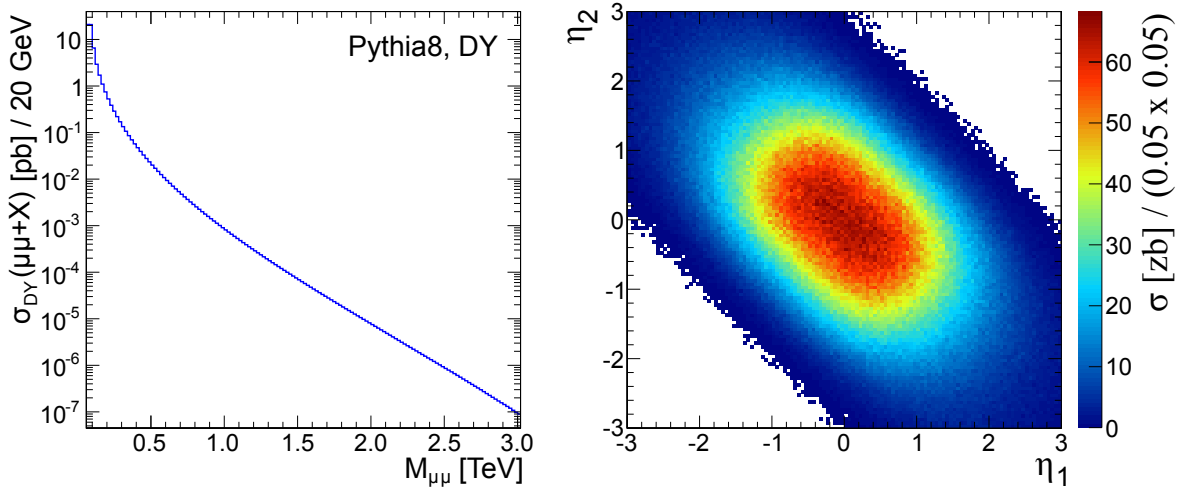
**Figure 8.1** (Left) Integrated DY cross section as a function of a lower mass threshold evaluated with Pythia8, including a basic event selection ($|\eta_\mu| < 2.1$ and $p_{T,\mu} > 45$ GeV). (Right) Angular distribution of the two final state muons ordered by $p_T$ for $M_{\mu\mu} > 1.3$ TeV (1 zb = $10^{-21}$ b).

muon system but not part of the L1 muon trigger. Figure 8.1 (Right) shows the full $(\eta_1, \eta_2)$ distribution for $M_{\mu\mu} > 1.3$ TeV, where the index 1 labels the muon with highest $p_T$.

## 8.2 QCD Corrections up to NNLO

Next-to-leading order (NLO) corrections to the DY process [213, 214] in $\alpha_s$ are known to have a strong influence on many observables, including the dilepton mass distribution. Examples of QCD NLO Feynman graphs are shown in figure 8.12 (diagrams ii−iv). Generally, a correct inclusion of higher order QCD terms in proton-proton collisions requires a consistent treatment of renormalization and factorization schemes between the calculation of hard interactions and the definition of PDFs (e.g. [215]). QCD NNLO corrections to the DY process have also been calculated [216, 217]. A few of the Feynman graphs that are connected to the calculation of QCD NNLO corrections are shown in figure 8.12 (diagrams v−vii).

### 8.2.1 Simulation of Drell-Yan Dimuon Events with MC@NLO

MC@NLO [210, 211] allows to simulate Drell-Yan dimuon events including full NLO QCD corrections. The parton level events used for the presented study are generated with MC@NLO, version 3.4.1, interfaced to the lhapdf library, version 5.8.5 [218]. The applied PDFs are the central set of CTEQ66 [219]. Herwig6 [220] is used for parton showering and hadronisation. Additionally, the Photos [221] (final state photon radiation) and Jimmy [222] (multiple parton interactions) tools are applied.

The detector simulation follows standard procedures[1]. Pileup is included in the simulation to allow for a reweighting of events according to the pileup distribution measured in the 2011 dataset. The possibility of an influence from pileup effects on the DY background prediction has been discussed in section 7.4. The simulation is subdivided into different mass ranges to avoid

---

[1]Summer11 sequence with CMSSW_4_1_4 up to GEN level and CMSSW_4_2_3_patch2 for all further steps
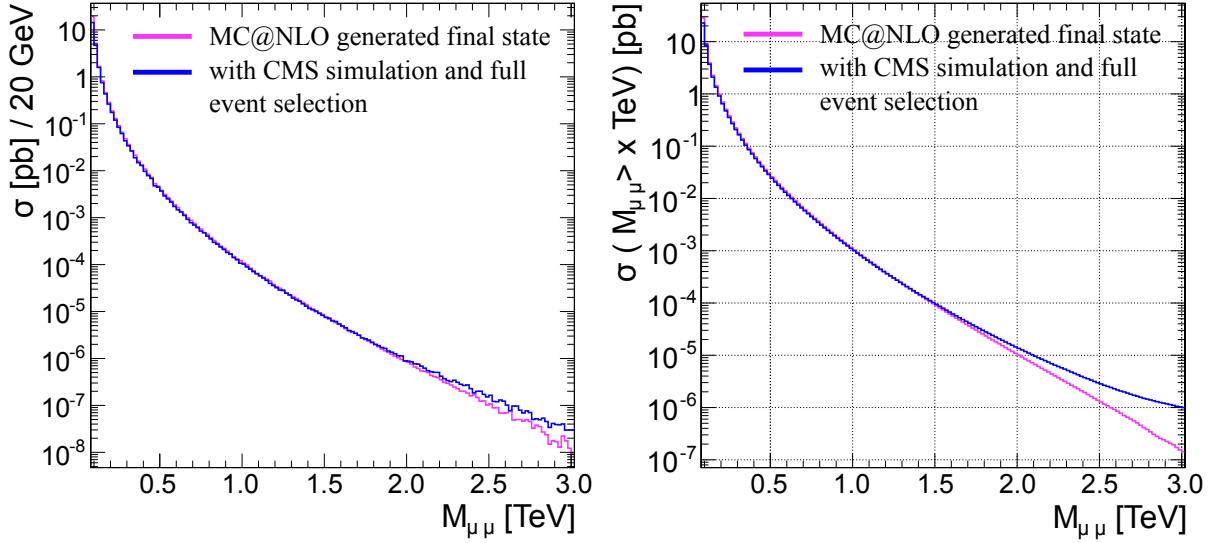
**Figure 8.2** (Left) DY dimuon cross sections evaluated with MC@NLO, as a function of the dimuon mass at generated final state with basic selection criteria ($|\eta_\mu| < 2.1$ and $p_{T,\mu} > 45$ GeV) and after simulation of the event reconstruction in the detector including all selection criteria. (Right) Corresponding integrated cross sections (from left bin border), as a function of the dimuon mass threshold.

statistical limitations due to low event numbers in the tail of the mass distribution. Table D.2 lists the generated event samples.

Mass dependent cross sections for selected events at generator level and after application of all selection criteria on the reconstructed event are shows in figure 8.2. Figure 8.2 (Left) presents the cross sections contained in mass bins of 20 GeV width. Figure 8.2 (Right) shows the cross sections integrated from a lower mass threshold. In both cases, the results are shown with only a basic set of selection requirements ($|\eta| < 2.1$ and $p_T > 45$ GeV) on the final state at generator level and under inclusion of the detector response and the application of the full set of event selection criteria. For masses of up to about 1 TeV, the expected cross section including the detector simulation are slightly lower as the overall efficiency is approximately 90%. Influences from the dimuon mass scale and resolution become more visible at very high masses and result in an increased mass tail for the events with included detector simulation.

Figure 8.3 (Left) shows mass dependent LO→QCD NLO K-factors defined as ratios between the cross section simulated with MC@NLO and Pythia8. They illustrate that care needs to be taken in applying such corrections, as their size can strongly depend on the choice of the PDFs and specifics of the LO simulation. The results show that applying NLO PDFs to the Born level changes the K-factor. This demonstrates the importance of a consistent choice of PDFs in the definition and application of K-factors. One can also see that the Pythia parton shower increases the effective K-factor as the events are shifted towards lower dimuon masses.

The simulated mass-dependent selection efficiency is shown in figure 8.3 (Right). This efficiency includes trigger simulation, muon reconstruction, and the application of the full set of event selection criteria. The result is evaluated with respect to final state muons with $|\eta| < 2.1$ and $p_T > 45$ GeV. Including an additional track based isolation criterion on the final state muons that reflects the isolation criterion applied on the reconstructed muon pair does not alter the resulting efficiencies in a relevant way. These simulation results demonstrate that over a wide range of dimuon masses the event selection is expected to be efficient at a level of above
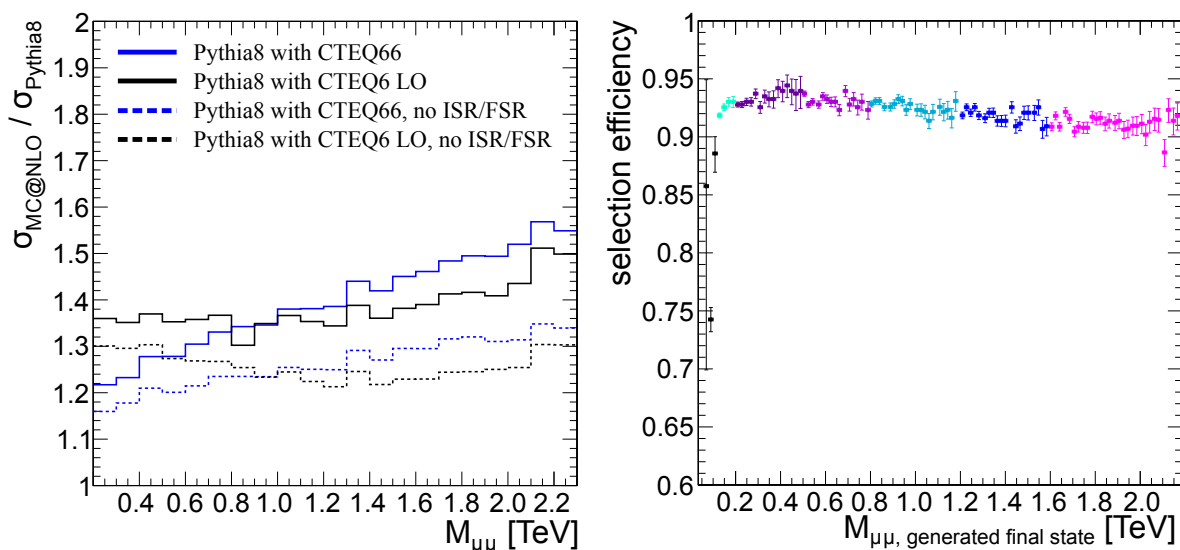
**Figure 8.3** (Left) Mass dependent LO→QCD NLO K-factors ($|\eta| < 2.1$ and $p_{\mathrm{T}} > 45$ GeV) derived from DY simulations with MC@NLO and Pythia8. (Right) Mass dependent selection efficiency (i.e. fraction of MC@NLO events with $|\eta| < 2.1$ and $p_{\mathrm{T}} > 45$ GeV that passes the selection criteria applied on the simulated CMS detector response and event reconstruction). Changes in color indicate thresholds between the different mass binned event samples used to evaluate the efficiency at a given mass value.

90%. The efficiency in the interval $0.2 \, \mathrm{TeV} < M_{\mu\mu} < 2 \, \mathrm{TeV}$ is found to be varying by only about 3%.

At a given dimuon mass, one can use the variable $\theta^*$ (defined in section 2.3) to fully specify the LO DY process in the center-of-mass frame. Figure 8.4 provides a comparison between the $\cos\theta^*$ distributions evaluated with MC@NLO and Pythia8 in the ranges $0.9 \, \mathrm{TeV} < M_{\mu\mu} < 1.1 \, \mathrm{TeV}$ and $1.3 \, \mathrm{TeV} < M_{\mu\mu} < 1.5 \, \mathrm{TeV}$. The simulations indicate that the LO shape of the distributions is approximately maintained in the NLO result. Also the reconstruction is found to have only little influence on the obtained shape.

## 8.2.2 Comparison between DY Dimuon Events Simulated with MC@NLO and Powheg

Simulation results for the expected dimuon mass spectrum at QCD NLO with MC@NLO have been discussed in section 8.2.1. Another simulation tool that allows for a prediction of the DY dimuon background at QCD NLO including matching to a QCD parton shower simulation is Powheg [223, 224]. DY dimuon events generated with Powheg that use the latest version of the CMS detector simulation for the analysis of 2011 data have been generated within the CMS collaboration. A list of the corresponding data samples is provided in table D.3. The PDF set that has been applied for these simulations is CT10 [225]. Pythia6 [209] is used to include a QCD and EW parton shower.

Comparing the DY background to the dimuon mass spectrum as evaluated from the Powheg samples with the results from MC@NLO provides a first idea of the uncertainties that one should expect from differences in the used PDF sets and the varying implementation of NLO calculations and parton showering. Ratios of the predicted dimuon mass spectra can be evaluated
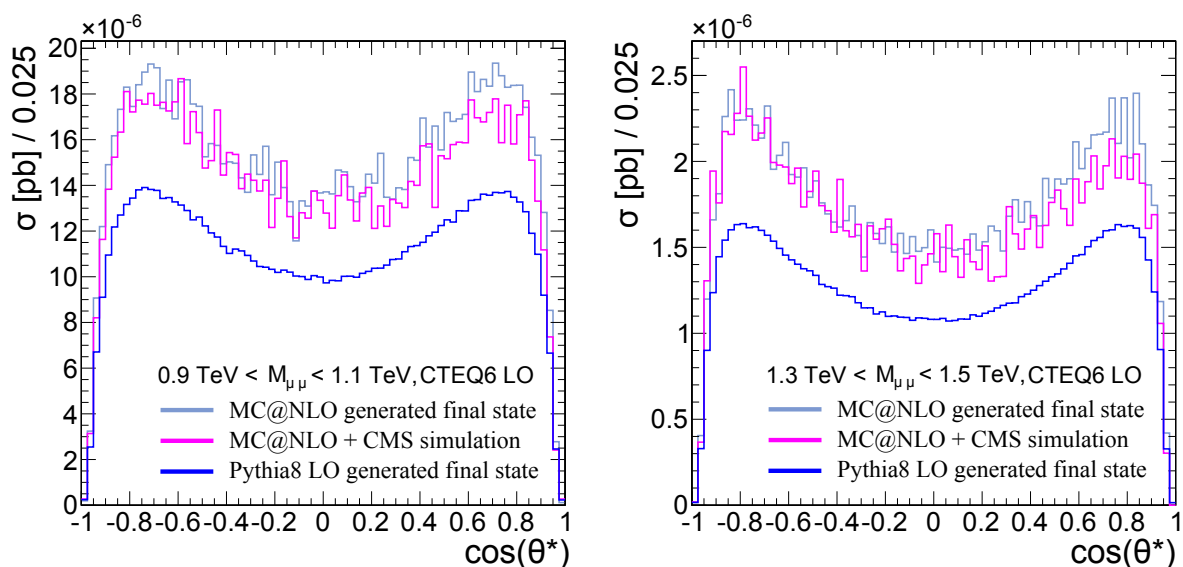
**Figure 8.4** Comparison between the distribution of $\cos\theta^*$ ($|\eta_\mu| < 2.1$ and $p_{\mathrm{T},\mu} > 45$ GeV) at LO (PYTHIA8) and QCD NLO (MC@NLO) for different dimuon mass regions.

based on the final states from MC@NLO and Powheg and the respective predictions after the detector simulation and the subsequent event reconstruction. Comparing these ratios allows for an estimate of how relevant differences between the CMS software versions used for the simulation with Powheg and the simulation with MC@NLO (somewhat older version) are for the evaluation of the DY background expectation.

Figure 8.5 (Top Left) shows the DY dimuon mass spectrum from the simulation with Powheg. Integrated cross sections as a function of a lower mass threshold are given in figure 8.5 (Top Right). A comparison between the mass dependent cross sections from the Powheg and the MC@NLO simulation is shown in figures 8.5 (Bottom Left) and 8.5 (Bottom Right). Including the influence of parton showering and hadronization, the differences between the two simulations are found to be rising with the dimuon mass. The deviation is about 7% for the integrated cross section above 0.2 TeV and increases to about 18% for the integrated cross section above 1.5 TeV.

Uncertainties on the assumed parton density functions at QCD NLO (section 8.4) make it likely that a large part of the deviation is due to the different PDF sets used in the two simulations. Including the CMS simulation and event selection increases the difference between the simulation with Powheg and MC@NLO by about 3%. This suggests a mild influence of the newer version of the CMS simulation software on the prediction of the DY background. However, the size of the effect is considerably below the leading uncertainties on the background prediction in the signal region[2].

### 8.2.3 Evaluation of the Dimuon Mass Spectrum at QCD NNLO with FEWZ

The program FEWZ [226] allows to calculate LO, QCD NLO, and QCD NNLO parton level cross sections for the DY process[3]. It is possible to evaluate the cross sections as a function of the dilepton mass, and additional kinematic cuts on the final state particles can be specified. To specify an approximate NLO→NNLO correction factor on the NLO background estimate

---

[2]A summary of these uncertainties is given in table 11.1, including references to the sections in which they are discussed in more detail.

[3]In this section, the terms NLO and NNLO always refer to QCD calculations.

calculated with MC@NLO, the mass dependent DY cross sections at NLO and NNLO have been evaluated with FEWZ (version 2.0). The applied PDF sets are the central NLO MSTW08 [215] PDF set for the calculation of NLO cross sections and the central MSTW08 NNLO PDF set for the calculation of NNLO cross sections. To be consistent with the muon selection used in the presented analysis, both final state muons are required to be in the range $|\eta_\mu| < 2.1$. Resulting NLO→NNLO correction factors for several mass ranges between 0.8 TeV and 1.4 TeV are shown in table 8.2. The renormalization and factorization scales are selected at the center of the evaluated mass range.

These results show that the NLO→NNLO correction factors are small if compared to the LO→NLO corrections discussed in section 8.2.1. This suggests that the perturbative approach
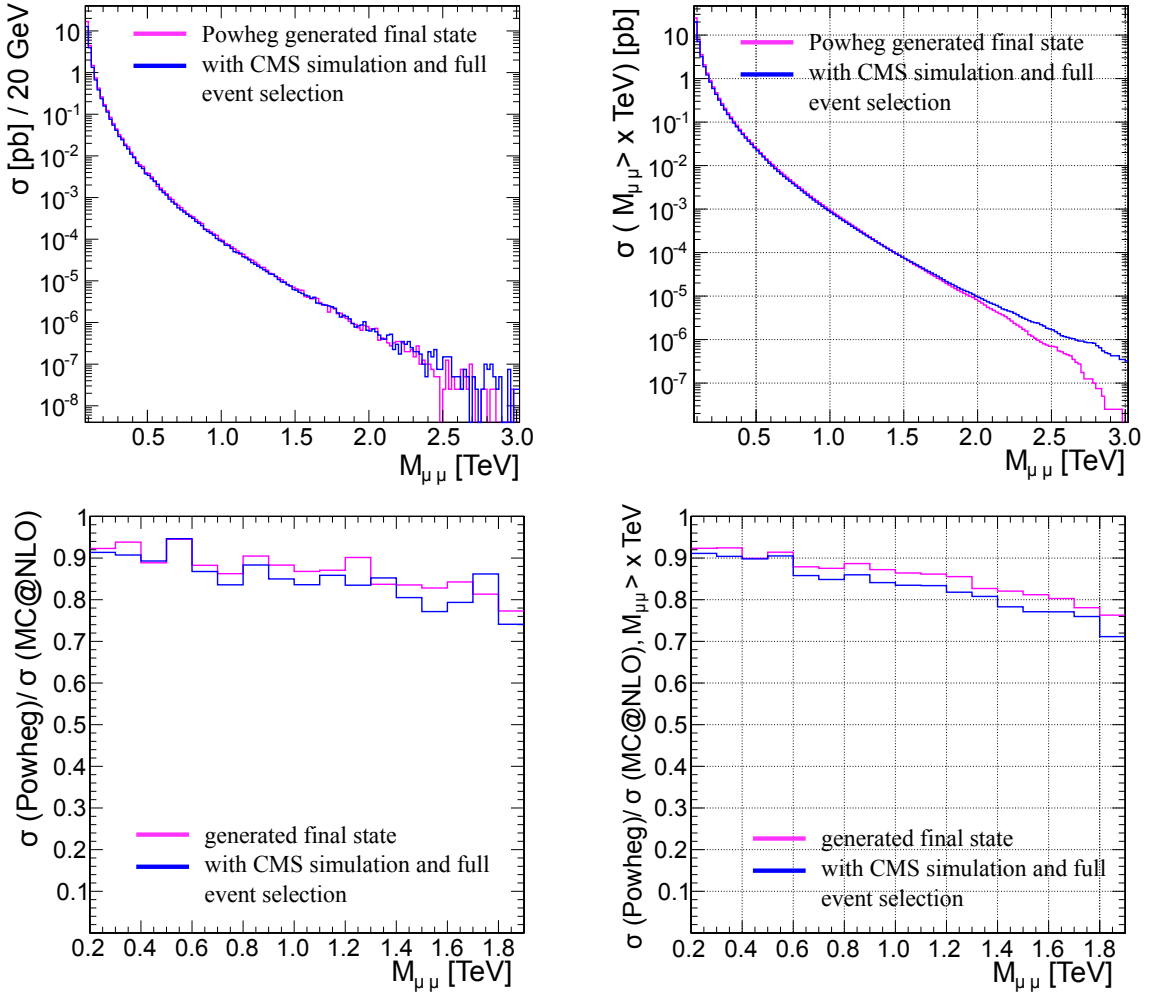


**Figure 8.5** (Top Left) DY dimuon cross sections evaluated with Powheg, as a function of the dimuon mass at generated final state with basic acceptance selection criteria ($|\eta_\mu| < 2.1$ and $p_{T,\mu} > 45$ GeV) and after simulation of the event reconstruction in the detector including all selection criteria. (Top Right) Corresponding integrated cross sections (from left bin border), as a function of the dimuon mass. (Bottom Left) Ratio of mass dependent DY cross sections evaluated with Powheg and MC@NLO ($|\eta_\mu| < 2.1$ and $p_{T,\mu} > 45$ GeV). (Bottom Right) Corresponding ratio of integrated DY dimuon cross sections as a function of the lower mass threshold (left bin border).

**Table 8.2** DY QCD NLO→NNLO correction factors for several dimuon mass regions as evaluated with FEWZ.

| mass region [TeV] | QCD NLO→NNLO correction factor |
|:---:|:---:|
| $0.8 - 0.9$ | 1.02 |
| $1.1 - 1.2$ | 1.04 |
| $1.3 - 1.4$ | 1.03 |

in $\alpha_s$ converges roughly as one would naively expected. Generally, studies indicate that NNLO results are stable at the level of $\approx 1\%$ with respect to typical scale variations [217]. For the presented study it is found that varying the renormalization and factorization scales by a factor of 2 changes the NLO→NNLO K-factors by at most 2%. The FEWZ output indicates that the uncertainty on the calculated results due to limitations in the numerical precision related to the invested time for computing the results is about 1%. This implies that the results are in agreement with a K-factor that is flat in the dimuon mass. An NLO→NNLO K-factor of 1.02 is applied on the NLO background prediction at masses of several hundred GeV and above[4]. For the statistical evaluation of results, an uncertainty of 3% is applied to cover the systematic uncertainty due to the limitations in the precision of higher order QCD corrections.

## 8.3 Electroweak NLO Corrections

Complete calculations of higher order matrix elements for the DY process in electroweak perturbation theory have been calculated at NLO [228, 229] and are implemented in simulation software [230]. The corresponding Feynman graphs for the quark anti-quark initial parton state comprise

- virtual electroweak radiative corrections, for example diagram 8.12 (viii)

- photon emission from the initial or final state fermions, for example diagram 8.12 (ix)

- corrections due to boson self energies, for example diagram 8.12 (x)

- box diagrams with the exchange of 2 gauge bosons, for example diagram 8.12 (xi)

The influence of box diagrams becomes more relevant at high energies, because they involve Sudakov factors of the form $ln\left(\hat{s}/M_{W,Z}^2\right)$. It has been found [229] that the strongest effect of the box diagrams at high dilepton masses for LHC proton-proton collisions is due to the *WW* box diagram.

A full treatment of EW NLO effects also requires an electroweak evolution of the PDFs [231, 232]. As a result, one receives photon contributions to the parton densities and modifications to the quark and (less importantly) gluon densities. PDF fits including QED evolution at $O\left(\alpha_{\text{QED}}\right)$ are available in the MRSTQED04 PDF set [233]. The inclusion of a photon PDF results in additional contributions to the dimuon mass spectrum from the Born level $\gamma\gamma \to \mu\mu$ and $\gamma q \to \mu\mu + $ jet processes. One of the diagrams that are relevant for the photon induced contributions is shown in figure 8.12 (xii).

So far, no complete calculation of a combined treatment of QCD NLO and EW NLO corrections to the DY observables has been presented. As long as this situation persists one needs to take a pragmatic approach to combining both types of NLO corrections. It is therefore necessary

---

[4]This particular choice is compatible with the results shown in table 8.2 and allows for best consistency with other studies of NLO→NNLO corrections [227].

to consider different possibilities that allow to arrive at a reasonable estimate for the cross section uncertainties. Two different calculation schemes for a combination of EW NLO and QCD NLO corrections to a given observable are discussed in [234]. It has been suggested to take their difference as an indicator for the uncertainty due to $O\left(\alpha\alpha_s\right)$ terms. The evaluation of the EW corrections with Horace in section 8.3.1 relates to this approach and follows a similar strategy. The presented evaluation is certainly not exhaustive of the possibilities to study electroweak DY corrections. While it is unlikely that a substantially more precise evaluation of the electroweak DY corrections at high masses is possible with the currently available calculations and software tools, further studies could help to improve the estimate of the corresponding systematic uncertainties in future iterations of the analysis.

### 8.3.1 Evaluation with Horace

The HORACE [230] event generator (version 3.1) has been used to evaluate electroweak corrections to the DY dimuon mass spectrum. For the simulation of the QCD parton shower and hadronisation, HORACE is interfaced to HERWIG. The factorization scale is set to the invariant mass of the lepton pair. The aim of this study of electroweak NLO effects is to derive correction factors that can be applied on the MC@NLO prediction at generated final state.

Most of the presented results are evaluated based on the CT10 QCD NLO PDFs [225]. As briefly outlined in the previous section, a fully consistent treatment of the NLO EW corrections requires a PDF set with the corresponding QED parton evolution. The choice of the used PDFs for this study is motivated by the decision to apply the EW corrections on top of the QCD NLO sample. Another reason is the lack of a recent PDF set with QED NLO evolution taking into account improvements in the methodology and input of available data for PDF fits from the last decade. To get an estimate of the influence of photon induced effects, they are evaluated as a separate effect. For this purpose, HORACE is interfaced to the MRSTQED04 PDF set.

As PHOTOS [221] is used for the showering step of the event generation with MC@NLO, the effect of photon radiation is already largely accounted for in this simulation. In consequence, PHOTOS also needs to be applied for calculating the DY LO observables with HORACE to derive a meaningful correction factor. The electroweak K-factor factor can then be defined as

$$K_{\mathrm{EW},1} = \frac{\left(\ \mathrm{HORACE}\ (\mathrm{NLO})\right)_{M_{\mu\mu}}}{\left(\ \mathrm{HORACE}\ (\mathrm{LO+FSR})\right)_{M_{\mu\mu}}} \quad . \tag{8.1}$$

As a cross check of the simulation of final state radiation (FSR) with HORACE one can also calculate

$$K_{\mathrm{EW},1'} = \frac{\left(\ \mathrm{HORACE}\ (\mathrm{NLO})\right)_{M_{\mu\mu}}}{\left(\ \mathrm{HORACE}\ (\mathrm{LO}) + \mathrm{PHOTOS}\right)_{M_{\mu\mu}}} \quad , \tag{8.2}$$

where the final state radiation is simulated by PHOTOS. Alternatively, one can consider to take the EW corrections to the LO cross sections as an additive correction to the observable, with the correction factor defined as

$$K_{\mathrm{EW},2} = 1 + \frac{\left(\ \mathrm{HORACE}\ (\mathrm{NLO})\right)_{M_{\mu\mu}} - \left(\ \mathrm{HORACE}\ (\mathrm{LO+FSR})\right)_{M_{\mu\mu}}}{\left(\mathrm{MC@NLO}\right)_{M_{\mu\mu}}} \quad . \tag{8.3}$$

The correction factor $K_{\gamma-\mathrm{ind}}$ quantifies the influence of photon induced contributions as

$$K_{\gamma-\mathrm{ind}} = 1 + \frac{\left(\ \mathrm{HORACE}\ (\mathrm{NLO,photon\ induced})\right)_{M_{\mu\mu}}}{\left(\mathrm{MC@NLO}\right)_{M_{\mu\mu}}} \quad . \tag{8.4}$$
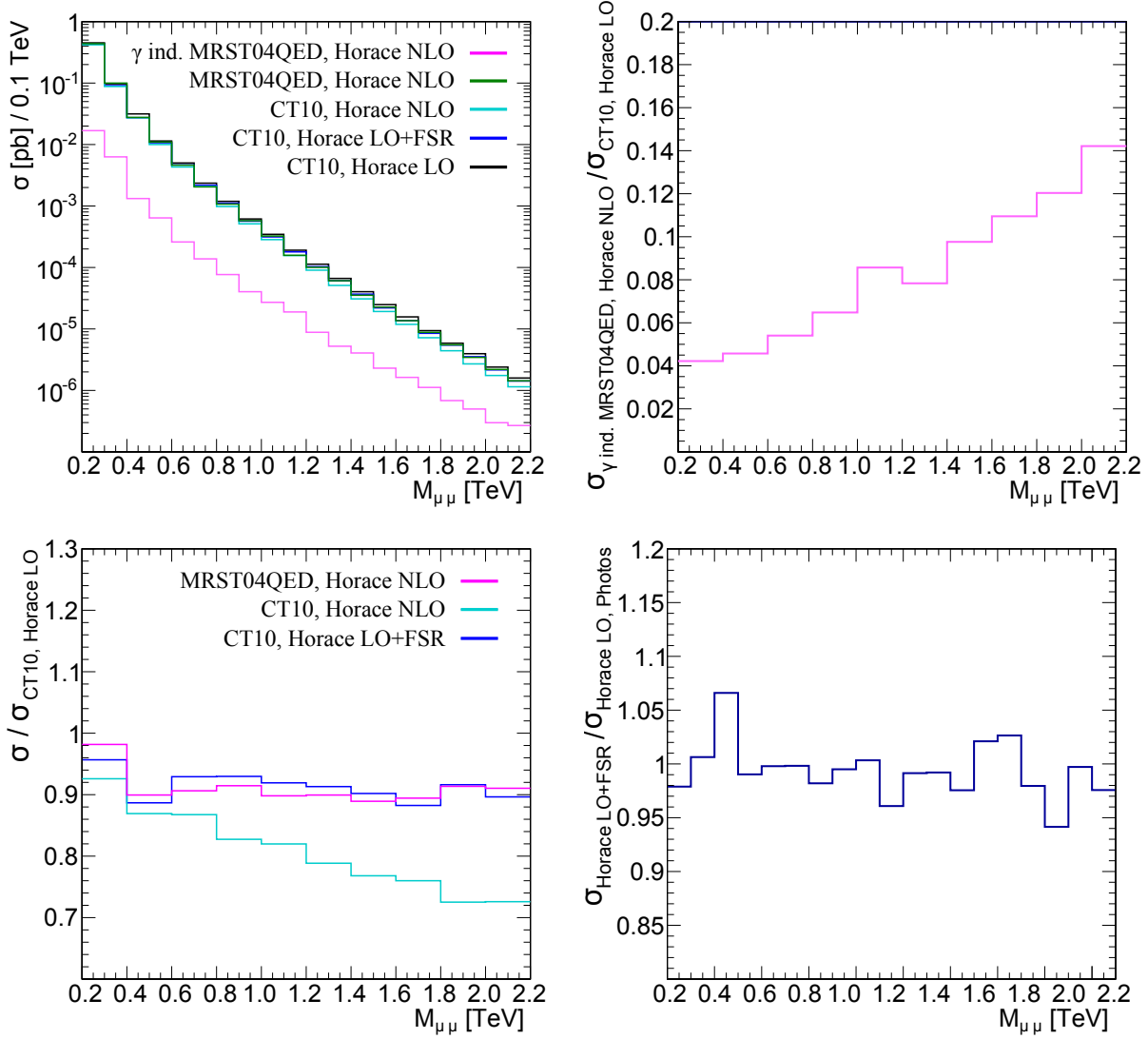
**Figure 8.6** (Top Left) DY dimuon cross sections as a function of the dimuon mass evaluated with HORACE. (Top Right) Ratios of the cross section from photon induced processes at EW NLO and the LO cross section as a function of the dimuon mass. (Bottom Left) Ratios of DY EW NLO or LO+FSR cross sections and the LO cross section as a function of the dimuon mass. (Bottom Right) Ratios between the cross sections from HORACE LO including final state radiation and HORACE LO interface to the EW shower simulation with Photos.

Events are generated in mass binned samples with $M_{\mu\mu}$ in the range of $[0.2\,\mathrm{TeV}, 0.5\,\mathrm{TeV}]$, $[0.5\,\mathrm{TeV}, 0.8\,\mathrm{TeV}]$, $[0.8\,\mathrm{TeV}, 1.2\,\mathrm{TeV}]$, $[1.2\,\mathrm{TeV}, 1.6\,\mathrm{TeV}]$, and $[1.6\,\mathrm{TeV}, \sqrt{s}]$. An overview of these samples is given in table D.1. The events in a given sample are generated with event specific weights of $\pm 1$ and the thresholds for the hit-or-miss based unweighting procedure are set sufficiently high to avoid any relevant bias of the result. Here, unweighting refers to the procedure of accepting events into the final sample according to their relative probability in the considered phase space. This avoids statistical problems related to samples that are dominated by events with small weights. All shown results include a basic muon selection of $p_{\mathrm{T},\mu} > 45$ GeV
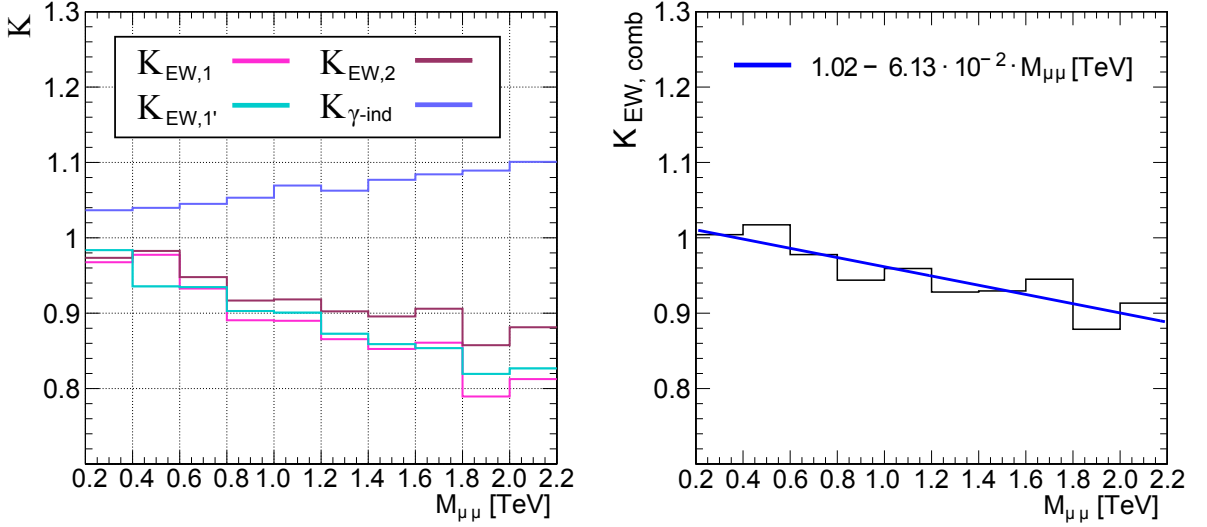
**Figure 8.7** (Left) Mass dependent EW correction factors as defined in equations 8.1 to 8.4 ($|\eta_\mu| < 2.1$). (Right) Combined EW correction factor as defined in equation 8.5.

and $|\eta| < 2.1$ to take the experimental constraints on trigger threshold and selected acceptance range into account.

Figure 8.6 (Top Left) shows the evaluated HORACE mass spectra at LO, LO with FSR, and NLO. It can be seen that there are no significant steps at the thresholds between samples covering different mass ranges. This indicates that the chosen thresholds for the unweighting procedure are appropriate. The cross sections for the photon induced processes $\gamma\gamma \to \mu^+\mu^-$ and $\gamma q \to \mu^+\mu^- q$ are evaluated with the corresponding subset of events simulated at EW NLO using the MRSTQED04 PDFs . Ratios between the evaluated mass distributions and the LO mass distribution are shown in figure 8.6 (Top Right, Bottom Left). At a given mass interval, the FSR corrections to the DY process result in reduced cross sections. For the combined effects from virtual contributions and photon radiation the downwards trend increases for high masses as expected from the amplitudes of the box diagrams. The EW NLO evaluation with MRSTQED04 PDFs predicts a decreased amount of the downwards correction due to the photon induced processes. This shows that it is important to consider not only the EW NLO matrix elements for gluon and quark induced processes but also the influence of the photon PDF that arises in a consistent EW NLO calculation. The relative contribution of the photon induced processes with respect to the LO cross section is found to be increasing with the dimuon mass which seems compatible with results from detailed calculations of EW corrections to the neutral DY process presented in [235].

Mass dependent ratios between the HORACE LO+FSR distribution and the HORACE LO with PHOTOS EW showering are shown in figure 8.6 (Bottom Right). As one does not expect any local features for this ratio, it can be concluded that, within the statistical uncertainties, the ratios are compatible with a value of 1. Accordingly, $K_{EW,1}$ and $K_{EW,1'}$ are equivalent with respect to the obtained precision of the evaluated results. The resulting EW correction factors as defined in equations 8.1 to 8.4 are shown in figure 8.7 (Left). Figure 8.7 (Right) shows the combined EW correction factor

$$K_{EW,comb} = \frac{(\text{MC@NLO})_{M_{\mu\mu}} \cdot K_{EW,1} + (\text{HORACE (NLO,photon induced)})_{M_{\mu\mu}}}{(\text{MC@NLO})_{M_{\mu\mu}}} \quad . \tag{8.5}$$

At 0.5 TeV, $K_{EW,comb}$ is compatible with 1 but decreases to about 0.9 at 2 TeV. The trend of the seen effect is compatible with evaluations of EW correction factors to the DY process for pp collisions at different center-of-mass energies [236, 228, 237, 238]. An uncertainty of 3% covers the difference between $K_{EW,1}$ and $K_{EW,2}$ and statistical uncertainties. Additional uncertainties are expected due to the choice of the factorization scale and higher order corrections. Taking this into consideration it seems reasonable to assign an uncertainty of 0.05 to $K_{EW,comb}$. For the results discussed in the following chapters, the MC@NLO simulation is corrected for EW effects according to $K_{EW,comb}$.

## 8.4 Mass Dependent PDF Uncertainty on the DY Cross Section at QCD NLO

Limitations on the precision to which the proton parton distribution functions are known result in an important source of uncertainty on the dimuon SM DY cross sections at high dilepton masses. As the considered BSM signature is a non-resonant enhancement of high mass dimuon events, it is important to quantify the PDF related uncertainties on the dominant background source. The applied procedure for the estimation of the PDF uncertainties makes use of input from the CTEQ66 [219], MSTW08 [215] and NNPDF21 [239] PDF sets. The overall approach is close to what is suggested in the interim recommendations of the PDF4LHC group [31]. Specific studies of the influence of $\alpha_s$ variations suggest that the associated uncertainty is considerably smaller than the combined influence from other PDF related factors. For practical reasons, the study of PDF sets which do not use the respective best fitting value for $\alpha_s$ is restricted to MSTW08 PDFs.

Within each of the three considered PDF sets, the reweighting technique [240] is applied to study the effects of varying the fit parameters (MSTW08 and CTEQ66) or switching between
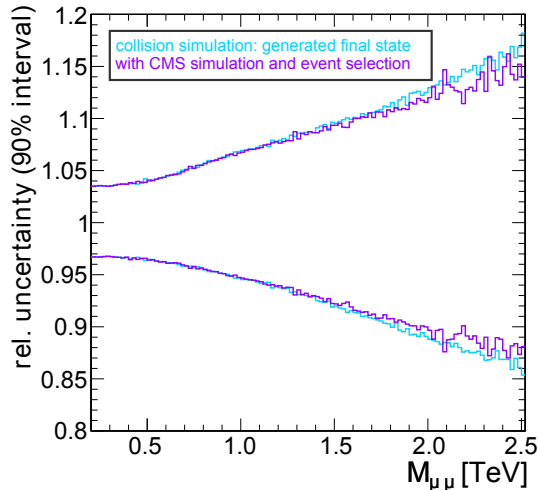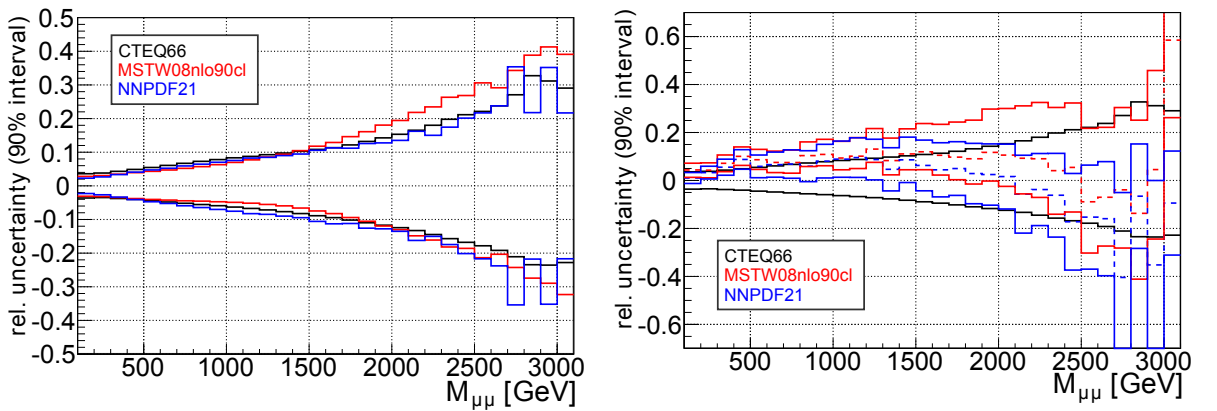


**Figure 8.8** Relative PDF uncertainties on the DY dimuon cross sections evaluated with CTEQ66 as a function of the dimuon mass ($|\eta_\mu| < 2.1$) at the final state of the collision simulation and after simulation of the detector response and event selection.

different replica (NNPDF21). Here, *reweighting* refers to the method of switching from a PDF set $a$ to a PDF set $b$ by applying an event specific weight factor

$$w_{ij}^k = \frac{f_i^b\left(x_i, Q^2\right) \cdot f_j^b\left(x_j, Q^2\right)}{f_i^a\left(x_i, Q^2\right) \cdot f_j^a\left(x_j, Q^2\right)} \quad , \tag{8.6}$$

where the indices $i, j$ label the types of the initial state partons. A more detailed discussion of PDF reweighting including a list of advantages and potential drawbacks may be found in [241]. The PDF uncertainty is evaluated in dependence on the considered dimuon mass. The PDF uncertainties are changing sufficiently slowly with the dimuon mass to make uncertainty variations in an interval of 100 GeV irrelevant for the analysis. Accordingly, results are evaluated in steps of 100 GeV. This also reduces statistical uncertainties due to limitations in the number of simulated events. At a given mass, the uncertainty for each given PDF set is constructed according to the PDF4LHC recommendations. For the statistical evaluation of the uncertainties on the integrated background above a given dimuon mass threshold one may weight the uncertainties in the contributing mass range according to the mass dependent background cross section. Averaging in this way may in principle result in an overestimation of the uncertainty, because the uncertainties at different masses are not necessarily fully correlated. In practice, the influence of uncorrelated components of the uncertainties at different masses may be neglected as the background is dominated by events close to the considered mass threshold. An inspection of the MSTW08 and CTEQ66 error PDFs confirms that the contributions to the uncertainty in mass intervals of relevant size are highly correlated.

MC@NLO (section 8.2.1) is used to simulate events with the respective central (CTEQ66 and MSTW08) or average (NNPDF21) PDFs. The PDF information is provided by LHGRID files accessed via the LHAPDF interface [218]. A summary of the input data is given in table D.4. To reduce the required computing resources to a reasonable level, only the simulation with CTEQ66 is passed through the full CMSSW simulation and reconstruction sequence. Figure 8.8 compares the dimuon mass dependent CTEQ66 PDF uncertainty ( $|\eta_\mu| < 2.1$ ) before and after inclusion of the CMS detector simulation and the event selection. For high masses, it is expected that at a given dimuon mass $M_{\mu\mu}$ the uncertainties without the CMS simulation are somewhat larger as



**Figure 8.9** (Left) PDF uncertainty bands from CTEQ66, MSTW08 and NNPDF21 ($|\eta_\mu| < 2.1$). Each band is centered on the central (average) PDF from the respective PDF set. (Right) PDF uncertainty bands for the DY dimuon process from CTEQ66, MSTW08 and NNPDF21 ($|\eta_\mu| < 2.1$). The bands for the uncertainties from MSTW08 and NNPDF21 are shown with respect to the offset between their central (average) PDF and the CTEQ66 central PDF (dashed lines).
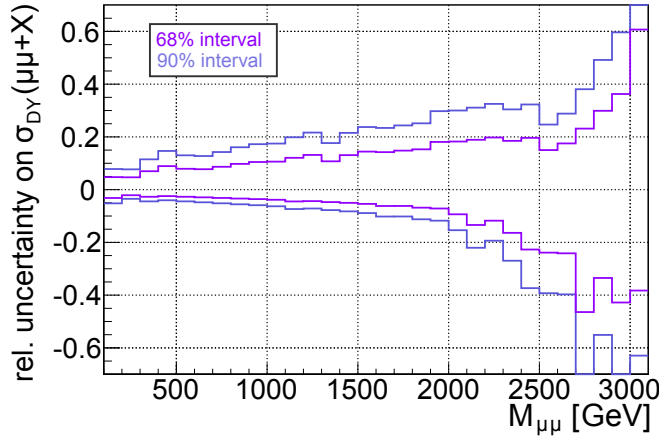
**Figure 8.10** Envelopes for the relative PDF uncertainties on the (inclusive) DY dimuon cross sections at 90% and 68% confidence level. ($|\eta_\mu| < 2.1$).

a result of the limited dimuon mass resolution of the reconstructed event. In the steeply falling DY spectrum more events are shifted from a mass $M_{\mu\mu} - \Delta M_{\mu\mu}$ towards mass $M$ than from $M_{\mu\mu} + \Delta M_{\mu\mu}$. However, with the current event selection the effect is found to be $< 1\%$ up to masses of $1.5$ TeV. Figure 8.8 demonstrates this for the central CTEQ66 PDF set. Accordingly, it is not a problem that the following analysis is based on the final states from simulating proton-proton collisions without taking into account the influence of the CMS event reconstruction.

Figure 8.9 (Left) shows the PDF uncertainty evaluated for a wide range of invariant masses with respect to the central (average) PDF estimates of a given set. The overall behavior is found to be similar for each of the three sets. The respective uncertainties at 90% CL increase with the dimuon mass. At $200$ GeV, the uncertainty estimate from each set is $\approx 4\%$. The uncertainties increase to about 15% at 2 TeV. In addition to the variations within each set, one may also take into account the differences between the central (average) fits. The relative offset between the central (average) PDF estimate from each set with respect to the baseline estimate with CTEQ66 is depicted by the dashed lines in figure 8.9 (Right). The uncertainty bands for MSTW08 and NNPDF21 shown in this figure are then evaluated while taking into account the offset towards the CTEQ66 central PDF. It can be seen that the offset between the central (average) PDFs surpasses the evaluated CTEQ66 90% uncertainty for masses from about $300$ GeV to above $1$ TeV. Such differences between the central (average) PDF sets are encountered more often than one would naively expect. This drives the idea that that it is necessary to include these differences into the estimation of the PDF uncertainties.

It has been suggested to estimate the overall PDF uncertainty from the different sets by constructing the envelope of the PDF uncertainties with respect to the observable of interest (in this case the cross section for a given mass bin) [31]. The result of this procedure is shown in figure 8.10. A factor of $1/1.64$, motivated by the relation between the corresponding central normal (i.e. gaussian) probability intervals, is used to translate the 90% into 68% uncertainties.

The central sets of the LHGRID files with $\alpha_s$ varied within a 90% confidence interval are used to evaluate the influence of variations in $\alpha_s$. Corresponding relative differences with respect to the prediction based on the MSTW08 central set with best fit value for $\alpha_s$ are depicted in figure 8.11. The respective (90% C.L.) variations are considerably smaller than those evaluated based on the 90% uncertainty envelope in figure 8.10. For the MSTW08 PDFs, the best fit value is $\alpha_s\left(m_z^2\right) = 0.1202$ and the 90% C.L. interval is bounded by $\alpha_s\left(m_z^2\right) = 0.1163$ and
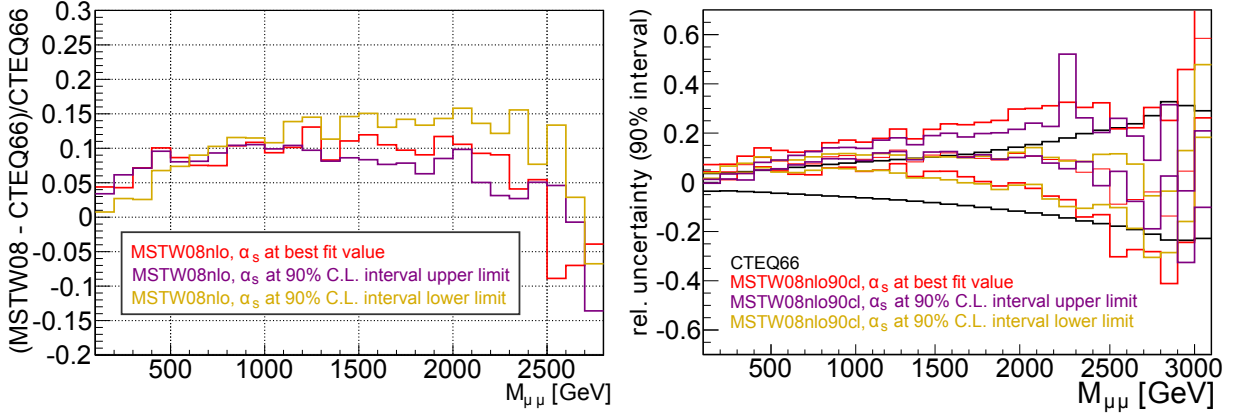
**Figure 8.11** (Left) Mass-dependent relative differences ($|\eta_\mu| < 2.1$) between the central CTEQ66 DY prediction and the MSTW08 results with and without $\alpha_s$ variations. (Right) PDF uncertainty bands from MSTW08 with and without $\alpha_s$ variations and CTEQ66 and . The MSTW08 bands are shown under inclusion of the offset between their central (average) PDF set and the CTEQ66 central PDF set.

$\alpha_s\left(m_z^2\right) = 0.1234$ [215]. In the following analysis steps, an additional uncertainty of 3% is applied to cover the 68% uncertainty related to the choice of $\alpha_s$.
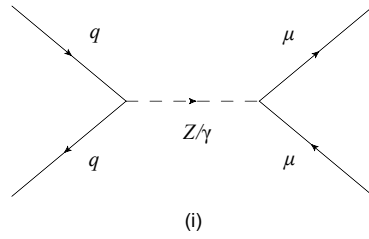
The overall PDF uncertainty is then estimated by combining the uncertainty from the envelope (figure 8.10) with the uncertainty from evaluating the $\alpha_s$ variations with MSTW08.
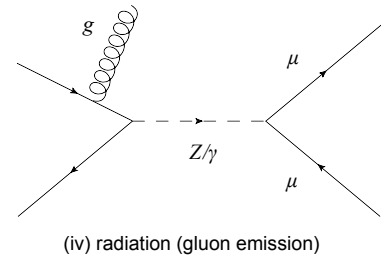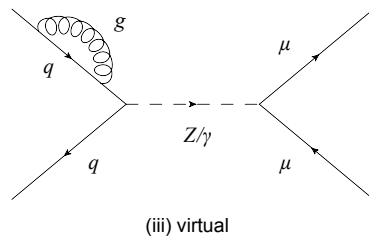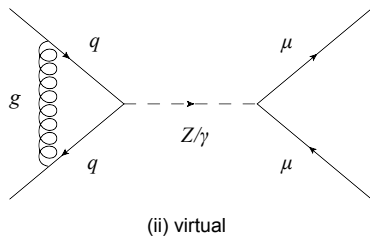
## 8.5 Combination of Results

The baseline description of the DY background used for the optimization of the dimuon mass range that defines the signal region (chapter 11) and the analysis of the measured mass spectrum (chapters 12 and 13) is based on the MC@NLO estimate. As described in section 8.2.1, this result includes a simulation of the detector response. Correction factors for QCD NNLO and EW NLO contributions are applied as specified in sections 8.2.3 and 8.3. The considered uncertainties include estimates of the limitations in the calculation of higher order matrix elements and the mass dependent PDF uncertainties evaluated in section 8.4. For the purpose of statistical inference, these uncertainties are treated as statistically independent. Further uncertainties, that are related to the measurement of events with the CMS detector, are discussed in chapter 7.
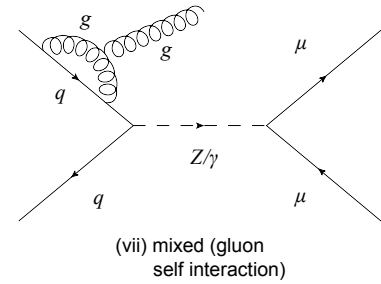
(a)  LO diagram (Born level)



(i)

(b)  QCD NLO diagrams (examples)



(ii) virtual                    (iii) virtual                    (iv) radiation (gluon emission)

(c)  QCD NNLO diagrams (examples)



(v) virtual                    (vi) radiation                    (vii) mixed (gluon
                                                                      self interaction)

(c)  EW NLO diagrams (examples)



(viii) virtual                (ix) radiative (photon emission)      (x) boson self energy



(xi) Box                        (xii) photon induced
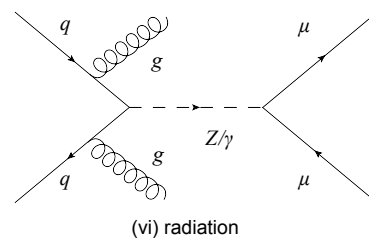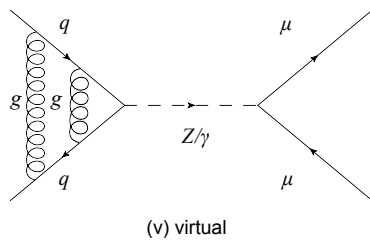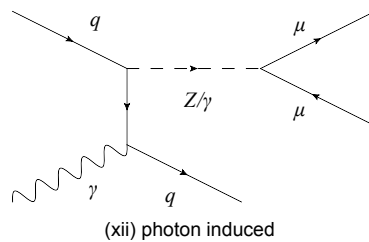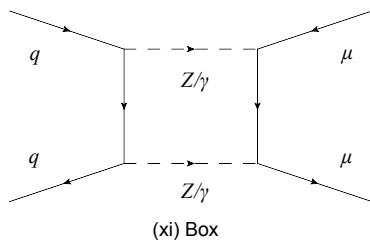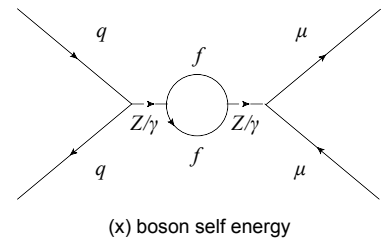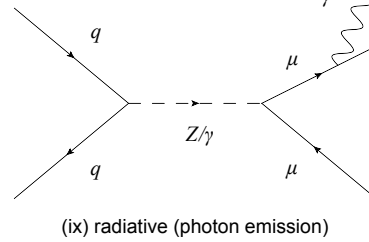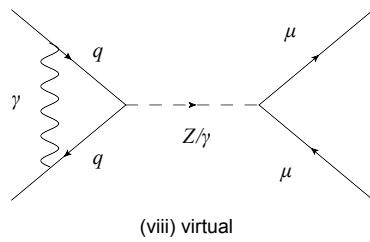
**Figure 8.12** Some of the relevant Feynman diagrams for calculating the dimuon mass distri-
bution from the neutral DY process.

# 9 Non-DY Background Sources

Background sources other than the SM DY process are discussed in this chapter. Further processes including *prompt* muon pairs that are created in the (perturbatively calculated) hard interaction are evaluated in section 9.1. It is found that the influence of these backgrounds restricted to a level of less than 10% of the dominant DY contributions.

Potential backgrounds from QCD multijet events and the muon component of cosmic radiation are discussed in section 9.2. Based on results from studies performed within the CMS collaboration, those contributions can be considered as negligible for the presented search.

## 9.1 Processes with Prompt Muons

Events with prompt muons are not only expected due to the neutral DY process but are also created in the charged DY process ($W + $ jets), heavy diboson ($WW$, $WZ$, $ZZ$) production and the $t\bar{t}$ process, which generates muon pairs via $t\bar{t} \to bW^+ \bar{b}W^-$. Table 9.1 lists the simulated event samples and cross section estimates that are used to study the impact of these backgrounds on the expected dimuon mass spectrum[1].

| Process | generator | cross section [pb] | cross section reference |
|---|---|---|---|
| $t\bar{t}$+Jets | Madgraph5 [242] | 165 | QCD NNLL [243] |
| $WW$ | Pythia6 | 43.0 | QCD NLO with MCFM [244] |
| $WZ$ | Pythia6 | 18.2 | QCD NLO with MCFM |
| $ZZ$ | Pythia6 | 5.9 | QCD NLO with MCFM |
| $W$+Jets | MadGraph5 | 239.6 | QCD NNLO corrected (FEWZ [226]) |

**Table 9.1** Samples for the evaluation of $W + $ jets, $t\bar{t}$ and diboson backgrounds.

The stacked dimuon mass dependent contributions from these background simulations are shown in figure 9.1 (Left). For a direct comparison, the neutral DY process at QCD NLO is also included as a stacked contribution. As expected, the DY process is found to dominate the background. Contributions from $W + $ jets production are highly suppressed as one of the two muon candidates that are necessary for passing the event selection needs to be created in the decay of hadronic final state particles. The probability of high mass dimuon pairs being created in this way is low and the muons from hadron decays in jets will mostly fail the isolation requirements. Ratios between the expected cross sections above a given mass threshold from neutral DY events and the other considered backgrounds with prompt leptons are given in figure 9.1 (Right). The resulting values are found to be decreasing with the dimuon mass, approaching approximately 2% at a mass threshold of 1 TeV.

The statistical evaluation of the measured dimuon spectrum in later chapters assumes a background contribution from $t\bar{t}$ and diboson backgrounds of 2% for masses in the range $M_{\mu\mu} \gtrsim 1$ TeV. An uncertainty of 100% is assigned to this estimate. In terms of the corresponding cross section differences, this uncertainty is still considerably lower than the leading

---

[1]The storage paths for the samples are given in table D.5 in appendix D.
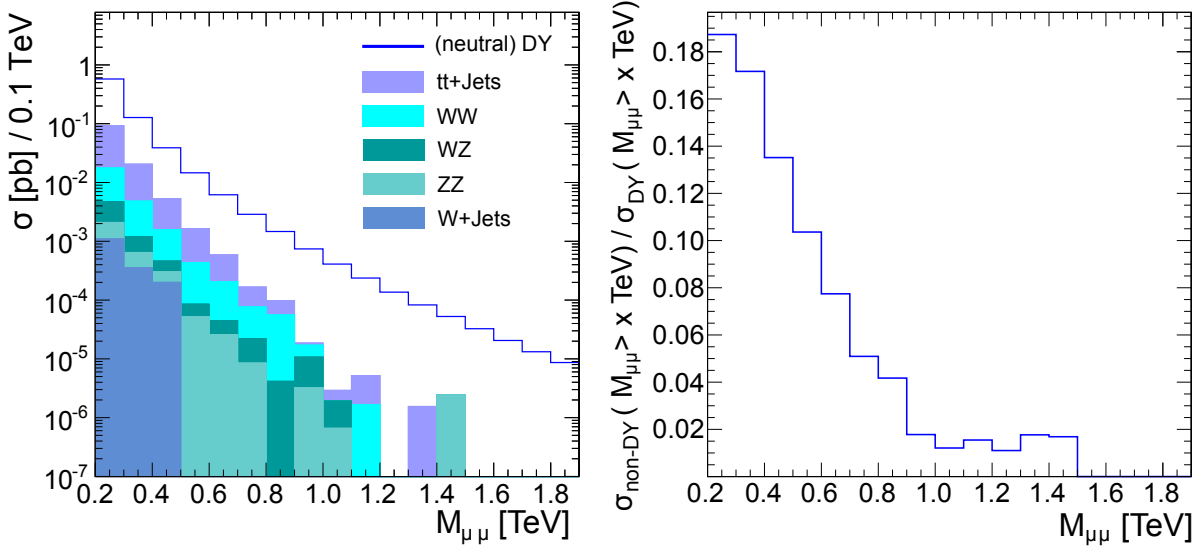
**Figure 9.1** (Left) Expected dimuon mass dependent cross sections ($|\eta_\mu| < 2.1$ and $p_{T,\mu} > 45$ GeV) for $W + $ jets, $t\bar{t}$ and diboson processes including the simulation of the CMS detector. (Right) Ratio of these cross sections and the corresponding DY cross section (QCD NLO) as a function of a lower mass threshold.

uncertainties on the DY background. Accordingly, any more detailed studies of non-DY backgrounds with prompt muons would not result in a significant improvement of the analysis.

All lepton flavors ($e$, $\mu$, and $\tau$) in the SM have equal couplings to the gauge bosons [245]. This property is often referred to as *lepton universality*. As a consequence, $t\bar{t}$ and diboson production are expected to be symmetric between the dimuon and electron-muon final states[2]. Uncertainties on the ratio between the contributions of the discussed processes to the $e\mu$ and $\mu\mu$ mass spectra are therefore mainly due to experimental uncertainties like for example energy scale corrections or identification efficiencies. This situation allows for a cross check of the $\mu\mu$ background estimate with the measured $e\mu$ spectrum. The $e\mu$ spectrum is expected to be dominated by $t\bar{t}$ and diboson events. If the $e\mu$ measurement is found to be compatible with the simulated background expectation this increases the confidence one can place in the simulated background expectation for the $\mu\mu$ spectrum. If there are inconsistencies, they might point towards flaws in the object reconstruction and identification or an underestimation of cross section uncertainties.

A more detailed description of how to check dimuon backgrounds with prompt muons with $e\mu$ events can be found in [246]. An analysis specific application of this cross check with $e\mu$ events corresponding to 1.1 fb$^{-1}$ of the 2011 dataset did not indicate problems of the background simulation. In the context of the CMS search for dilepton resonances with 2011 data [103], the $e\mu$ cross check has been applied to the full 2011 dataset. As the main result, the $e\mu$ spectrum in the data is found to be consistent with the simulation of $t\bar{t}$ and diboson processes, and the correction factors between data and simulation are close to 1. Hence, no additional correction needs to be applied to the simulation of these background in the dimuon mass spectrum. The method runs out of statistics before reaching the mass range of 1 TeV and above. It can therefore not be used for a straightforward estimate of the background uncertainty in the signal region. Nonetheless, the described results increase the overall trust in the simulation of non-DY

---

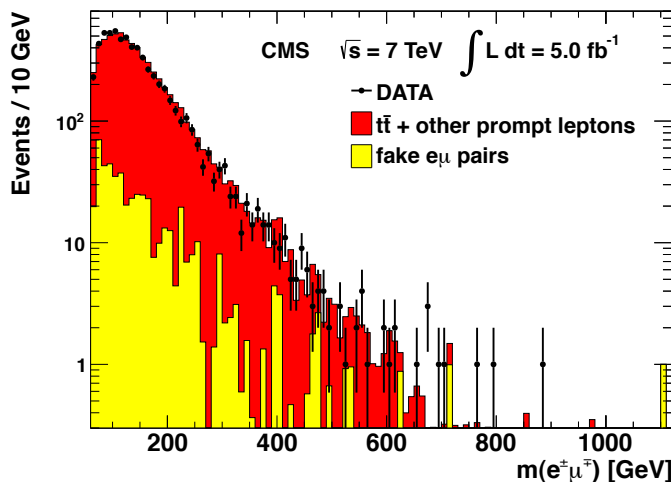[2]except for negligible differences due to the differing lepton masses

**Figure 9.2** Opposite sign $e\mu$ mass spectrum [103].

backgrounds with prompt leptons in the final state. Figure 9.2 shows the $e\mu$ (opposite-sign) mass spectrum with 5.0 fb$^{-1}$ as presented in [103].

## 9.2 Backgrounds from Multijet Events and Cosmic Radiation

While the overall cross section for multijet events is large, requiring isolated high energy lepton candidates provides strong rejection power against this background source. QCD multijet contributions can only produce such muon candidates if a significant amount of the energy from the created hadrons is transfered into leptonic decay products. It is expected that the background contributions from multijet events in the same-sign dimuon mass spectrum are of the same order as the respective opposite sign contributions. The observation that there are no same-sign dimuon events above 0.45 TeV provides therefore a strong argument for the hypothesis that the multijet background in the mass range $\gtrsim 1$ TeV is negligible[3]. Also simple cross checks of the data distributions with relaxed isolation requirements do not point towards a relevant background contributions from such events.

A more detailed evaluation of potential background contributions from QCD multijet events has been performed in [247]. In this study, the probability that a loosely isolated muon passes the complete event selection is evaluated based on events with a single muon candidate. Combining the obtained results with simulation results for the influence of SM processes with prompt muons in the final state (e.g. $W+$Jets), one extracts the probability that a jet with a loosely isolated muon candidate results in a reconstructed isolated muon. A QCD multijet background estimate can then be derived from a sample of dimuon events in which both muon candidates fail isolation by applying the previously calculated *fake* probability. The results support the assumption that the influence of QCD multijet background is negligible for the given event selection.

Muons from cosmic radiation can generate an additional potential background source if they pass through the beam interaction region and are compatible with the timing of a bunch crossing. Such muons are expected to be reconstructed as opposite sign muon pairs as they pass the CMS magnetic field first from the outside to the inside while creating the first muon candidate and in opposite direction while creating the second. The included selection requirements on the impact parameter $d_{xy}$ and the angle $\alpha_{\mu\mu}$ are chosen for the specific purpose of reducing the background

---

[3]The mass spectrum of same-sign muon pairs in the 2011 dataset is shown in figure 12.1.
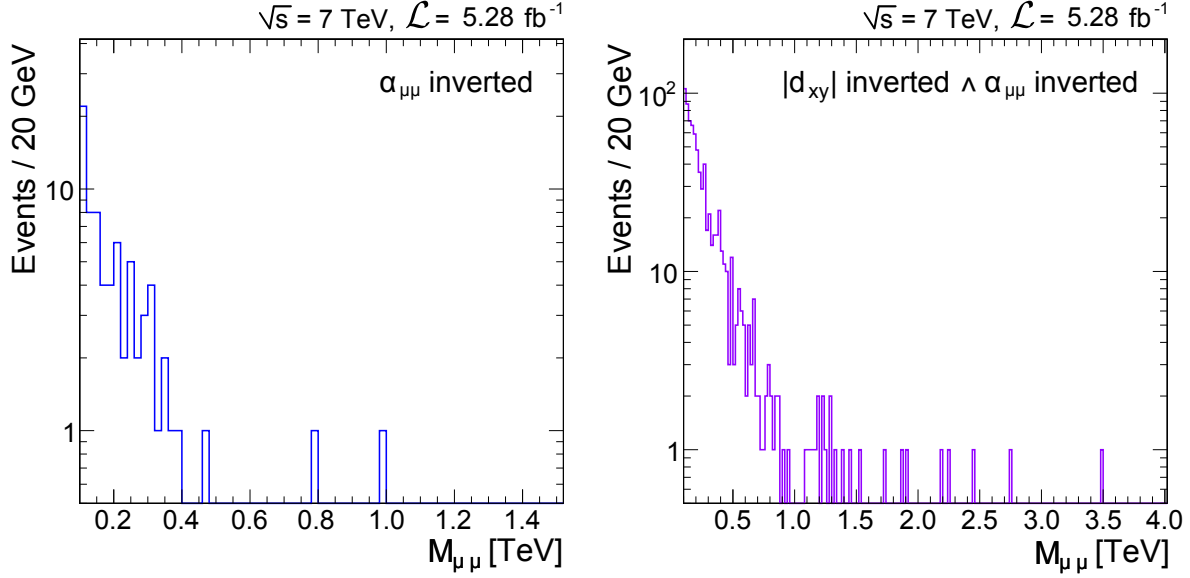
**Figure 9.3** Measured dimuon mass spectra of events with inverted $\alpha_{\mu\mu}$ selection criterion ($\rightarrow$ $\pi - \alpha_{\mu\mu} < 0.02$) (Left) and inverted $\alpha_{\mu\mu}$ and $d_{xy}$ ($\rightarrow |d_{xy}| > 0.2$ cm ) selection criteria (Right). There are no events which pass an inversion of only the $d_{xy}$ selection criterion.

from cosmic ray muons to a negligible level. Figure 9.3 (Right) shows the measured dimuon spectrum with inverted $d_{xy}$ and $\alpha_{\mu\mu}$ selection, which is expected to have a large contribution from cosmic ray muons. As there are no events that pass the inversion of the $d_{xy}$ selection but meet the $\alpha_{\mu\mu}$ criterion, it can be deduced that the $\alpha_{\mu\mu}$ requirement is highly efficient in rejecting background contributions from cosmic rays. If one makes the reasonable assumption that the events failing both of the considered selection criteria are dominated by the cosmic ray background one can deduce an upper limit on the probability that a comic background event with $|d_{xy}| > 0.2$ cm passes the $\alpha_{\mu\mu}$ selection. Just taking into account the events above 1 TeV (23 events with both $\alpha_{\mu\mu}$ and $d_{xy}$ inverted), the Clopper-Pearson upper limit[4] [248] on the Binomial success rate at 95% confidence level evaluates to 15%. This implies a lower limit on the rejection probability of 85%. Figure 9.3 (Left) shows the events that pass the $d_{xy}$ requirement but fail the $\alpha_{\mu\mu}$ selection. The performance of the angular reconstruction of the muon candidates for the measurement of $\alpha_{\mu\mu}$ is not expected to be strongly dependent on $d_{xy}$. If one therefore applies the lower limit on the rejection probability from above it can be seen that cosmic events provide at most a small background component at high dimuon masses ($\lesssim 0.1$ events above 1 TeV) if compared to the estimated DY background mean above 1 TeV which is $> 5$ events.

---

[4]This type of interval construction is suggested by the particle data group [26].

# 10 Evaluation of ADD Signal Contributions to the Dimuon Final State

In chapter 3, virtual graviton exchange has been introduced as a phenomenological consequence of an effective field theory that is motivated by the ADD model of extra dimensions. To design a search that is sensitive to such a signal and to study the implications of the measurement, one needs to be able to establish and quantify expected differences between the predictions of the SM and the effective field theory description of the ADD model. This can be achieved through a simulation of signal and SM contributions for those variables that are considered to be potentially relevant. The application of the PYTHIA8 event generator to simulate the LO DY process with virtual graviton contributions is discussed in section 10.1. Implications of NLO QCD corrections to DY dimuon production in the ADD model are reviewed in section 10.2.

## 10.1 Simulation with Pythia8

The leading order amplitudes of virtual s-channnel graviton exchange in the ADD model are implemented in PYTHIA8 [60, 212]. This allows for a detailed study of kinematic variables, including the effects of parton shower and hadronisation. The interference between the graviton and the leading order SM DY amplitude is taken into account by the simulation. Generated signal events can then be passed to the CMSSW framework to simulate the detector response. All numerical results presented in this chapter are based on the PYTHIA version 8.142. Available options for event generation include the

- choice of the used PDF set (CTEQ6 if not stated otherwise).

- selection of the ADD model parameter $\Lambda_{\mathrm{T}}$.

- choice of the *tune*, which includes for example the selected value of $\alpha_s$. The shown results use the options 3 for the "*ee* tune" and 5 (4C) for the "*pp* tune". More detailed information about these tunes can be found in the PYTHIA8 online documentation [249].

- configuration of the lower mass threshold on $\hat{s}$.

The lower threshold on $\hat{s}$ is important for an efficient generation of signal events as the SM DY contribution dominates the mass spectrum up to at least several hundred GeV,. During event generation, no restriction in $\hat{s}$ is applied on the validity of the ADD amplitude. Later on, an upper threshold on the dimuon mass is considered as a way of parametrizing the effects of restricting the validity range of the signal[1].

Figure 10.1 (Left) shows the simulated dimuon mass distributions for several values of $\Lambda_{\mathrm{T}}$ and the limiting SM case. As expected, the signal cross sections decrease with rising values of $\Lambda_{\mathrm{T}}$ and start to deviate from the SM shape at higher masses. To arrive at a consistent leading order result, the interference effects between the amplitude from the virtual graviton exchange and the SM DY amplitude require the inclusion of the SM DY amplitude in the signal simulation. An *effective signal* for a given distribution can then be defined by subtracting the SM prediction from the result for the selected ADD model.

---

[1]A visualization of the simulation of a typical ADD event with PYTHIA8 is shown in figure D.2.
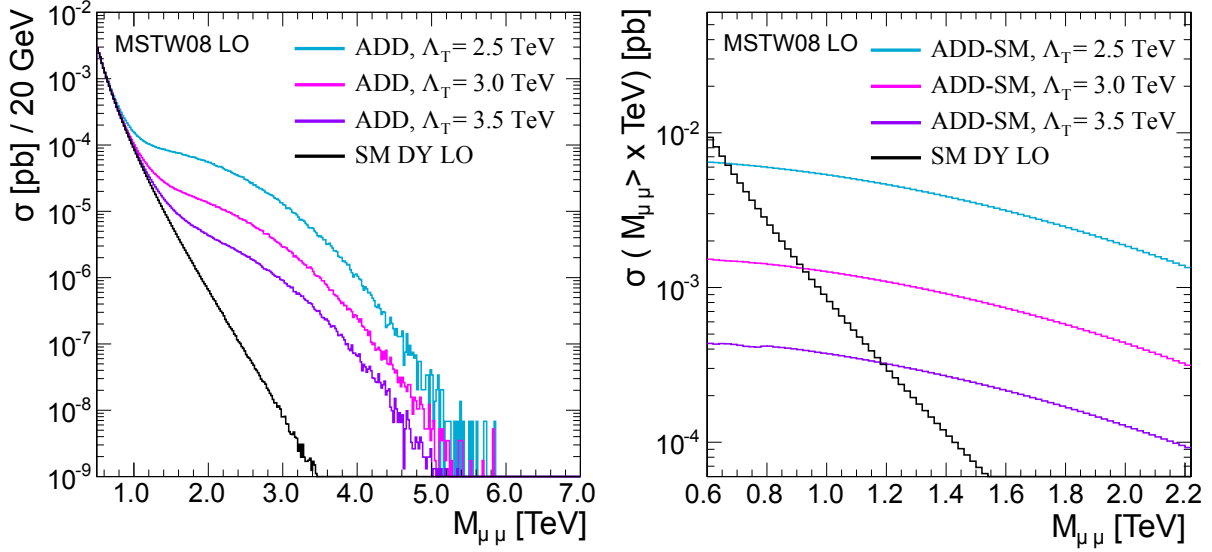
**Figure 10.1** ADD DY cross sections for several values of $\Lambda_T$ and the SM limit evaluated with PYTHIA8. Basic kinematic cuts ($|\eta_\mu| < 2.1$ and $p_{T,\mu} > 45$ GeV) are applied. (Left) Cross sections as a function of the dimuon mass. (Right) Integrated cross sections as a function of a lower dimuon mass threshold. The integrated ADD cross sections are shown with subtracted SM expectation to quantify the effective signal.
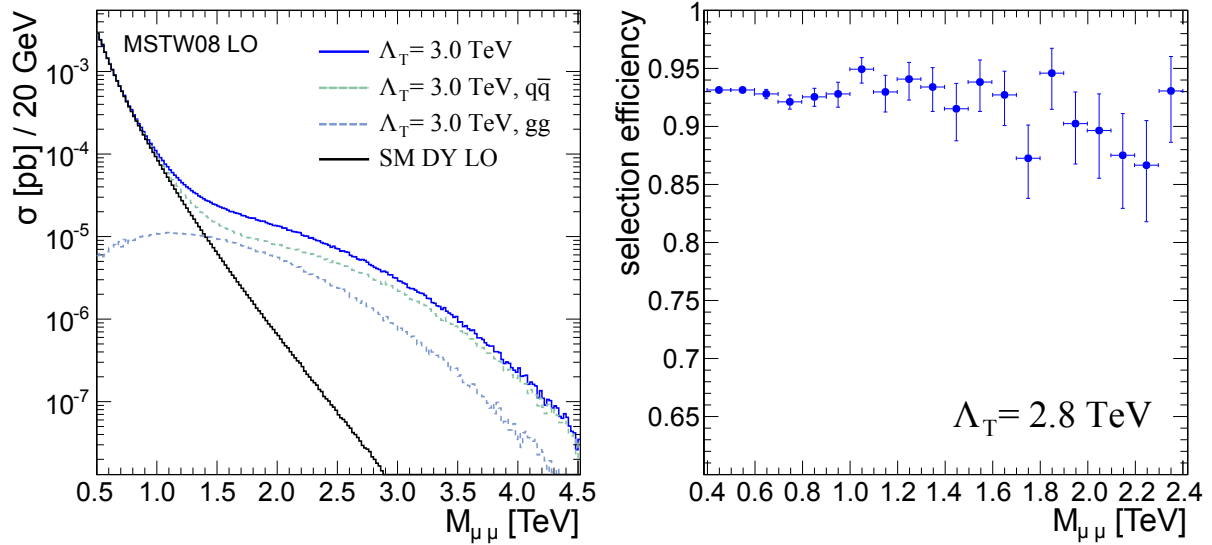


**Figure 10.2** (Left) Mass dependent cross sections for the SM DY process and the ADD DY process at $\Lambda_T = 3.0$ TeV. The ADD process is shown both in total and subdivided into contributions from gluon-gluon fusion and, quark-antiquark annihilation ($|\eta_\mu| < 2.1$ and $p_{T,\mu} > 45$ GeV). (Right) Mass dependent selection efficiency for the ADD DY process with $\Lambda_T = 2.8$ TeV (i.e. fraction of PYTHIA8 events with $\eta < 2.1$ and $p_{T,\mu} > 45$ GeV that pass the full set of selection criteria).

| | $M_{\mu\mu} > 1.1$ TeV | $M_{\mu\mu} > 1.3$ TeV | $M_{\mu\mu} > 1.5$ TeV |
|---|---|---|---|
| $\Lambda_\mathrm{T} = 2.5$ TeV | 0.03 | 0.03 | 0.03 |
| $\Lambda_\mathrm{T} = 3.0$ TeV | 0.03 | 0.03 | 0.03 |
| $\Lambda_\mathrm{T} = 3.5$ TeV | 0.02 | 0.03 | 0.03 |

**Table 10.1** Ratio $\frac{\#\mathrm{events}(1\mu, 2.1 < |\eta| < 2.4)}{\#\mathrm{events}(2\mu, |\eta| < 2.1)}$ between the number of events (PYTHIA8 including parton shower) with one muon falling into the acceptance interval $2.1 < |\eta| < 2.4$ and the number of high mass events with both muons within $|\eta| < 2.1$ for different lower mass thresholds and different values of the ADD model parameter $\Lambda_\mathrm{T}$.

Cumulative cross sections for such effective signal contributions with different values of $\Lambda_\mathrm{T}$ are shown in figure 10.1 (Right) as a function of a lower mass threshold. It can be seen that for a 5 fb$^{-1}$ scenario with $\Lambda_\mathrm{T} = 3.0$ TeV one still expects about 5 events in a region where the SM expectation falls below 1. Using arguments outlined in the discussion of a simple counting experiment in section 4.4, one can hence already guess at this point that $\Lambda_\mathrm{T} = 3.0$ TeV provides a rough estimate of the expected exclusion limit (without any truncation of the signal amplitude).

The ADD dimuon signal contains events from gluon-gluon fusion and quark-antiquark annihilation. Figure 10.2 (Left) illustrates for the example $\Lambda_\mathrm{T} = 3.0$ TeV that both of these processes contribute to the signal in a relevant way. Mass dependent selection efficiencies for a scenario with $\Lambda_\mathrm{T} = 2.8$ TeV are shown in figure 10.2 (Right). They are found to be compatible with the corresponding efficiencies for the SM DY process as evaluated in section 8.2.1. The same holds true for other values of $\Lambda_\mathrm{T}$. A complete list of the ADD event samples that have been generated under inclusion of the detector simulation can be found in table D.6.

As mentioned in section 5.5, the L1 muon trigger system requires at least one muon in the range $|\eta| < 2.1$. In principle, one could consider relaxing this criterion for one of the muons towards $|\eta| < 2.4$ to gain additional sensitivity. In the presented search, this is not done for several reasons. As a first point, dimuon events with one muon above $|\eta| = 2.1$ are subject to higher systematic uncertainties due to the increase of jet rates in the forward regions and
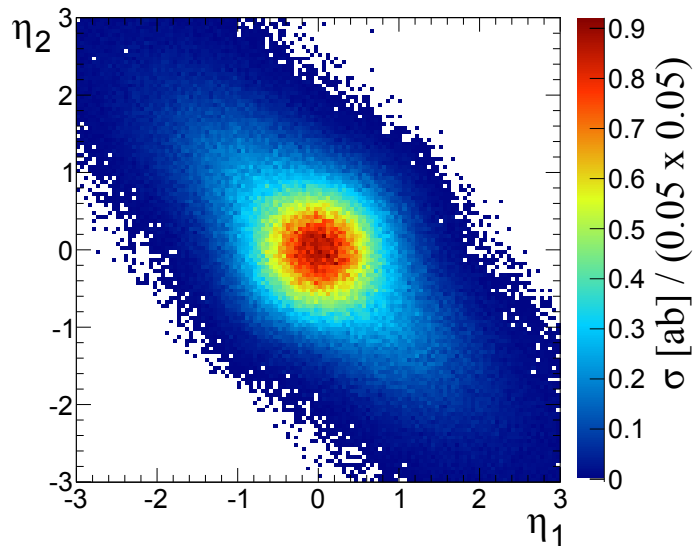


**Figure 10.3** Effective signal cross section for $\Lambda_\mathrm{T} = 3.0$ TeV as a function of $\eta_{\mu,1}$ and $\eta_{\mu,2}$ with $M_{\mu\mu} > 1.3$ TeV. Index 1 is used to label the muon with higher $p_\mathrm{T}$ (1 ab = $10^{-18}$ b).
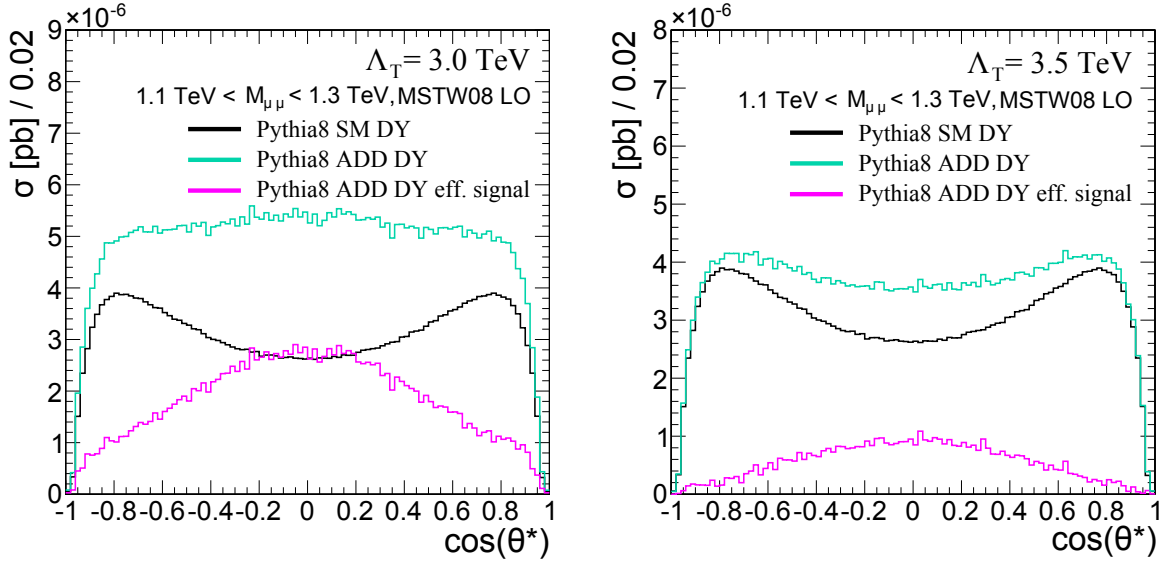
**Figure 10.4** Comparison between the $\cos\theta^*$ distributions ($|\eta_\mu| < 2.1$ and $p_{\mathrm{T},\mu} > 45$ GeV) of SM LO DY process and an ADD signal in the mass interval 1.1 TeV $< M_{\mu\mu} < 1.3$ TeV for $\Lambda_{\mathrm{T}} = 3.0$ TeV (Left) and $\Lambda_{\mathrm{T}} = 3.5$ TeV (Right).

because of the missing second chance to fire the trigger. Additionally, there is only little gain in signal efficiency. Table 10.1 shows that extending the $\eta$ range for one muon could increase the expected number of signal events by about 3%. At the same time, table 8.1 shows that the background can be expected to rise by about 5%. Combining these considerations, it has been decided that is is the better choice not to apply the proposed relaxation of the $\eta$ range for one of the muon candidates.

It has been reviewed in section 3.1 that the considered ADD dimuon signal would not only lead to a change in the dimuon mass spectrum but also in the angular distributions of the produced muon pairs. It is therefore interesting to study also angular variables. One can start by comparing the $(\eta_1, \eta_2)$ distributions of the SM DY muon pairs in the range $M_{\mu\mu} > 1.3$ TeV as shown in figure 8.1 with the respective result for the effective signal contribution with $\Lambda_{\mathrm{T}} = 3.0$ TeV as shown in figure 10.3. The seen shape differences already indicate the possibility of an angular optimization of the analysis. The effect is somewhat more evident and more directly related to the spin of the exchanged virtual particle if one considers the cosine of the decay angle $\cos\theta^*$ in the dimuon center-of-mass frame.

A quantitative study of the effect was first presented in [59]. Figure 10.4 compares the $\cos\theta^*$ distributions of the ADD dimuon signal and the SM DY process in the mass range 1.1 TeV $< M_{\mu\mu} < 1.3$ TeV for $\Lambda_{\mathrm{T}} = 3.0$ TeV (Left) and $\Lambda_{\mathrm{T}} = 3.5$ TeV (Right). Corresponding results for 0.9 TeV $< M_{\mu\mu} < 1.1$ TeV and 1.3 TeV $< M_{\mu\mu} < 1.5$ TeV can be found in figure D.1. These results suggest that an ADD dimuon search might be improved by implementing either a direct selection requirement on $\cos\theta^*$ or directly including the $\cos\theta^*$ into the likelihood function used in the statistical evaluation of the observed data. To implement any of these options would require a detailed study of the influence of systematic uncertainties on the $\cos\theta^*$ distribution. Additionally, the shown results for $\Lambda_{\mathrm{T}} = 3.5$ TeV indicate that the increase in sensitivity will be rather limited. This is because for $\Lambda_{\mathrm{T}} = 3.5$ TeV which is not too far above the expected exclusion range without considering any optimization with respect to $\theta^*$ the distributions are either rather close to the SM expectation or correspond to only few expected events.

With the steeply increasing amount of data becoming available during 2010 and 2011, the analysis focuses on a robust strategy for a search of a non-resonant signal in the dimuon high-mass tail. For the currently ongoing analysis of 2012 data a more model specific approach that takes into account the angular differences between signal and background muons might become more attractive as the dataset taken by end of 2012 will not increase until the end of the shutdown period expected for late 2014 [250]. In any case, it is clear that with increasing data the angular distributions would play an important role in establishing any potential excess in the dimuon mass spectrum as a graviton signature.

Some basic cross checks with the implementation of the decay of virtual gravitons to dimuon pairs in Sherpa [251] and a privately maintained parton level generator [252] indicate consistency with the PYTHIA8 results.

## 10.2 QCD NLO Corrections

In section 8.2 it has been reviewed that QCD NLO corrections change the expected DY background for high dimuon masses by roughly 30%. It is therefore intuitive to expect that QCD NLO corrections can also have a significant influence on the corresponding effective field theory predictions in the ADD model. The framework for calculating QCD NLO corrections to the DY process in the ADD model has been worked out in [253]. The mentioned reference also contains numerical results, including LO→NLO K-factors on $d\sigma/dQ^2$ (here, $Q^2 = M_{\mu\mu}^2$) for proton-proton collisions at $\sqrt{s} = 14$ TeV. Interestingly, studies of $d\sigma/dQ^2 d\cos\theta^*$ [254] suggest that NLO QCD contributions could also somewhat enhance the angular differences between the DY process in the SM and the ADD model.

K-factors for dilepton production in the ADD model have also been calculated for LHC proton-proton collisions at $\sqrt{s} = 7$ TeV, with application of the CTEQ6 LO PDF set [255]. The results indicate that for many of the relevant combinations of model parameters and mass ranges the K-factor is between 1.3 and 1.8. This is illustrated in figure 10.5, which shows examples for ADD QCD NLO K-factors with $n = 4$ (UV cutoff set to $M_s$).
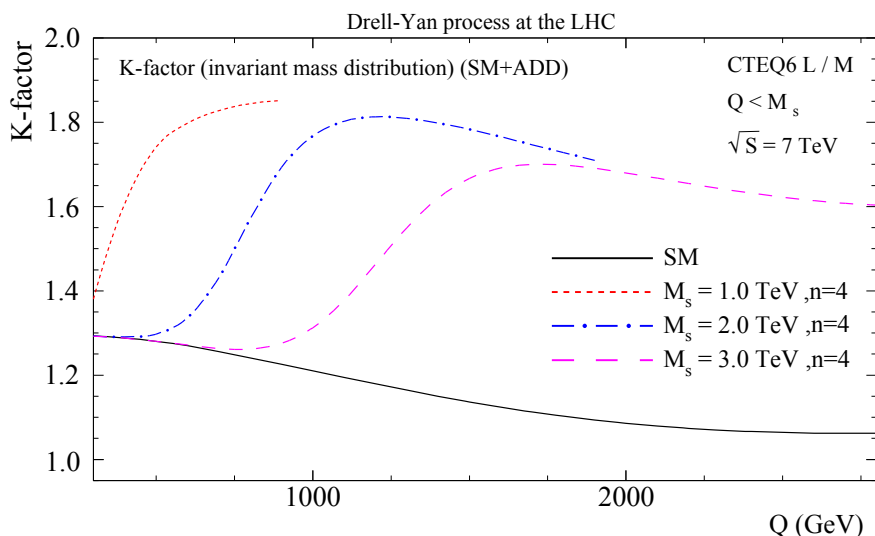


**Figure 10.5** Dimuon mass dependent ADD QCD NLO K-factors for the DY process with $n = 4$ for several choices of $M_s$. Kindly provided by M. C. Kumar, P. Mathews, and V. Ravindran.
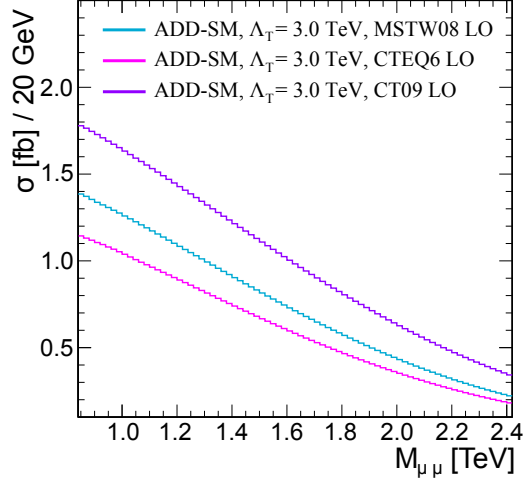
**Figure 10.6** Dimuon mass dependent ADD effective signal cross sections for different LO PDF sets ($|\eta_\mu| < 2.1$ and $p_{T,\mu} > 45$ GeV), as simulated with Pythia8.

In applying the K-factors to the PYTHIA8 simulations described in the previous section, one needs to keep in mind that the LO prediction depends on the selected LO PDF set. This is illustrated in figure 10.6. Accordingly, CTEQ6 PDFs need to be used for a consistent application of the provided K-factors. Further uncertainties apart from those due to scale choices and higher order effects are introduced when applying the K-factors on the simulation with PYTHIA8. They are related to the application of a parton shower and the selected acceptance range ($|\eta| < 2.1$). The CMS dimuon mass measurement presented in chapter 12 is interpreted in terms of a K-factor of 1.3, which is a conservative choice with respect to the range of dimuon masses and model parameters of interest if the UV cutoff is set to $M_s$. Uncertainties on the QCD NLO corrections in the ADD model, including the effects of different choices of the UV cutoff, have been studied in [256]. The numerical results are however limited to the case $M_s = 2$ TeV, $n = 3$ at $\sqrt{s} = 14$ TeV and hence not directly applicable to the presented search. As a rough estimate one might extract that the QCD related combined PDF and scale related relative uncertainties on the ADD predictions in the parameter range of interest in QCD NLO at $M_{\mu\mu} \approx 1$ TeV are expected to be at a level of 10%.

# 11 Optimization of the Lower Dimuon Mass Threshold

The discussion of the expected ADD signal in chapter 10 shows that only selected events with dimuon masses much larger than the $Z$ resonance can provide relevant separation power between the ADD parameter ranges of interest and the SM expectation. Since signal and background diverge in a region where the overall background expectation corresponds to only a few events, it is reasonable to design the statistical analysis as a counting experiment. The corresponding statistical model is outlined in section 4.5. The difference between background and background plus signal expectation increases with the dimuon mass. It is therefore sufficient to consider only a lower mass threshold $M_{\text{threshold}}$ and leave the selection unbounded towards higher dimuon masses. Due to the steeply falling background, limits derived in this way are still expected to perform well in the case of an applied mass cutoff on the signal as long as the cutoff is not too close to the selected lower mass threshold. Here, the main method that is adopted for selecting the lower mass threshold that defines the mass interval used in the counting experiment is to optimize on the expectation value of the Bayesian limits. Other optimization procedures that are considered are based on expected $\text{CL}_\text{S}$ limits or use the evaluation of expected signal cross section thresholds for p-values corresponding to an observation at a significance of $3\,\sigma$. It needs to be stressed that the optimization procedure is performed without including any information about the actual high mass data. The potential danger of any statistical bias due to the continuous analysis of collision data during the period of data taking is considered to be negligible.

After the discussion of backgrounds and systematic uncertainties in the previous chapters, one has all the input available that is needed to parametrize the Poisson mean of the counting experiment. This model is then used for the optimization of the mass cut and is also applied for the evaluation of observed limits in chapter 13. The selected parametrization for the Poisson mean $a$ of the counting experiment is

$$a = \mathcal{L} \cdot [\epsilon_{\text{scale,b}} \cdot \epsilon_{\text{res,b}} \cdot \epsilon_{\text{reco,b}} \cdot (\sigma_{\text{b,DY}} + \sigma_{\text{b,nonDY}}) + (\epsilon_{\text{reco,s}} \cdot \sigma_s)] \tag{11.1}$$

Table 11.1 defines the used symbols and summarizes the included relative systematic uncertainties for dimuon high-mass events. The influence of the muon momentum scale and muon momentum resolution on the comparatively flat ADD signal is considerably smaller than for the background and hence not included in the statistical model. In the statistical evaluation, the systematic uncertainties are accounted for by multiplying the likelihood with additional terms. For Bayesian limits they can be interpreted as prior distributions. For the evaluation of $\text{CL}_\text{S}$ limits, a clear statistical interpretation of such terms is less straightforward, but it may be useful to think of them as additional likelihoods constraining the nuisance parameters that have been derived from supplementary measurements. At least for the mainly experimental uncertainties this seems to be a reasonable interpretation.

Prior/constraint terms for the parameters $\mathcal{L}$, $\epsilon_{\text{scale,b}}$, $\epsilon_{\text{res,b}}$, $\epsilon_{\text{reco,b}}$, and $\epsilon_{\text{reco,s}}$ are implemented as normal distributions with variances $\sigma^2$, where $\sigma$ refers to the systematic uncertainty. Log-normal terms with $k = 1 + \sigma_r$ are used for the nuisance parameters $\sigma_{\text{b,nonDY}}$ and $\sigma_{\text{b,DY}}$, where $\sigma_r$ is the relative uncertainty. Some basic information about lognormal distributions and the motivation for using them to model nuisance parameters with large relative uncertainties can
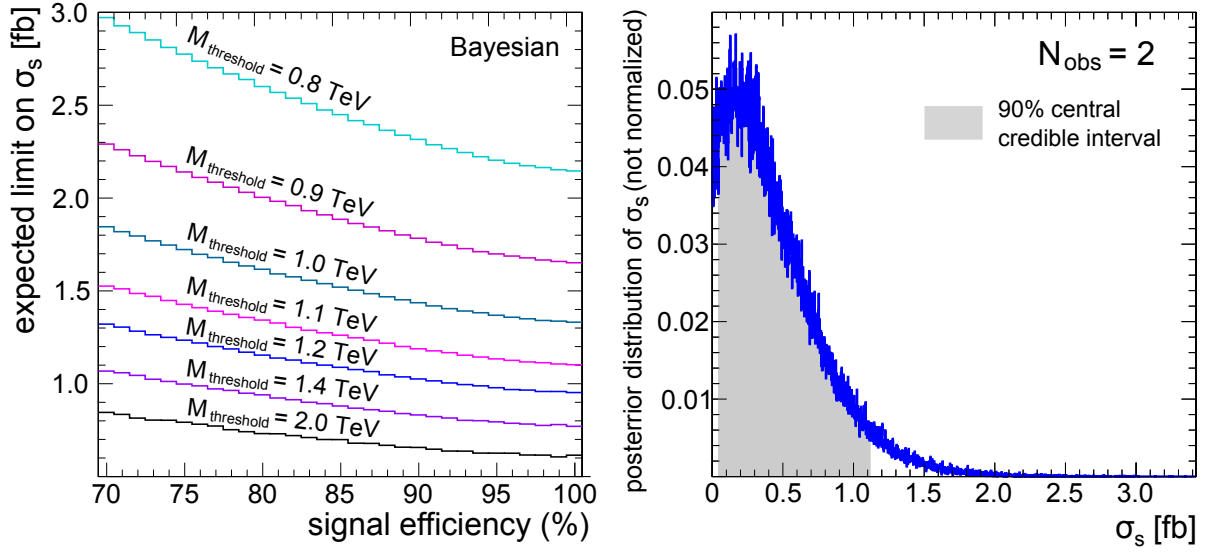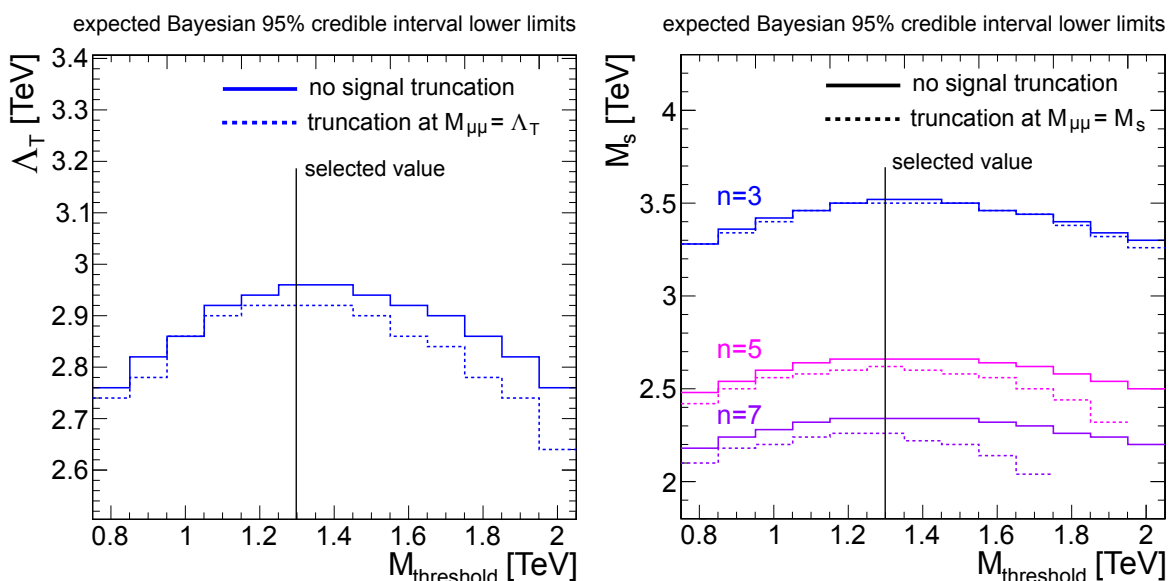
**Figure 11.1** (Left) Bayesian 95% upper limits on the signal cross section as a function of the signal efficiency $\epsilon_{\mathrm{reco,s}}$ for several choices of $M_{\mathrm{threshold}}$. (Right) Posterior probability distribution of the signal cross section $\sigma_s$ ($|\eta_\mu| < 2.1$ and $p_{\mathrm{T},\mu} > 45$ GeV) for an exemplary hypothetical experiment with 2 observed events. The assumed lower mass threshold is $M_{\mathrm{threshold}} = 1.3$ TeV at a signal reconstruction efficiency $\epsilon_{\mathrm{reco,s}} = 0.9$. The grey shaded area indicates the central 90% credible region.

be found in appendix C. The overall uncertainty $\sigma_{\mathrm{b,DY}}$ is calculated by adding the contributing uncertainties in quadrature via $(\sigma_{\mathrm{b,DY}})^2 = \sum_i (\sigma_{\mathrm{b,DY,i}})^2$.

Bayesian upper limits on the signal cross section corresponding to a 95% credible interval are evaluated as outlined in section 4.4. The calculation adopts a uniform (flat) prior on the signal cross section. Bayesian expected limits are here defined as the median observed limit from a set of hypothetical experimental outcomes of the counting experiment under the $H_0$ (SM) hypothesis. The observed event numbers are assumed to be distributed as expected from fixing all nuisance parameters to their "best guess" values. This choice of the ensemble of hypothetical observations has the advantage that one can simply loop over an appropriate range of numbers of observed events and weigh the resulting limits with the corresponding Poisson probability at fixed values

| symbol | source of uncertainty | estimated rel. uncertainty, ($M_{\mathrm{threshold}}$ in TeV) | section |
|--------|----------------------|--------------------------------------------------------------|---------|
| $\mathcal{L}$ | integrated luminosity | 2.2% | 5.6 |
| $\epsilon_{\mathrm{scale,b}}$ | dimuon mass scale | $-0.034 + 0.14 \cdot M_{\mathrm{threshold}}$ | 7.3 |
| $\epsilon_{\mathrm{res,b}}$ | dimuon mass resolution | $0.52 \cdot M_{\mathrm{threshold}} - 0.548 \cdot M_{\mathrm{threshold}}^2$ $+0.227 \cdot M_{\mathrm{threshold}}^3 - 0.16$ | 7.2 |
| $\epsilon_{\mathrm{reco,b}}$ | background efficiency | 3.0% | 7.1 |
| $\epsilon_{\mathrm{reco,s}}$ | signal efficiency | 4.0% | 7.1 |
| $\sigma_{\mathrm{b,DY}}$ | DY cross section $\times$ acceptance | mass dependent | 8.5 |
| $\sigma_{\mathrm{b,nonDY}}$ | non-DY cross section $\times$ acceptance | 100% | 9.1 |
| $\sigma_s$ | signal cross section $\times$ acceptance | — | 10 |

**Table 11.1** Explanation of the symbols that are used to model the Poisson mean of the counting experiment and summary of the estimated relative systematic uncertainties on the expectation of dimuon high-mass events.

**Figure 11.2** Expected Bayesian 95% limits with uniform (flat) prior on $\sigma_s$. (Left) Expected lower limits on $\Lambda_T$ in dependence on $M_{\text{threshold}}$ without restricting an upper mass threshold on the considered signal contributions and with signal truncation at $M_{\mu\mu} = \Lambda_T$. (Right) Expected lower limits on $M_s$ in dependence on $M_{\text{threshold}}$ with and without signal truncation at $M_{\mu\mu} = M_s$.

of the nuisance parameters. An alternative would be to sample a number of observed limits to approximate the expectation value $E[\sigma_{s,\text{lim}}]$ of the observed signal cross section limit $\sigma_{s,\text{lim}}$. The latter approach tends to be considerably slower for the selected range of parameters. One might also consider other ensembles of hypothetical experiments in which the selected values of the nuisance parameters are varied. In this case it will typically not be realistic to avoid establishing the expected limit through the approximation from a sampling procedure. Tests from earlier iterations of the analysis that adopted a similar model and comparable systematic uncertainties indicate that results for the expected limit derived from a set of hypothetical observations with varied nuisance parameters do not lead to strong differences in the outcome of the optimization procedure. For these cross checks, the selected nuisance parameters with leading uncertainties were sampled from their prior distributions for each hypothetical experiment.

The statistical model is implemented with the ROOFIT [257] and ROOSTATS [258] software packages. All posterior probabilities are evaluated with Markov Chain methods as introduced in section 4.4.1, using the ROOSTATS→BAT interface. Further information on this interface can be found in appendix B.

The optimization procedure assumes an integrated luminosity of 5.3 fb$^{-1}$. Based on the signal expectation, masses between 0.8 TeV and 2.0 TeV are considered as potential lower mass thresholds for the counting experiment. In this range, the expected limits are evaluated in steps of 0.1 TeV. To establish that the optimization procedure is stable and well-behaved, the limits can be evaluated as a function of one or more of the input parameters. As examples, the expected limits for some of the considered mass thresholds are shown in figure 11.1 (Left) as a function of the assumed signal reconstruction efficiency. The considered ADD dimuon signals correspond to values of $\epsilon_{\text{reco,s}} \approx 0.9$. Figure 11.1 (Right) depicts an exemplary posterior probability distribution of $\sigma_s$ for the case $N_{\text{obs}} = 2$ (2 observed events in the signal region), $\epsilon_{\text{reco,s}} = 0.9$, and $M_{\text{threshold}} = 1.3$ TeV.
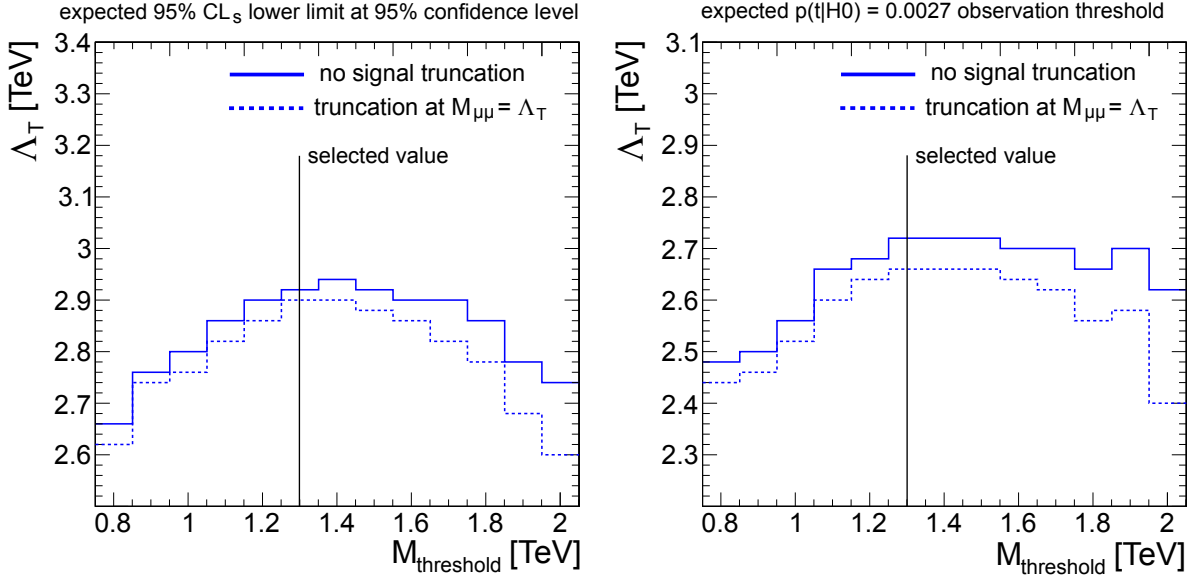
**Figure 11.3** (Left) Expected $CL_S$ lower limits on $\Lambda_T$ at 95% confidence level. (Right) Expected observation thresholds for a signal observation at $3\sigma$ significance based on p-values with profile likelihood test statistic.

Cross section limits as shown in figure 11.1 (Left) do by themselves not allow to select an optimal value of $M_{\text{threshold}}$ as they do not include any information about the distribution of the ADD signal in $M_{\mu\mu}$. Applying the mass dependent signal cross sections is therefore necessary to translate the cross section limits into expected exclusion ranges on the parameters of the considered ADD signal. Expected lower limits on $\Lambda_T$ in the GRW convention are given in figure 11.2 (Left). The two shown graphs correspond to the model prediction without any high mass truncation (solid blue line) and a scenario with $M_{\text{max}} = \Lambda_T$ (dashed blue line). Optimal choices of $M_{\text{threshold}}$ correspond to those values for which one expects the best limit on $\Lambda_T$. Considering the theoretical uncertainties on the signal expectation it is not useful to differentiate between mass threshold resulting in very small differences of the expected limit on $\Lambda_T$. The selected step size in $\Lambda_T$ for the optimization procedure is 0.02 TeV. With this setup, optimal thresholds are in the range of 1.2 TeV to 1.4 TeV with truncation at $M_{\mu\mu} = \Lambda_T$. (expected limit $\Lambda_T = 2.92$ TeV) and 1.2 TeV to 1.3 TeV without truncation (expected limit $\Lambda_T = 2.96$ TeV). Truncating the considered signal contributions at $M_{\mu\mu} = \Lambda_T$ is one possible way of including a high-energy threshold on the validity range of the effective ADD theory. The expected $\Lambda_T$ limits drops if $M_{\text{threshold}}$ is selected too low because the increase in the expected background outweighs the increase in the signal expectation. Also values of $M_{\text{threshold}}$ that are very high decrease the expected limit on $\Lambda_T$, because further reduction in the background expectation (which after some point is 0 for all practical purposes) no longer compensates for the decreased signal expectation from discarding lower dimuon mass values.

Figure 11.2 (Right) depicts expected limits in the HLZ convention with model parameters $M_s$ and $n$. It can be seen that the ranges of optimal mass cuts do not vary strongly with the number of considered extra dimensions. Specifically, $M_{\text{threshold}} = 1.3$ TeV is optimal for all choices of $n$ in the range of 3 to 7. For $n \geq 5$ not all cut values up to 2 TeV are considered because of limitations in the range of ADD models simulated for this study. This is no problem for the optimization procedure because the expected limits already start to decrease before reaching this $n$-dependent practical threshold.

One may wonder how the results of the cut optimization change if one considers other limit setting procedures or an optimization with respect to the range of models that one expects to observe at a given significance. An alternative limit setting procedure is provided by the $CL_S$ type limits based on a profile likelihood ratio test statistic defined in section 4.3. With the $CL_S$ approach, expected cross section limits can be calculated as suggested in the statistical procedure that has been established for the LHC Higgs search [127]. The adopted approach is to evaluate a set of hypothetical experiments for which the nuisance parameters are fixed at their profiled values $\hat{\Theta}$ and $\hat{\hat{\Theta}}$. Figure 11.3 (Left) shows the resulting expected limits on $\Lambda_T$ in dependence on $M_{\text{threshold}}$. The results are similar to the outcome of the optimization based on the Bayesian limits. Without signal truncation, the optimal lower mass threshold is found to be 1.4 TeV (expected limit $\Lambda_T = 2.94$ TeV). With signal truncation at $M_{\mu\mu} = \Lambda_T$, the optimal range for $M_{\text{threshold}}$ is 1.3 TeV to 1.4 TeV (expected limit $\Lambda_T = 2.90$ TeV).

An expected significance can be defined based on the p-value of the observed number of events under $H_0$ (the SM hypothesis). The profile likelihood ratio is selected as the employed test statistic and the ensemble of hypothetical experiments is again based on the profiled values of the nuisance parameters. The signal cross section corresponding to an expected p-value of 0.0027 is determined with a a simple binary search procedure. A p-value of 0.0027 corresponds to the $3\sigma$ criterion conventionally used to claim evidence of an *observation*. Corresponding expected observation thresholds on $\Lambda_T$ are shown in figure 11.3 (Right). Both with and without signal truncation at $M_{\mu\mu} = \Lambda_T$, the optimal mass threshold is between 1.3 TeV and 1.5 TeV.

As a lower mass threshold of $M_{\text{threshold}} = 1.3$ TeV is found to be within or close to the optimal range for all considered model specifications and optimization criteria, this value is selected as the lower mass threshold of the counting experiment from which the observed limits are established.

# 12 Evaluation of the Measured Dimuon Mass Spectrum

After evaluating the background expectation for the dimuon mass spectrum above the $Z$ resonance (sections 8 and 9) and its mass dependent uncertainties with respect to the event selection (summarized in table 11.1), one can use the measured dimuon mass spectrum to validate the SM background expectation for masses below the signal region specified in section 11. In figure 12.1 (Left), the dimuon mass distribution above 0.14 TeV is compared to the SM expectation. The shown spectrum corresponds to the full 2011 dataset with an estimated integrated luminosity of $\mathcal{L} = 5.28\,\mathrm{fb}^{-1}$.

As for all other figures in this section, error bars on a number of observed events approximate a confidence interval at 68% confidence level on the mean of the Poisson distribution from which the event number has been drawn. An overview table of possible definitions of confidence intervals for a Poisson mean can be found in [259]. The approximation used here is given by the interval [260]

$$\left( \frac{1}{2} F\left( 0.16, N \cdot 2 \right) \; ; \; \frac{1}{2} F\left( 0.84, (N+1) \cdot 2 \right) \right) \quad , \tag{12.1}$$

where $N$ is the number of observed events and $F(x, k)$ the x-quantile of the $\chi^2$ distribution with $k$ degrees of freedom. For any range of possible Poisson means, it is guaranteed that the CL of the approximate 68% interval defined in this way has overcoverage, implying that the CL is *at least* 68%. Figure 12.2 shows the dimuon mass distribution with variable bin sizes that
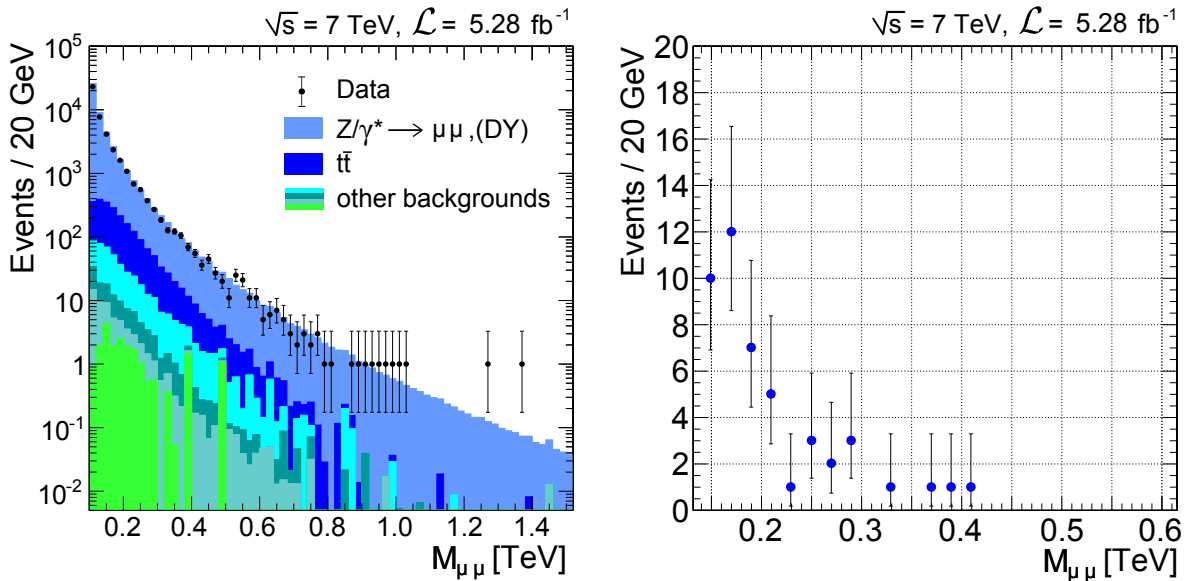


**Figure 12.1** (Left) Dimuon mass spectrum at 5.28 fb$^{-1}$ compared to the stacked expected background contributions from all relevant SM processes. The shown error bars on the observed event numbers reflect the statistical uncertainty. (Right) Observed mass spectrum of muon pairs with same charge.
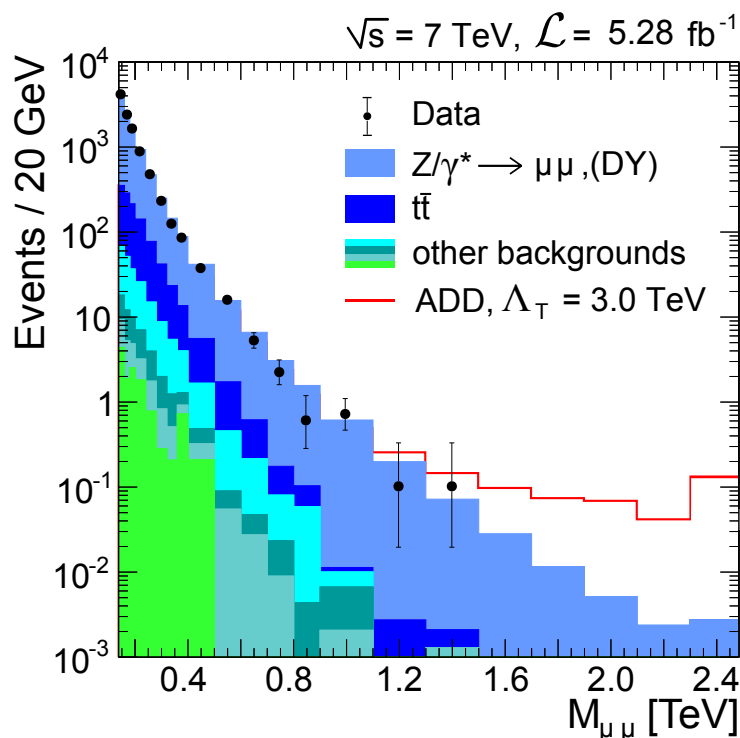
**Figure 12.2** Dimuon mass spectrum at 5.28 fb$^{-1}$ (variable binning) compared to the stacked expected background contributions from all relevant SM processes. Also shown are the expected additional contributions (stacked on top of the SM backgrounds) from an ADD signal with $\Lambda_T$ = 3.0 TeV (without QCD NLO correction, no signal truncation). The shown error bars on the observed event numbers reflect the statistical uncertainty. All contributions above 2.3 TeV are included in the highest mass bin ($> 2.3$ TeV).

approximately reflect the decreasing mass resolution. Predicted additional contributions from an ADD signal with $\Lambda_T$ = 3.0 TeV are shown on top of the SM prediction to illustrate the expected influence from an ADD model with parameters close to the exclusion threshold.

Figures 12.1 (Left) and 12.2 indicate good agreement between the measurement and the SM expectation over the whole evaluated mass range. Integrated event numbers and corresponding SM expectation as a function of a lower dimuon mass threshold are shown in figure 12.3. The SM prediction includes all considered SM background simulations. In figure 12.3 (Right), the baseline DY simulation with MC@NLO is replaced with a simulation based on Powheg (section 8.2.2). It can be seen that the Powheg simulation seems to provide a slightly better description of the measured spectrum. However, the results of both considered DY simulations are found to be compatible with the data if the systematic uncertainties are taken into account.

This claim is directly quantified by the numbers given in table 12.1. In this table, the number of observed events in several control regions for masses below 1.3 TeV is compared to the SM expectation. To give an estimate of the approximate overall uncertainty on the SM prediction, all systematic uncertainties are added in quadrature. While the comparison including the MC@NLO simulation is fully compatible with the measurement, results from section 8.2.2 indicate that the overall agreement with the data would be even slightly better if the simulation were available with the latest CMS simulation software as applied for the POWHEG simulation. *p*-values for the control regions and the signal region are given in table 12.2. The applied definition of the
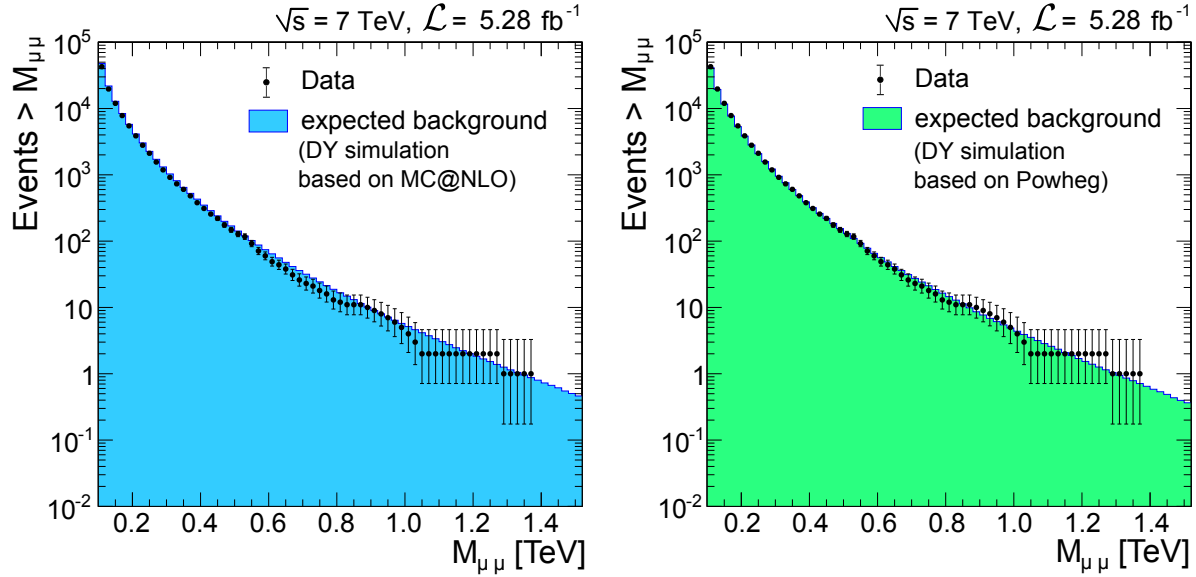
**Figure 12.3** Integrated number of observed events and corresponding SM expectation as a function of a lower dimuon mass threshold. The shown error bars on the observed event numbers reflect the statistical uncertainty. (Left) DY background expectation from the simulation with MC@NLO. (Right) DY background expectation from the simulation with Powheg.

*p*-value corresponds to a choice used for example in the context of model unspecific searches like those described in references [190, 261]. No control region corresponds to a significant deviation from the background expectation. It is therefore not necessary to include a discussion of the look-elsewhere effect (e.g. [262]). An event display of the event with highest dimuon mass ($M_{\mu\mu} = 1.38$ TeV) is shown in figure 12.5.

**Table 12.1** Comparison of the observed and expected number of events in several control regions and the signal region. Expected effective signal contributions are shown for $\Lambda_\mathrm{T} = 3.0$ TeV (ADD LO prediction, signal truncation at $M_\mathrm{max} = \Lambda_\mathrm{T}$). The uncertainties on the background expectations reflect the systematic uncertainties. Statistical uncertainties on the background expectations due to the limited numbers of simulated events are negligible).

| $\mu\mu$, $\mathcal{L} = 5.28\,\mathrm{fb}^{-1}$ | | | | |
|---|---|---|---|---|
| Mass region [TeV] | $N_\mathrm{obs}$ | SM bkg. expectation (DY process with MC@NLO) | SM bkg. expectation (DY process with POWHEG) | Signal exp. $\Lambda_\mathrm{T} = 3.0$ TeV |
| Control regions | | | | |
| 0.14–0.20 | 8101 | 8718±435 | 7861±393 | - |
| 0.20–0.40 | 3562 | 3784±227 | 3514±210 | - |
| 0.40–0.60 | 262 | 285±22 | 263±21 | - |
| 0.60–0.80 | 37 | 47.7±5.2 | 41.7±4.5 | - |
| 0.80–1.00 | 8 | 11.5±1.6 | 10.2±1.4 | 1.0 |
| 1.00–1.30 | 3 | 4.01±0.72 | 3.43±0.61 | 1.5 |
| Signal region | | | | |
| > 1.30 | 1 | 1.14±0.25 | 0.95±0.20 | 4.5 |

**Table 12.2** *p*-values in the control regions and the signal region.

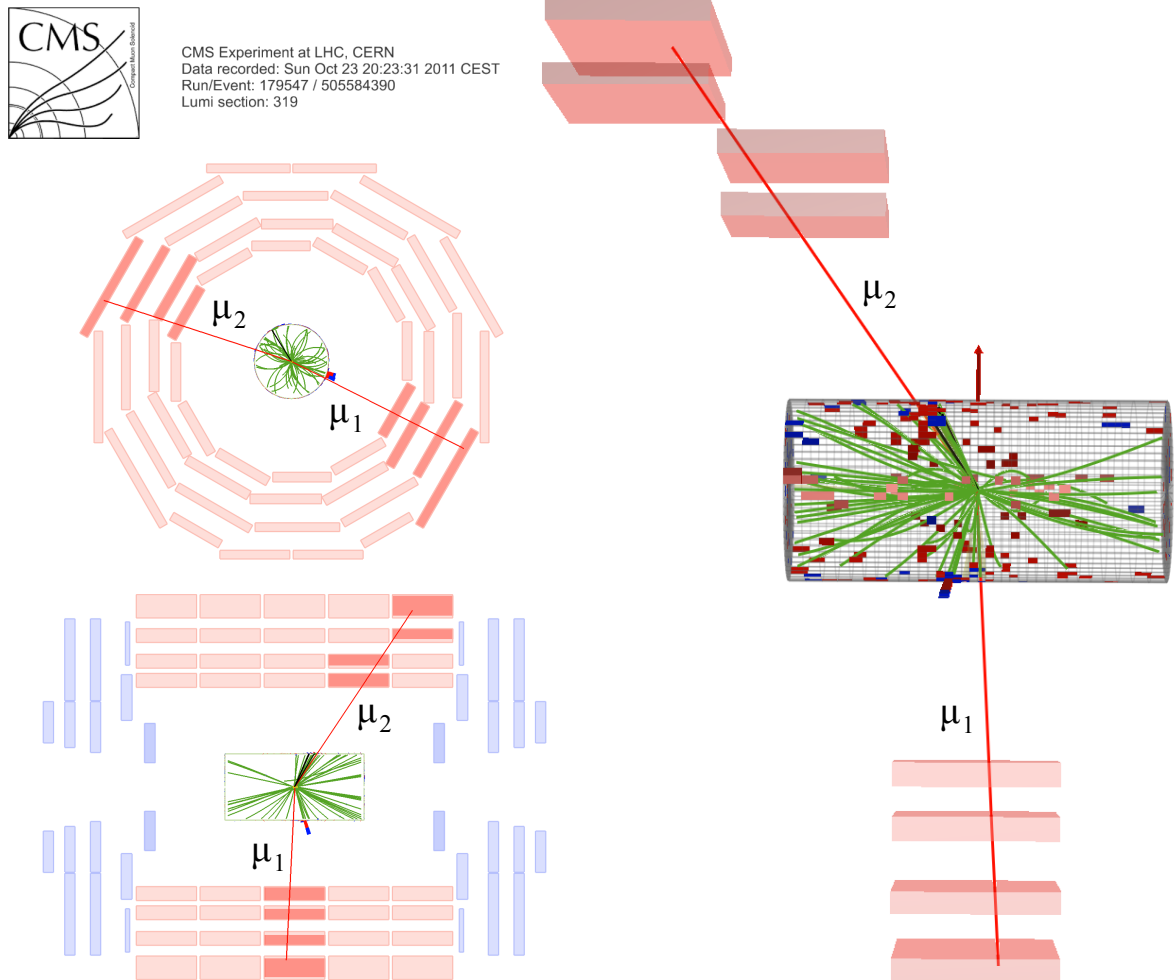| $\mu\mu$, $\mathcal{L} = 5.28\,\mathrm{fb}^{-1}$ | | |
|---|---|---|
| Mass region [TeV] | *p*-value (DY process with MC@NLO) | *p*-value (DY process with POWHEG) |
| Control regions | | |
| 0.14–0.20 | 0.08 | 0.28 |
| 0.20–0.40 | 0.17 | 0.41 |
| 0.40–0.60 | 0.21 | 0.50 |
| 0.60–0.80 | 0.11 | 0.31 |
| 0.80–1.00 | 0.22 | 0.33 |
| 1.00–1.30 | 0.44 | 0.56 |
| Signal region | | |
| > 1.30 | 0.69 | 0.61 |

The observed dimuon mass spectrum including only muon pairs with the same charge (*same-sign events*) is shown in figure 12.1 (Right). Over the whole mass range the observed number of same-sign events is far below the corresponding number of opposite sign events. No same-sign event is observed above 0.45 TeV. These results strongly support the claim (section 9.2) that for the given set of event selection criteria those background contributions providing same charge and opposite charge dimuon background contributions of roughly equal size are negligible. This argument specifically concerns potential contributions from QCD multijet events.

Even without a detailed evaluation of the significance of the observed event observed in the signal region of $M_{\mu\mu} \geq 1.3$ TeV, it is clear from the background expectations that the evaluated data does not provide any significant indications of a potential contribution from BSM physics. Accordingly, the following discussion in section 13 focuses on the question which range of ADD signals is found to be disfavored by the data.

An ADD signal with virtual spin-2 gravitons would not only change the dilepton mass spectra, but also influence the angular distribution of the leptons at a given mass. It has been argued in section 10 that a direct inclusion of the lepton angular distributions in the limit setting procedure can be expected to give an at best moderate improvement to the analysis performance. However, it is clear that if any significant BSM contribution were found in the signal region a detailed evaluation of the angular distribution would be relevant for establishing that the signature is compatible with virtual spin-2 particle propagation. Hence, even in the absence of a significant signal in the dimuon mass distribution, it is interesting to study potential differences between the SM expectation and the measured distribution of angular variables like $\cos\theta^*$. The $\cos\theta^*$ distribution in several mass regions is shown in figure 12.4. The results are compared to the SM DY simulation normalized to the number of observed events in the mass interval. It can be seen that the shapes of the expected SM DY distributions are compatible with the observed data. They don't feature any significant enhancement in the central range $\cos\theta^* \approx 0$ as it could result from a spin-2 signal.
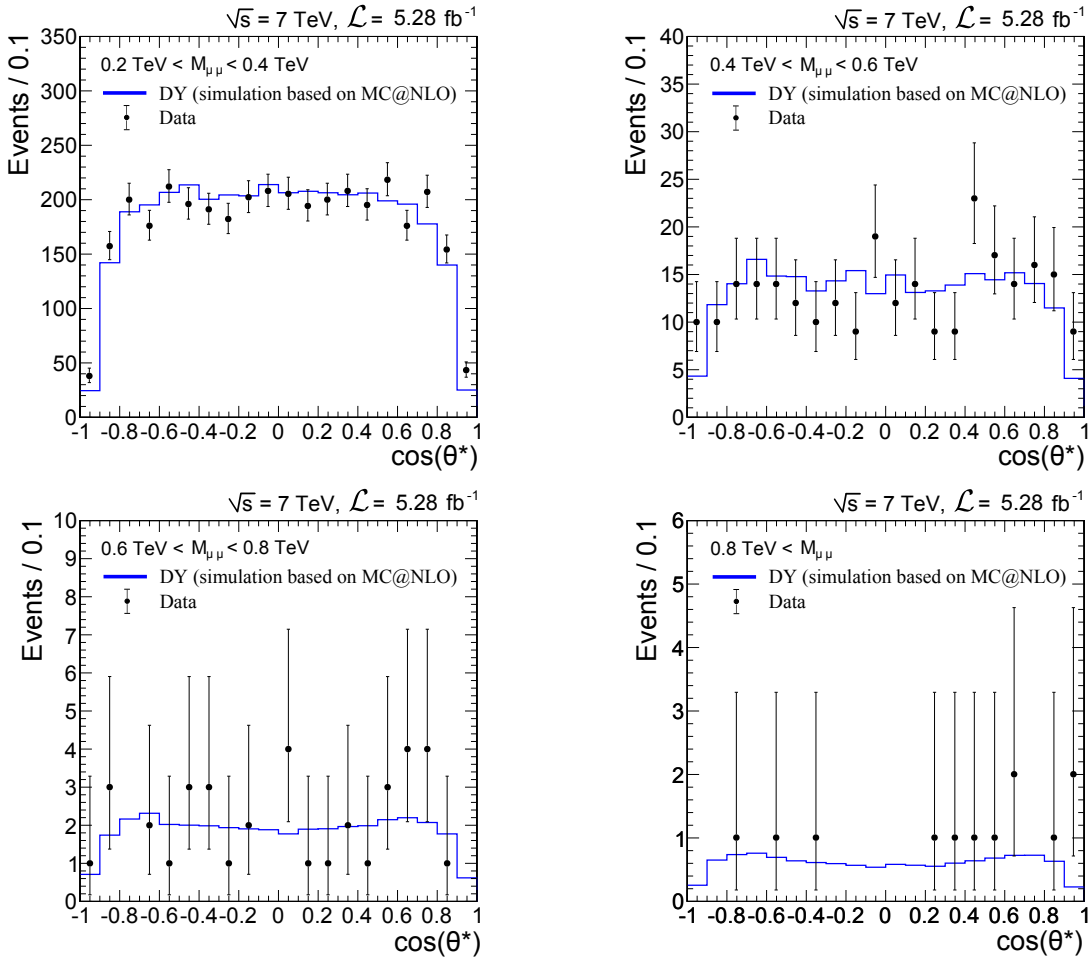
**Figure 12.4** Comparison between the observed $\cos\theta^*$ distribution and the SM DY expectation in several dimuon mass intervals. The error bars reflect the statistical uncertainty on the mean of the Poisson distribution from which the observed number of events has been drawn. The SM DY expectation based on the simulation with MC@NLO is normalized to the observed number of events in the selected dimuon mass range.

CMS Experiment at LHC, CERN
Data recorded: Sun Oct 23 20:23:31 2011 CEST
Run/Event: 179547 / 505584390
Lumi section: 319

**Figure 12.5** Display of the highest mass dimuon event in the 2011 dataset. The estimated dimuon mass is 1.38 TeV. The muon $p_{\mathrm{T}}$ values are 0.7 TeV ($\mu_1$) and 0.6 TeV ($\mu_2$).

# 13 Evaluation of Observed Limits and Interpretation of Results

As the measured dimuon mass spectrum evaluated with the full 2011 dataset at 5.28 fb$^{-1}$ of integrated luminosity is found to be compatible with the SM expectation, it suggests itself to use this result to derive limits on the range of new physics models that are likely to not yet have left a signature in the data. Such limits are presented and discussed in section 13.1. As a virtual graviton is expected to decay into multiple final states it is possible to improve limits on the parameters in the ADD models by combining results from multiple final states. Limits evaluated with a combination of dimuon, dielectron and diphoton data based on a partial 2011 dataset are discussed in section 13.2. A short discussion of results from the latest iteration of the presented search for ADD models with data at $\sqrt{s} = 8$ TeV is presented in section 13.3. The chapter concludes with a summary of the development of limits on $M_{\mathrm{s}}$ in the course of LHC data taking from 2010 to early 2013 and some further thoughts on physics implications of the obtained results.

## 13.1 Observed Limits from the Dimuon Mass Spectrum

The observed limits from the full 2011 dataset are calculated with the statistical model that has been specified for the optimization of limits discussed in section 11. For this analysis, Bayesian 95% credible interval limits with a flat prior on the signal cross section are used as the main results. The corresponding signal cross section limits with respect to dimuon events with $|\eta_\mu| < 2.1$ and $p_{\mathrm{T},\mu} > 45$ GeV are shown in figure 13.1 (Left) for several selected lower mass thresholds. To allow for a straightforward comparison with the expected limits presented in figure 11.1, the limits are shown as a function of the assumed signal efficiency. Independent of the specific choice of model parameters, the considered ADD signature has an efficiency of close to 90% in the signal region. For the example $\Lambda_{\mathrm{T}} = 2.8$ TeV this has been shown in figure 10.2 (Right). With the selected statistical procedure, the observed limits are not dependent on the background expectation if te data contains no event in the signal region. This is why the limit with $M_{\mathrm{threshold}} = 1.4$ TeV is (within the numerical precision of the Markov chain integration) identical to the limits with $M_{\mathrm{threshold}} = 2.0$ TeV.

Figure 13.1 (Right) shows a comparison with limits at 95% confidence level evaluated using the $\mathrm{CL_S}$ approach with profile likelihood test statistic. The $\mathrm{CL_S}$ cross section limits are found to be somewhat below the Bayesian results. The influence of this differences on the exclusion range for the ADD parameters $\Lambda_{\mathrm{T}}$ and $M_{\mathrm{s}}$ is however limited to $\lesssim 0.1$ TeV. It may be added that the comparison with the $\mathrm{CL_S}$ results is expected to depend to some degree on subtle choices within the definition of the $\mathrm{CL_S}$ procedure, including the details of the treatment of nuisance parameters.

In section 11, a lower mass threshold of $M_{\mathrm{threshold}} = 1.3$ TeV has been selected for the evaluation of limits on the ADD model. At an efficiency of 90%, the observed (expected) 95% credible interval cross section limit with $M_{\mathrm{threshold}} = 1.3$ TeV is 0.84 fb (0.92 fb). As argued above, a value of 90% provides an estimate for the efficiency of the ADD dimuon signal and is hence used for the following results. The observed cross section limits can be interpreted in
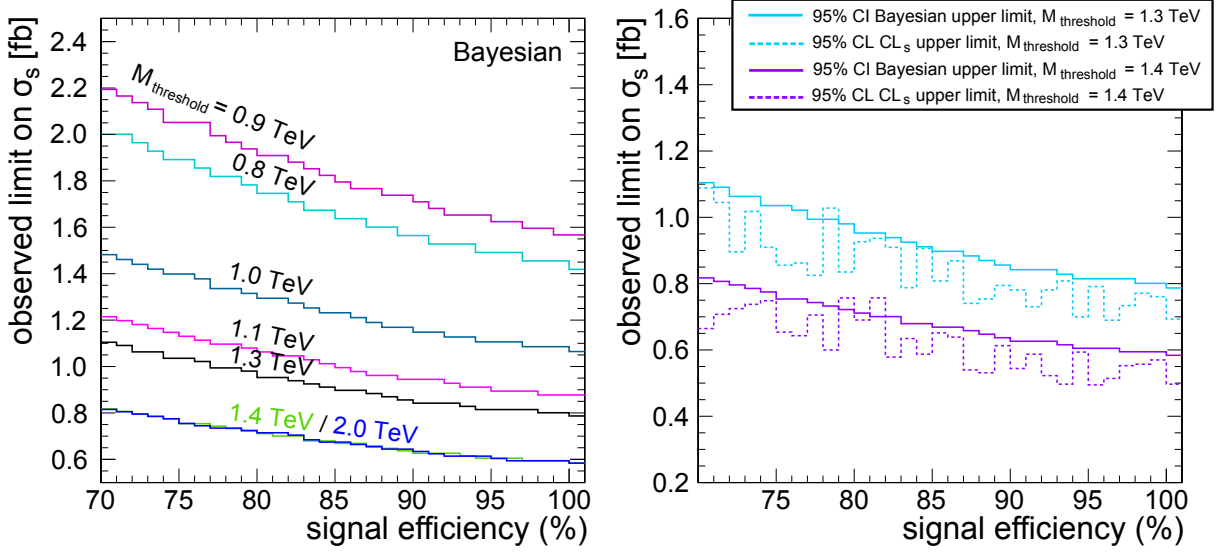
**Figure 13.1** (Left) Observed 95% credible interval upper limits on the signal cross section of dimuon events with $|\eta_\mu| < 2.1$ and $p_{\mathrm{T},\mu} > 45$ GeV, obtained with 5.28 fb$^{-1}$ of integrated luminosity. The results are shown with different mass cut values $M_{\mathrm{threshold}}$ and estimated signal efficiencies in the range 0.7 to 1.0. (Right) Comparison between the observed Bayesian limits and corresponding CL$_{\mathrm{S}}$ based limits with profile likelihood test statistic for $M_{\mathrm{threshold}} = 1.3$ TeV (1 observed event) and $M_{\mathrm{threshold}} = 1.4$ TeV (0 observed events).
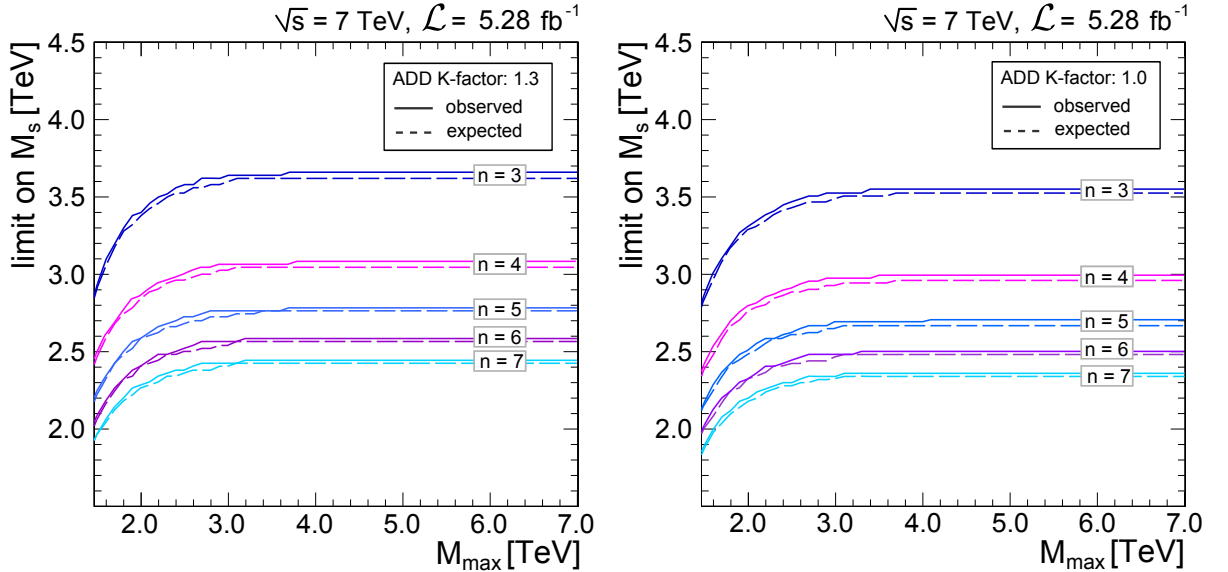


**Figure 13.2** Observed and expected 95% credible interval lower limits on $M_{\mathrm{s}}$, obtained with 5.28 fb$^{-1}$ of integrated luminosity, for different numbers of extra dimensions $n$. The results are shown with (Left) and without (Right) application of a signal K-factor of 1.3.

**Table 13.1** Observed 95% lower limits ($\mu\mu$, 5.28 fb$^{-1}$ at $\sqrt{s} = 7$ TeV) in TeV in the GRW and HLZ conventions with and without truncation at $M_{\max} = M_s$ (HLZ) or $M_{\max} = \Lambda_T$ (GRW).

| $\Lambda_T$ [TeV] (GRW) | $M_{\mathrm{s}}$ [TeV] (HLZ) | | | | | |
|---|---|---|---|---|---|---|
| | $n = 2$ | $n = 3$ | $n = 4$ | $n = 5$ | $n = 6$ | $n = 7$ |
| $\mu\mu$, with signal truncation: | | | | | | |
| ADD K-factor: 1.0 | | | | | | |
| 2.96 | 3.0 | 3.54 | 2.96 | 2.64 | 2.42 | 2.26 |
| ADD K-factor: 1.3 | | | | | | |
| 3.06 | 3.2 | 3.64 | 3.06 | 2.74 | 2.52 | 2.36 |
| $\mu\mu$, no signal truncation: | | | | | | |
| ADD K-factor: 1.0 | | | | | | |
| 2.98 | 3.0 | 3.54 | 2.98 | 2.70 | 2.50 | 2.36 |
| ADD K-factor: 1.3 | | | | | | |
| 3.08 | 3.2 | 3.66 | 3.08 | 2.78 | 2.58 | 2.44 |

terms of disfavored parameter ranges for virtual graviton exchange in the ADD model. Figure 13.2 shows limits on the parameter $M_{\mathrm{s}}$ as a function of the upper mass threshold of included signal contributions $M_{\max}$ for different choices of the number of extra dimensions $n$. Results are given with and without application of an QCD NLO K-factor of 1.3 on the signal cross section. The $M_{\mathrm{s}}$ limits with $n = 4$ in the HLZ convention correspond to the $\Lambda_{\mathrm{T}}$ limits in the GRW convention. Table 13.1 summarizes the limits for signal truncation at $M_{\max} = M_s$ or $M_{\max} = \Lambda_T$ with and without any additional mass restrictions on the signal contributions. The table also gives a limit for $n = 2$, which has however tight astrophysics bounds (references given in section 3.4.1), at least if one does not introduce modifications to the considered ADD scenario.

## 13.2 Comparison with the Combined Limits from Dimuon, Dielectron, and Diphoton Events with an Intermediate 2011 Dataset

As virtual gravitons in the ADD model are expected to decay into several final states it is possible to evaluate model limits not only from the dimuon final state but also in combination with other search channels. The combined limits from dimuon, dielectron, and diphoton events

**Table 13.2** Observed lower limits in TeV at 95% CL within GRW and HLZ conventions for truncation at $M_{\max} = \Lambda_{\mathrm{T}}$ (GRW) or $M_{\max} = M_{\mathrm{s}}$ (HLZ) [9, 263].

| ADD K-factor | $\Lambda_{\mathrm{T}}$ [TeV] (GRW) | $M_{\mathrm{s}}$ [TeV] (HLZ) | | | | | |
|---|---|---|---|---|---|---|---|
| | | $n = 2$ | $n = 3$ | $n = 4$ | $n = 5$ | $n = 6$ | $n = 7$ |
| $\mu\mu$ and ee, $\sigma_{\mathrm{s},\mu\mu+\mathrm{ee}} < 1.4$ fb (2.2 fb expected) at 95% CL | | | | | | | |
| 1.0 | 3.1 | 3.7 | 3.7 | 3.1 | 2.8 | 2.5 | 2.4 |
| 1.3 | 3.2 | 3.8 | 3.8 | 3.2 | 2.9 | 2.7 | 2.5 |
| $\mu\mu$, ee and $\gamma\gamma$ | | | | | | | |
| 1.3 ($\mu\mu$ and ee), 1.6 ($\gamma\gamma$) | 3.3 | 4.1 | 3.9 | 3.3 | 3.0 | 2.8 | 2.6 |

based on an intermediate 2011 dataset previously presented in [9] were evaluated as part of the studies summarized in this thesis. For these results, the integrated luminosities of the data are 2.3 $fb^{-1}$ in the dimuon channel, 2.1 $fb^{-1}$ in the dielectron channel, and 2.2 $fb^{-1}$ in the diphoton channel. The mass distributions for each of the final states is found to be compatible with the SM expectation. Limits have been set with the $CL_S$ approach, using a profile likelihood test statistic. The complete likelihood for the statistical evaluation is given by the product of the
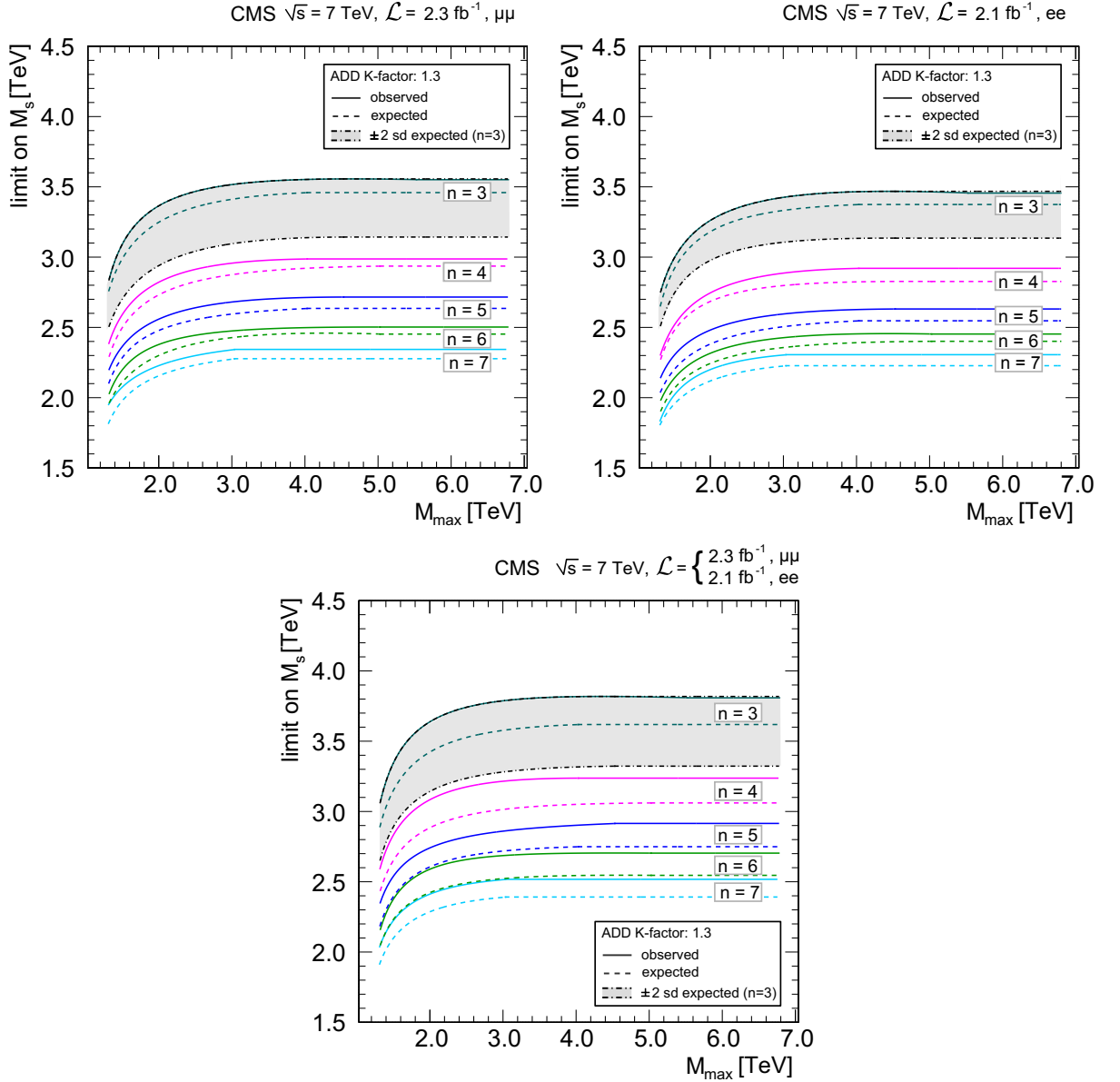


**Figure 13.3** Observed and expected 95% CL lower limits on $M_s$, obtained by the single channel $\mu\mu$ and ee results and their statistical combination, for different numbers of extra dimensions $n$, applying a signal K-factor of 1.3. A confidence interval for the expected limit corresponding to 2 standard deviations (sd) is shown for the case $n = 3$ [9] (figure caption adapted).

likelihoods of the three single channel counting experiments including additional terms that are used to model the influence of the uncertainty on the nuisance parameters.

$$L_{\text{combined}} = \prod_{\substack{i \\ i=\mu,\text{e},\gamma}} L_i \left( N_{\text{obs},i}, \sigma_{s,i}, \vec{\theta}_i \right) \tag{13.1}$$

The uncertainty on the luminosity is treated as fully correlated between all of the included channels. The predicted signal cross section ratios between the three models are used to convert the combined limit into a model with a single parameter of interest. In this way it can be avoided to calculate the exclusion threshold in a 3-dimensional space of signal cross sections.

Combined dielectron and dimuon limits for the specific conventional choice of truncating the signal at $M_{\text{max}} = \Lambda_{\text{T}}$ (GRW) or $M_{\text{max}} = M_{\text{s}}$ (HLZ) are listed in table 13.2. For this case, limits have also been calculated for a combination of $\mu\mu$, ee and $\gamma\gamma$ results.

Figure 13.3 shows the ADD model limits as a function of an upper mass threshold on the included signal contributions obtained from the dielectron and dimuon data and their combination. The combined observed limits evaluated with the partial 2011 dataset are still somewhat better than the dimuon limits from the full 2011 dataset, with more than twice of the integrated luminosity. Comparing the two results in more detail, the main reason for this behavior is found to be of statistical nature. The observed number of events in the signal region for the evaluation of the full 2011 dataset matches closely the background expectation. In contrast, a (statistically acceptable) downwards fluctuation that leads to observed limits that are somewhat better than the corresponding expected limits was observed in the partial 2011 dataset of dielectron and dimuon events.

## 13.3 Preliminary Results with 2012 Data at $\sqrt{s} = 8$ TeV

The steeply increasing amount of data during the years 2010 to 2012 allowed for a frequent update of those analysis results that profit from a increase in integrated luminosity and/or the increase of the center-of-mass energy from 7 TeV to 8 TeV. Many searches for BSM physics fall into this category. While the general search strategy of a given analysis often stays stable over a longer period of time, the importance of any specific set of search results is comparatively

**Table 13.3** Observed and expected lower limits in TeV at 95% CL in the GRW and HLZ parameter conventions for truncation at $M_{\text{max}} = \Lambda_{\text{T}}$ (GRW) or $M_{\text{max}} = M_{\text{s}}$ (HLZ) evaluated with the 2012 dataset [8, 95].

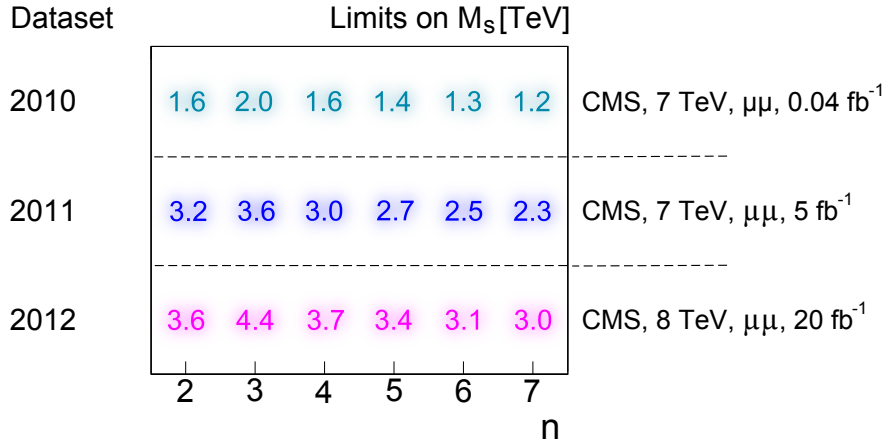| ADD K-factor | $\Lambda_T$ [TeV] (GRW) | $M_s$ [TeV] (HLZ) | | | | | |
|---|---|---|---|---|---|---|---|
| | | $n=2$ | $n=3$ | $n=4$ | $n=5$ | $n=6$ | $n=7$ |
| $\mu\mu, \sigma_{\text{s},\mu\mu} < 0.25$ fb (0.25 fb expected) at 95% CL | | | | | | | |
| 1.0 (observed) | 3.6 | 3.4 | 4.3 | 3.6 | 3.2 | 3.0 | 2.8 |
| 1.0 (expected) | 3.6 | 3.5 | 4.3 | 3.6 | 3.3 | 3.0 | 2.9 |
| 1.3 (observed) | 3.7 | 3.6 | 4.4 | 3.7 | 3.4 | 3.1 | 3.0 |
| 1.3 (expected) | 3.7 | 3.7 | 4.5 | 3.7 | 3.4 | 3.1 | 3.0 |
| $\mu\mu$ and ee, per channel $\sigma_{\text{s}} < 0.12$ fb (0.12 fb expected) at 95% CL | | | | | | | |
| 1.0 (observed) | 4.0 | 4.1 | 4.7 | 4.0 | 3.6 | 3.3 | 3.1 |
| 1.0 (expected) | 4.0 | 4.1 | 4.7 | 4.0 | 3.6 | 3.3 | 3.1 |
| 1.3 (observed) | 4.1 | 4.3 | 4.9 | 4.1 | 3.7 | 3.4 | 3.3 |
| 1.3 (expected) | 4.1 | 4.3 | 4.9 | 4.1 | 3.7 | 3.4 | 3.3 |
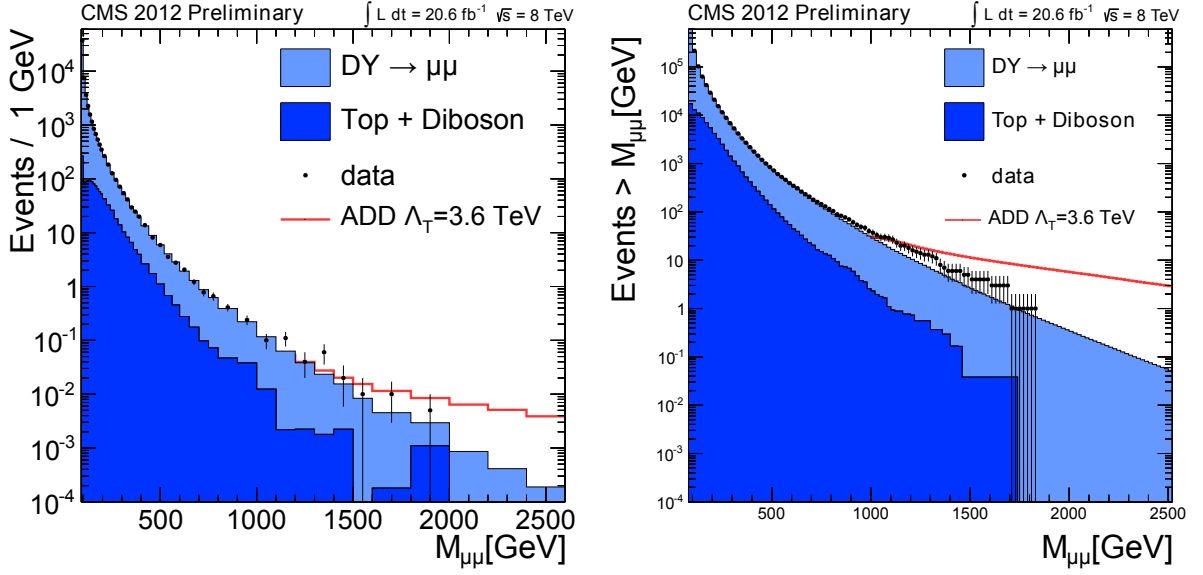
**Figure 13.4** (Left) Dimuon mass spectrum with $\sqrt{s} = 8$ TeV data at an integrated luminosity of 20.6 fb$^{-1}$ [8]. (Right) Corresponding integrated number of events as a function of a lower dimuon mass threshold. Error bars are given as $\sqrt{N_{obs}}$ [265].

short-lived. Recently, CMS has presented preliminary results on the CMS search for large extra dimensions in dimuon events with data at $\sqrt{s} = 8$ TeV, recorded in 2012 [8]. While in the context of the presented thesis major contributions have also been made to this latest iteration of the presented analysis, the discussion here is limited to a brief review of results. However, the way of how the analysis is performed is mostly unchanged with respect to the 2011 iteration. More detailed descriptions are given in [8, 264].

The measured dimuon spectrum with the full 2012 dataset for muon analyses (20.6 fb$^{-1}$) presented in figure 13.4 shows good agreement with the SM expectation. A single event is observed in the signal region above 1.8 TeV. The corresponding median of the background expectation is 0.73 with a systematic uncertainty of $\pm 0.21$. The signal cross section limit at 95% certainty level evaluates to 0.25 fb. A combination with results from a dielectron study with the 2012 dataset (19.6 fb$^{-1}$) [95] sets a signal cross section limit of 0.12 fb per channel. The corresponding limits on the ADD model parameters $\Lambda_T$ and $M_s$ are shown in table 13.3. These results provide a substantial improvement of the limits evaluated with 2011 data (table 13.2), raising the limit on $\Lambda_T$ from 3.3 TeV to 4.1 TeV.

## 13.4 Comparison with Other Collider Studies and Further Implications of the Results

It has been argued in the preceding sections that there is so far no evidence for a signal from virtual s-channel graviton exchange with a dimuon final state as suggested by the ADD model. As summarized in section 3.4, there are currently also no other experimental results hinting at the presence of spatial extra dimensions. The development of CMS limits on virtual s-channel graviton exchange in the dimuon channel from first results evaluated in 2010 to the latest world's best limits with 2012 data is summarized in figure 13.5. Figure 13.6 compares recent best limits on virtual s-channel graviton exchange from the ATLAS and CMS collaborations with the best corresponding collider limits outside of the LHC experiments, set by the D0 collaboration.

Dataset            Limits on $M_s$ [TeV]

| 2010 | 1.6 2.0 1.6 1.4 1.3 1.2 | CMS, 7 TeV, $\mu\mu$, 0.04 fb[-1] |
| 2011 | 3.2 3.6 3.0 2.7 2.5 2.3 | CMS, 7 TeV, $\mu\mu$, 5 fb[-1] |
| 2012 | 3.6 4.4 3.7 3.4 3.1 3.0 | CMS, 8 TeV, $\mu\mu$, 20 fb[-1] |

2 3 4 5 6 7

n

**Figure 13.5** Development of CMS lower limits on virtual s-channel graviton exchange in the dimuon final state. The presented analysis of 2011 data [9] (here also extended to the full 2011 dataset) and the recent results with 2012 data [4] are a direct evolution of the first iteration of the CMS ADD dimuon analysis with 2010 data [8] which has not been discussed in this work as it is superseded by the newer results.

The hierarchy problem has been a relevant incentive for the development of the ADD scenario of large extra dimensions. Hence, one may wonder about possible implications of the latest limits on $M_s$ in terms of the required fine-tuning. A possible approach is to consider the fine-tuning indicator $f$, defined in equation 2.12 via the one-loop Higgs mass corrections. Equations 3.19 to 3.21 allow to link the limits on the model parameters $\Lambda_T$ or $M_s$ to the UV cutoff $\Lambda$ and the

Limits on $M_s$ [TeV]

| 2.0 1.9 1.6 1.4 1.3 1.2 | DØ, 1.96 TeV, ee+$\gamma\gamma$, 1.1 fb[-1] |
| 4.1 3.9 3.3 3.0 2.8 2.6 | CMS, 7 TeV, ee+$\mu\mu$+$\gamma\gamma$, 2 fb[-1] |
| 4.1 3.5 3.1 2.9 2.7 | ATLAS, 7 TeV, ee+$\mu\mu$+$\gamma\gamma$, 5 fb[-1] |
| 4.3 4.9 4.1 3.7 3.4 3.3 | CMS, 8 TeV, ee+$\mu\mu$, 20 fb[-1] |

2 3 4 5 6 7

n
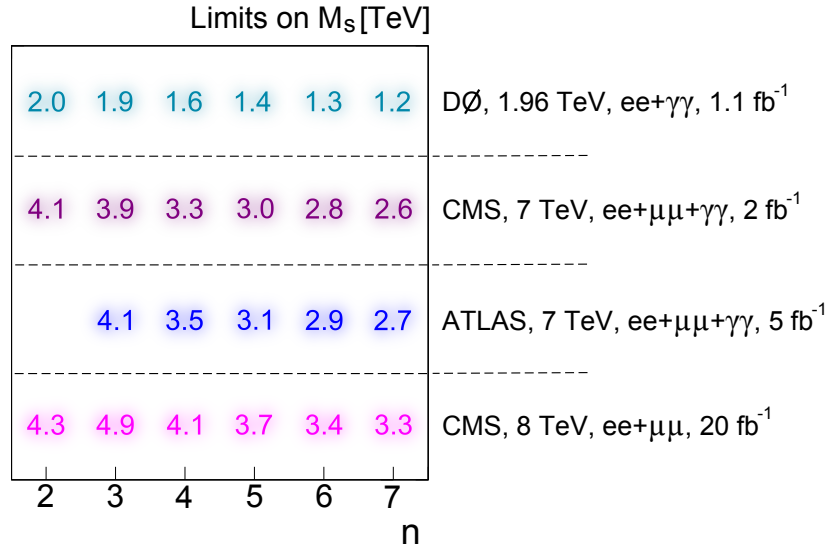
**Figure 13.6** Comparison of best lower limits on virtual s-channel graviton exchange from the CMS, ATLAS and D0 collaborations [90, 9, 92, 8, 95]. The CMS limits are directly linked to analysis results from the presented work.

fundamental Planck mass $M_{\mathrm{D}}$. If one uses these equations[1] and follows the naive expectation $\Lambda \approx M_{\mathrm{D}}$, then $f$ results in values of $10 < f < 100$ for $3 \le n \le 7$. This suggests that the results do probe the parameter space where the considered ADD model starts to loose its appeal as a solution of the SM Higgs fine-tuning problem. This can be avoided by considering higher numbers of extra dimensions. If the analysis of future LHC data at increased luminosity and center-of-mass energy does not find a signal, it will be possible to strongly reduce the attractiveness of the discussed ADD scenario as a possible reinterpretation of the hierarchy problem. However, actually seeing evidence for the existence of extra dimensions would of course be the by far more exciting possibility.

From a more general point of view, the obtained cross section limits on high mass dimuon events may also be of relevance for other new physics models. For example, dilepton signatures from KK modes in RS models can be so broad that they could in practice look like a non-resonant enhancement of the dimuon high mass tail [266]. Signals predicting a dimuon- or more generally dilepton-resonance require a somewhat different analysis approach. A discussion of recent statistical results on a CMS search for dielectron and dimuon resonances is presented in appendix A.

---

[1]A more detailed argument would actually need to resort to equation 3.17 as it is not evident how well the $s \ll \Lambda$ approximation is met.

# 14 Conclusion

In summary, a search for large spatial extra dimensions with a CMS measurement of the dimuon mass spectrum obtained from LHC proton-proton collisions has been presented. Results derived in this thesis have been the basis for all iterations of the CMS search for large extra dimensions in dimuon events since the beginning of LHC data taking, and have also been important for the combination of the dimuon measurement with results from other final states. The first iteration of the dimuon analysis used 2010 data. More recently, dimuon results and their statistical combination with dielectron and diphoton data have been published based on a partial 2011 dataset. Results being presented for the first time in this work extend the analysis of dimuon events to the full 2011 dataset. Also newest preliminary results with $\sqrt{s} = 8$ TeV have been briefly outlined.

The background expectations for muon pairs at high invariant mass from proton-proton collisions at CMS have been studied. Both electroweak and QCD higher order corrections on the dominant DY background are taken into account. Uncertainties of theoretical and experimental origin have been quantified and are included in the analysis. Both of these types of uncertainties are found to play a relevant role for the precision of the background estimate. The mass range defining the ADD signal region has been optimized based on simulation results. With 5.3 fb of data at $\sqrt{s} = 7$ TeV, no evidence for new physics has been found in the observed spectrum of dimuon high mass events. The measurement extends the study of muon pair production into mass regions that have not yet been probed at any pre-LHC experiment.

Above a dimuon mass of 1.3 TeV, new physics signals with a cross section of above 0.84 fb$^{-1}$ are found to be excluded at 95% confidence level. Limits on the ADD model parameters have been evaluated both in the HLZ and GRW conventions. The results restrict the ADD model parameter $\Lambda_{\mathrm{T}}$ to values above 3.0 TeV. Also the latest iteration of the analysis with the 2012 dataset does not provide evidence of a BSM signature and provides the current world best limit on virtual graviton decay in the ADD model ($\Lambda_{\mathrm{T}} > 4.1$ TeV for the combination of dimuon and dielectron data). While the LHC results suggest that the reduced Planck scale in a model with large extra dimensions is at least in the range of several TeV, large spatial extra dimensions continue to offer the exciting prospect that quantum gravity could be probed in collider experiments. It remains possible to find evidence for their existence in the further course of data analysis at CMS.

# A Updated Statistical Evaluation of the Dimuon and Dielectron Mass Spectra in Search for a new Dilepton Resonance at $\sqrt{s} = 8$ TeV with an Intermediate 2012 Dataset

The statistical evaluation of the measured dimuon and dielectron mass spectra with respect to models of new physics predicting additional resonances at high invariant dilepton masses[1] are discussed in the following sections A.1 to A.7. The updated code structure features smaller class units to improve maintainability and to simplify future development. An important new functionality is the extension of the code to cases with more than two search channels. This is required for a statistical combination of the 2011 and 2012 datasets. The code is written in C++. Its statistical functionality builds upon classes from the ROOSTATS [258] and ROOFIT [257] packages.

Building upon preceding studies [267, 268], further details of the current procedure for the statistical evaluation of limits are documented in [269] for CMS internal reference. CMS internal references for detailed studies on the dimuon and dielectron mass measurements include [270] and [271].

Section A.1 outlines aspects of some of the BSM models that motivate a search for new heavy neutral gauge bosons decaying to lepton pairs at CMS. The statistical model employed for the analysis is discussed in section A.2. An overview of the structure of the statistics code is presented in section A.3. Results including the 2011 dataset at $\sqrt{s} = 7$ TeV and a part of the 2012 dataset at $\sqrt{s} = 8$ TeV [6, 10] are discussed in sections A.4 and A.5. A short discussion of preliminary limits based on the full 2012 dataset [7] is presented in section A.6.

## A.1 New Heavy Dilepton Resonances

There is a wide range of models that suggest the possibility of new dilepton resonances [272]. Here the discussion is restricted to some basic aspects of those scenarios that provide the benchmark signatures used to interpret the statistical results in terms of ranges of excluded model parameters (section A.4).

One relevant group of models featuring new high mass dilepton resonances are characterized by an energy range at which the gauge group of the SM is extended to

$$SU(3)_C \times SU(2)_W \times U(1)_Y \times U(1)'^k \quad , \tag{A.1}$$

where the $k$ additional $U(1)'$ symmetries then lead to additional neutral gauge bosons $Z'$. The set of the $Z'$ mass eigenstates is model dependent. Both in scenarios with or without supersymmetry, Grand Unified Theories (GUTs) like $SO(10)$ or $E_6$ can be broken into symmetry groups as given

---

[1]in collaboration with Gena Kukartsev, who developed the statistics code version used for the previous iteration of the analysis [103].

by equation A.1. One such scenario is associated with a possible breaking scenario for $E_6$ which predicts a new gauge boson $Z'_\psi$. A review of the phenomenology in this particular model is given in [273]. A simple model that has no strong motivation from a specific GUT scenario but often provides a useful benchmark signature is the Sequential Standard Model which assumes the existence of a new heavy gauge boson with couplings identical to the SM $Z$ boson [273]. Usually, GUTs predict not only new neutral gauge bosons but also further beyond SM phenomenology. For example, assuming $k = 1$ and identical coupling strength of the new gauge boson to all SM fermions, additional exotic fermions need to be introduced to avoid anomalies [272].

Another possibility for new heavy dilepton resonances at the TeV scale arises in the scenarios with extra dimensions that have been briefly outlined in section 3.3. In models with extra dimensions, the new dilepton resonances can be created by the KK modes of the bulk particles. One such framework allowing for new dilepton resonances is given by models with warped spatial extra dimensions. Gravitons decaying into lepton pairs are a signature in the original RS-1 setup. In the UED model [72], all SM fields are located in the bulk. While in the UED scenario KK-parity suppresses dilepton final states from the first excited KK mode of the SM $Z$ boson, a dilepton resonance could be created via the second excited mode $Z_2$ [274]. A recent interpretation of the CMS dilepton resonance search with 2012 data in the context of UED models has been presented in [275].

A dilepton search for a resonant new physics signature in the dilepton mass distribution can benefit from the clear distinction between the signal shape (resonance) and the background (monotonously falling with $M_{\mu\mu}$). Accordingly, one takes an approach to the statistical analysis that differs from the methods employed in a search for a non-resonant signal.

## A.2  Statistical Model

The likelihood function of the full statistical model $L_{\text{full}}$ is given by the product of likelihoods of the individual events in each channel.

$$L_{\text{full}}(x; \nu, \Theta) = \prod_{j=1}^{N_{\text{channels}}} \prod_{i=1}^{N_{\text{events},j}} L_j(x_{i,j}, \nu, \Theta_j) \quad , \tag{A.2}$$

where $j$ runs over the included search channels and $i$ over the events of a given channel. $\Theta_j$ is the set of nuisance parameters in channel $j$. The observable used to characterize each event is its dilepton mass M ($x_{ij} = M_{ij}$). To improve the robustness of the analysis against systematic uncertainties, one can make use of the correlation of systematic uncertainties between events from the $Z'$ signal and the dominant DY background and define the parameter of interest $\nu$ as the ratio of signal and background cross sections.

$$\nu = R_\sigma = \sigma_{Z'}/\sigma_{Z^0} \tag{A.3}$$

This also has the advantage that the inference on $\nu$ is not influenced by the uncertainty on the CMS luminosity measurement. The definition of $R_\sigma$ implicitly depends on the proton-proton center-of-mass energy. To present results from data taken at differing center-of-mass values $a$ and $b$ in terms of a single cross section ratio parameter, one needs to evaluate the relation between $R_{\sigma,b}$ and $R_{\sigma,a}$. The factor between the two ratio variables needs to be evaluated as a function of the $Z'$ model parameters as the difference between the parton distribution functions at two center-of-mass energies depends on the parton type and the dilepton mass. In the models

discussed here, a mass parameter $M_{Z'}$ is sufficient to characterize the signal hypothesis. To relate $R_{\sigma,b}$ and $R_{\sigma,a}$, one can simply expand $R_{\sigma,b}(M_{Z'})$ as

$$R_{\sigma,b}(M_{Z'}) = R_{\sigma,a}(M_{Z'}) \cdot \frac{\frac{\sigma_{Z',b}(M_{Z'})}{\sigma_{Z',a}(M_{Z'})}}{\frac{\sigma_{Z^0,b}}{\sigma_{Z^0,a}}} = c_{ab}(M_{Z'}) \cdot R_{\sigma,a}(M_{Z'}) \quad . \tag{A.4}$$

As the factor $c_{ab}$ is found to vary only slowly with $M_{Z'}$, it does not differ much between models with different shapes of the narrow resonance as long as the relative couplings to the initial state partons are unchanged. However, there are prominent examples for which the latter prerequisite does not hold true. For example, the production of the SSM $Z'$ is completely driven by the quark PDFs while a KK graviton production receives also relevant contributions from gluon PDFs. In such cases, $c_{ab}$ needs to be reevaluated for the specific model.

The single channel likelihoods $L_j$ are given by

$$L_j\left(x_j; \nu, \Theta\right) = p_{\text{sig}}\left(\nu, \Theta\right) \cdot f_{j,\text{sig}}\left(x_j, \Theta_{j,sig}\right) + \left(1 - p_{\text{sig}}\left(\nu, \Theta\right)\right) \cdot f_{j,\text{bkg}}\left(x_j, \Theta_{j,bkg}\right) \quad , \tag{A.5}$$

where $f_{\text{sig}}$ and $f_{\text{bkg}}$ are probability density functions parametrizing the mass distributions of signal and background. $p_{\text{sig}}$ controls the signal strength relative to the background as a function of the parameter of interest $\nu$ and the nuisance parameters $\theta$. The functions $f_{j,\text{sig}}$ and $f_{j,\text{bkg}}$ are determined from simulation and can be approximated with the functions

$$\begin{aligned} f_{j,\text{sig}} &= \text{Voigt}\left(x_j; \sigma_{V,j}, \mu_{V,j}\right) \quad , \\ f_{j,\text{bkg}} &= c_{1,j} \cdot e^{c_{2,j} \cdot x_j} \cdot x_j^{c_{3,j}} \quad . \end{aligned} \tag{A.6}$$

$\sigma_{V,j}$, $\mu_{V,j}$, $c_{1,j}$, $c_{1,j}$, and $c_{1,j}$ are constants that parametrize the two distributions. The main motivation of the choice of $f_{j,\text{bkg}}$ is of empirical nature, given by the good resulting approximation of the simulated background shape with a simple analytic form. The Voigt distribution is selected to model $f_{j,\text{sig}}$, as it is defined as the convolution of a Cauchy (Breit-Wigner) distribution and a Normal (Gaussian) distribution. The Cauchy function provides a reasonable approximation of the dimuon mass distribution from the hard interaction. Its convolution with a Normal distribution is used to take into account the increased width of the signal shape resulting from the limited detector resolution.

Depending on the type of inference, nuisance parameters can be treated either by working in terms of prior distributions (in a Bayesian context) or in terms of additional constraints of the likelihood function derived from supplementary measurements.

The selected baseline method for presenting limits are Bayesian limits with a flat prior on the signal cross section that are evaluated as described in section 4.4. A noteworthy feature of this approach is that the limits can be made insensitive to the background normalization if the corresponding prior is selected sufficiently broad. In tests, $\pm 20\%$ uncertainty on the background normalization has been found to ensure that the limits are determined completely through the shape information provided by the likelihood.

## A.3 Code Structure

Most of input for the statistics code is read from RooFit workspaces [257] that are separately prepared for each included search channel. The workspaces contain input parameters, functional forms of parametrizations, and define the likelihood in the respective channel. In a following step, the combined model for the included channels is constructed. This allows to evaluate the combined likelihood. According to the requested type of inference, variables and functions are

associated with their statistical meaning. For example, in the case of Bayesian limits the nuisance parameters are defined and subsequently associated with prior functions. The combination of single channel models also specifies the peak position of the signal and controls the identification of variables that are shared between different channels (e.g. the parameter of interest). It is also possible to restrict the mass range of events that are included in the likelihood. Apart from potential statistical advantages, this can be used to improve the code performance for signals whose relevant contributions are significantly above the default lower mass threshold of included events. The RooStats software package [258] is used to perform multiple high level tasks like the evaluation of the posterior distribution via Markov Chain integration or the evaluation of the profile likelihood test statistic. In addition to a structured output of the main results, the code offers the possibility to write additional output that can be used to check the convergence properties and the statistical robustness of results. An overview of the $Z'$- specific code structure is shown in figure D.4. The core classes provide the following main functionalities:

- combination of the single channel workspaces and final specification of the statistical model (ModelConfigurator, ModelConfiguratorZprime)

- management of data from the actual measurement or hypothetical experiments (DataBox)

- calculation of limits and significances (Resultator)

## A.4  Results: $Z'$

Detailed CMS internal documentation of the studies in the dielectron and dimuon channels can be found in [270] and [271]. Figure A.1 shows the obtained 95% credible interval upper limits on $R_{\sigma,8\,\mathrm{TeV}}$. To calculate the combined limit including both dielectron and dimuon data it is assumed that the new heavy neutral gauge boson couples to electrons and muons with identical coupling strength. The factor $c_{7\,\mathrm{TeV},\,8\,\mathrm{TeV}}$ which relates $R_{\sigma,8\,\mathrm{TeV}}$ and $R_{\sigma,7\,\mathrm{TeV}}$ in the combination of data at $\sqrt{s}=7$ TeV and $\sqrt{s}=8$ TeV has been calculated from simulations of the SM DY process and the $Z'_\psi$ scenario. The theory predictions for the $Z'_\psi$ and $Z'_\mathrm{SSM}$ benchmark models have been derived in the same way as described in [103]. Single channel limits from just dimuon or dielectron events at $\sqrt{s}=8$ TeV may be found in [6]. The observed limits on the benchmark models are summarized in table A.1.

| dataset | Mass Limits [ TeV] | |
| --- | --- | --- |
| | $Z'_\psi$ | $Z'_\mathrm{SSM}$ |
| $\mu\mu$, 4.1 fb$^{-1}$ at $\sqrt{s}=8$ TeV | 1.94 | 2.27 |
| $ee$, 3.6 fb$^{-1}$ at $\sqrt{s}=8$ TeV | 1.87 | 2.20 |
| $\mu\mu$, 4.1 fb$^{-1}$ at $\sqrt{s}=8$ TeV, $ee$, 3.6 fb$^{-1}$ at $\sqrt{s}=8$ TeV | 2.11 | 2.44 |
| $\mu\mu$, 4.1 fb$^{-1}$ at $\sqrt{s}=8$ TeV, 5.3 fb$^{-1}$ at $\sqrt{s}=7$ TeV $ee$, 3.6 fb$^{-1}$ at $\sqrt{s}=8$ TeV, 5.0 fb$^{-1}$ at $\sqrt{s}=7$ TeV | 2.27 | 2.59 |

**Table A.1** Observed 95% credible interval lower mass limits for the $Z'_\mathrm{SSM}$ and $Z'_\psi$ benchmark models.
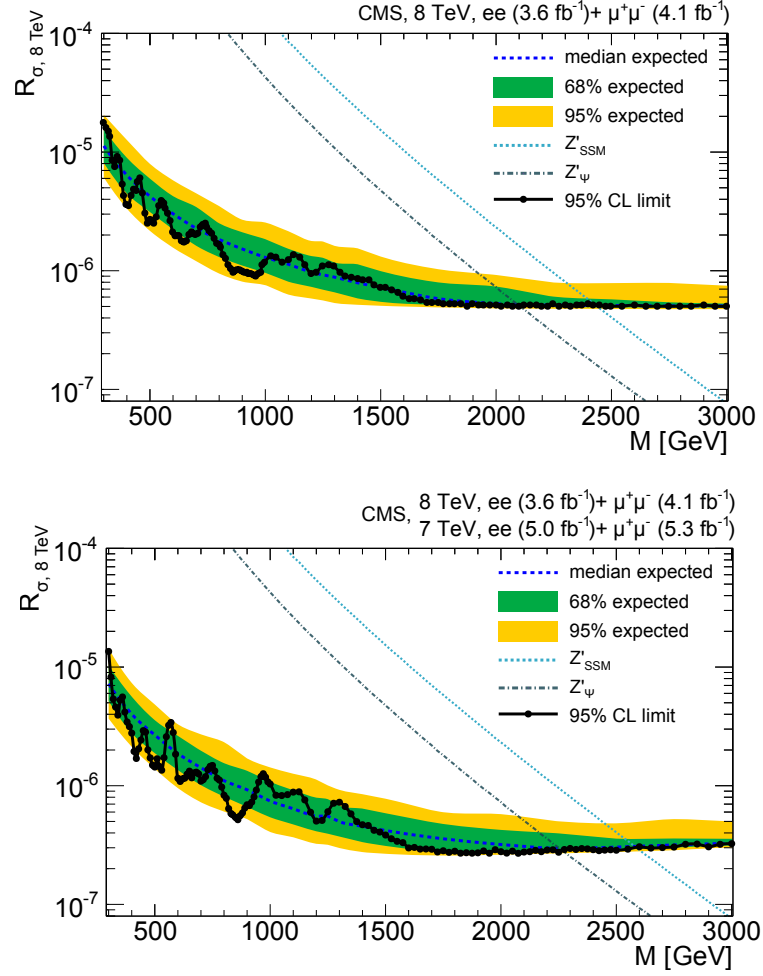
**Figure A.1** 95% credible interval upper limits on the $Z'$ to SM $Z^0$ cross section ratio $R_{\sigma,8\,\text{TeV}}$ from measurements of dielectron and dimuon mass spectra at CMS [10]:

- combination at $\sqrt{s} = 8$ TeV (upper figure):
  dimuon channel, 4.1 fb$^{-1}$
  dielectron channel, 3.6 fb$^{-1}$

- combination at $\sqrt{s} = 7$ TeV and $\sqrt{s} = 8$ TeV (lower figure):
  dimuon channel, 4.1 fb$^{-1}$ at $\sqrt{s} = 8$ TeV and 5.3 fb$^{-1}$ at $\sqrt{s} = 7$ TeV;
  dielectron channel, 3.6 fb$^{-1}$ at $\sqrt{s} = 8$ TeV and 5.0 fb$^{-1}$ at $\sqrt{s} = 7$ TeV

## A.5  Results: RS Graviton Resonance

The simulation of the RS-1 model at LO is implemented in Pythia8 [276, 212]. The following settings are selected to define a benchmark scenario:

- program version: 8.165

- PDFs: MSTW08 LO

- selected tunes pp: 5, ee: 3
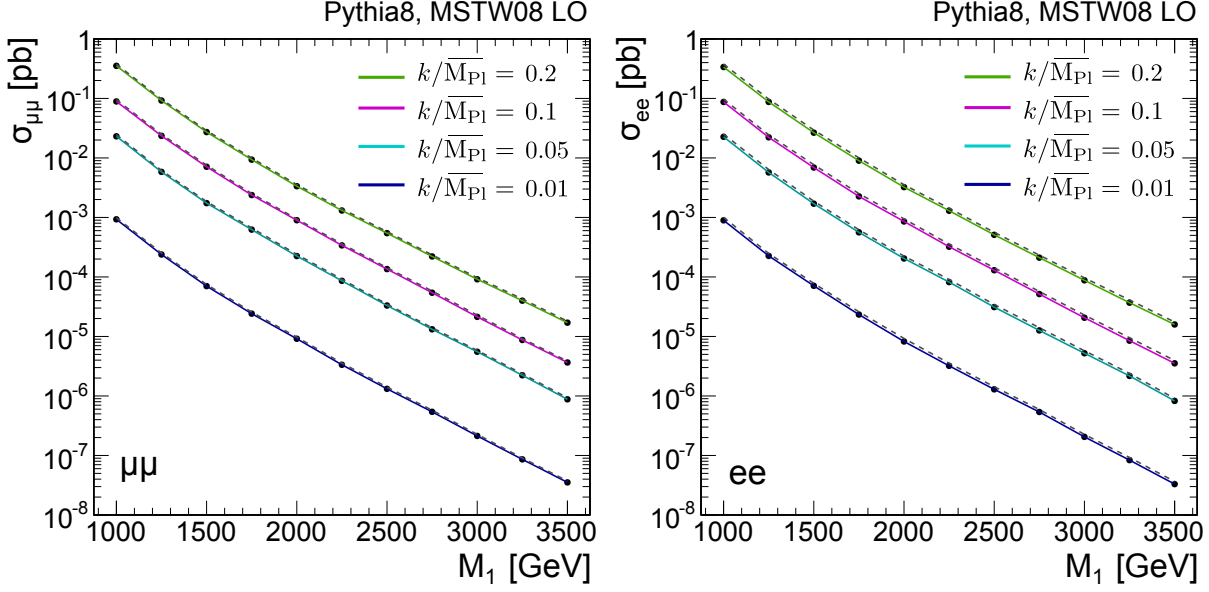
**Figure A.2** Cross sections at $\sqrt{s} = 8$ TeV for the processes $G_1 \to \mu\mu$ (Left) and $G_1 \to ee$ (Right) in the RS-1 model (LO). The dashed lines show the cross sections without cuts on $\eta$ and $p_{\mathrm{T}}$.

The model parameters are the mass $M_1$ of the first graviton KK mode and the coupling parameter $k/\bar{\mathrm{M}}_{\mathrm{Pl}}$. The expected RS signal is simulated for the $k/\bar{\mathrm{M}}_{\mathrm{Pl}}$ values 0.01, 0.05, 0.1, and 0.2. Basic selection criteria are applied to take the geometrical acceptance and the $p_{\mathrm{T}}$ detection threshold of the detector into account.

- two muons or electrons produced directly from the $G_1 \to ll$ decay

- muons: $p_{\mathrm{T}} > 45$ GeV, $|\eta| < 2.4$

- electrons: $p_{\mathrm{T}} > 35$ GeV, $|\eta| < 1.44$ or $1.56 < |\eta| < 2.5$

The resulting PYTHIA8 cross sections at $\sqrt{s} = 8$ TeV are shown in figure A.2. The signal cross sections decrease with rising values of $M_1$ and falling values of $k/\bar{\mathrm{M}}_{\mathrm{Pl}}$. As expected from the identical coupling of the graviton to the different SM lepton families, the predicted cross sections are very similar for the dimuon and dielectron case. Acceptance restrictions are taken into account for the evaluation of signal cross sections. By comparing the cross sections shown in figure A.2 with and without applying transverse momentum and $\eta$ cuts it can be seen that the resulting loss of signal events from these restrictions is $< 10\%$ for masses above 1 TeV. In this mass range acceptance differences between the RS-1 signal and contributions from the SM DY process and the considered $Z'$ models are found to be negligible. However, acceptance differences become increasingly relevant for lower masses. To give an example, the acceptance in the dimuon channel at a dimuon mass of 0.5 TeV evaluates to 0.93 for the SM DY process and to 0.77 for the RS-1 signal. The validity of assuming compatibility of the signal and SM DY efficiencies has been tested with signal simulations including the detector response. It is in the following assumed that differences in the efficiency of trigger and identification between the RS-1 signal and the considered $Z'$ models are negligible.

The selected statistical procedure for calculating limits with data at $\sqrt{s} = 7$ TeV and $\sqrt{s} = 8$ TeV requires an evaluation of the signal cross section ratios between the two center-of-mass energies. In figure A.3, these ratios are shown as a function of $M_1$ for several values of $k/\bar{\mathrm{M}}_{\mathrm{Pl}}$.
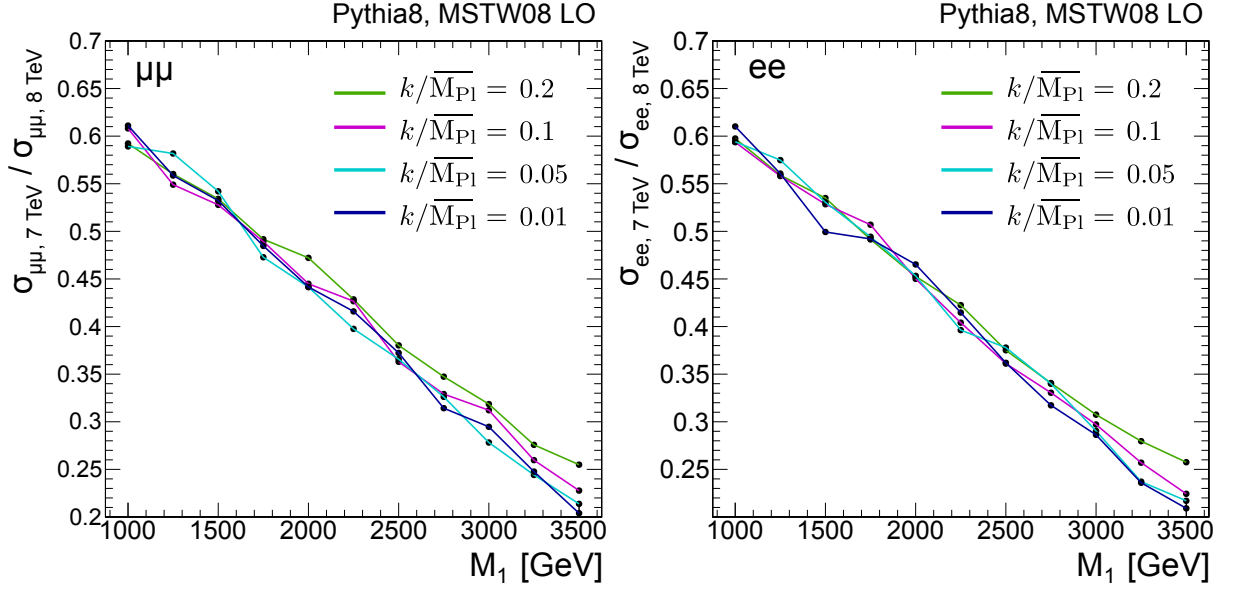
**Figure A.3** Cross section ratio between collisions at $\sqrt{s} = 7$ TeV and $\sqrt{s} = 8$ TeV for the processes $G \to \mu\mu$ (Left) and $G \to ee$ (Right) in the RS-1 model (LO).

It can be seen that in the considered parameter range the results depend only weakly on the choice of $k/\overline{M}_{Pl}$. For a given value of $k/\overline{M}_{Pl}$, the cross section ratio in the evaluated mass range of 1000 GeV $\leq M_1 \leq$ 3500 GeV is found to be approximately linear in $M_1$. As expected, the results do not vary significantly between the graviton decay to muon and electron pairs. Accordingly, it is reasonable to use the linear fit shown in figure A.4 as a common input for the limit calculation. The statistical evaluation assumes that the signal shape can be approximated
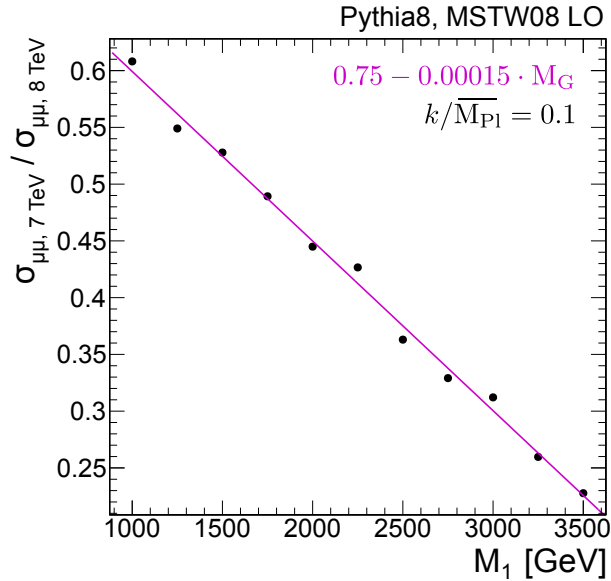


**Figure A.4** Linear fit to the cross section ratio between collisions at $\sqrt{s} = 7$ TeV and $\sqrt{s} = 8$ TeV for the process $G \to \mu\mu$ in the RS-1 model with $k/\overline{M}_{Pl} = 0.1$.
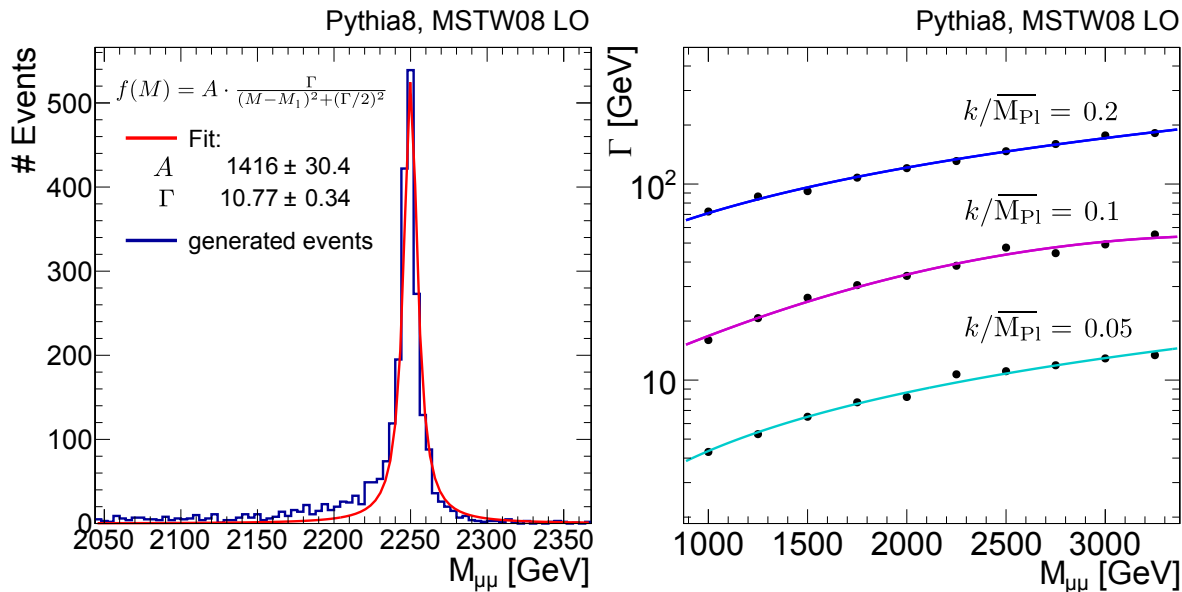
**Figure A.5** (Left) Mass distribution of the generated events and fitted Breit-Wigner shape for $M_1 = 2250$ GeV and $k/\bar{\mathrm{M}}_{\mathrm{Pl}} = 0.05$. (Right) FWHM $\Gamma$ as a function of the mass of the lowest KK dimuon resonance in the RS-1 model (LO) for different values of $k/\bar{\mathrm{M}}_{\mathrm{Pl}}$.

by a Breit-Wigner distribution which then is convoluted with a normal distribution to model the detector resolution. The Breit-Wigner distribution can be parametrized as

$$f_{\mathrm{BW}}(M) = A \cdot \frac{\Gamma}{(M - M_1)^2 + (\Gamma/2)^2} \quad , \tag{A.7}$$

with FWHM (full-width-half-maximum) $\Gamma$ and and normalization constant $A$. Figure A.5 (Left) shows the fit for the RS-1 parameters $M_1 = 2250$ GeV and $k/\bar{\mathrm{M}}_{\mathrm{Pl}} = 0.05$. It is found that the probability distribution close to the peak of the resonance is well approximated by the fit while the low mass tail is not described perfectly. This behavior is found to be qualitatively similar for other parameter combinations. In any case, deviations from the LO distribution are expected from higher order corrections like photon radiation or the QCD NLO corrections studied in [277]. Accordingly, a somewhat simplified description of the resonance shape is acceptable. Improving upon the BW-fit would probably complicate the analysis with the requirement of additional fit parameters and lead to a convolution with the normal distribution resulting in a shape that is likely to be less understood than the Voigt profile. Results for the FWHMs from the Breit-Wigner fits are summarized in figure A.5 (Right) for the graviton decay to two muons. The estimated shape parameters are found to be robust against reasonable variations in the fit range. The colored lines depict linear fits to the widths for given $k/\bar{\mathrm{M}}_{\mathrm{Pl}}$. These linear approximations are used for the derivations of statistical results. No significant differences are found between the evaluated dimuon and the dielectron widths.

The resulting limits on the cross section ratio $R_{\sigma,8\,\mathrm{TeV}}$ evaluated with an intermediate 2012 dataset at $\sqrt{s} = 8$ TeV are shown in figure A.6 (top). Figure A.6 (bottom) shows the limits obtained from a combination of data at $\sqrt{s} = 8$ TeV and the 2011 dataset at $\sqrt{s} = 7$ TeV. The calculations follow the statistical procedure described in section A.2. The results discussed above have been extended to masses between 0.3 TeV and 1.0 TeV to be able to also calculate limits in this mass range. The presented linear fits to the signal cross section ratio and the resonance
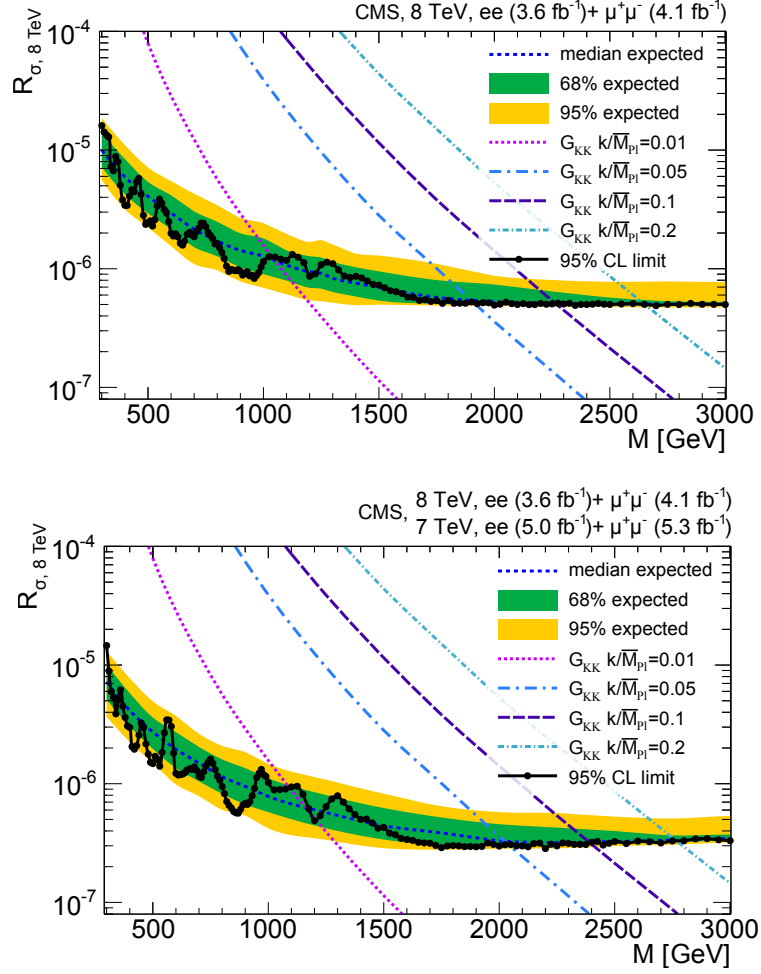
**Figure A.6** 95% credible interval upper limits on the RS KK resonance to SM $Z^0$ cross section ratio $R_{\sigma,8\,\text{TeV}}$ from measurements of dielectron and dimuon mass spectra at CMS [10].

widths are found to be also applicable down to masses of 0.3 TeV. Acceptance differences with respect to the SM DY process for RS-1 models below 1 TeV are applied as correction factors to the RS signal curves shown in figure A.6 to keep differences in the statistical treatment of the RS and $Z'$ models at a minimum.

Figure A.7 shows the observed limits and signal expectations for different values of $k/\bar{\text{M}}_{\text{Pl}}$. It can be seen that the observed limits converge for masses that are sufficiently higher than the range of observed events. On average, the excluded cross section upper limits increase with rising values of $k/\bar{\text{M}}_{\text{Pl}}$. This is expected as the signal becomes less resonant with increasing $k/\bar{\text{M}}_{\text{Pl}}$ and therefore more compatible with the background shape. The results indicate to which extend the limits depend on the assumed signal widths and can be used to assess the implications of the evaluated data for any models with widths corresponding to the range $0.01 < k/\bar{\text{M}}_{\text{Pl}} < 0.2$ in the RS-1 model. In table A.2, the mass limits on a graviton resonance in the RS-1 model (rounded down to the level of 0.1 TeV) derived from the limits on $R_{\sigma,8\,\text{TeV}}$ (previously published in [6]) shown in figure A.6 are compared with the RS-1 graviton mass limits from CMS and ATLAS evaluated with the full 2011 ($\sqrt{s} = 7$ TeV) datasets [103, 278].

|  | this study (CMS) | CMS [103] | ATLAS [278] |
|---|---|---|---|
| datasets | 2011 (full), 2012 (partial) | 2011 (full) | 2011 (full) |
| graviton decay modes | $\mu\mu$, $ee$ | $\mu\mu$, $ee$ | $\mu\mu$, $ee$ |
| $k/\bar{\mathrm{M}}_{\mathrm{Pl}} = 0.01$ | 1.0 | – | 0.9 |
| $k/\bar{\mathrm{M}}_{\mathrm{Pl}} = 0.05$ | 2.0 | 1.8 | 1.7 |
| $k/\bar{\mathrm{M}}_{\mathrm{Pl}} = 0.1$ | 2.2 | 2.1 | 2.1 |
| $k/\bar{\mathrm{M}}_{\mathrm{Pl}} = 0.2$ | 2.7 | – | – |

**Table A.2** 95% lower limits on $M_1$ (rounded down to the level of 0.1 TeV) from this study and results presented in [103, 278].

## A.6 Preliminary Results with the Full 2012 Dataset

Recently, CMS has presented results that extend the CMS search for heavy dilepton resonances to the full 2012 dataset [7]. Corresponding limits have been calculated as part of the presented work, using an updated version of the software setup for limit setting described in section A.3. The limits for the full 2012 dataset have been obtained with a procedure which does not include all events above masses of 200 GeV in the likelihood. A mass interval of at least $\pm 6$ times the standard deviation of a normal fit to the detector resolution evaluated at the signal mass hypothesis defines the window of events being included in the likelihood. One of the reasons for this choice was to ensure that the available computing capacities were still sufficient for calculating the results within an acceptable amount of time. The updated procedure passed several checks that tested its robustness against reasonable variations in the choice of the signal window and the background normalization. In the dielectron final state, the events have been split into two subcategories that are treated as separate search channels. In one category of dielectron events both electron candidates are measured in the ECAL barrel. The other channel
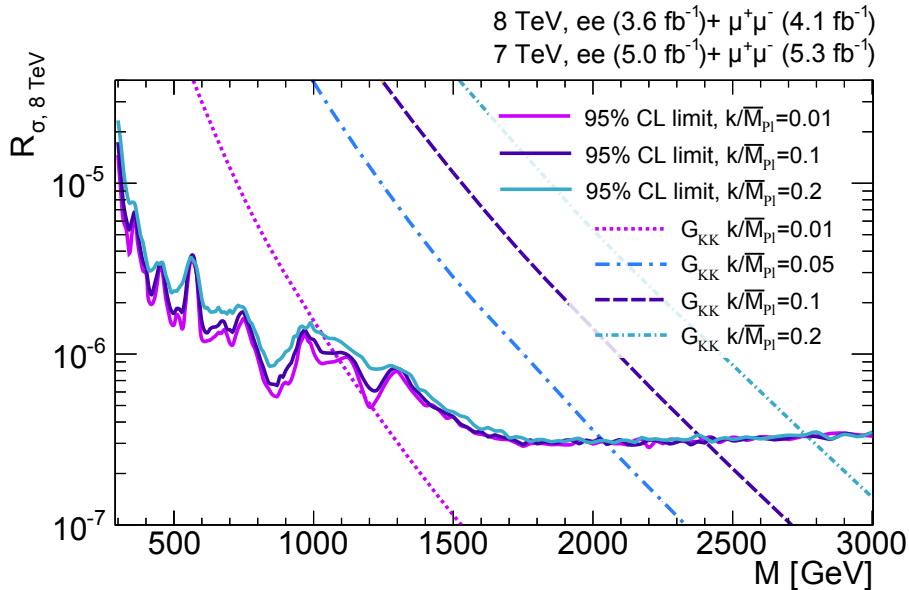


**Figure A.7** 95% credible interval upper limits on the cross section ratio $R_{\sigma,8\,\mathrm{TeV}}$ and theory predictions for different values of $k/\bar{\mathrm{M}}_{\mathrm{Pl}}$.
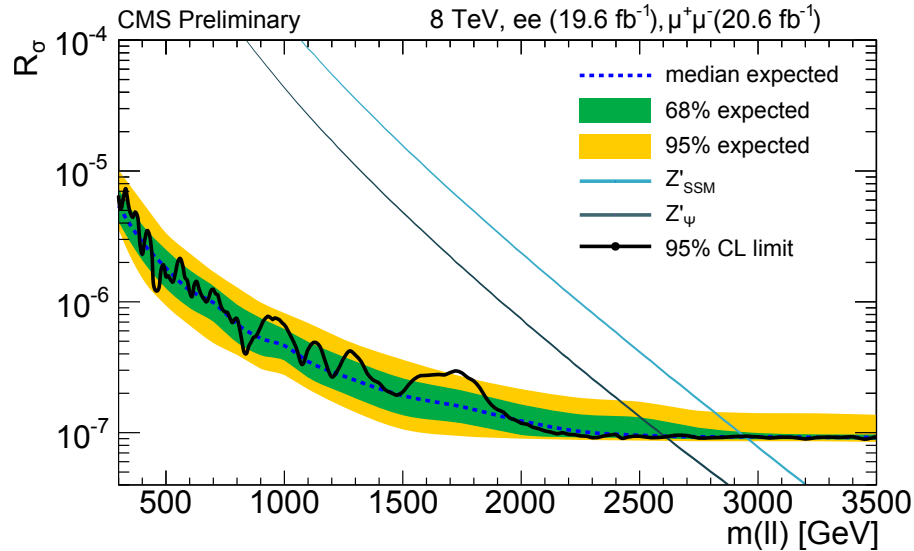
**Figure A.8** 95% credible interval upper limits on the $Z'$ to the SM $Z^0$ cross section ratio $R$ from measurements of dielectron and dimuon mass spectra at CMS evaluated with the full 2012 dataset [7].

includes events in which only one of the electron is measured in the ECAL barrel and the other in the ECAL endcap region. This splitting of the dielectron data allows for an improved treatment of systematic uncertainties which are higher for events with one electron measured in the endcap region. The combined limits obtained with the full 2012 dataset are shown in figure A.8. Corresponding single channel limits can be found in [7].

## A.7 Conclusion

The statistical analysis of the dimuon and dielectron mass spectra has been updated with an intermediate 2012 dataset. A previously used limit setting code has been partially redesigned and extended for use cases with more than two channels. These changes allow to set combined limits including data at both $\sqrt{s} = 7$ TeV and $\sqrt{s} = 8$ TeV. At the time of publication (December 2012), the presented statistical results provided the most stringent limits on the considered classes of BSM signatures. The considered signals include dilepton resonances in the $Z'_\psi$ and $Z'_{SSM}$ models, for which limits of $m(Z'_\psi) < 2.2$ TeV and $m(Z'_{SSM}) < 2.5$ TeV are obtained at 95% CL. Also dilepton signatures of KK graviton modes in the RS-1 model are evaluated for several choices of $k/\bar{M}_{Pl}$. With $k/\bar{M}_{Pl} = 0.05$, parameter values of $M_1 < 2.0$ are found to be excluded at 95% CL. The limits for the $Z'_\psi$ and $Z'_{SSM}$ models have been been further improved with a study based on the full 2012 dataset. This latest analysis excludes model hypotheses with $m(Z'_\psi) < 2.6$ TeV and $m(Z'_{SSM}) < 2.9$ TeV at 95% CL.

# B The BATCalculator Interface[1] between RooStats and BAT

Bayesian inference often involves multidimensional integration. In section 4.4.1, it has been outlined why in many statistical models Markov Chain methods are an important tool for the evaluation of posterior distributions. As the respective algorithms are quite complex, it is beneficial to cross-check results with different software implementations. In this way one reduces the possibility of overlooking convergence problems or errors in the respective implementations of the algorithms. For computing intensive use-cases it can also be useful to compare the computational performance of the different tools. The RooStats [258] software package provides Markov Chain integration with the Metropolis Hastings algorithm. This functionality is usually accessed via the MCMCCalculator class. The statistical models are defined using RooStats and RooFit [257]. An implementation of the Metropolis Hastings algorithm is also included in the Bayesian Analysis Toolkit (BAT) package [279]. The purpose of the BATCalculator class is to provide an interface that allows to use the Markov Chain integration in BAT with statistical models implemented in RooFit/RooStats and that can be used in a way which is similar to other classes for the calculation of confidence or credible intervals provided by RooStats. Internally, the BATCalculator class uses BAT for evaluating the posterior distribution. Starting from version 0.4, the interface is included in the BAT release.

## B.1 Basic Usage

The recommended way to construct a BATCalculator object is to use the constructor that requires an object of the RooStats ModelConfig class as an argument. The respective constructor is

```
BATCalculator( RooAbsData & data, ModelConfig & model, bool fillChain
    = false );
```

The ModelConfig class helps the user to associate the objects in a given workspace with their statistical meaning. A RooFit RooAbsData object stores the dataset of a measurement (or alternatively hypothetical measurement). The fillChain argument controls whether a RooStats MarkovChain object is constructed from the Markov chain that is evaluated in BAT. After adjusting the length of the Markov chain and the requested posterior probability of the interval, the Markov chain algorithm is run by calling one of the interval functions. The BATCalculator supports both *central* and *shortest* intervals for models with one parameter of interest. Interval objects and limits are returned by the functions

```
simpleInterval* myCentralInterval = myBATCalculator->GetInterval1D()
    const;
upperLimit = myCentralInterval->UpperLimit();
lowerLimit = myCentralInterval->LowerLimit();
```

---

[1]developed in collaboration with Grégory Schott

```
simpleInterval* myShortestInterval = myBATCalculator−>
    GetShortestInterval1D() const;
upperLimit = myShortestInterval−>UpperLimit();
lowerLimit = myShortestInterval−>LowerLimit();
```

In the current version, the only way to evaluate 2-dimensional credible regions is to construct them from the RooStats MarkovChain object.

```
virtual MCMCInterval* GetInterval() const;
```

This requires the option *fillChain = true* in the constructor. However, tests of this functionality have so far been very limited. Additional features of the BATCalculator class include visualization of 1-dimensional posterior distributions and accessibility of the interfaces from the underlying BAT classes.

## B.2 Test Scenarios

### B.2.1 Single Bin Counting Experiment

Single bin counting experiments are a frequently encountered statistical model in searches for new physics in collider experiments. One starts from a set of event selection criteria that are supposed to improve the relation between signal and background. Often this involves increasing the ratio of signal and background expectation. Afterwards, one draws statistical conclusions from the relation between the measured number of events and the expected signal and remaining background. If one searches for a rare type of events, the likelihood of observing $N$ events is given by the Poisson distribution. Here we consider an example with three nuisance parameters corresponding to the luminosity $L$, signal efficiency $\epsilon$ and background expectation $b$. The parameter of interest (poi) is given by the signal cross section $\sigma$. The posterior distribution $\Pi_{\text{post}}$ for an observation of $N_{\text{obs}}$ events is modeled as

$$\Pi_{\text{post}}(\sigma|N_{\text{obs}}) = \int dL \, d\epsilon \, db \, \frac{(\sigma \cdot L \cdot \epsilon + b)^{N_{\text{obs}}}}{N_{\text{obs}}!} \cdot e^{-(\sigma \cdot L \cdot \epsilon + b)} \cdot \pi(b) \cdot \pi(L) \cdot \pi(\epsilon) \cdot \pi_{\text{poi}}(\sigma) \quad \text{(B.1)}$$

For the test scenario, truncated normal prior functions $\pi$ are assumed for the nuisance parameters. A uniform distribution is used as prior function $\pi_{poi}$ of the parameter of interest. Credible intervals for a range of input parameters have been evaluated with the BATCalculator interface and validated against integration with RooStats internal tools and external code. Figure B.1 illustrates the good agreement between results from different tools for a set of test parameters (units are left unspecified):

- $\pi(L) = \text{Normal}(L; L_0, \sigma_L)$, with $L_0 = 10$ and $\sigma_L = 1$

- $\pi(b) = \text{Normal}(b; b_0, \sigma_b)$, with $b_0 = 0.52$ and $\sigma_b = 0.156$

- $\pi(\epsilon) = \text{Normal}(\epsilon; \epsilon_0, \sigma_\epsilon)$, with $\epsilon_0 = 0.51$ and $\epsilon_L = 0.0765$

### B.2.2 Shape Analysis with Unbinned Likelihood

The statistical model used in the search for new heavy dilepton resonances [6] is outlined in section A.2. This model can be used to test the BATCalculator interface in a more complex situation. Figure B.2 shows a comparison of the respective results for the observed limits calculated with the RooStats internal MCMCCalculator and the BATCalculator interface. The results from the two classes are found to be in good agreement.
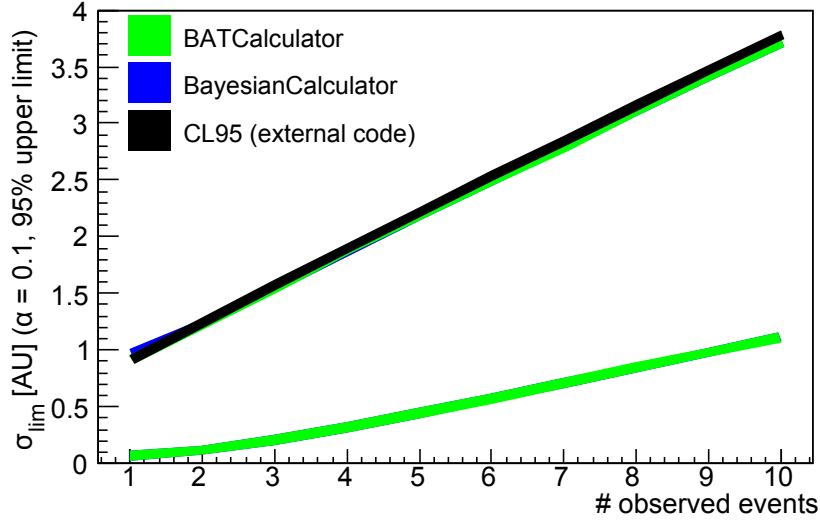
**Figure B.1** Comparison of 90% central credible intervals as a function of the number of observed events for a benchmark counting experiment as defined in equation B.1. The shown upper cross section thresholds correspond to 95% upper limits. Results are evaluated with the BATCALCULATOR interface, the ROOSTATS internal BAYESIANCALCULATOR class, and the CL95 tool (the pre-LHC version written by Greg Landsberg).
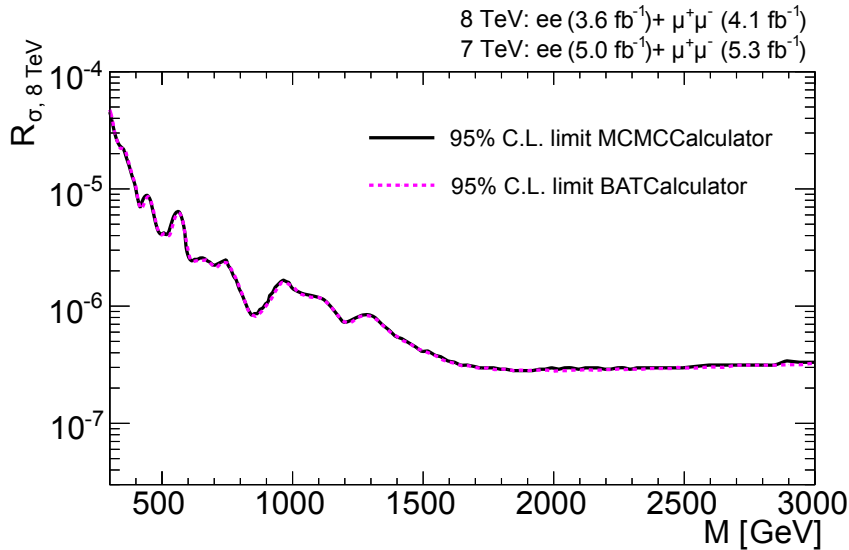


**Figure B.2** Comparison of 95% CL upper limits from preliminary results of a search for new heavy dilepton resonances [6] calculated with the ROOSTATS internal MCMCCALCULATOR and the BATCALCULATOR interface.

# C Implementation of the Lognormal- and Gamma-Distributions in the RooFit software[1]

The RooFit software for statistical modeling in physics analyses [257] includes generic ways to create probability distributions. However, it is advantageous to have some frequently employed distributions available as pre-built classes. This way, users can resort to these well-tested standard classes and benefit from the implementation of formulas for analytic integration and algorithms for efficient generation of random variables without the need to design them by themselves. At the same time the pre-built distributions provide convenient building blocks for creating more complex models.

The density function of the Gamma distribution can be parametrized as

$$f(x; \gamma, \beta, \mu) = \frac{(x - \mu)^{\gamma - 1} \cdot e^{-(x-\mu)/\beta}}{\Gamma(\gamma) \cdot \beta^{\gamma}} \quad . \tag{C.1}$$

The Gamma distribution has support $[\mu, \infty)$ and the parameters $\gamma$, $\beta$, and $\mu$ are restricted to combinations with $\gamma > 0$ and $\beta > 0$.

The implemented method for generating Gamma-distributed random variables is derived from a code example presented in [280]. Interesting properties of the Gamma distribution in the context of the statistical analysis of data from collider experiments include that the Gamma distribution is the conjugate prior to the Poisson likelihood. Taking $\mu = 0$, $\gamma = 0$ and $\beta \to \infty$ this implies that a Poisson likelihood with parameter $\lambda$ and an assumed uniform prior for $\lambda$ in the interval $(0, a)$ leads to a (truncated) Gamma-distributed posterior.

A possible way of parametrizing the density function of the lognormal distribution is given by

$$f(x) = \frac{1}{\sqrt{2\pi} \cdot \ln k} \cdot \frac{1}{b} \exp\left[ -\frac{\ln^2 (b/b_0)}{2 \ln^2 k} \right] \quad , \tag{C.2}$$

with domain $x \geq 0$ and $k, b_0 > 0$. An important property of the lognormal distribution is that products of independent random variables tend towards a lognormal density distribution in the same way as sums of independent variables approach a normal distribution. A precise mathematical formulation of this property is given in [281, page 13 et seq.]. An interval $[b_0 * k^c, b_0/k^c]$, $c > 0$ of the lognormal density contains a fixed probability corresponding to an interval $[-c, c]$ of a normal variable $N(0, 1)$. In analyses of collision data, this property can be appealing for modeling reasonable prior distributions for the means of backgrounds with large uncertainties.

Figure C.1 shows examples of the lognormal and Gamma distributions evaluated with their implementation in RooFit. The corresponding class names are *RooLognormal* and *RooGamma*. As they inherit from the base class for probability functions in RooFit (*RooAbsPdf*), the classes can be used analogously to classes like *RooGaussian*, for which code examples can be found in [257].

---

[1]in collaboration with Grégory Schott
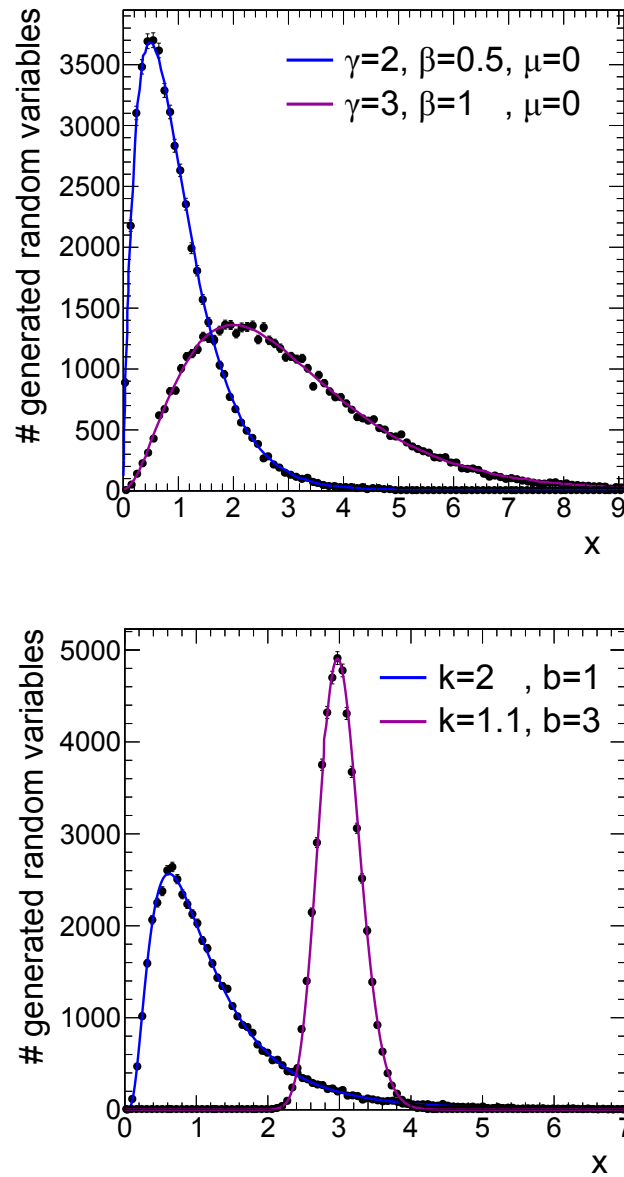
**Figure C.1** Distributions of $N = 5 \cdot 10^4$ generated variables compared with the probability densities normalized to $N$ for two examples of Gamma (Top) and lognormal (Bottom) distributions.

# D Supplementary Material

## D.1 Differential Cross Section of the SM Neutral Current DY Process at LO

Starting from the amplitudes as given in [34], the differential cross section of the SM DY process is given by equation 2.8, with

$$|D_z(s)|^2 = \left|\frac{1}{s - m_z^2 + im_z\Gamma_z}\right|^2 = \frac{1}{\left[(s - m_z^2)^2 + (m_z\Gamma_z)^2\right]^2} \qquad c_1 = 128 \cdot Q_q^2$$

$$c_2 = \frac{1}{16 \cdot \sin^4\theta_W \cos^4\theta_W}\left(L_l^2 \cdot R_q^2 + R_l^2 \cdot L_q^2\right) \qquad c_3 = -\frac{2 \cdot Q_q}{\sin^2\theta_W \cos^2\theta_W}\left(L_l \cdot R_q + R_l \cdot L_q\right)$$

$$c_4 = \frac{1}{16 \cdot \sin^4\theta_W \cos^4\theta_W}\left(L_l^2 \cdot L_q^2 + R_l^2 \cdot R_q^2\right) \qquad c_4 = -\frac{2 \cdot Q_q}{\sin^2\theta_W \cos^2\theta_W}\left(L_l \cdot L_q + R_l \cdot R_q\right)$$

$$R_l = 4 \cdot \sin^2\theta_W \qquad\qquad L_q = 4 \cdot \left(T_{3q} - Q_q \cdot \sin^2\theta_W\right)$$
$$L_l = 4 \cdot \sin^2\theta_W - 2 \qquad\qquad R_q = -4 \cdot Q_q \cdot \sin^2\theta_W \quad .$$

$Q_q$ is the electric charge of the initial quark (in units of the electron charge $e$), $\theta_W$ the weak mixing (Weinberg) angle, and $T_{3q}$ the third component of the quark's weak isospin.

## D.2 Type-I Error Rate of Classical $p$-Values

Consider a $p$-value $p$ defined with respect to the test statistic $t$. If one assumes that we have introduced an ordering relation $>$ on the test statistic $t$, so that

$$t_2 > t_1 \quad \Leftrightarrow \quad p(t_2) < p(t_1)$$

and define $t_{\lim}$ as $t_{\lim} := \min\{t : p(t) \leq \alpha\}$, then

$$
\begin{aligned}
Pr(p < \alpha) &= Pr(Pr(t > t'|H_0) < \alpha) &= Pr(Pr(t > t'|H_0) < Pr(t > t_{\lim}|H_0)) \\
&= \textstyle\sum_{\{t':t'>t_{\lim}\}} Pr(t'|H_0) &= Pr(t' > t_{\lim}|H_0) \\
&= p(t_{\lim}) &\leq \alpha \quad .
\end{aligned}
$$

# D.3 Figures and Tables

| mass range | # events | cross section [pb] |
|---|---|---|
| Horace LO (CT10 PDFs) → Photos → Herwig6 | | |
| $0.2 - 0.5$ TeV | 1e5 | $9.57 \cdot 10^{-1}$ |
| $0.5 - 0.8$ TeV | 1e5 | $2.46 \cdot 10^{-2}$ |
| $0.8 - 1.2$ TeV | 1e5 | $2.81 \cdot 10^{-3}$ |
| $1.2 - 1.6$ TeV | 1e5 | $2.78 \cdot 10^{-4}$ |
| $1.6 - \sqrt{s}$ TeV | 1e5 | $4.61 \cdot 10^{-5}$ |
| Horace LO with photon radiation (CT10 PDFs) → Herwig6 | | |
| $0.2 - 0.5$ TeV | 1e5 | $9.11 \cdot 10^{-1}$ |
| $0.5 - 0.8$ TeV | 1e5 | $2.30 \cdot 10^{-2}$ |
| $0.8 - 1.2$ TeV | 1e5 | $2.59 \cdot 10^{-3}$ |
| $1.2 - 1.6$ TeV | 1e5 | $2.52 \cdot 10^{-4}$ |
| $1.6 - \sqrt{s}$ TeV | 1e5 | $4.11 \cdot 10^{-5}$ |
| Horace NLO (CT10 PDFs) → Herwig6 | | |
| $0.2 - 0.5$ TeV | 1e5 | $8.77 \cdot 10^{-1}$ |
| $0.5 - 0.8$ TeV | 1e5 | $2.13 \cdot 10^{-2}$ |
| $0.8 - 1.2$ TeV | 1e5 | $2.31 \cdot 10^{-3}$ |
| $1.2 - 1.6$ TeV | 1e5 | $2.17 \cdot 10^{-4}$ |
| $1.6 - \sqrt{s}$ TeV | 1e5 | $3.40 \cdot 10^{-5}$ |
| Horace NLO (MRST04QED PDFs) → Herwig6 | | |
| $0.2 - 0.5$ TeV | 1e5 | $9.49 \cdot 10^{-1}$ |
| $0.5 - 0.8$ TeV | 1e5 | $2.41 \cdot 10^{-2}$ |
| $0.8 - 1.2$ TeV | 1e5 | $2.69 \cdot 10^{-3}$ |
| $1.2 - 1.6$ TeV | 1e5 | $2.62 \cdot 10^{-4}$ |
| $1.6 - \sqrt{s}$ TeV | 1e5 | $4.46 \cdot 10^{-5}$ |

**Table D.1** Horace Drell-Yan samples.

| mass range | | # events |
|---|---|---|
| | path in dbs | |
| 40 − 120 GeV | | 1e5 |
| /DYToMuMu_Minv_40_120_mcatnlo_photos_ForSummer11_cff_py_GEN/ | | |
| antonius-DYToMuMu_Minv_40_120_mcatnlo_photos_ForSummer11_cff_py_AOD-a05cf0eb7984cf13d5f09bb99ec2fa47/USER | | |
| 120 − 200 GeV | | 1e5 |
| /DYToMuMu_Minv_120_200_mcatnlo_photos_ForSummer11_cff_py_GEN/ | | |
| antonius-DYToMuMu_Minv_120_200_mcatnlo_photos_ForSummer11_cff_py_AOD-a05cf0eb7984cf13d5f09bb99ec2fa47/USER | | |
| 200 − 500 GeV | | 1e5 |
| /DYToMuMu_Minv_200_500_mcatnlo_photos_ForSummer11_cff_py_GEN/ | | |
| antonius-DYToMuMu_Minv_200_500_mcatnlo_photos_ForSummer11_cff_py_AOF-a05cf0eb7984cf13d5f09bb99ec2fa47/USER | | |
| 500 − 800 GeV | | 1e5 |
| /DYToMuMu_Minv_500_800_mcatnlo_photos_ForSummer11_cff_py_GEN/ | | |
| antonius-DYToMuMu_Minv_500_800_mcatnlo_photos_ForSummer11_cff_py_AOD-a05cf0eb7984cf13d5f09bb99ec2fa47/USER | | |
| 800 − 1200 GeV | | 1e5 |
| /DYToMuMu_Minv_800_1200_mcatnlo_photos_ForSummer11_cff_py_GEN/ | | |
| antonius-DYToMuMu_Minv_800_1200_mcatnlo_photos_ForSummer11_cff_py_AOD-a05cf0eb7984cf13d5f09bb99ec2fa47/USER | | |
| 1200 − 1600 GeV | | 1e5 |
| /DYToMuMu_Minv_1200_1600_mcatnlo_photos_ForSummer11_cff_py_GEN/ | | |
| antonius-DYToMuMu_Minv_1200_1600_mcatnlo_photos_ForSummer11_cff_py_AOD-a05cf0eb7984cf13d5f09bb99ec2fa47/USER | | |
| 1600 − inf GeV | | 1e5 |
| /DYToMuMu_Minv_1600_inf_mcatnlo_photos_ForSummer11_cff_py_GEN/ | | |
| antonius-DYToMuMu_Minv_1600_inf_mcatnlo_photos_ForSummer11_cff_py_AOD-a05cf0eb7984cf13d5f09bb99ec2fa47/USER | | |

**Table D.2** MC@NLO Drell-Yan samples.

| Sample | cross section (pb) | # events |
|---|---|---|
| | path in *das* | |
| DY dimuon, $M_{\mu\mu} > 20$ GeV | 1 629 | 29.6e6 |
| /DYToMuMu_M-20_CT10_TuneZ2_7TeV-powheg-pythia/Fall11-PU_S6_START44_V9B-v1/AODSIM | | |
| DY dimuon, $M_{\mu\mu} > 200$ GeV | 1.23 | 48.8e3 |
| /DYToMuMu_M-200_TuneZ2_7TeV-powheg-pythia/Fall11-PU_S6_START44_V9B-v1/AODSIM | | |
| DY dimuon, $M_{\mu\mu} > 500$ GeV | 0.0332 | 47.9e3 |
| /DYToMuMu_M-500_TuneZ2_7TeV-powheg-pythia/Fall11-PU_S6_START44_V9B-v1/AODSIM | | |
| DY dimuon, $M_{\mu\mu} > 800$ GeV | 0.00378 | 46.1e3 |
| /DYToMuMu_M-800_TuneZ2_7TeV-powheg-pythia/Fall11-PU_S6_START44_V9B-v1/AODSIM | | |
| DY dimuon, $M_{\mu\mu} > 1000$ GeV | 0.00116 | 46.5e3 |
| /DYToMuMu_M-1000_TuneZ2_7TeV-powheg-pythia/Fall11-PU_S6_START44_V9B-v1/AODSIM | | |

**Table D.3** Powheg Drell-Yan samples (dimuon final state).

| PDF set | mass ranges [GeV] | # events per mass bin |
|---|---|---|
| cteq66.LHgrid central PDF central PDF | $40 - 120$, $120 - 200$, $200 - 500$, , $500 - 800$, $800 - 1200$, $1200 - 1600$, $1600-$inf | $10^5$ |
| NNPDF21_100.LHgrid average PDF | $40 - 120$, $120 - 200$, $200 - 500$, $500 - 800$, $800 - 1200$, $1200 - 1600$, $1600-$inf | $10^5$ |
| MSTW2008nlo90cl.LHgrid central PDF | $40 - 120$, $120 - 200$, $200 - 500$, $500 - 800$, $800 - 1200$, $1200 - 1600$, $1600-$inf | $10^5$ |
| MSTW2008nlo90cl_asmz+90cl.LHgrid central PDF | $40 - 120$, $120 - 200$, $200 - 500$, $500 - 800$, $800 - 1200$, $1200 - 1600$, $1600-$inf | $10^5$ |
| MSTW2008nlo90cl_asmz$-$90cl.LHgrid central PDF | $40 - 120$, $120 - 200$, $200 - 500$, $500 - 800$, $800 - 1200$, $1200 - 1600$, $1600-$inf | $10^5$ |

**Table D.4** MC@NLO (+ Herwig6 shower) generator level events for the study of PDF uncertainties.

| Sample | cross section (pb) | # events |
|---|---|---|
| | path in *das* | |
| $t\bar{t}$+Jets | 160 | 82.7e6 |
| /TTJets_TuneZ2_7TeV-madgraph-tauola/Fall11-PU_S6_START44_V9B-v1/AODSIM | | |
| $WW$ | 43.0 | 4.2e6 |
| /WW_TuneZ2_7TeV_pythia6_tauola/Fall11-PU_S6_START44_V9B-v1/AODSIM | | |
| $WZ$ | 18.2 | 4.3e6 |
| /WZ_TuneZ2_7TeV_pythia6_tauola/Fall11-PU_S6_START44_V9B-v1/AODSIM | | |
| $ZZ$ | 5.9 | 4.2e6 |
| /ZZ_TuneZ2_7TeV_pythia6_tauola/Fall11-PU_S6_START44_V9B-v1/AODSIM | | |
| $W$+Jets ($p_{\mathrm{T}} > 100$ GeV) | 239.6 | 8.1e6 |
| /WJetsToLNu_PtW-100_TuneZ2_7TeV-madgraph/Fall11-PU_S6_START42_V14B-v1/AODSIM | | |

**Table D.5** Samples for the evaluation of $W$ + jets, $t\bar{t}$ and diboson backgrounds in the dimuon mass spectrum.

| Parameters | cross section (pb) | # events |
|---|---|---|
| path in dbs | | |
| $\Lambda_T = 800\,\text{GeV}$, $s_{min} = 300\,\text{GeV}$ | 166.6 | 0.8e5 |
| /pythia8_ADD_Dilepton_LambdaT_800_cff_py_GEN/ | | |
| antonius-pythia8_ADD_Dilepton_LambdaT_800_cff_py_RECO-075b2ab990267830cab00471fbd36a19/USER | | |
| $\Lambda_T = 1000\,\text{GeV}$, $s_{min} = 300\,\text{GeV}$ | 28.5 | 0.8e5 |
| /pythia8_ADD_Dilepton_LambdaT_1000_cff_py_GEN_v2/ | | |
| antonius-pythia8_ADD_Dilepton_LambdaT_1000_cff_py_RECO-075b2ab990267830cab00471fbd36a19/USER | | |
| $\Lambda_T = 1200\,\text{GeV}$, $s_{min} = 300\,\text{GeV}$ | 7.2 | 0.8e5 |
| /pythia8_ADD_Dilepton_LambdaT_1200_cff_py_GEN_v2/ | | |
| antonius-pythia8_ADD_Dilepton_LambdaT_1200_cff_py_RECO-075b2ab990267830cab00471fbd36a19/USER | | |
| $\Lambda_T = 1400\,\text{GeV}$, $s_{min} = 300\,\text{GeV}$ | 2.5 | 0.8e5 |
| /pythia8_ADD_Dilepton_LambdaT_1400_cff_py_GEN/ | | |
| antonius-pythia8_ADD_Dilepton_LambdaT_1400_cff_py_RECO-f54f1ed6928c22b8f0e6f9b65bfc4d70/USER | | |
| $\Lambda_T = 1500\,\text{GeV}$, $s_{min} = 300\,\text{GeV}$ | 1.7 | 1.0e5 |
| /pythia8_ADD_Dilepton_LambdaT_1500_cff_py_GEN/ | | |
| antonius-pythia8_ADD_Dilepton_LambdaT_1500_cff_py_RECO-075b2ab990267830cab00471fbd36a19/USER | | |
| $\Lambda_T = 1600\,\text{GeV}$, $s_{min} = 300\,\text{GeV}$ | 1.3 | 0.8e5 |
| /pythia8_ADD_Dilepton_LambdaT_1600_cff_py_GEN/ | | |
| antonius-pythia8_ADD_Dilepton_LambdaT_1600_cff_py_RECO-f54f1ed6928c22b8f0e6f9b65bfc4d70/USER | | |
| $\Lambda_T = 1640\,\text{GeV}$, $s_{min} = 300\,\text{GeV}$ | 1.15 | 1.0e5 |
| /pythia8_ADD_Dilepton_LambdaT_1640_cff_py_GEN/ | | |
| antonius-pythia8_ADD_Dilepton_LambdaT_1640_cff_py_RECO-075b2ab990267830cab00471fbd36a19/USER | | |
| $\Lambda_T = 1660\,\text{GeV}$, $s_{min} = 300\,\text{GeV}$ | 1.12 | 1.0e5 |
| /pythia8_ADD_Dilepton_LambdaT_1660_cff_py_GEN/ | | |
| antonius-pythia8_ADD_Dilepton_LambdaT_1660_cff_py_RECO-075b2ab990267830cab00471fbd36a19/USER | | |
| $\Lambda_T = 1680\,\text{GeV}$, $s_{min} = 300\,\text{GeV}$ | 1.08 | 1.0e5 |
| /pythia8_ADD_Dilepton_LambdaT_1680_cff_py_GEN/ | | |
| antonius-pythia8_ADD_Dilepton_LambdaT_1680_cff_py_RECO-075b2ab990267830cab00471fbd36a19/USER | | |
| $\Lambda_T = 1700\,\text{GeV}$, $s_{min} = 300\,\text{GeV}$ | 1.04 | 1.0e5 |
| /pythia8_ADD_Dilepton_LambdaT_1700_cff_py_GEN/ | | |
| antonius-pythia8_ADD_Dilepton_LambdaT_1700_cff_py_RECO-075b2ab990267830cab00471fbd36a19/USER | | |
| $\Lambda_T = 1720\,\text{GeV}$, $s_{min} = 300\,\text{GeV}$ | 1.00 | 1.0e5 |
| /pythia8_ADD_Dilepton_LambdaT_1720_cff_py_GEN/ | | |
| antonius-pythia8_ADD_Dilepton_LambdaT_1720_cff_py_RECO-075b2ab990267830cab00471fbd36a19/USER | | |
| $\Lambda_T = 1740\,\text{GeV}$, $s_{min} = 300\,\text{GeV}$ | 0.97 | 1.0e5 |
| /pythia8_ADD_Dilepton_LambdaT_1740_cff_py_GEN/ | | |
| antonius-pythia8_ADD_Dilepton_LambdaT_1740_cff_py_RECO-075b2ab990267830cab00471fbd36a19/USER | | |
| $\Lambda_T = 1760\,\text{GeV}$, $s_{min} = 300\,\text{GeV}$ | 0.94 | 1.0e5 |
| /pythia8_ADD_Dilepton_LambdaT_1760_cff_py_GEN/ | | |
| antonius-pythia8_ADD_Dilepton_LambdaT_1760_cff_py_RECO-075b2ab990267830cab00471fbd36a19/USER | | |
| $\Lambda_T = 1780\,\text{GeV}$, $s_{min} = 300\,\text{GeV}$ | 0.92 | 1.0e5 |
| /pythia8_ADD_Dilepton_LambdaT_1780_cff_py_GEN/ | | |
| antonius-pythia8_ADD_Dilepton_LambdaT_1780_cff_py_RECO-075b2ab990267830cab00471fbd36a19/USER | | |
| $\Lambda_T = 1800\,\text{GeV}$, $s_{min} = 300\,\text{GeV}$ | 0.89 | 1.0e5 |
| /pythia8_ADD_Dilepton_LambdaT_1800_cff_py_GEN_v2/ | | |
| antonius-pythia8_ADD_Dilepton_LambdaT_1800_cff_py_RECO-075b2ab990267830cab00471fbd36a19/USER | | |

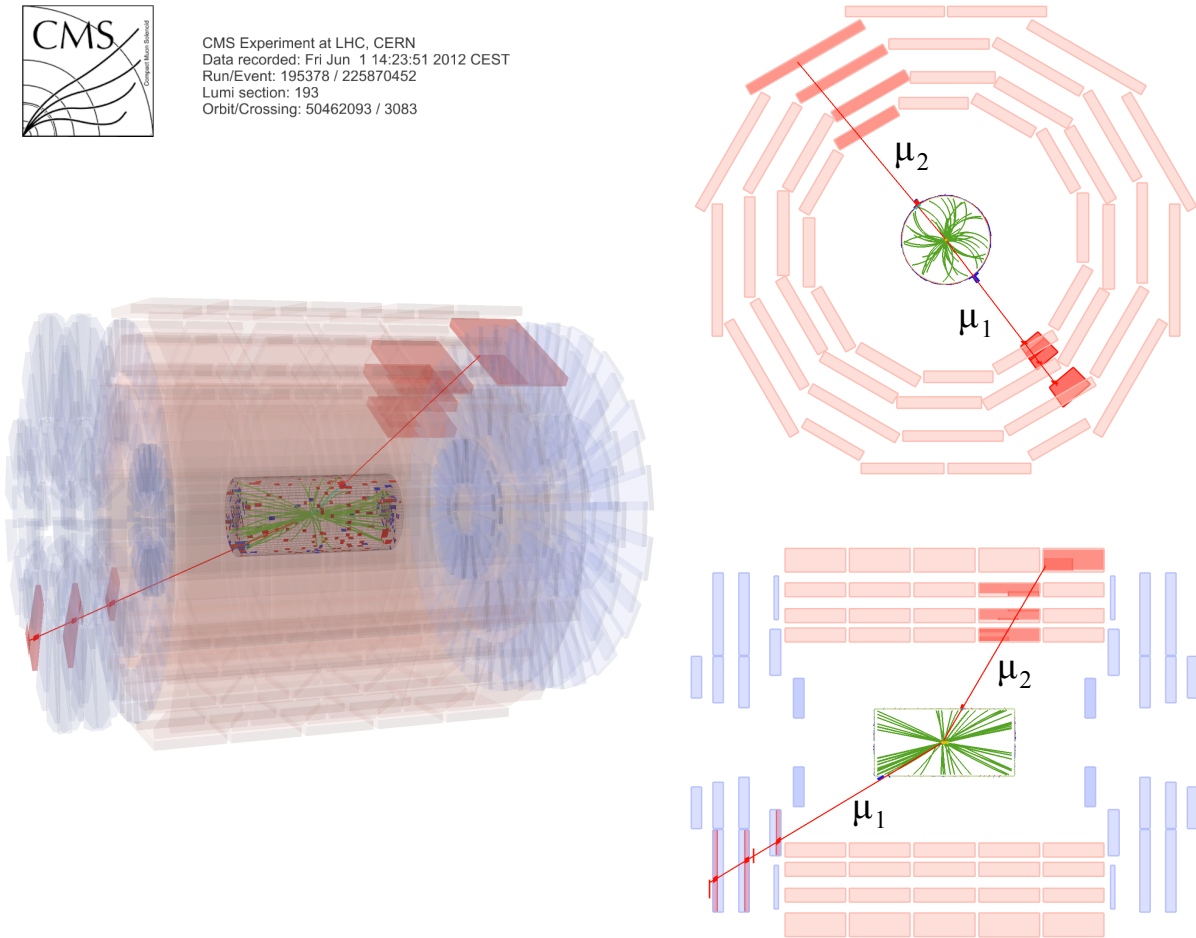**Table D.6** Pythia8 signal samples.
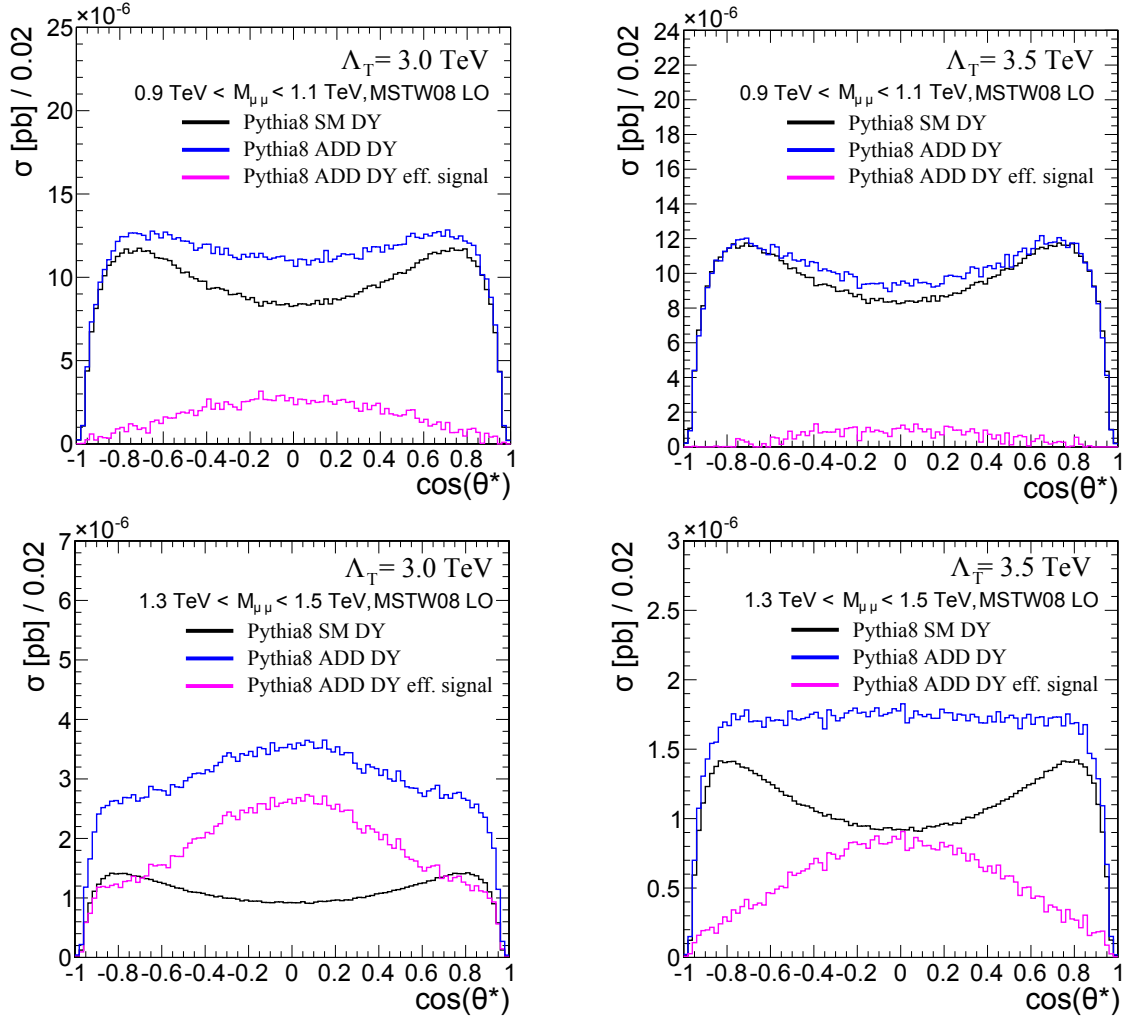
**Figure D.1** Comparison between the $\cos\theta^*$ distributions ($|\eta_\mu| < 2.1$ and $p_{\mathrm{T},\mu} > 45$ GeV) of the SM LO DY process and an ADD signal in the mass intervals 0.9 TeV $< M_{\mu\mu} >$ 1.1 TeV and 1.3 TeV $< M_{\mu\mu} >$ 1.5 TeV for $\Lambda_T = 3.0$ TeV (Left) and $\Lambda_T = 3.5$ TeV (Right).
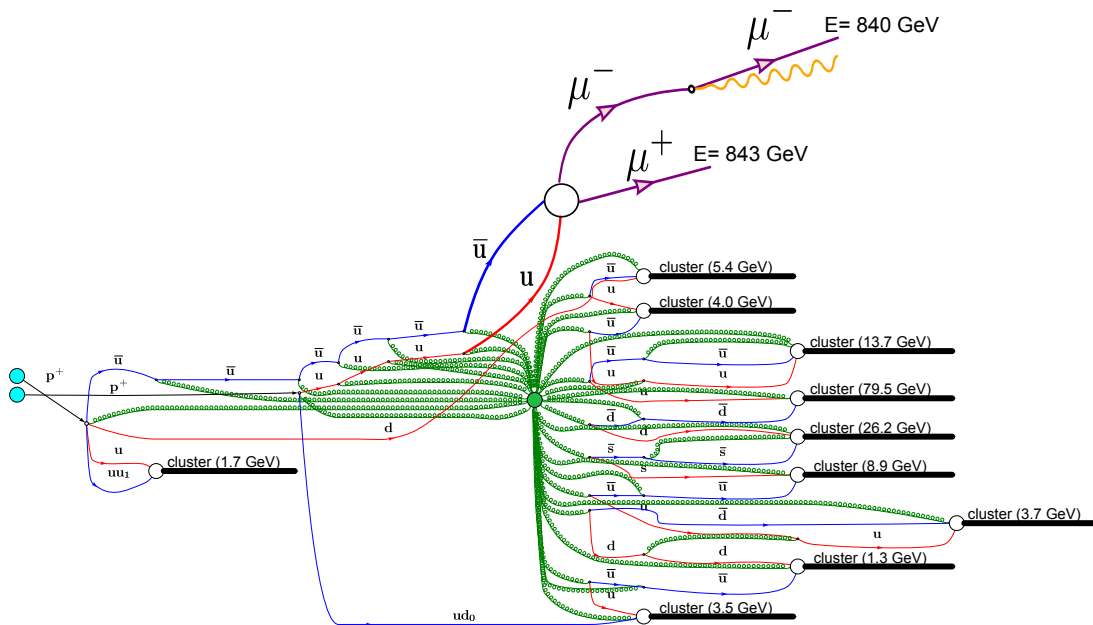
**Figure D.2** Pythia 8 event visualization of an ADD dimuon event. (Modified version of a PYTHIA8 event visualization with the mcviz tool developed by Johannes Ebke and Peter Waller.) One can see the hard interaction generating a muon pair an a final state photon and some aspects of the underlying event and the treatment of multiple parton interactions.

**Figure D.3** Highest mass dimuon event in a 4.1 fb$^{-1}$ dataset at $\sqrt{s} = 8$ TeV. The estimated dimuon mass is 1.42 TeV. Both muons have $p_{\mathrm{T}}$ values of about 0.5 TeV.

**Support Classes**

Estimates required range of the parameter of interest

**PoiRangeEstimator**

Variant of the Resultator class using the BAT package for numerical integration

**ResultatorWithBAT**

Handling of dilepton mass restrictions for building the likelihood

**DataPruner**

Miscellaneous: string handling,, etc.

**Pixie**

**Scripts for Batch Jobs**

- bash scripts and jdl files for condor
- bash scripts for torque (qsub)

**Main Class Structure**

General functionality for combining the single channel workspaces

**ModelConfigurator**

\# _CombinedWS: RooWorkspace *
\# _CombinedModelConfig: ModelConfig *
\# _channelnames: std::vector<std::string>
...
+<<virtual >> Setup(): void
+WriteCombinedWS(filename:std::string): void
...()

observed spectra, information about H0 and H1

Z' specific functionality for combining the single channel workspaces

**ModelConfiguratorZprime**

_ _peak: double
+<<constructor>> ModelConfiguratorZprime(WSmap:std::map<std::string, RooWorkspace*>)
...
+Setup(): void
+Setup_channel(channelname:std::string): void
+Setup_ModelConfig(): void
...()

information about H0 and H1

Provides unbinned observed mass spectra and constructs pseudo data from hypothetical experiments

**DataBox**

_ _configurator: ModelConfiguratorZprime *
_ _myWS: RooWorkspace *
_ _myModelConfig: ModelConfig *
...
+<<constructor>> DataBox(configurator:ModelConfiguratorZprime*, myDataPruner:DataPruner *)
+createObservedData(): RooDataSet *
+createToyMc(): RooDataSet *
...()

collect datasets (observed/hypothetical)

Calculates limits and estimates of significance; Provides additional figures for a detailed investigation of the results

**Resultator**

_ _configurator: ModelConfiguratorZprime *
_ _databox: DataBox *
_ _poiUpperRange: double
...
+<<constructor>> Resultator(plotfile:std::string,
                           myDataPruner:DataPruner *,
                           configurator:ModelConfiguratorZprime* )
+calculateMCMClimit(mcmc_iter:UInt_t ,...,
                    ntoys:UInt_t ,mode :std::string): void
+calculateRatioSignificance(mode:std::string,
                            ntoys:Int_t ): Double_t
+makeMcmcPosteriorPlot(mcInt:MCMCInterval *,
                       filename:std::string): void
+...()

**Executables**

**Limit2012**

**Significance2012**

- read single channel models (workspaces constructed from ExoSt configuration files)
- handle object configuration
- initialize construction of the combined model
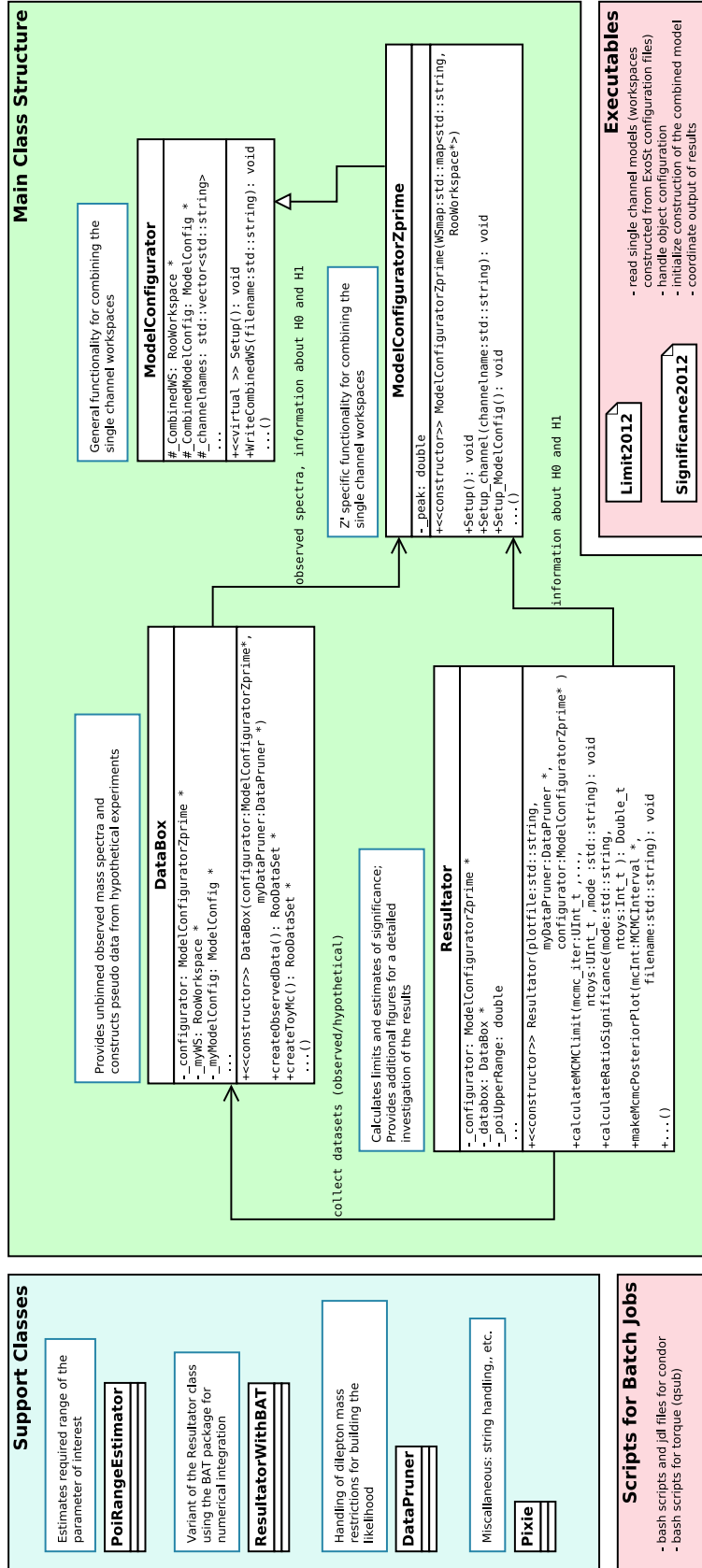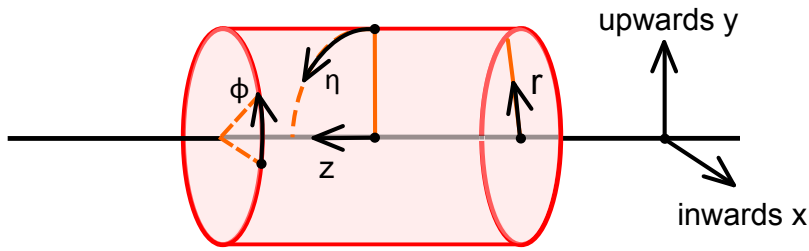- coordinate output of results

**Figure D.4** Basic structure of the Z' statistics code.

# E Notation, Units, Conventions and Used Software

## E.1 The CMS Coordinate System[1]



**Figure E.1** The CMS Coordinate System [11].

The coordinates used to describe the positions of the detector components are $z$ , $r$ , $\phi$ and $\eta$. They are defined as shown in figure E.1. The starting points of the arrows indicating the angular coordinates $\phi$ and $\eta$ correspond to the coordinates $\phi = 0$, and $\eta = 0$.

The rapidity $\psi$ is defined as

$$\tanh \psi = \frac{v_z}{c} \quad , \tag{E.1}$$

where $v_z$ is the speed of the particle into the $z$ direction and $c$ the speed of light.

Angular differences in $\psi$ are invariant under Lorentz boosts into the z direction. This property is of relevance for parton-parton interactions within the proton as the center-of-mass frame is approximately related to the zero momentum frame of the detector by a boost along the $z$-direction[2].

Often the pseudo rapidity $\eta$ is stated instead of $\psi$. The coordinate transformation between the polar angle $\theta$ and $\eta$ is defined as

$$\eta = -\ln \left[ \tan \left( \frac{\theta}{2} \right) \right] \quad . \tag{E.2}$$

The pseudo rapidity of particles in the ultra relativistic limit (i.e. particle masses can be neglected) is equal to the rapidity $\psi$.

The angular distance $\Delta R$ between two particles is given by

$$\Delta R = \sqrt{(\Delta \eta)^2 + (\Delta \phi)^2} \quad . \tag{E.3}$$

$\Delta R$ is often used to define isolation criteria for reconstructed objects.

---

[1]partially adapted from [11]

[2]the small momentum imbalance in the plane orthogonal to $z$ can often be neglected

## E.2 Units and Conventions

If not mentioned otherwise, units are stated in either *SI units* or *natural units* with $\hbar = c = 1$. Cross sections are stated in units of barns (b), with $1\,\mathrm{b} = 10^{-28}\,\mathrm{m}^2$ and integrated luminosities are stated in units of $\mathrm{b}^{-1}$. The signature of the Minkowski metric $\eta$ is chosen as (+,-,-,-). Dirac matrices are written as $\gamma^\mu$ with $\gamma_5$ defined as $\gamma_5 := i\gamma^0\gamma^1\gamma^2\gamma^3$. If not stated otherwise, uncertainties are implicitly assumed to correspond to 68% confidence level (CL) or credible intervals.

Lorentz indices $\hat{\mu}, \hat{\nu}, \ldots$ run from 0 to $3 + n$, indices $\mu, \nu, \ldots$ run from 0 to 3. $4 + n$ component vectors $z$ contain the 3+1 space-time coordinates and $n$ additional coordinates for the extra dimensions. The $3 + 1$ space-time coordinates are labeled as $x$ and the extra dimension coordinates as $y$. $\hat{h}$ denotes a perturbation of the metric in $4 + n$, $n > 0$ dimension. The label $h$ is used for the corresponding perturbation with $n = 0$.

Several mass variables are used throughout this work. Those that reoccur frequently are listed below.

- $M_{\mu\mu}$, the dimuon mass of an event with two muons (either measured or simulated).

- $M_{\mathrm{threshold}}$, the lower threshold on the dimuon masses that are used to specify the considered region for the statistical evaluation with a counting experiment.

- $M_{\mathrm{max}}$, the upper threshold on the dimuon mass range that is considered for signal contributions.

- $M_{\mathrm{Pl}}$, the reduced Planck mass in $4 + 1$ dimensional space-time.

- $M_{\mathrm{D}}$, the fundamental Planck mass in the ADD model of large spatial extra dimensions

- $M_{\mathrm{s}}$, a string scale which under certain assumptions may be set into relation with the UV cutoff on the virtual Graviton exchange or $M_{\mathrm{D}}$.

There are text passages for which supplementary background information can be found in CMS internal documents (for example in analysis notes). Though such references are only accessible for people in the CMS collaboration, they are still sometimes referenced if they are found to provide useful extra information for potential readers that are CMS members.

In some cases, theses, review articles or didactic texts may give the reader a more helpful access point to certain facts or topics than original journal articles. For this reason the former types of references are in a few cases preferred, including some situations where the relevant piece of information has become "textbook knowledge".

## E.3 Software Used in Preparing this Document

The list below acknowledges some software that has been helpful while preparing graphics and text body of the presented document.

- ROOT `http://root.cern.ch/drupal/`
- JabRef `http://jabref.sourceforge.net/`
- TeXnicCenter `http://www.texniccenter.org/`
- MiKTeX `http://miktex.org/`
- Inkscape `http://inkscape.org/`
- Jaxodraw `http://jaxodraw.sourceforge.net/`

# Bibliography

[1] T. Kaluza. On the Problem of Unity in Physics. *Sitzungsber.Preuss.Akad.Wiss.Berlin*, Juli-Dezember:966, 1921.

[2] O. Klein. Quantum Theory and Five-Dimensional Theory of Relativity. *Z.Phys.*, 37:895, 1926. doi: 10.1007/BF01397481.

[3] N. Arkani-Hamed, S. Dimopoulos, and G. Dvali. The hierarchy problem and new dimensions at a millimeter. *Phys. Lett. B*, 429:263, 1998. doi: 10.1016/S0370-2693(98)00466-3.

[4] CMS Collaboration. Search for Large Extra Dimensions in Dimuon Events in pp Collisions at $\sqrt{s} = 7$ TeV. CMS Physics Analysis Summary CMS-PAS-EXO-10-020, CMS, 2011. URL http://cdsweb.cern.ch/record/1335097.

[5] CMS Collaboration. Search for Large Extra Dimensions in Dimuon Events in pp Collisions at $\sqrt{s} = 7$ TeV. CMS Physics Analysis Summary CMS-PAS-EXO-11-039, CMS, 2011. URL http://cdsweb.cern.ch/record/1376670.

[6] CMS Collaboration. Search for Resonances in the Dilepton Mass Distribution in pp Collisions at $\sqrt{s} = 8$ TeV. CMS Physics Analysis Summary CMS-PAS-EXO-12-015, CMS, 2012. URL http://cds.cern.ch/record/1461216.

[7] CMS Collaboration. Search for Resonances in the Dilepton Mass Spetra in pp Collisions at $\sqrt{s} = 8$ TeV. CMS Physics Analysis Summary CMS-PAS-EXO-12-061, CMS, 2012. URL http://cds.cern.ch/record/1519132.

[8] CMS Collaboration. Search for Large Extra Dimensions in Dimuon Events in pp Collisions at $\sqrt{s} = 8$ TeV. CMS Physics Analysis Summary CMS-PAS-EXO-12-027, CMS, 2013.

[9] CMS Collaboration. Search for large extra dimensions in dimuon and dielectron events in pp collisions at $\sqrt{s} = 7$ TeV. *Phys. Lett. B*, 711:15, 2012.

[10] CMS Collaboration. Search for heavy narrow dilepton resonances in pp collisions at $\sqrt{s} = 7$ TeV and $\sqrt{s} = 8$ TeV. *Phys. Lett. B*, 720:63, 2013. URL http://arxiv.org/abs/1212.6175. CMS-EXO-12-015.

[11] S. A. Schmitz. Model Unspecific Search for New Physics with High $p_\mathrm{T}$ Photons in CMS. Master's thesis, RWTH Aachen University, 2009. URL http://web.physik.rwth-aachen.de/~hebbeker/theses/schmitz_diploma.pdf. Diplomarbeit.

[12] Jonathan L. Rosner. The Standard model in 2001, 2001. URL http://arxiv.org/abs/hep-ph/0108195.

[13] W. Buchmüller and C. Lüdeling. Field Theory and the Standard Model, 2006. URL http://arxiv.org/abs/hep-ph/0609174.

[14] P. Langacker. Introduction to the Standard Model and Electroweak Physics, 2009. URL http://arxiv.org/abs/0901.0241.

[15] F. Halzen and A D. Martin. *Quarks and Leptons*. Wiley, 1984.

[16] S. Weinberg. The Making of the Standard Model. *Eur.Phys.J.C*, 34:5, 2004. doi: 10.1140/epjc/s2004-01761-1. URL `http://arxiv.org/abs/hep-ph/0401010v1`.

[17] CTEQ Collaboration. Handbook of perturbative QCD: Version 1.0. *Rev.Mod.Phys.*, 67: 157, 1995. doi: 10.1103/RevModPhys.67.157. URL `http://www.phys.psu.edu/~cteq/handbook/v1.1/handbook.pdf`. url links to version 1.1.

[18] S.L. Glashow. Partial Symmetries of Weak Interactions. *Nucl.Phys.*, 22:579, 1961. doi: 10.1016/0029-5582(61)90469-2.

[19] A. Salam and J. C. Ward. Electromagnetic and weak interactions. *Phys.Lett.*, 13:1681, 1964. doi: 10.1016/0031-9163(64)90711-5.

[20] S. Weinberg. A Model of Leptons. *Phys.Rev.Lett.*, 19:1264, 1967. doi: 10.1103/PhysRevLett.19.1264.

[21] A. Salam. Weak and Electromagnetic Interactions. *Conf.Proc.*, C680519:367, 1968.

[22] S. F. King. Neutrino Mass. *Contemporary Physics*, 48(4):195, 2007. doi: 10.1080/00107510701770539. URL `http://arxiv.org/abs/0712.1750v1`.

[23] H. D. Politzer. Reliable Perturbative Results for Strong Interactions? *Phys.Rev.Lett.*, 30: 1346, 1973. doi: 10.1103/PhysRevLett.30.1346.

[24] D.J. Gross and F. Wilczek. Ultraviolet Behavior of Nonabelian Gauge Theories. *Phys.Rev.Lett.*, 30:1343, 1973. doi: 10.1103/PhysRevLett.30.1343.

[25] J. C. Collins, D. E. Soper, and G. F. Sterman. Factorization of Hard Processes in QCD. *Adv.Ser.Direct.High Energy Phys.*, 5:1, 1988. URL `http://arxiv.org/abs/hep-ph/0409313`.

[26] Particle Data Group. Review of Particle Physics (RPP). *Phys.Rev.D*, 86:010001, 2012. doi: 10.1103/PhysRevD.86.010001. URL `http://prd.aps.org/abstract/PRD/v86/i1/e010001`.

[27] F. Maltoni, T. McElmurry, R. Putman, and S. Willenbrock. Choosing the Factorization Scale in Perturbative QCD, 2007. URL `http://arxiv.org/abs/hep-ph/0703156`.

[28] V.N. Gribov and L.N. Lipatov. Deep inelastic e p scattering in perturbation theory. *Sov.J.Nucl.Phys.*, 15:43, 1972.

[29] G. Altarelli and G. Parisi. Asymptotic Freedom in Parton Language. *Nucl. Phys. B*, 126: 298, 1977. doi: 10.1016/0550-3213(77)90384-4.

[30] Y. L. Dokshitzer. Calculation of the Structure Functions for Deep Inelastic Scattering and e+ e- Annihilation by Perturbation Theory in Quantum Chromodynamics. *Sov.Phys.JETP*, 46:641, 1977.

[31] Sergey Alekhin et al. The PDF4LHC Working Group Interim Report, 2011. URL `http://arxiv.org/abs/1101.0536v1`.

[32] M. Botje et al. The PDF4LHC Working Group Interim Recommendations, 2011. URL `http://arxiv.org/abs/1101.0538v1`.

[33] S. D. Drell and T. M. Yan. Massive Lepton-Pair Production in Hadron-Hadron Collisions at High Energies. *Phys. Rev. Lett.*, 25:316, 1970.

[34] A. K. Gupta, N. K. Mondal, and R. Sreerup. Constraining large extra dimensions using dilepton data from the Tevatron collider, 1999. URL `http://arxiv.org/abs/hep-ph/9904234`.

[35] F. Englert and R. Brout. Broken Symmetry and the Mass of Gauge Vector Mesons. *Phys. Rev. Lett.*, 13:32, 1964. doi: 10.1103/PhysRevLett.13.321. URL `http://link.aps.org/doi/10.1103/PhysRevLett.13.321`.

[36] G. S. Guralnik, C. R. Hagen, and T. W. B. Kibble. Global Conservation Laws and Massless Particles. *Phys. Rev. Lett.*, 13:585, 1964. doi: 10.1103/PhysRevLett.13.585. URL `http://link.aps.org/doi/10.1103/PhysRevLett.13.585`.

[37] P. W. Higgs. Broken Symmetries and the Masses of Gauge Bosons. *Phys. Rev. Lett.*, 13:508, 1964. doi: 10.1103/PhysRevLett.13.508. URL `http://link.aps.org/doi/10.1103/PhysRevLett.13.508`.

[38] P. W. Higgs. Spontaneous Symmetry Breakdown without Massless Bosons. *Phys. Rev.*, 145:1156, 1966. doi: 10.1103/PhysRev.145.1156. URL `http://link.aps.org/doi/10.1103/PhysRev.145.1156`.

[39] T. W. B. Kibble. Symmetry Breaking in Non-Abelian Gauge Theories. *Phys. Rev.*, 155:1554, 1967. doi: 10.1103/PhysRev.155.1554. URL `http://link.aps.org/doi/10.1103/PhysRev.155.1554`.

[40] G. 't Hooft. Renormalizable Lagrangians for Massive Yang-Mills Fields. *Nucl.Phys.B*, 35:167, 1971. doi: 10.1016/0550-3213(71)90139-8.

[41] M. E. Peskin and D. V. Schroeder. *An Introduction To Quantum Field Theory (Frontiers in Physics)*. Westview Press, 1995. ISBN 0201503972.

[42] CMS Collaboration. Observation of a new boson at a mass of 125 GeV with the CMS experiment at the LHC. *Phys.Lett.*, B716:30, 2012. doi: 10.1016/j.physletb.2012.08.021. URL `http://arxiv.org/abs/1207.7235`.

[43] ATLAS Collaboration. Observation of a new particle in the search for the Standard Model Higgs boson with the ATLAS detector at the LHC. *Phys.Lett.*, B716:1, 2012. doi: 10.1016/j.physletb.2012.08.020. URL `http://arxiv.org/abs/1207.7214`.

[44] L.-T. Wang. HCPSS 2012 Lectures on New Physics Beyond the Standard Model, 2012. URL `http://projects.fnal.gov/hcpss/hcpss12/`.

[45] A. Djouadi. The Anatomy of electro-weak symmetry breaking. I: The Higgs boson in the standard model. *Phys.Rept.*, 457:1, 2008. doi: 10.1016/j.physrep.2007.10.004. URL `http://arxiv.org/abs/hep-ph/0503172v2`.

[46] C. F. Kolda and H. Murayama. The Higgs mass and new physics scales in the minimal standard model. *JHEP*, 07:035, 2000. doi: doi:10.1088/1126-6708/2000/07/035. URL `http://arxiv.org/abs/hep-ph/0003170v1`.

[47] R. Barbieri and G. F. Giudice. Upper bounds on supersymmetric particle masses. *Nucl.Phys.B*, 396:63, 1988. doi: 10.1016/0550-3213(88)90171-X. URL `http://cds.cern.ch/record/180560`.

[48] G. F. Giudice, R. Rattazzi, and J. D. Wells. Quantum gravity and extra dimensions at High-Energy Colliders. *Nucl. Phys. B*, 544:3, 1999. doi: 10.1016/S0550-3213(99)00044-9. URL http://arxiv.org/abs/hep-ph/9811291v2.

[49] T. Han, J. D. Lykken, and R. Zhang. On Kaluza-Klein States from Large Extra Dimensions. *Phys. Rev. D*, 59:105006, 1999. doi: 10.1103/PhysRevD.59.105006. URL http://arxiv.org/abs/hep-ph/9811350v4.

[50] J. L. Hewett. Indirect collider signals for extra dimensions. *Phys.Rev.Lett.*, 82:4765, 1999. doi: 10.1103/PhysRevLett.82.4765. URL http://arxiv.org/abs/hep-ph/9811356.

[51] G. F. Giudice and A. Strumia. Constraints on extra dimensional theories from virtual graviton exchange. *Nucl.Phys.B*, 663:3773, 2003. doi: 10.1016/S0550-3213(03)00404-8. URL http://arxiv.org/abs/hep-ph/0301232v1.

[52] R. Franceschini, G. F. Giudice, P. P. Giardino, P. Lodone, and A. Strumia. LHC bounds on large extra dimensions. *JHEP*, 092:1105, 2011. doi: 10.1007/JHEP05(2011)092. URL http://arxiv.org/abs/1101.4919v3.

[53] G. Landsberg. Extra Dimensions and More.... In *36th Rencontre de Moriond*, Les Arcs, France, 2001. URL http://cdsweb.cern.ch/record/476781.

[54] R. Gabadadze. ICTP Lectures on Large Extra Dimensions, 2003. CERN-TH/2003-157, arXiv:hep-ph/0308112v1.

[55] G. D. Kribs. TASI 2004 Lectures on the Phenomenology of Extra Dimensions, 2006. arXiv:hep-ph/0605325v1.

[56] R. Rattazzi. Cargese Lectures on Extra Dimensions, 2006. CERN-PH-TH/2006-029 arXiv:hep-ph/0607055v1.

[57] C. Ewerz. Extra Dimensions, 06/07. Lecture course at Heidelberg University http://www.thphys.uni-heidelberg.de/~ewerz/scriptum/dimensions_ce.pdf.

[58] I. Antoniadis, N. Arkani-Hamed, S. Dimopoulos, and G. Dvali. New dimensions at a millimeter to a Fermi and superstrings at a TeV. *Phys.Lett.B*, 436:257, 1998. doi: 10.1016/S0370-2693(98)00860-0. URL http://arxiv.org/abs/hep-ph/9804398v1.

[59] K. Cheung and G. Landsberg. Drell-Yan and Diphoton production at Hadron Colliders and Low Scale Gravity Model. *Phys. Rev.*, D62:076003, 2000. doi: 10.1103/PhysRevD.62.076003.

[60] S. Ask et al. Real emission and virtual exchange of gravitons and unparticles in PYTHIA8. *Comp. Phys. Comm.*, 181:1593, 2009. doi: 10.1016/j.cpc.2010.05.013. URL http://arxiv.org/abs/0912.4233.

[61] S. Weinberg. Ultraviolet divergences in quantum theories of gravitation. In S. W. Hawking & W. Israel, editor, *General Relativity: An Einstein centenary survey*, pages 790–831, 1979.

[62] R. Percacci. *Approaches to Quantum Gravity: Toward a New Understanding of Space, Time and Matter*, chapter Asymptotic Safety, page 111. Cambridge University Press, 2009. URL http://arxiv.org/abs/0709.3851v2. Oriti, D. (ed.).

[63] P. Fischer and D. F. Litim. Fixed points of quantum gravity in higher dimensions. *AIP Conf.Proc.*, 861:336, 2006. doi: 10.1063/1.2399593. URL `http://arxiv.org/abs/hep-th/0606135v1`.

[64] Daniel F. Litim. Fixed Points of Quantum Gravity and the Renormalisation Group, 2008. URL `http://arxiv.org/abs/0810.3675v1`.

[65] D. F. Litim and T. Plehn. Virtual gravitons at the LHC, 2007. URL `http://arxiv.org/abs/0710.3096`.

[66] J. Hewett and T. Rizzo. Collider Signals of Gravitational Fixed Points. *JHEP*, 0712:009, 2007. doi: 10.1088/1126-6708/2007/12/009. URL `http://arxiv.org/abs/0707.3182`.

[67] Er. Gerwick, D. Litim, and T. Plehn. Asymptotic safety and Kaluza-Klein gravitons at the LHC. *Phys. Rev.*, D83:084048, 2011. doi: 10.1103/PhysRevD.83.084048.

[68] E. Gerwick. *Phenomenology of Asymptotic Safety*. PhD thesis, University of Edinburgh, 2011. URL `http://www.thphys.uni-heidelberg.de/~plehn/includes/theses/gerwick.pdf`.

[69] G. Hiller. private communication, 2013.

[70] L. Randall and R. Sundrum. A Large Mass Hierarchy from a Small Extra Dimension. *Phys. Rev. Lett.*, 83:3370, 1999. doi: 10.1103/PhysRevLett.83.3370.

[71] M. Gabella. The Randall-Sundrum Model, 2006. URL `http://www-thphys.physics.ox.ac.uk/people/MaximeGabella/rs.pdf`.

[72] T. Appelquist, H.-C. Cheng, and B. A. Dobrescu. Bounds on universal extra dimensions. *Phys.Rev.D*, 64:035002, 2001. doi: 10.1103/PhysRevD.64.035002. URL `http://arxiv.org/abs/hep-ph/0012100`.

[73] W. D. Goldberger and M. B. Wise. Modulus stabilization with bulk fields. *Phys.Rev.Lett.*, 83:4922, 1999. doi: 10.1103/PhysRevLett.83.4922. URL `http://arxiv.org/abs/hep-ph/9907447v2`.

[74] L. Randall and R. Sundrum. An Alternative to compactification. *Phys.Rev.Lett.*, 83:4690, 1999. doi: 10.1103/PhysRevLett.83.4690. URL `http://arxiv.org/abs/hep-th/9906064v1`.

[75] D. Hooper and S. Profumo. Dark matter and collider phenomenology of universal extra dimensions. *Phys.Rept.*, 453:29, 2007. doi: 10.1016/j.physrep.2007.09.003. URL `http://arxiv.org/abs/hep-ph/0701197v2`.

[76] E.G. Adelberger, J.H. Gundlach, B.R. Heckel, S. Hoedl, and S. Schlamminger. Torsion balance experiments: A low-energy frontier of particle physics. *Prog.Part.Nucl.Phys.*, 62:102, 2009. doi: 10.1016/j.ppnp.2008.08.002.

[77] C. Hanhart, D. R. Phillips, S. Reddy, and M. J. Savage. Extra dimensions, SN1987a, and nucleon-nucleon scattering data. *Nucl.Phys.B*, 595:335, 2001. doi: 10.1016/S0550-3213(00)00667-2. URL `http://arxiv.org/abs/nucl-th/0007016`.

[78] C. Hanhart, J. A. Pons, D. R. Phillips, and S. Reddy. The Likelihood of GODs' existence: Improving the SN1987a constraint on the size of large compact dimensions. *Phys.Lett.B*, 509:1, 2001. doi: 10.1016/S0370-2693(01)00544-5. URL `http://arxiv.org/abs/astro-ph/0102063`.

[79] S. Hannestad and G. G. Raffelt. Supernova and neutron star limits on large extra dimensions reexamined. *Phys.Rev. D*, 67:125008, 2003. doi: 10.1103/PhysRevD.69.029901,10.1103/PhysRevD.67.125008. URL http://arxiv.org/abs/hep-ph/0304029.

[80] G. F. Giudice, T. Plehn, and A. Strumia. Graviton collider effects in one and more large extra dimensions. *Nucl.Phys.B*, 706:455, 2005. doi: 10.1016/j.nuclphysb.2004.10.056. URL http://arxiv.org/abs/hep-ph/0408320v2.

[81] H1 Collaboration. Search for Compositeness, Leptoquarks and Large Extra Dimensions in *eq* Contact Interactions at HERA. *Phys. Lett. B*, 479:358, 2000. doi: 10.1016/S0370-2693(00)00332-4.

[82] ZEUS Collaboration. Search for contact interactions, large extra dimensions and finite quark radius in *ep* collisions at HERA. *Phys. Lett. B*, 591:23, 2004. doi: 10.1016/j.physletb.2004.03.081.

[83] L3 Collaboration. Search for extra dimensions in boson and fermion pair production in $e^+e^-$ interactions at LEP. *Phys. Lett. B*, 470:281, 1999. doi: 10.1016/S0370-2693(99)01310-6.

[84] L3 Collaboration. Search for low scale gravity effects in $e^+e^-$ collisions at LEP. *Phys. Lett. B*, 464:135, 1999. doi: 10.1016/S0370-2693(99)01011-4.

[85] DELPHI Collaboration. Measurement and interpretation of fermion-pair production at LEP energies of 183 and 189 GeV. *Phys. Lett. B*, 485:45, 2000. doi: 10.1016/S0370-2693(00)00675-4.

[86] DELPHI Collaboration. Determination of the e+ e- $\rightarrow \gamma \gamma (\gamma)$ Cross-Section at Centre-of-Mass Energies Ranging from 189 GeV to 202 GeV. *Phys. Lett. B*, 491:67, 2000. doi: 10.1016/S0370-2693(00)01013-3.

[87] OPAL Collaboration. Multi-photon production in e$^+$ e$^-$ collisions at $\sqrt{s} = 181 - 209\,\text{GeV}$. *Eur. Phys. J. C*, 26:331, 2003. doi: 10.1140/epjc/s2002-01074-5.

[88] OPAL Collaboration. Tests of the standard model and constraints on new physics from measurements of fermion pair production at 189 GeV at LEP. *Eur. Phys. J. C*, 13:553, 2000. doi: 10.1007/s100520050718.

[89] ALEPH Collaboration. Fermion pair production in $e^+e^-$ collisions at 189-209-GeV and constraints on physics beyond the standard model. *Eur.Phys.J.C*, 49:411, 2007. doi: 10.1140/epjc/s10052-006-0156-8. URL http://arxiv.org/abs/hep-ex/0609051.

[90] D0 Collaboration. Search for Large Extra Spatial Dimensions in the Dielectron and Diphoton Channels in p anti-p Collisions at $\sqrt{s} = 1.96$ TeV. *Phys. Rev. Lett.*, 102:051601, 2009. doi: 10.1103/PhysRevLett.102.051601. URL http://arxiv.org/abs/0809.2813.

[91] D0 Collaboration. Search for Large Extra Spatial Dimensions in Dimuon Production at D0. *Phys. Rev. Lett.*, 95:161602, 2005. doi: 10.1103/PhysRevLett.95.161602.

[92] ATLAS Collaboration. Search for contact interactions and large extra dimensions in dilepton events from *pp* collisions at $\sqrt{s} = 7$ TeV with the ATLAS detector. *Phys.Rev.D*, 87:015010, 2013. URL http://arxiv.org/abs/1211.1150.

[93] ATLAS Collaboration. Search for Extra Dimensions using diphoton events in 7 TeV proton-proton collisions with the ATLAS detector. *Phys.Lett. B*, 710:538, 2012. doi: 10.1016/j.physletb.2012.03.022. URL http://arxiv.org/abs/1209.2535.

[94] CMS Collaboration. Search for signatures of extra dimensions in the diphoton mass spectrum at the Large Hadron Collider. *Phys.Rev.Lett.*, 108:111801, 2012. doi: 10.1103/PhysRevLett.108.111801. URL http://arxiv.org/abs/1112.0688v2.

[95] CMS Collaboration. Search for Large Extra Spatial Dimensions in Dielectron Production with the CMS Detector. CMS Physics Analysis Summary CMS-PAS-EXO-12-031, CMS, 2013.

[96] CMS Collaboration. Measurement of Dijet Angular Distributions and Search for Quark Compositeness in pp Collisions at $\sqrt{s} = 7$ TeV. *Phys.Rev.Lett.*, 106:201804, 2011. doi: 10.1103/PhysRevLett.106.201804. URL http://arxiv.org/abs/1102.2020.

[97] ATLAS Collaboration. Search for Quark Contact Interactions in Dijet Angular Distributions in pp Collisions at $\sqrt{s} = 7$ TeV Measured with the ATLAS Detector. *Phys.Lett.B*, 694:327, 2011. doi: 10.1016/j.physletb.2010.10.021. URL http://arxiv.org/abs/1009.5069.

[98] ATLAS Collaboration. Search for dark matter candidates and large extra dimensions in events with a jet and missing transverse momentum with the ATLAS detector. *JHEP*, 1304:075, 2012. doi: 10.1007/JHEP04(2013)075. URL http://arxiv.org/abs/1210.4491v2.

[99] ATLAS Collaboration. Search for dark matter candidates and large extra dimensions in events with a photon and missing transverse momentum in pp collision data at $\sqrt{s} = 7$ TeV with the ATLAS detector. *Phys.Rev.Lett.*, 110:011802, 2012. doi: 10.1103/PhysRevLett.110.011802. URL http://arxiv.org/abs/1209.4625.

[100] CMS Collaboration. Search for dark matter and large extra dimensions in monojet events in pp collisions at $\sqrt{s} = 7$ TeV. *JHEP*, 094:1, 2012. doi: 10.1007/JHEP09(2012)094. URL http://arxiv.org/abs/1206.5663v1. CMS-EXO-11-059.

[101] CMS Collaboration. Search for Dark Matter and Large Extra Dimensions in pp Collisions Yielding a Photon and Missing Transverse Energy. *Phys.Rev.Lett.*, 108:261803, 2012. doi: 10.1103/PhysRevLett.108.261803. URL http://arxiv.org/abs/1204.0821.

[102] ATLAS Collaboration. Search for high-mass resonances decaying to dilepton final states in pp collisions at a center-of-mass energy of 7 TeV with the ATLAS detector. *JHEP*, 1211:138, 2012. doi: 10.1007/JHEP11(2012)138. URL http://arxiv.org/abs/1209.2535.

[103] CMS Collaboration. Search for narrow resonances in dilepton mass spectra in pp collisions at sqrt(s) = 7 TeV. *Phys.Lett.B*, 714:158, 2012. doi: 10.1016/j.physletb.2012.06.051. URL http://arxiv.org/abs/arXiv:1206.1849. CMS-EXO-11-019.

[104] ATLAS Collaboration. Search for new phenomena in the WW to l nu l' nu' final state in pp collisions at sqrt(s) = 7 TeV with the ATLAS detector. *Phys.Lett.B*, 718:860, 2013. doi: 10.1016/j.physletb.2012.11.040. URL http://arxiv.org/abs/1208.2880v2.

[105] ATLAS Collaboration. Search for new particles decaying to ZZ using final states with leptons and jets with the ATLAS detector in $\sqrt{s} = 7$ TeV proton-proton collisions. *Phys.Lett.B*, 712:331, 2012. doi: 10.1016/j.physletb.2012.05.020. URL http://arxiv.org/abs/1203.0718.

[106] ATLAS Collaboration. Search for Diphoton Events with Large Missing Transverse Energy with 36 pb$^{-1}$ of 7 TeV Proton-Proton Collision Data with the ATLAS Detector. *Eur.Phys.J.C*, 71:1744, 2011. doi: 10.1140/epjc/s10052-011-1744-9. URL `http://arxiv.org/abs/1107.0561`.

[107] CMS Collaboration. Search for leptonic decays of $W'$ bosons in pp collisions at $\sqrt{s} = 7$ TeV. *JHEP*, 1208:023, 2012. doi: 10.1007/JHEP08(2012)023. URL `http://arxiv.org/abs/1204.4764`. CMS-EXO-11-024.

[108] M. Cavaglia. Black hole and brane production in TeV gravity: A Review. *Int.J.Mod.Phys.A*, 18:1843, 2003. doi: 10.1142/S0217751X03013569. URL `http://arxiv.org/abs/hep-ph/0210296v1`.

[109] B. Webber. Black holes at accelerators, 2005. URL `http://arxiv.org/abs/hep-ph/0511128v3`. SSI-2005-T030, CAVENDISH-HEP-05-20.

[110] G. Landsberg. Black Holes at Future Colliders and Beyond. *J.Phys.G*, 32:337–365, 2006. doi: 10.1088/0954-3899/32/9/R02. URL `http://arxiv.org/abs/hep-ph/0607297`.

[111] CMS Collaboration. Search for microscopic black holes in pp collisions at $\sqrt{s} = 7$ TeV. *JHEP*, 1204:061, 2012. doi: 10.1007/JHEP04(2012)061. URL `http://arxiv.org/abs/1202.6396`. CMS-EXO-11-071.

[112] ATLAS Collaboration. Search for TeV-scale gravity signatures in final states with leptons and jets with the ATLAS detector at $\sqrt{s} = 7$ TeV. *Phys. Lett. B*, 716:122, 2012. URL `http://arxiv.org/abs/1204.4646`.

[113] ATLAS Collaboration. Search for strong gravity signatures in same-sign dimuon final states using the ATLAS detector at the LHC. *Phys.Lett. B*, 709:32, 2012. doi: 10.1016/j.physletb.2012.02.049. URL `http://arxiv.org/abs/1111.0080`.

[114] M. J. Bayarri and J. O. Berger. The Interplay of Bayesian and Frequentist Analysis. *Statist. Sci.*, 19(1):58, 2004.

[115] H. B. Prosper and Louis (ed.) Lyons, editors. *PHYSTAT 2011 Workshop on Statistical Issues Related to Discovery Claims in Search Experiments and Unfolding*, 2011.

[116] F. James. *Statistical Methods in Experimental Physics*. World Scientific Pulishing, 2nd edition, 2006.

[117] J. Neyman and E. S. Pearson. The testing of statistical hypotheses in relation to probabilities a priori. *Mathematical Proceedings of the Cambridge Philosophical Society*, 29:492, 1933. doi: 10.1017/S030500410001152X.

[118] J. Neyman and E. S. Pearson. On the Problem of the Most Efficient Tests of Statistical Hypotheses. *Phil. Trans. R. Soc. Lond. A*, 231:289–337, 1933. doi: doi:10.1007/978-3-8348-8264-6.

[119] G. J. Feldman and R. D. Cousins. A Unified Approach to the Classical Statistical Analysis of Small Signals. *Phys.Rev.D*, 57:3873, 1998. doi: 10.1103/PhysRevD.57.3873. URL `http://arxiv.org/abs/physics/9711021v2`.

[120] L. Demortier. P Values: What They Are and How to Use Them. CDF memo, 2006. URL `http://www-cdf.fnal.gov/~luc/statistics/cdf0000.ps`.

[121] R. A. Fisher. *Statistical Methods for Research Workers*. Oliver and Boyd, 1925.

[122] M. J. Bayarri and J. O. Berger. Quantifying Surprise in the Data and Model Verification. In J. M. Bernardo, James O. Berger, A. P. Dawid, and Adrian F. M. Smith, editors, *Bayesian Statistics 6*, page 53, 1998. URL `http://isds.duke.edu/~berger/papers/98-16.ps`.

[123] L. Demortier. P Values and Nuisance Parameters. In H. B. Prosper, L. Lyons, and A. De Roeck, editors, *PHYSTAT LHC Workshop on Statistical Issues for LHC Physics*, page 23, 2008. (PHYSTAT 2007) `http://phystat-lhc.web.cern.ch/phystat-lhc/`.

[124] A. L. Read. Presentation of Search Results: The CL(s) Technique. *J. Phys. G*, 28:2693, 2002. doi: 10.1088/0954-3899/28/10/313.

[125] G. Cowan, K. Cranmer, E. Gross, and O. Vitells. Power-Constrained Limits, 2011. URL `http://arxiv.org/abs/1105.3166`.

[126] G. Cowan, K. Cranmer, E. Gross, and O. Vitells. Asymptotic formulae for likelihood-based tests of new physics. *Eur. Phys. J. C*, 71:1554, 2011. doi: 10.1140/epjc/s10052-011-1554-0.

[127] ATLAS Collaboration, CMS Collaboration, and LHC Higgs Combination Group. Procedure for the LHC Higgs boson search combination in summer 2011. Technical Report ATL-PHYS-PUB-2011-818, CMS NOTE-2011/005, ATLAS, 2011. URL `http://cdsweb.cern.ch/record/1375842/`.

[128] J. M. Bernardo and A. F. M. Smith. *Bayesian Theory*. John Wiley & Sons, 2000. URL `ISBN-13:978-0471494645`.

[129] E. T. Jaynes. Confidence Intervals vs Bayesian Intervals. *Foundations of Probability Theory, Statistical Inference, and Statistical Theories of Science*, 2:W. L. Harper and C. A. Hooker, 1976. URL `http://bayes.wustl.edu/etj/articles/confidence.pdf`.

[130] R. E. Kass and L. Wasserman. The Selection of Prior distributions by Formal Rules. *Journal of the American Statistical Association*, 91(435):1343, 1996.

[131] J. M. Bernardo. Reference Posterior Distributions for Bayesian Inference. *J. R. Statist. Soc. B*, 41(2):113, 1979.

[132] J. O. Berger, J. M. Bernardo, and D. Sun. The Formal Definition of Reference Priors. *The Annals of Statistics*, 37(2):905, 2009. doi: dx.doi.org/10.1214/07-AOS587.

[133] L. Demortier, S. Jain, and H. B. Prosper. Reference priors for high energy physics. *Phys. Rev. D*, 82(3):034002, 2010. doi: 10.1103/PhysRevD.82.034002. URL `http://arxiv.org/abs/1002.1111v2`.

[134] M. Pierini, H. Prosper, S. Sekmen, and M. Spiropulu. Model Inference with Reference Priors. In *Proceedings of PHYSTAT11*, 2011. URL `http://arxiv.org/abs/1107.2877`.

[135] *Integrated Objective Bayesian Estimation and Hypothesis Testing*, 2010. Bayesian Statistics 9 (Proceedings of the Ninth Valencia International Meeting on Bayesian Statistics).

[136] I. Murray. *Advances in Markov chain Monte Carlo methods*. PhD thesis, University of London, University College, 2007. URL `http://homepages.inf.ed.ac.uk/imurray2/pub/07thesis/murray_thesis_2007.pdf`.

[137] N. Metropolis, A. W. Rosenbluth, M. N. Rosenbluth, A. H. Teller, and E. Teller. Equation of State Calculations by Fast Computing Machines. *The Journal of Chemical Physics*, 21 (6):1087, 1953. doi: 10.1063/1.1699114. URL `http://dx.doi.org/10.1063/1.1699114`.

[138] W. K. Hastings. Monte Carlo Sampling Methods Using Markov Chains and Their Applications. *Biometrika*, 57(1):97, 1970. doi: 10.1093/biomet/57.1.97.

[139] L. Evans (ed.) and P. Bryant (ed.). LHC Machine. *JINST*, 3:S08001, 2008. doi: 10. 1088/1748-0221/3/08/S08001. contains abridged material from the LHC design reports CERN-2004-003-V-1, CERN-2004-003-V-2,CERN-2004-003-V-3.

[140] ALICE Collaboration. The ALICE experiment at the CERN LHC. *JINST*, 3:S08002, 2008. doi: 10.1088/1748-0221/3/08/S08002.

[141] ATLAS Collaboration. The ATLAS Experiment at the CERN Large Hadron Collider. *JINST*, 3:S08003, 2008. doi: 10.1088/1748-0221/3/08/S08003.

[142] LHCb Collaboration. The LHCb Detector at the LHC. *JINST*, 3:S08005, 2008. doi: 10.1088/1748-0221/3/08/S08005.

[143] LHCf Collaboration. The LHCf detector at the CERN Large Hadron Collider. *JINST*, 3: S08006, 2008. doi: 10.1088/1748-0221/3/08/S08006.

[144] TOTEM Collaboration. The TOTEM experiment at the CERN Large Hadron Collider. *JINST*, 3:S08007, 2008. doi: 10.1088/1748-0221/3/08/S08007.

[145] MoEDAL Collaboration. Technical design report of the moedal experiment, 2009. URL `http://cds.cern.ch/record/1181486/`.

[146] The scale of the LHC, 2001. URL `http://cdsweb.cern.ch/record/42370`. ©CERN.

[147] CMS Collaboration. public figure: integrated luminosity at CMS, 2011. URL `https://twiki.cern.ch/twiki/bin/view/CMSPublic/LumiPublicResults2011`.

[148] CMS Collaboration. The CMS magnet project: Technical Design Report, 1997. URL `http://cmsdoc.cern.ch/ftp/TDR/MAGNET/magnet.html`. CERN-LHCC-97-031.

[149] R. Adolphi et al. The CMS experiment at the CERN LHC. *JINST*, 3:S08004, 2008. doi: 10.1088/1748-0221/3/08/S08004.

[150] M. Brice (photographer), 2007. URL `http://cdsweb.cern.ch/record/1107805#02`. ©CERN.

[151] CMS Collaboration. The CMS electromagnetic calorimeter project : Technical Design Report, 1997. URL `http://cmsdoc.cern.ch/ftp/TDR/ECAL/ecal.html`. CERN-LHCC-97-033,.

[152] CMS Collaboration. The CMS Collaboration. CMS Physics TDR Volume I: "Detector Performance and Software", 2006. URL `http://cmsdoc.cern.ch/cms/cpt/tdr/`. CERN-LHCC-2006-001.

[153] C. Berger. *Elementarteilchenphysik.* Springer, 2nd edition, 2006. doi: 10.1007/ 3-540-33594-3.

[154] P. Adzic, R. Alemany-Fernandez, C.B. Almeida, N.M. Almeida, G. Anagnostou, et al. Energy resolution of the barrel of the CMS electromagnetic calorimeter. *JINST*, 2:P04004, 2007. doi: 10.1088/1748-0221/2/04/P04004.

[155] CMS Collaboration. Performance of the CMS ECAL with $5\,\mathrm{fb}^{-1}$ of data at $\sqrt{s} = 7\,\mathrm{TeV}$, 2011. CMS PAS EGM-11-001, publication in preparation.

[156] M. Anfrevilleb, D. Bailleuxa, J. P. Bardb, et al. Laser monitoring system for the CMS lead tungstate crystal calorimeter. Technical report, CMS, 2007. URL `http://cdsweb.cern.ch/record/1073694`. CMS-NOTE-2007-028.

[157] G. Della Ricca. Performance of the CMS Electromagnetic Calorimeter at the LHC. Technical report, CMS, 2011. URL `http://cdsweb.cern.ch/record/1455282`. CMS-CR-2011-297, presented at IEEE2011.

[158] Sh. Elgammal, B. Clerbaux, P. Marage, and P. Miné. Validation of ECAL calibration at high energy using electrons in $\sqrt{s} = 7$ TeV data, 2011. CMS AN-2011/085.

[159] D. Green. *The Physics of Particle Detectors*. Cambridge University Press, 2000.

[160] CMS Collaboration. The hadron calorimeter project: technical design report, 1997. URL `http://cmsdoc.cern.ch/ftp/TDR/HCAL/hcal.html`. CERN-LHCC-97-031.

[161] CMS Collaboration. The Tracker Project: Technical Design Report, 1998. URL `http://cmsdoc.cern.ch/ftp/TDR/TRACKER/tracker.html`. CERN/LHCC 98-6.

[162] CMS Collaboration. The CMS tracker : addendum to the Technical Design Report, 2000. URL `http://cds.cern.ch/record/490194`. CERN-LHCC-2000-016.

[163] C. Bloch. *Studies for the Commissioning of the CERN CMS Silicon Strip Tracker*. PhD thesis, Technische Universität Wien, 2008. URL `http://cds.cern.ch/record/1081755`. CERN-THESIS-2008-004.

[164] O. Pooth. *The CMS Silicon Strip Tracker: Concept, Production and Commissioning*. Vieweg+Teubner, 2010. ISBN-13: 978-3834810038.

[165] D. A. Strom. Operation of the CMS Silicon Tracker. Technical report, CMS, 2012. CMS CR-2012/159.

[166] J. Behr. Alignment procedures for the CMS silicon tracker. Technical report, CMS, 2012. URL `http://cdsweb.cern.ch/record/1457428/`. CMS CR-2012/071.

[167] CMS Collaboration. The CMS muon project: Technical Design Report. Technical report, CERN, 1997. URL `http://cdsweb.cern.ch/record/343814/`.

[168] F. Sauli. *Experimental techniques in high energy physics*, chapter Principles of operation of multiwire proportional and drift chambers, page 79. Addison-Wesley, 1987. URL `http://cdsweb.cern.ch/record/117989/`. ISBN-13: 978-0201114874.

[169] K. Hoepfner. ACT Lectures on Detectors - Muon systems, 2011. URL `http://cdsweb.cern.ch/record/1350257`. CERN Academic Training Lecture.

[170] G. Pugliese. Operations and Performance of the CMS DT and RPC muon systems at LHC. Technical report, CMS, 2012. URL `http://cdsweb.cern.ch/record/1497241`. CMS-CR-2012-327, presented at ICHEP12.

[171] CMS Collaboration. CMS The TriDAS Project Technical Design Report, Volume 1: The Trigger Systems. Technical report, CMS, 200. URL `http://cdsweb.cern.ch/record/706847`. CERN-LHCC-2000-038, CMS-TDR-006-1.

[172] P. R. Klabbers. Operation and Performance of the CMS Level-1 Trigger during 7 TeV Collisions. Technical report, CMS, 2011. URL `http://cdsweb.cern.ch/record/1395417`. CMS-CR-2011-183.

[173] C. Diez Pardos. *Search for Heavy $W'$ Bosons Decaying into Muon and Neutrino in pp Collisions at $\sqrt{s} = 7$ TeV in the CMS Experiment at the LHC.* PhD thesis, CIEMAT-Madrid, 2011. URL `http://cdsweb.cern.ch/record/1446574`. CERN-THESIS-2012-038.

[174] F. Thyssen. Performance of the Resistive Plate Chambers in the CMS experiment. *Journal of Instrumentation*, 7(01):C01104, 2012. doi: doi:10.1088/1748-0221/7/01/C01104. CMS-CR-2011-192.

[175] W. Smith. HCPSS12 lectures on Trigger & DAQ, 2012. URL `http://projects.fnal.gov/hcpss/hcpss12/index.html`.

[176] CMS Collaboration. Absolute Calibration of the CMS Luminosity Measurement: Summer 2011 Update. CMS Physics Analysis Summary CMS-PAS-EWK-11-001, CMS, 2011. URL `http://cdsweb.cern.ch/record/1376102`.

[177] CMS Collaboration. Absolute Calibration of the Luminosity Measurement at CMS: Winter 2012 Update. CMS Physics Analysis Summary CMS-PAS-SMP-12-008, CMS, 2012. URL `http://cdsweb.cern.ch/record/1434360`.

[178] J. Hegeman and H. D. Yoo. CMS luminosity calibration results / Prospects with 2012 Luminosity Measurement in CMS Experiment, 2012. URL `http://cdsweb.cern.ch/record/1428504,http://cdsweb.cern.ch/record/1428071`. LHC Lumi Days, CERN.

[179] D. Bělohrad. *Fast Beam Intensity Measurements for the LHC.* PhD thesis, Czech Technical University in Prague, 2010. URL `http://cdsweb.cern.ch/record/1301517`. CERN-THESIS-2010-131.

[180] A. Alici et al. LHC Bunch Current Normalisation for the October 2010 Luminosity Calibration Measurements. Technical report, LHC, 2011. URL `http://cdsweb.cern.ch/record/1333997/`. CERN-ATS-Note-2011-016.

[181] S. van der Meer. Calibration of the effective beam height in the ISR. Technical report, CERN, 1986. URL `http://cdsweb.cern.ch/record/296752`. CERN-ISR-PO-68-31.

[182] S. White. *Determination of the Absolute Luminosity at the LHC.* PhD thesis, Université Paris-Sud, 2010. CERN-THESIS-2010-139.

[183] C. Eck et al. LHC Computing Grid Technical Design Report. Technical report, CERN, 2005. URL `http://cdsweb.cern.ch/record/840543/`. CERN-LHCC-2005-024.

[184] C. Rovelli. The detailed simulation of the CMS detector. In *10th ICATPP Conference*, 2007. URL `http://cdsweb.cern.ch/record/1096432`. CERN-CMS-CR-2007-082.

[185] S. Agostinelli et al. GEANT4–a simulation toolkit. *Nucl. Instrum. Meth.*, A506:250, 2003. doi: 10.1016/S0168-9002(03)01368-8.

[186] J. Allison, K. Amako, J. Apostolakis, H. Araujo, P.A. Dubois, et al. Geant4 developments and applications. *IEEE Trans.Nucl.Sci.*, 53:270, 2006. doi: 10.1109/TNS.2006.869826. URL `http://slac.stanford.edu/cgi-wrap/getdoc/slac-pub-11870.pdf`.

[187] B. Stroustrup. *The C++ Programming Language.* Addison-Wesley Longman Publishing Co., Inc., Boston, MA, USA, 3rd edition, 2000. ISBN 0201700735.

[188] Python webpage, 2012. URL `http://www.python.org/`.

[189] R. Brun and F. Rademakers. ROOT: An object oriented data analysis framework. *Nucl.Instrum.Meth.A*, 389:81, 1997. doi: 10.1016/S0168-9002(97)00048-X. project webpage: `http://root.cern.ch/`.

[190] CMS Collaboration. Model Unspecific Search for New Physics in pp Collisions at $\sqrt{s} =$ 7 TeV. Technical Report CMS-PAS-EXO-10-021, CMS, 2011. URL `http://cdsweb.cern.ch/record/1360173`.

[191] H. Pieta. *MUSiC - A Model Unspecific Search in CMS based on 2010 LHC data.* PhD thesis, RWTH Aachen Univerity, 2012. URL `http://darwin.bth.rwth-aachen.de/opus3/volltexte/2012/4194/`.

[192] H. P. Bretz, M. Brodski, M. Erdmann, R. Fischer, A. Hinzmann, et al. A Development Environment for Visual Physics Analysis. *JINST*, 7:T08005, 2012. doi: 10.1088/1748-0221/7/08/T08005. URL `http://arxiv.org/abs/1205.4912`. webpage of the PXL/Vispa projects: `http://www.vispa.physik.rwth-aachen.de`.

[193] CMS Collaboration. Performance of CMS muon reconstruction in pp collision events at sqrt(s) = 7 TeV. *JINST*, 7:P10002, 2012. URL `http://arxiv.org/abs/1206.4071`. CMS-MUO-10-004.

[194] CMS Collaboration. Performance of muon identifiaction in pp collisions at $\sqrt{s} = 7$ TeV. Technical report, CMS, 2010. URL `http://cdsweb.cern.ch/record/1279140/`. CMS-PAS-MUO-10-002.

[195] G. Abbiendi et al. Muon Reconstruction in the CMS Detector. Technical report, CMS, 2009. CMS-AN-2008-097.

[196] R. Frühwirth. Application of Kalman filtering to track and vertex fitting. *Nucl.Instrum.Meth.*, A262:444, 1987. doi: 10.1016/0168-9002(87)90887-4.

[197] R. Frühwirth, M. Regler, R. K. Bock, H. Grote, and D. Notz. *Data Analysis Techniques for High-Energy Physics.* Cambridge University Press, second edition, 2000.

[198] A. Strandlie and R. Frühwirth. Track and vertex reconstruction: From classical to adaptive methods. *Rev. Mod. Phys.*, 82:1419, 2010. doi: 10.1103/RevModPhys.82.1419.

[199] R. Mankel. A concurrent track evolution algorithm for pattern recognition in the HERA-B main tracking system. *Nucl. Instrum. Meth. A*, 395:169, 1997.

[200] R. Mankel and A. Spiridonov. The Concurrent Track Evolution algorithm: extension for track finding in the inhomogeneous magnetic field of the HERA-B spectrometer. *Nucl. Instrum. Meth. A*, 426:268, 1999. URL `http://arxiv.org/abs/hep-ex/9809021v1`.

[201] S. Cucciarelli, M. Konecki, D. Kotlinski, and T. Todorov. Track reconstruction, primary vertex finding and seed generation with the Pixel Detector. Technical report, CMS, 2006. URL `http://cdsweb.cern.ch/record/927384/`. CMS-NOTE-2006-026.

[202] W. Adam et al. Track Reconstruction in the CMS tracker. Technical report, CMS, 2006. URL `http://cdsweb.cern.ch/record/934067/`. CMS-NOTE-2006-041.

[203] S. Iyer Dutta, M.H. Reno, I. Sarcevic, and D. Seckel. Propagation of Muons and Taus at High Energies. *Phys. Rev. D*, 63:094020, 2001. doi: 10.1103/PhysRevD.63.094020. URL `http://arxiv.org/abs/hep-ph/0012350v1`.

[204] W. Lohmann, R. Kopp, and R. Voss. Energy Loss of Muons in the Energy Range 1-10000 GeV. Technical report, CERN, 1985. URL `http://cdsweb.cern.ch/record/158706`. CERN-85-03.

[205] CMS Collaboration. Tracking and Primary Vertex Results in First 7 TeV Collisions. Technical report, CMS, 2010. URL `http://cdsweb.cern.ch/record/1279383`. CMS-PAS-TRK-10-005.

[206] CMS Collaboration. Performance of CMS Muon Reconstruction in Cosmic-Ray Events. *JINST*, 5:T03022, 2010. doi: 10.1088/1748-0221/5/03/T03022. URL `http://arxiv.org/abs/0911.4994v2`.

[207] CMS Collaboration. Measurement of the charge asymmetry of atmospheric muons with the CMS detector. Technical report, CMS, 2010. URL `http://cdsweb.cern.ch/record/1259232`. CMS-PAS-MUO-10-001.

[208] M. Hildreth. Pileup Issues and Simulation in CMS, 2011. URL `https://indico.cern.ch/conferenceOtherViews.py?view=standard&confId=144956`. presentation given at the workshop: LHC detector simulations: status, needs and prospects.

[209] T. Sjöstrand, S. Mrenna, and P. Z. Skands. PYTHIA 6.4 Physics and Manual. *JHEP*, 05:26, 2006. doi: 10.1088/1126-6708/2006/05/026. URL `http://arxiv.org/abs/arXiv:hep-ph/0603175`.

[210] S. Frixione and B. R. Webber. Matching NLO QCD Computations and Parton Shower Simulations. *JHEP*, 06:29, 2002. doi: 10.1088/1126-6708/2002/06/029.

[211] S. Frixione, F. Stoeckli, P. Torrielli, and B. R. Webber. NLO QCD corrections in Herwig++ with MC@NLO. *JHEP*, 01:53, 2011. doi: 10.1007/JHEP01(2011)053. URL `http://arxiv.org/abs/1010.0568`. CERN-TH/2010-212.

[212] T. Sjöstrand, S. Mrenna, and P. Skands. A Brief Introduction to PYTHIA 8.1. *Comp. Phys. Comm.*, 178:852, 2008. doi: 10.1016/j.cpc.2008.01.036.

[213] G. Altarelli, R. K. Ellis, and G. Martinelli. Leptoproduction and Drell-Yan Processes Beyond the Leading Approximation in Chromodynamics. *Nucl.Phys.B*, 143:521, 1978. doi: 10.1016/0550-3213(78)90067-6.

[214] G. Altarelli, R. K. Ellis, and G. Martinelli. Large Perturbative Corrections to the Drell-Yan Process in QCD. *Nucl. Phys. B*, 157:461, 1979. doi: 10.1016/0550-3213(79)90116-0.

[215] A. D. Martin et al. Parton distributions for the LHC. *Eur. Phys. J. C*, 63:189, 2009. doi: 10.1140/epjc/s10052-009-1072-5. URL `http://arxiv.org/abs/0901.0002v3`.

[216] R. Hamberg, W. L. van Neerven, and T. Matsuura. A Complete calculation of the order $\alpha - s^2$ correction to the Drell-Yan $K$ factor. *Nucl.Phys.B*, 359:343, 1991. doi: 10.1016/0550-3213(91)90064-5.

[217] K. Melnikov and F. Petriello. Electroweak gauge boson production at hadron colliders through $O(\alpha_s^2)$. *Phys. Rev. D*, 74:114017, 2006. doi: 10.1103/PhysRevD.74.114017. URL http://arxiv.org/abs/hep-ph/0609070.

[218] M. R. Whalley, D. Bourilkov, and R. C. Group. The Les Houches Accord PDFs (LHAPDF) and Lhaglue, 2005. URL http://arxiv.org/abs/hep-ph/0508110.

[219] P. M. Nadolsky et al. Implications of CTEQ global analysis for collider observables. *Phys. Rev. D*, 78:013004, 2008. doi: 10.1103/PhysRevD.78.013004.

[220] G. Corcella et al. HERWIG 6.5: an event generator for hadron emission reactions with interfering gluons (including supersymmetric processes). *JHEP*, 01:10, 2001. doi: 10.1088/1126-6708/2001/01/010.

[221] P. Golonka and Z. Was. PHOTOS Monte Carlo: a precision tool for QED corrections in Z and W decays. *Eur. Phys. J. C*, 45:97, 2006. doi: 10.1140/epjc/s2005-02396-4.

[222] J. M. Butterworth, Jeffrey R. Forshaw, and M. H. Seymour. Multiparton interactions in photoproduction at HERA. *Z. Phys. C*, 72:637, 1996. doi: 10.1007/s002880050286.

[223] S. Frixione, P. Nason, and C. Oleari. Matching NLO QCD computations with Parton Shower simulations: the POWHEG method. *JHEP*, 0711:070, 2007. doi: 10.1088/1126-6708/2007/11/070. URL http://arxiv.org/abs/0709.2092.

[224] S. Alioli, P. Nason, C. Oleari, and E. Re. A general framework for implementing NLO calculations in shower Monte Carlo programs: the POWHEG BOX. *JHEP*, 1006:043, 2010. doi: 10.1007/JHEP06(2010)043. URL http://arxiv.org/abs/1002.2581.

[225] H.-L. Lai et al. New parton distributions for collider physics. *Phys. Rev. D*, 82:074024, 2010. doi: 10.1103/PhysRevD.82.074024. URL http://arxiv.org/abs/arXiv:1007.2241.

[226] R. Gavin, Y. Li, F. Petriello, and S. Quackenbush. FEWZ 2.0: A code for hadronic Z production at next-to-next-to-leading order. *Comp. Phys. Comm.*, 182:2388, 2011. doi: 10.1016/j.cpc.2011.06.008.

[227] D. Bourilkov. private communication, 2011.

[228] U. Baur, O. Brein, W. Hollik, C. Schappacher, and D. Wackeroth. Electroweak radiative corrections to neutral current Drell-Yan processes at hadron colliders. *Phys. Rev. D*, 65:033007, 2002. doi: 10.1103/PhysRevD.65.033007. URL http://arxiv.org/abs/hep-ph/0108274v1.

[229] V. A. Zykunov. Weak radiative corrections to the Drell-Yan process for large invariant mass of a dilepton pair. *Phys. Rev. D*, 75:073019, 2007. URL http://www.arxiv.org/abs/hep-ph/0509315v2.

[230] C. M. Carloni Calame, G. Montagna, O. Nicrosini, and A. Vicini. Precision electroweak calculation of the production of a high transverse-momentum lepton pair at hadron colliders. *JHEP*, 10:109, 2007. doi: 10.1088/1126-6708/2007/10/109.

[231] H. Spiesberger. QED Radiative Corrections for Parton Distributions. *Phys. Rev. D*, 52: 4936, 1995. URL `http://arxiv.org/abs/hep-ph/9412286`.

[232] M. Roth and S. Weinzierl. QED corrections to the evolution of parton distributions. *Phys. Lett. B*, 590:190, 2004. URL `http://arxiv.org/abs/hep-ph/9412286`.

[233] A.D. Martin, R.G. Roberts, W.J. Stirling, and R.S. Thorne. Parton distributions incorporating QED contributions. *Eur.Phys.J. C*, 39:155, 2005. doi: 10.1140/epjc/s2004-02088-7. URL `http://arxiv.org/abs/hep-ph/0411040v1`.

[234] G. Balossini et al. Electroweak and QCD corrections to Drell-Yan Processes. *Acta Phys. Polon. B*, 39:1675, 2008.

[235] S. Dittmaier and M. Huber. Radiative corrections to the neutral-current Drell-Yan process in the Standard Model and its minimal supersymmetric extension. *JHEP*, 1001:060, 2010. doi: 10.1007/JHEP01(2010)060. URL `http://arxiv.org/abs/0911.2329v2`.

[236] S. Haywood, P.R. Hobson, W. Hollik, Z. Kunszt, G. Azuelos, et al. Electroweak physics, 1999. URL `http://arxiv.org/abs/hep-ph/0003275`.

[237] C. Buttar et al. Standard Model Handles and Candles Working Group: Tools and Jets Summary Report, 2008. URL `http://arxiv.org/abs/0803.0678v1`.

[238] L. Barzè, G. Montagna, P. Nason, O. Nicrosini, F. Piccinini, and A. Vicini. Neutral current Drell-Yan with combined QCD and electroweak corrections in the POWHEG BOX, 2013. URL `http://arxiv.org/abs/1302.4606v1`.

[239] R. D. Ball et al. Fitting parton distribution data with multiplicative normalization uncertainties. *JHEP*, 05:75, 2010. doi: 10.1007/JHEP05(2010)075.

[240] A. Tricoli, A. M. Cooper-Sarkar, and C. Gwenlan. Uncertainties on W and Z production at the LHC. In *HERA@LHC workshop 2005 Proceedings*, 2005. URL `http://arxiv.org/abs/hep-ex/0509002v1`. ATLAS-COM-PHYS-2005-045.

[241] C. Hof. *Implementation of a Model-Independent Search for New Physics with the CMS Detector Exploiting the World-Wide LHC Computing Grid.* PhD thesis, RWTH Aachen University, 2009. URL `http://web.physik.rwth-aachen.de/~hebbeker/theses/hof_phd.pdf`.

[242] J. Alwall, M. Herquet, F. Maltoni, O. Mattelaer, and T. Stelzer. MadGraph 5 : Going Beyond. *JHEP*, 1106:128, 2011. doi: 10.1007/JHEP06(2011)128. URL `http://arxiv.org/abs/arXiv:1106.0522`. MadGraph homepage: `http://madgraph.hep.uiuc.edu/`.

[243] N. Kidonakis. Higher-order corrections to top-antitop pair and single top quark production, 2009. URL `http://arxiv.org/abs/0909.0037v1`.

[244] J. M. Campbell and R.K. Ellis. MCFM for the Tevatron and the LHC. *Nucl.Phys.Proc.Suppl.*, 205-206:10, 2010. doi: 10.1016/j.nuclphysbps.2010.08.011. URL `http://arxiv.org/abs/1007.3492`. MCFM homepage: `http://mcfm.fnal.gov/`.

[245] A. Lusiani. Experimental Review on Lepton Universality and Lepton Flavour Violation tests at the B-factories. In *Proceedings of the International Conference Kaon'07*, 2008. URL `http://arxiv.org/abs/0709.1599v1`.

[246] D. Acosta et al. Search for High-Mass Resonances Decaying to Muon Pairs with $15\,\mathrm{pb}^{-1}$ of Collisions Gathered at $\sqrt{s} = 7\,\mathrm{TeV}$, 2010. CMS AN-10-317.

[247] D. Acosta et al. Search for High-Mass Resonances Decaying to Muon Pairs with $40\,\mathrm{pb}^{-1}$ of Collisions Gathered at $\sqrt{s} = 7\,\mathrm{TeV}$, 2011. CMS AN-11-278,CMS AN-11-472.

[248] C. J. Clopper and E. S. Pearson. The Use of Confidence or Fiducial Limits Illustrated in the Case of the Binomial. *Biometrika*, 26(4):404, 1934. doi: http://dx.doi.org/10.2307/2331986. URL `http://www.jstor.org/discover/10.2307/2331986`.

[249] Pythia8 webpage, 2012. URL `http://home.thep.lu.se/~torbjorn/pythiaaux/present.html`. HTML manual: `http://home.thep.lu.se/~torbjorn/pythia81html/Welcome.html`.

[250] F. Bordry and K. Foraz. summary of sessions 5 and 6: long shutdown 1 (LS1) 2013-2014, 2012. URL `https://espace.cern.ch/acc-tec-sector/Chamonix/Chamx2012/papers/FBKF_0_56.pdf`. Proceedings of the Chamonix 2012 workshop on LHC performance.

[251] T. Gleisberg, S. Hoeche, F. Krauss, M. Schonherr, S. Schumann, et al. Event generation with SHERPA 1.1. *JHEP*, 0902:007, 2009. doi: 10.1088/1126-6708/2009/02/007. URL `http://arxiv.org/abs/arXiv:0811.4622`.

[252] G. Landsberg. private communication, 2011.

[253] P. Mathews et al. Next-to-Leading order QCD corrections to the Drell-Yan cross section in models of TeV-scale gravity. *Nucl. Phys. B*, 713:333, 2005. doi: 10.1016/j.nuclphysb.2005.01.051. URL `http://arxiv.org/abs/hep-ph/0411018`.

[254] P. Mathews and V. Ravindran. Angular distribution of Drell-Yan process at hadron colliders to NLO-QCD in models of TeV scale gravity. *Nucl.Phys.B*, 753:1, 2006. doi: 10.1016/j.nuclphysb.2006.06.039. URL `http://arxiv.org/abs/hep-ph/0507250v2`.

[255] M. C. Kumar, P. Mathews, and V. Ravindran. private communication, 2011.

[256] M. C. Kumar, P. Mathews, and V. Ravindran. PDF and scale uncertainties of various DY distributions in ADD and RS models at hadron colliders. *Eur. Phys. J. C*, 49:599, 2007. doi: 10.1140/epjc/s10052-006-0054-0. URL `http://arxiv.org/abs/hep-ph/0604135v2`.

[257] W. Verkerke and D. Kirkby. RooFit Users Manual v2.91, 2008. URL `ftp://root.cern.ch/root/doc/RooFit_Users_Manual_2.91-33.pdf`.

[258] L. Moneta et al. The RooStats Project, 2010. URL `http://arxiv.org/abs/1009.1003v2`. ACAT2010 Conference Proceedings.

[259] V. V. Patil and H. V. Kulkarni. Comparison of Confidence Intervals for the Poisson Mean: some new Aspects. *REVSTAT*, 10(2):211, 2012. URL `http://www.ine.pt/revstat/pdf/rs120203.pdf`.

[260] F. Garwood. Fiducial limits for the Poisson distribution. *Biometrika*, 28:437, 1936. URL `http://www.jstor.org/stable/10.2307/2333958`.

[261] H1 collaboration. A General search for new phenomena in ep scattering at HERA. *Phys. Lett. B*, 602:14, 2004. doi: 10.1016/j.physletb.2004.09.057. URL `http://arxiv.org/abs/hep-ex/0408044v1`.

[262] L. Lyons. Open statistical issues in particle physics. *Ann. Appl. Stat*, 2(3):887, 2008. URL `http://arxiv.org/abs/0811.1663v1`.

[263] Physics Results EXO-11-087, 2012. URL `https://twiki.cern.ch/twiki/bin/view/CMSPublic/PhysicsResultsEXO11087`.

[264] M. Brodski, T. Hebbeker, A. Meyer, T. Pook, S. A. Schmitz, and S. Thüer. Search for Large Extra Dimensions in Dimuon Events in pp Collisions at $\sqrt{s} = 8\,\text{TeV}$, 2012. CMS AN-12-496.

[265] Physics Results EXO-11-027, 2013. URL `https://twiki.cern.ch/twiki/bin/view/CMSPublic/PhysicsResultsEXO12027`.

[266] R. Kelley, L. Randall, and B. Shuve. Early (and Later) LHC Search Strategies for Broad Dimuon Resonances. *JHEP*, 1102:014, 2011. doi: 10.1007/JHEP02(2011)014. URL `http://arxiv.org/abs/1011.0728v2`.

[267] B. Clerbaux et al. Statistical Analysis of a Resonant Signal Search in Multiple Final State Modes, 2010. CMS AN-10-312.

[268] J. M. Tucker. *High transverse momentum muon reconstruction, a search for narrow dimuon resonances, and statistical techniques for LHC analyses.* PhD thesis, University of California, Los Angeles, 2011.

[269] CMS $Z'$ analysis group. Statistical Inference in a Search for a Narrow Resonance, 2012. CMS AN-12-185.

[270] CMS $Z'$ dimuon analysis group. Search for High Mass Resonances Decaying to Muon Pairs at $\sqrt{s} = 8$ TeV, 2012. CMS AN-12-182.

[271] CMS $Z'$ dielectron analysis group. Search for High Mass Resonances Decaying to Electron Pairs at 8 TeV, 2012. CMS AN-12-171.

[272] P. Langacker. The Physics of Heavy $Z'$ Gauge Bosons. *Rev.Mod.Phys.*, 81:1199–1228, 2009. doi: 10.1103/RevModPhys.81.1199.

[273] A. Leike. The Phenomenology of extra neutral gauge bosons. *Phys.Rept.*, 317:143, 1999.

[274] AK Datta, K. Kong, and K. T. Matchev. Discrimination of supersymmetry and universal extra dimensions at hadron colliders. *Phys.Rev.*, D72:096006, 2005. doi: 10.1103/PhysRevD.72.096006,10.1103/PhysRevD.72.119901.

[275] L. Edelhäuser, T. Flacke, and M. Krämer. Constraints on models with universal extra dimensions from dilepton searches at the LHC, 2013. URL `http://arxiv.org/abs/1302.6076v1`.

[276] J. Bijnens, P. Eerola, M. Maul, A. Mansson, and T. Sjöstrand. QCD signatures of narrow graviton resonances in hadron colliders. *Phys. Lett. B*, 503:341, 2001. doi: 10.1016/S0370-2693(01)00238-6.

[277] P. Mathews, V. Ravindran, and K. Sridhar. NLO-QCD corrections to dilepton production in the Randall-Sundrum model. *JHEP*, 0510:031, 2005. doi: 10.1088/1126-6708/2005/10/031.

[278] ATLAS Collaboration. Search for high mass dilepton resonances with 5 fb$^{-1}$ of pp collisions at $\sqrt{s} = 7$ TeV with the ATLAS experiment. Technical report, ATLAS, 2012. URL http://cdsweb.cern.ch/record/1428547/.

[279] A. Caldwell, D. Kollar, and K. Kröninger. BAT - The Bayesian Analysis Toolkit. *Comp. Phys. Comm.*, 180:2197, 2009. doi: 10.1016/j.cpc.2009.06.026. URL http://www.mppmu. mpg.de/bat/.

[280] G. Marsaglia and W. W. Tsang. A simple method for generating gamma variables. *ACM Trans. Math. Softw.*, 26(3):363, 2000. URL http://doi.acm.org/10.1145/358407. 358414.

[281] J. Aitchison and J. A. C. Brown. *The Lognormal Distribution.* Cambridge University Press, 1957. reprinted 1981.

[282] T. Pratchett. *Monstrous Regiment.* Corgi, 2004. ISBN-13: 978-0552149419.

# Acknowledgments and Closing Quote

The stylistic device of concluding a piece of writing with borrowed words goes at least back to Seneca. The most fun part of the following quote may be that remaining undecided about its validity actually seems to be an attractive option. "The presence of those seeking the truth is infinitely to be preferred to the presence of those who think they've found it." [282]

# Curriculum Vitae

## Personal

| | |
|---|---|
| Name: | **Stefan Antonius Schmitz** |
| Address: | Fr.-v.-d.-Schulenburg-Str.41, |
| | 41466 Neuss, Germany |
| Telephone: | +49 241 80 27310  (office at RWTH Aachen) |
| | +49 157 84133509 (mobile phone) |
| | |
| Email: | staschmitz@physik.rwth-aachen.de |
| Citizenship: | German |
| Birth Date: | 14 November 1983 |
| Birth Place: | Düsseldorf |

## Education

| | |
|---|---|
| **12/2009 - 08/2013** | **doctoral candidate at RWTH Aachen University, III. Physikalisches Institut A**<br>thesis supervisor: Prof. Dr. Thomas Hebbeker |
| 05/2010 - 12/2011 | resident at CERN |
| 05/2010 - 08/2010 | short term studentship sponsored by the Helmholtz Alliance "Physics at the Terascale" for work on the RooStats software package for statistical analysis at CERN |
| | |
| **2003 - 2009** | **physics student at RWTH Aachen University**<br>Diplom, final grade: 1.1, sehr gut ("very good") |
| 2006 | participation in the ERASMUS programme, exchange semester at Queen Mary College, University of London, United Kingdom (field of study: physics) |
| 2005 | Vordiplom (intermediate examination at German universities) |
| | |
| **1994 - 2003** | **Nelly-Sachs-Gymnasium, Neuss, Germany** |
| 2003 | Abitur (secondary school degree qualifying for higher education), final grade: 1.6 |
| 2002 | participation in the Deutsche Schülerakademie (a summer programme for intellectually able and academically motivated students in Germany) |

## Main Research Interests

- searches for new physics at hadron colliders, with a focus on models with spatial extra dimensions

- methods and software development for statistical data analysis in high energy physics

## Research Experience

| | | |
|---|---|---|
| doctoral program | - | thesis topic: „Search for Large Spatial Extra Dimensions in Dimuon Events at CMS" |
| | - | contributions to the CMS search for new heavy dilepton resonances (since 2012) |
| | - | contributions to the CMS software for statistical analysis |
| | - | CMS service work: user support for statistics software, DAQ shifts |
| Diplom | - | thesis topic: „Model Unspecific Search for New Physics with High pT Photons in CMS " |

## Teaching Experience

- tutor at particle physics lab classes for undergraduate students

- tutor at experimental physics lecture courses

- supervision of students during their familiarization with research in the context of CMS searches for new physics

## Work Experience

| | |
|---|---|
| 12/2009 – 08/2013 | research assistant at RWTH Aachen University, III. Physikalisches Institut A |
| 2008-2009 | research student assistant at RWTH Aachen University, III. Physikalisches Institut A |

## Publications

| | |
|---|---|
| Refereed journals | CMS author since late 2009, major contributions to: |
| | - "Search for heavy narrow dilepton resonances in pp collisions at sqrt(s) = 7 TeV and sqrt(s) = 8 TeV" Phys. Lett. B 720 (2013) 63 , CMS-EXO-12-015 |
| | - "Search for large extra dimensions in dimuon and dielectron events in pp collisions at sqrt(s) = 7 TeV", Phys. Lett. B 711 (2012) 15, CMS-EXO-11-087 |
| Proceedings | - "Search for Large Extra Dimensions in Dimuon Events at CMS", Physics at LHC 2011, Perugia (Italy), CMS-CR-2011-205 |
| CMS Physics Analysis Summaries | - "Search for Large Extra Dimensions in Dimuon Events in pp Collisions at sqrt(s) = 8 TeV", CMS-PAS-EXO-12-027 |
| | - "Search for Narrow Resonances in Dilepton Mass Spectra in pp Collisions at sqrt(s) = 8 TeV", CMS-PAS-EXO-12-061 |
| | - "Search for Large Extra Dimensions in Dimuon Events in pp Collisions at sqrt(s) = 7 TeV", CMS-PAS-EXO-11-039, CMS-PAS-EXO-10-020 |
| | - "A Model Independent Search For New Physics in an Inclusive Di-lepton Event Sample", CMS-PAS-EXO-10-024 |
| | - "MUSiC – An Automated Scan for Deviations between Data and Monte Carlo Simulation", CMS PAS EXO-08-005 |

## Selected Presentations

| 04/2013 | "Searches for new heavy resonances and large extra dimensions at CMS", DIS 2013: XXI. International Workshop on Deep-Inelastic Scattering and Related Subjects, Marseille (France) |
| 03/2012 | "Search for ADD Extra Dimensions in Dimuon Events at CMS", DPG Spring meeting of the German Physical Society (DPG) 2012, Göttingen (Germany) |
| 12/2011 | "Search for large extra dimensions in di-muons with CMS", Annual Workshop of the Helmholtz Alliance "Physics at the Terascale", Bonn (Germany) |
| 08/2011 | "CMS Extra dimension signatures", Implications of LHC results for TeV-scale physics workshop, CERN (Switzerland) |
| 04/2011 | "Extra dimensions: CMS", LPCC BSM Jamboree, CERN (Switzerland) |

## Summer Schools

| 2012 | Hadron Collider Physics Summer School 2012, Fermilab (USA) |
| 2010 | The 2010 European School of High-Energy Physics, Raseborg (Finland) |
| 2009 | 41. Herbstschule fuer Hochenergiephysik Maria Laach, Bautzen (Germany) |

## Other Skills

| languages | German (mother tongue), English (fluent), French (basic) |
| programming/ scripting | C++ (advanced), bash shell (intermediate), Python, Java (basic) |
| operating systems | Linux, Windows |
| event generators | Pythia6/8, MC@NLO, Horace, fewz |
| other software | ROOT (including RooFit and RooStats), BAT, OpenOffice, LaTeX, LHAPDF, Inkscape, revision control: Git, SVN |

## Non-Academic Interests

iaido (shodan), piano playing

Aachen, 24 July 2013

**Stefan A. Schmitz**